Microsystem Technologies
https://doi.org/10.1007/s00542-020-04755-3

TECHNICAL PAPER

Perforated serpentine membrane with AlN as dielectric material shunt capacitive RF MEMS switch fabrication and characterization

Lakshmi Narayana Thalluri[1] · Koushik Guha[2] · K. Srinivasa Rao[3] · G. Venkata Hari Prasad[4] · K. Girija Sravani[2,3] · K. S. R. Sastry[5] · Appala Raju Kanakala[1] · P. Bose Babu[1]

Received: 16 October 2019 / Accepted: 18 January 2020

Abstract
In this communication, we have designed, simulated, performance improved, fabricated and characterized a shunt capacitive RF MEMS switch with perforated serpentine membrane (Au). Fabrication is done using surface micromachining with four masks. AlN dielectric material of 50 nm thickness is offering high isolation of − 58.5 dB at 31.5 GHz, and incorporation of perforation to the membrane the switch insertion loss is very low i.e., − 0.4 dB. The perforated serpentine membrane with non-uniform meanders of 500 nm thickness using Au material is helped to reduce the actuation voltage, the fabricated switch is requiring 4.5 V actuation voltage. DC sputtering PVD is used to deposit metal (Au) and dielectric (AlN) thin Films. S1813 photoresist is used as a sacrificial layer and the membrane structure is released using piranha, IPA and critical point drying (Pressure 1260 Psi, Temperature 31 °C).

1 Introduction

There is a need of modern technology to fulfill the requirements in the present day communication applications i.e., reconfigurable devices like reconfigurable antennas, filters, phase shifters, isolators especially in Ka band applications more and more in satellite communication (Dragoman et al. 2017; Sharma et al. 2014; Nejad and Hasani 2016; Park et al. 2009; Kolis et al. 2017; Liu et al. 2017; Zhang et al. 2017; Fouladi and Mansour 2010; Mulloni et al. 2015). For these all requirements MEMS technology based RF MEMS switches are giving the best solution when compared with traditional CMOS and GaAs technologies based FET and PIN diode RF switches. The MEMS miniaturize technology based RF switches fabrication can be possible using surface micromachining (Chawla and Khanna 2014). Quartz, Si, FR4 are generally used as a substrate materials. If the substrate is semiconductor to isolate it from the further conducting layers (CPW) an insulating material like SiO_2, Si_3N_4 need to deposit on semiconductor surface (Molaei and Ganji 2016; Guha et al. 2016; Mardivirin et al. 2009; Philippine et al. 2013; Guha et al. 2017). CPW transmission lines are best for shunt capacitive RF MEMS switches (Agarwal et al. 2016a, b; Rebeiz and Muldavin 2001). Cu is a high contamination material that why Au is used for CPW and actuation lines with Ti, TiW, Cr can be deposit between CPW and insulating layer for adhesion (Persano et al. 2011; Puyal et al. 2009; Ramadoss et al. 2003). Shunt capacitive switches the standard G/S/G dimensions for CPW transmission line are 90 µm/60 µm/90 µm (Rizk and Rebeiz 2003). To deposit the Au we can use sputtering or E-beam evaporation. For pattering CPW and actuation lines we can used ICP etching.

Si_xN_y, AlN can be used as dielectric materials because of their high dielectric constant ≈ 9.8 (Stefanini et al.

✉ Lakshmi Narayana Thalluri
drtln9@gmail.com

[1] Dr. A. P. J. Abdul Kalam Research Forum, Department of Electronics and Communication Engineering, Andhra Loyola Institute of Engineering and Technology, Vijayawada 520008, Andhra Pradesh, India

[2] MEMS Research Center, Department of ECE, Koneru Lakshmaiah Educational Foundation (Deemed to be University), Green Fields, Vaddeswaram 522502, Guntur, India

[3] National MEMS Design Center, Department of Electronics and Communication Engineering, National Institute of Technology, Silchar 788010, Assam, India

[4] Department of Electronics and Communication Engineering, CMRCET, Kandlakoya, Hyderabad, Telangana, India

[5] Department of Electronics and Communication Engineering, D V R and Dr. H S MIC College of Technology, Kanchikacherla, AP, India

Published online: 31 January 2020

2011; Shekhar et al. 2017; Badía et al. 2012). To deposit dielectric materials with ultra-low thickness we can use PECVD or sputtering. For patterning dielectric material we can use ICP or RIE. For any MEMS structure fabrication choosing the sacrificial layer is very difficult task, generally amorphous Si or AZ6130 or phospho-silicate glass (PSG) are used as sacrificial layers.

The sacrificial layer can be deposit using PECVD or spin coating based on the material, the thickness is in micrometer range. Al, Au materials we can use to design the membrane but Al is fatigue in nature so Au preferable. Finally releasing the membrane is the tricky process for this we can use XeF_2 Etch System, Isotropic O_2 plasma process, Plasma-Ashing depending on the type of sacrificial layer (Yang et al. 2015a, b). The major challenges in the fabrication of miniaturization of the switch are stiction, charge injection and releasing of the MEMS structure both will decide the switch reliability (Zhang et al. 2008).

The work presented in this paper mainly concentrate on fabrication of high reliable RF MEMS switch with best performance in terms of actuation voltage, insertion losses and isolation losses. The work we stated with design, simulation, and performance analysis of switch using FEM tools which will help to reduce the fabrication cost and switch with improved performance. In the design aspects, we have noticed that non uniform meanders based serpentine structure helps the switch to reduce the actuation voltage. We have extended our analysis on switch isolation property by placing different dielectric materials and observed that switch is offering high isolation for AlN as dielectric material. Eventually we have fabricated RF MEMS switch by using surface micromachining by incorporating simulation aspects.

This paper is organized as follows: Sect. 2 presents the proposed shunt capacitive RF MEMS switch behaviors and design procedure. The surface micromachining based switch fabrication procedure is explained in Sect. 3. Finally the switch characterization using Probe station and MSA is discussed in Sect. 4.

2 Shunt capacitive RF MEMS switch

2.1 Parametric modeling

The RF MEMS switches are designed by placing a micro/nano mechanically actuated structure on the top of the CPW transmission line. The switch performance is analyzed by using mechanical, electrical and radio frequency properties. The switch discussed in this paper is a electrostatically actuated vertical deflective capacitive shunt RF MEMS switch with CPW transmission line and two bottom electrodes. A perforated serpentine membrane with non-uniform meanders is used as an actuating structure.

With prior analysis on the serpentine structure, the spring constant of the non-uniform meander serpentine structure with seven legs to each meander can be expressed as (Zohur et al. 2013; Peroulis et al. 2003; Dussopt and Rebeiz 2003; Hijazi et al. 2003a, b; Alastalo et al. 2003),

$$\frac{1}{K}=\frac{1}{K_1}+\frac{1}{K_2}+\frac{1}{K_3}+\frac{1}{K_4}+\frac{1}{K_5}+\frac{1}{K_6}+\frac{1}{K_7} \tag{1}$$

where

$$K_{(1,2,3,4,5,6,7)}=\frac{Ewt^3}{l^3}$$

When the MEMS structure is electro statically actuated, with what frequency the membrane resonate is known as natural or resonant frequency (f_r) it can be expressed as,

$$f_r=\frac{1}{2\pi}\sqrt{\frac{K}{m}} \tag{2}$$

where m is the mass of the membrane. The actuation voltage (or) pull in voltage (Vp) is the minimum voltage required to pull the micro mechanical structure 2/3 down of the actual height or gap between the membrane and the bottom electrode.

In the switch designed in this paper we have incorporated the perforation to the top electrodes which will ease the switch actuation and membrane release in the fabrication processs. We can express the pull in voltage of the switch as,

$$V_p=\left(\frac{2}{3}g_2\right)V=\sqrt{\frac{8K}{27\left(2\left(A_e-A_p\right)\varepsilon_0\right)}(g_2)^3} \tag{3}$$

where g_2 is the gap between the electrodes, K is the spring constant of the membrane, A_e is the area under the electrodes, A_p is the area removed because the perforation, V is the supply voltage.

The switching time is the mechanical parameter, in electrostatic switch this will depends on the actuation voltage (V_P), supply voltage (V_s) and the natural resonant frequency (ω_0). It can be expressed as (Jensen et al. 2003; Saias et al. 2003)

$$t_s=3.67\frac{V_p}{V_s\omega_0} \tag{4}$$

$$\omega_0=\sqrt{\frac{K}{m}} \tag{5}$$

where m is the membrane mass, k is effective spring constant. From the personal analysis and investigation it is cleared that meander structure with low spring constant helps to reduce the actuation voltage.

Table 1 Serpentine membrane capacitive RF MEMS switch performance analysis in terms of dimensions, perforation and materials

Parameter	Material	Thickness (μm)	Length (μm)	Width (μm)	Pull-in Voltage (V)	Insertion losses (dB) (Range = 0.5–40 GHz)			Isolation losses (dB)	C_{up}	C_{down}
						Gap (or) membrane height (μm)					
						0.5	1	2			
Membrane dimensions	Au	1.5	320	200	10.5 V	Gap = 2 μm, 5 × 5 size perforation, AlN is dielectric material with 100 nm thick			5 × 5 size perforation, AlN is dielectric material with 100 nm thick.	Gap = 2 μm, 100 nm thick AlN	Gap = 0 μm, 100 nm thick AlN
		1	320	200	8.2 V						
		0.5	320	200	6.5 V						
	Al	1.5	320	200	7.1 V	Insertion loss = − 0.8 dB			Insertion loss = − 65 dB	C_{up} = 2.4 fF	C_{down} = 74.2 pF
		1	320	200	5.7 V						
		0.5	320	200	3.85 V						
	Cu	1.5	320	200	8.45 V						
		1	320	200	6.25 V						
		0.5	320	200	4.39 V						
Perforation	Au	15 × 15			6–6.5 V	Gap = 2 μm, 5 × 5 size perforation, AlN is dielectric material with 100 nm thick.			insertion loss = − 65 dB	1.9 fF	65.8 pF
		10 × 10								2.2 fF	70.5 pF
		5 × 5								2.4 fF	74.2 pF
		3 × 3				Insertion loss = -0.8 dB				2.4 fF	74.2 pF
Dielectric material	SiO_2 (ε_r = 4)	1	220	70	Membrane, thickness = 0.5 μm, length= 320 μm, width = 200 μm, Pull-in voltage = 6.5 V	− 0.04 to − 4.0	− 0.035 to − 2.3	− 0.03 to − 1.2	− 33@140 GHz	Gap = 2 μm, 100 nm thick AlN	Gap = 0 μm, 100 nm thick AlN
		0.5	220	70		− 0.035 to − 5.0	− 0.0324to − 2.5	− 0.03 to − 1.25	− 35@105 GHz	C_{up} = 2.4fF	C_{down} = 74.2pF
		0.1	220	70		− 0.035 to − 5.5	− 0.031 to − − 2.3	− 0.028 to − 0.88	− 37@65 GHz		
		0.05	220	70		− 0.034 to − 5.4	− 0.03 to − 2.3	− 0.029 to − 0.89	− 55@45 GHz		
	Si_3N_4 (ε_r = 4)	1	220	70		− 0.04 to − 3.9	− 0.035 to − 2.3	− 0.03 to − 1.1	− 37@110 GHz		
		0.5	220	70		− 0.035 to − 4.9	− 0.0324to − 2.5	− 0.03 to − 1.05	− 35@90 GHz		
		0.1	220	70		− 0.035 to − 5.1	− 0.031 to − 2.3	− 0.028 to − 0.82	− 38@55 GHz		
		0.05	220	70		− 0.034 to − 5.0	− 0.03 to − 2.3	− 0.028 to − 0.78	− 59@35 GHz		
	AlN (ε_r = 8.8)	1	220	70		− 0.04 to − 3.7	− 0.035 to − 2.3	− 0.03 to − 1.07	− 35@105 GHz		
		0.5	220	70		− 0.035 to − 4.75	− 0.0324to − 2.5	− 0.03 to − 1.04	− 38@85 GHz		
		0.1	220	70		− 0.035 to − 5.5	− 0.031 to − 2.3	− 0.028 to − 0.805	− 45@45 GHz		
		0.05	220	70		− 0.034 to − 5.4	− 0.03 to − 2.3	− 0.024 to − 0.76	− 72.4@31.5 GHz		

Table 1 (continued)

Parameter	Material	Thickness (μm)	Length (μm)	Width (μm)	Pull-in Voltage (V)	Insertion losses (dB) (Range = 0.5–40 GHz)			Isolation losses (dB)	C_{up}	C_{down}
						Gap (or) membrane height (μm)					
						0.5	1	2			
	HfO_2	1	220	70		− 0.04 to − 3.65	− 0.035 to − 2.3	− 0.03 to − 1.01	− 35@75 GHz		
	(ε_r = 25)	0.5	220	70		− 0.035 to − 4.73	− 0.0324to − 2.5	− 0.03 to − 0.95	− 37@55 GHz		
		0.1	220	70		− 0.035 to − 5.2	− 0.031 to − 2.3	− 0.027 to − 0.79	− 45@30 GHz		
		0.05	220	70		− 0.034 to − 5.3	− 0.03 to − 2.3	− 0.024 to − 0.76	− 74.5@25 GHz		
	TiO_2	1	220	70		− 0.04 to − 3.6	− 0.035 to − 2.3	− 0.03 to − 1.0	− 35@40 GHz		
	(ε_r = 80)	0.5	220	70		− 0.035 to − 4.7	− 0.0324to − 2.5	− 0.03 to − 0.945	− 40@35 GHz		
		0.1	220	70		− 0.035 to − 5.4	− 0.031 to − 2.3	− 0.026 to − 0.789	− 45@19 GHz		
		0.05	220	70		− 0.034 to − 5.3	− 0.03 to − 2.3	− 0.0235 to − 0.75	− 62.2@12 GHz		

Table 2 Performance improved shunt capacitive switch dimensions

Parameter	Value (μm)
CPW (G–S–G)	90–60–90
Substrate height	100
Substrate width	400
Substrate length	500
Dioxide (insulator) thickness	0.5
Dielectric thickness	0.045
Dielectric constant (ε_r)	12.9
Gap between strip and ground	90
Strip width	60
Bottom electrode width	60
Bottom electrode length	200
Gap between membrane and bottom electrode (g_2)	2.2
Overlap area under electrodes (A_e = 2(W × w))	2 (200 × 60)
Gap between dielectric and membrane (g_1)	2
Membrane length (*l*)	430
Membrane width (*w*)	200
Membrane thickness(*t*)	0.5
Area between membrane and CPW strip line (A_c)	200*60

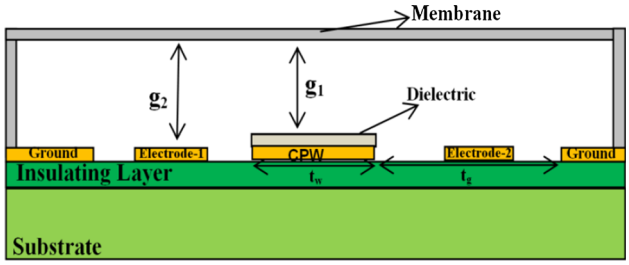

Fig. 1 Proposed serpentine membrane shunt capacitive RF MEMS switch model structure side view

The insertion and the isolation properties of the electrostatical RF MEMS switch depends on switch capacitance. If the actuation voltage is not applied the membrane structure is in upstate, the upstate capacitance (C_{up}) of the switch is (Mercado et al. 2003; Ok et al. 2003; Li et al. 2016),

$$C_{up} = \frac{\varepsilon_0 A_C}{g_1 + \frac{t_d}{\varepsilon_r}} + C_f \tag{6}$$

If we apply an actuation voltage the membrane structure will deform and comes to downstate, the downstate capacitance (C_{down}) of the switch is,

$$C_{down} = \frac{\varepsilon_0 \varepsilon_r A_c}{t_d} \tag{7}$$

Here, A_c is the area between the membrane and the CPW strip line, t_d is the dielectric thickness. The

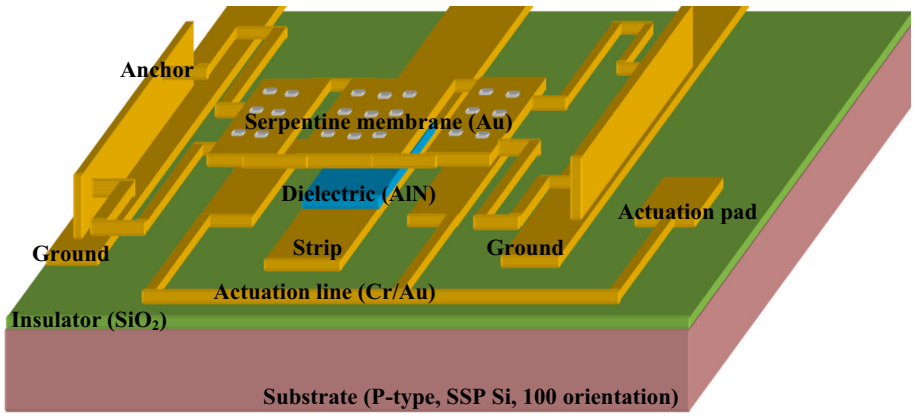

Fig. 2 Proposed serpentine membrane shunt capacitive RF MEMS switch model structure top view

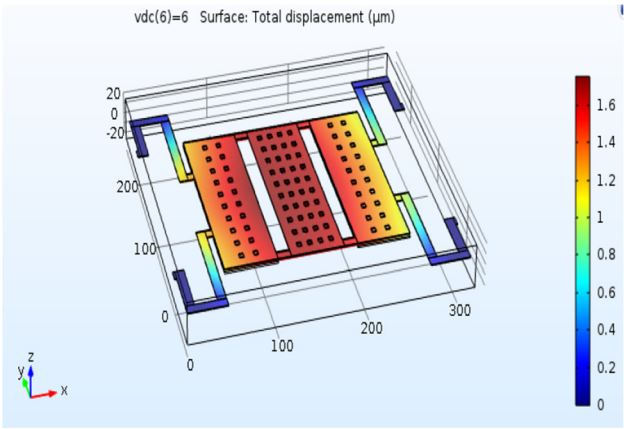

Fig. 3 Optimized switch electrostatic actuation

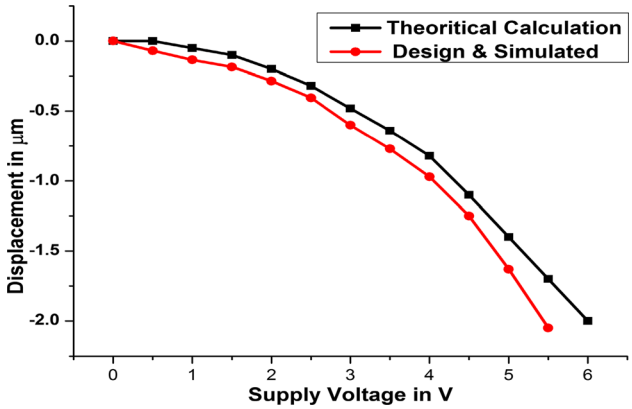

Fig. 4 Membrane displacement (Vs) supply voltage

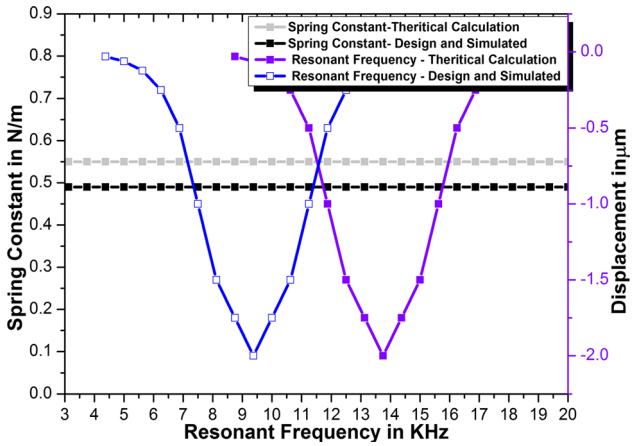

Fig. 5 Membrane spring constant and resonant frequency

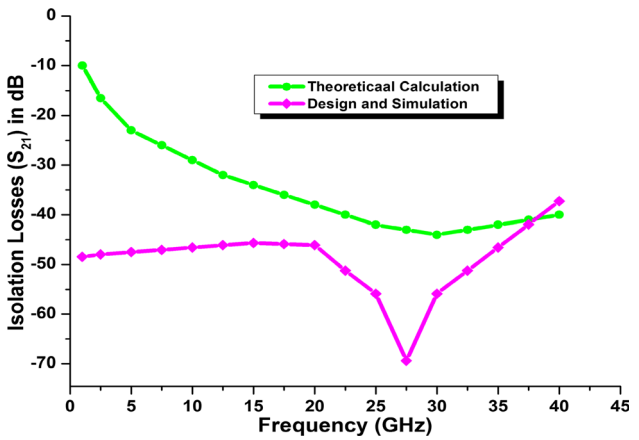

Fig. 6 Isolation losses (S_{21}) in dB, when membrane is in downstate

capacitance ratio of the switch is defined as the ratio of max capacitance (down state capacitance) to minimum capacitance (upstate capacitance) i.e., C_{down}/C_{up}.

In capacitive RF MEMS switches dielectric plays an important role. The dielectric constant and thickness decides the RF performance of the switch. Because of the perforation the overall cross sectional area is reducing and the capacitance is also reducing. The upstate and downstate capacitance of the switch with perforation can be express as

$$C_{up} = \frac{\varepsilon_0 (A_c - A_p)}{g_1 + \frac{t_d}{\varepsilon_r}} + C_f \tag{8}$$

$$C_{down} = \frac{\varepsilon_0 \varepsilon_r (A_e - A_p)}{t_d} \tag{9}$$

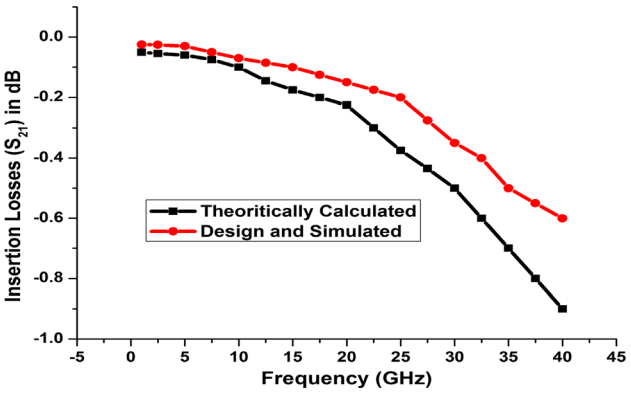

Fig. 7 Insertion losses (S_{21}) in dB, when membrane is in upstate

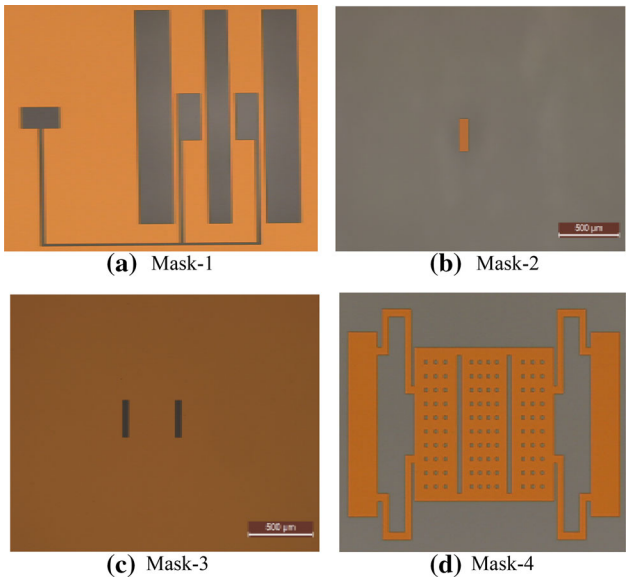

Fig. 8 Overall the proposed serpentine structure capacitive RF MEMS switch fabrication requires four masks **a** CPW and actuation line, **b** dielectric (AlN), **c** trenches for membrane anchors, **d** membrane structure

where A_p is the area removed because of perforation, it can be expressed as $A_p = 2Nl_hw_h$. Here, N is the number of holes to membrane because of perforation, l_h is the length and w_h is the width of the individual hole.

The characteristic impedance of the transmission line also influences the operating frequency of the RF MEMS switch. Most of the shunt type capacitive switch design is done using CPW transmission line as the base, the shunt capacitive switch isolation losses (S_{21}) and return losses (S_{11}) are can be expressed as (Li et al. 2016),

$$|S_{11}|^2 = \frac{\omega^2 C_{up}^2 Z_0^2}{4} \tag{10}$$

$$|S_{21}|^2 = \begin{cases} \dfrac{4}{\omega^2 C_{down}^2 Z_0^2} for\, f >> f_0 \\ \dfrac{4R_s^2}{Z_0^2} for\, f \approx f_0 \\ \dfrac{4\omega^2 L^2}{Z_0^2} for\, f << f_0 \end{cases} \tag{11}$$

Here, R_s is contact resistance, ω is the switch resonating radio frequency, L is the inductance, Z_0 is characteristic impedance, f_0 is resonant frequency, it can express as $(1/2\pi(LC_{down})^{-2})$.

2.2 Switch dimensions performance analysis

Prior to the fabrication, we have analyzed the role of switch dimensions on the performance. The serpentine structure with non-uniform meanders micromechanical structure is used as a membrane. Here, we have extended our analysis on the role of structure (membrane) thickness, perforation, meander dimensions and materials on the pull-in voltage and aspect ratio of the switch. For membrane material we have analyzed the performance with of Au, Cu and Al in that we have noticed that all the three material are offering best performance in terms of pull-in voltage. In that we have chosen Au because Al is little fatigue in nature and Cu will cause the contamination in the fabrication. The switch is a capacitive based switch, the isolation behavior depends on the properties of dielectric material. We have performed the simulation level analysis with different dielectric materials like SiO_2, Si_3N_4, AlN, HfO_2, TiO_2.

For AlN the switch is offering high isolation. The membrane thickness is showing significant impact on the pull-in voltage of the switch.

After dimensional analysis, we finalized the membrane dimensions as l = 320 µm, t = 0.5 µm, w = 200 µm. The perforation of the membrane will impact the structure release and the capacitance of the switch. From analysis it is revealed that, if the perforation holes dimension is below 10 µm × 10 µm, it is not impacting the capacitance of the switch. So, we have finalized the perforation dimension as 5 µm x 5 µm. If the dielectric thickness and relative permittivity is increasing the isolation properties of the switch is also increasing.

The major observation in the dielectric materials and its thickness is, if the dielectric constant and the material thickness are increasing the switch operating frequency is reducing. With this investigation, by incorporating these important points the switch dimensions and materials are optimized. The analysis on the dimensions, materials, and perforation are summarized in the Table 1. The

Table 3 Present shunt capacitive RF MEMS switch fabrication flow comparison with literature

Process	Sharma et al. (2017)	Demirel et al. (2016)	Li et al. (2016)	Present switch
Fabrication process	Surface micromachining	Surface micromachining	Surface micromachining	Surface micromachining
Wafer	Quartz	–	P-Type Si < 100 >, 270 µm	P-Type Si < 100 >, 270 µm
Oxide growth [insulating base]	–	Thermally grown, 0.5 µm	Thermally grown @ 1150 °C, 1 µm	Thermally grown @ 1150 °C, 1 µm
CPW and actuation lines	G/S/G::–/–/– Ti/Au::20 nm/1 µm Sputtering	G/S/G::90 µm/60 µm/90 µm, TiW/Au::50 nm/100 nm Sputtering and electroplating [200 W, 500 A, 2 m 45 s for TiW, 300 W, 1000 A, 1 m 10 s for Au, 400 mA, 1950s for electroplating]	G/S/G::–/–/– Cr /Au::300 nm/600 nm, UHV E-beam evaporation	G/S/G:90 µm/60 µm/90 µm, Cr/Au/Cr::20 nm/200 nm/2 0 nm, DC sputtering [101.68 W for Cr, 28.36 W for Au]
CPW and actuation lines patterning	–	Inductively coupled plasma (ICP), 600 W, 5 m 40 s	–	Wet etching, Lift-off: PG remover @ 60°C. LOR-S1813, AZ351B-MF26A, 130 s–25s.
Dielectric deposition	Si_xN_y, 300 nm, PECVD	Si_3N_4, 300 nm, PECVD, SiH4 (145 sccm) and NH3 (8.1 sccm), 50 °C, 3 Pa, 980s	Si_3N_4, 150 nm, PECVD	AlN, 100 nm, DC sputtering
Dielectric patterning	–	Inductively coupled plasma (ICP)	–	Reactive ion etching (RIE)
Sacrificial layer deposition	Amorphous Si, 2 µm, PECVD	AZ6130 positive PR, 3 µm, Spin coat	PMGI 0.7µm and phospho-silicate glass (PSG), 2 µm. Spin coat	S1813 positive, 1.8 µm, Spin coat
Bridge anchors lithography	DRIE	Wet etching	Wet etching	Wet etching
Membrane deposition	Au, 2 µm, sputtering	Au, 1µm, sputtering and gold electroplating	Au, 2µm, , UHV E-beam evaporation, electroplating	Au, 500 nm, DC sputtering at 90 °C which will develop the stress in the membrane.
Membrane (Au) patterning	–	–	–	Wet etching [KI:I_2:H_2O developer in 4:01:40]
Membrane release	XeF_2 etch system	Isotropic O_2 plasma process,400 W, 20 min, Rest for 10 min	1:50 diluted HF solutions (for PSG), Plasma-Ashing (for PMGI)	Piranha (5mic), IPA, Critical point drying (CPD), Pressure: 1260 Psi, Temperature:31 °C

performance improved RF MEMS switch design is discussed in subsequent.

2.3 Design procedure

Fabrication of micro devices is the costly affair, so initially we have designed the structure using FEM tools and try to improved the switch performance in terms of materials and dimensions. From investigation and the design analysis using FEM tools we have noticed that, the perforated serpentine structure with non-uniform meanders helping the structure to reduce the actuation voltage. We have taken a CPW transmission line with G/S/G values 90 µm/60 µm/90 µm. AlN is used as dielectric material with $\varepsilon_r = 9.8$ which is offering very high isolation.

The proposed switch structural dimensions are shown in Table 2. The performance improved shunt capacitive RF MEMS switch is mechanically resonating at 10.8 kHz, the serpentine membrane spring constant is 0.49 N/m and it requiring an actuation voltage of 5.5 V. Because of the perforation the insertion losses are limited to − 0.6 dB. A thin 50 nm AlN dielectric material is helped to increase the isolation of the switch and the optimized switch is offering − 72.4 dB isolation at 27 GHz. The upstate capacitance of the switch is 2.4 fF and the downstate capacitance is 74.2 pF (Figs. 1, 2, 3, 4, 5, 6 and 7).

Table 4 Present work comparison with literature

Shunt switches	Sharma et al. (2017)	Demirel et al. (2016)	Li et al. (2016)	Proposed switch
Suspender material	Au	Au	Au	Au
	[2 μm]	[1 μm]	[1 μm]	[0.5 μm]
Dielectric	Si_xN_y	Si_3N_4	–	AlN
Air gap (g_1)	2 μm	3 μm	–	1.8 μm
Up state capacitance	54 fF	9.8 fF	27 fF	1.8 fF
Down state capacitance	0.6 pF	0.83 pF	5.3 pF	65.8 pF
Insertion losses	– 0.4 dB	– 0.29 dB	–	– 0.4 dB
	@35 GHz	@35 GHz		@40 GHz
Isolation losses	– 38 dB	– 20.5 dB	– 43 dB	– 58.5 dB
	@35 GHz	@35 GHz	@35 GHz	@31.5 GHz
Actuation voltage	23 V	18.3 V	8 V	4.5 V
Switching time (t_s)	–	–	8.5 μs	12.5 μs
Spring constant (K)	–	–	–	0.35 N/m
Rigid Body Mass(m)	–	–	–	108×10^{-12} Kg
Resonant Frequency (f_r)	–	–	–	8.5 KHz

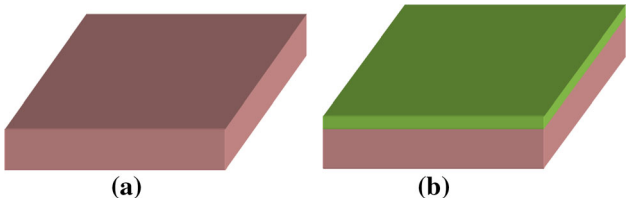

Fig. 9 Insulating thin film (SiO_2) deposition, **a** p-type SSP with 100 orientation Si substrate **b** SiO_2 of 1 μm thickness is deposited on substrate using thermal oxidation at 1150 °C

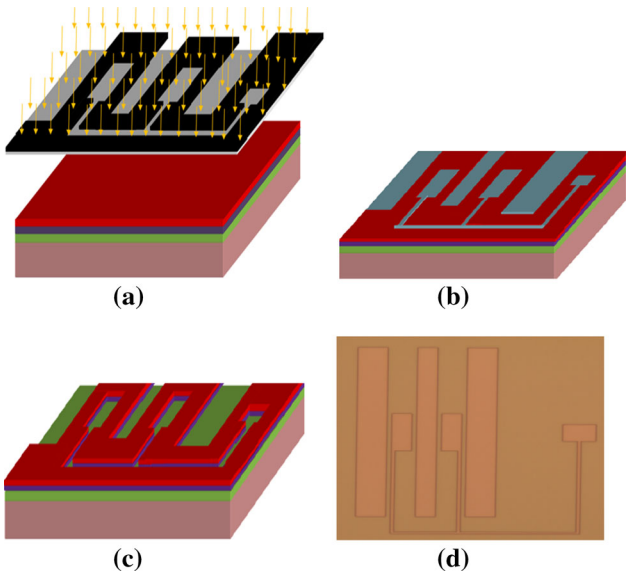

Fig. 10 Lithography using Mask-1, **a** UV exposure, **b** exposed PR, **c** after etching of exposed PR, **d** microscope image: after etching of exposed PR

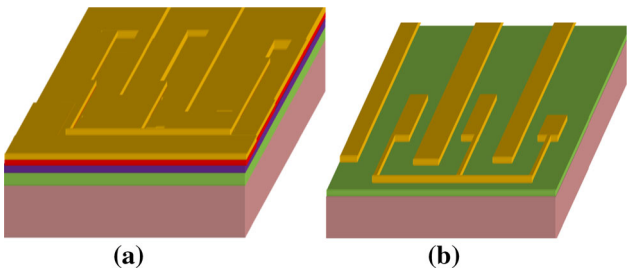

Fig. 11 CPW and actuation lines patterning, **a** Cr/Au/Cr deposition using DC sputtering, **b** after metal liftoff

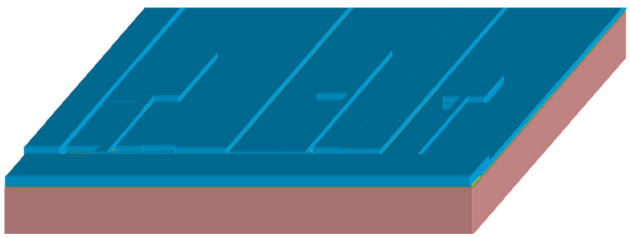

Fig. 12 AlN deposition using DC sputtering

3 Surface micromachining process flow

After design, simulation and switch performance analysis, eventually we have fabricated the shunt capacitive RF MEMS switch with electrostatic actuation using surface micromachining process. To fabricate the complete switch we use four masks shown in Fig. 8. In this section, we placed 3D images for better explanation of fabrication process (Tables 3 and 4).

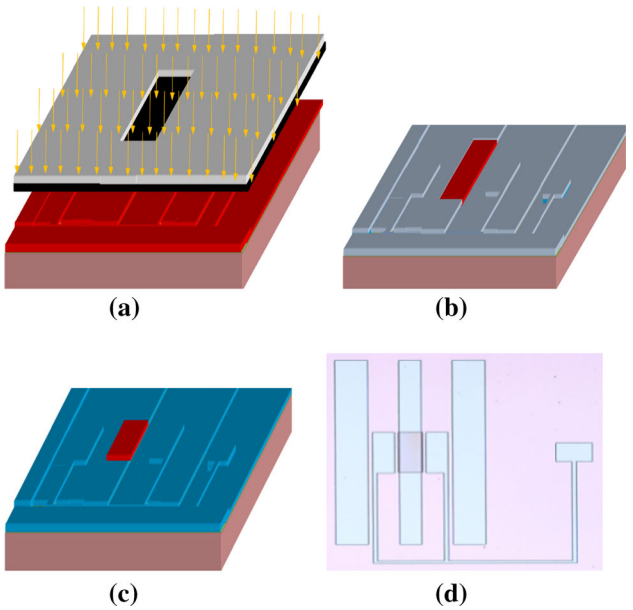

Fig. 13 Lithography using Mask-2, **a** UV exposure, **b** exposed PR **c** after etching of exposed PR. **d** Microscope image: after etching of exposed PR

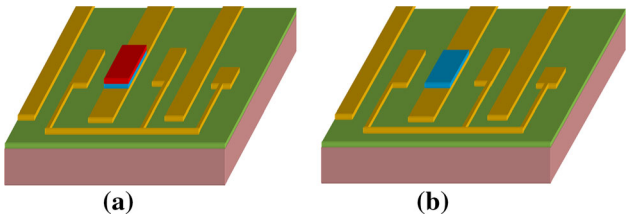

Fig. 14 Dielectric (AlN) patterning, **a** exposed AlN etching using RIE, **b** PR removed using asetone

We have taken 4 inch P-type Si < 100 > with single side polish (SSP) as a substrate. As first we did piranha cleaning to removing organic and metal contaminations on substrate using a mixture of concentrated H_2SO_4 and H_2O_2 solution in 3:1 ratio. After that we deposited 1 µm thickness SiO_2 (insulator) on substrate using Thermal Oxidation at 1150 °C (Figs. 9 and 10).

UV lithography with Mask-1, in this process first LOR photoresist is deposited on SiO_2 surface after that S1813 photoresist is deposited on LOR surface. After lithography MF26A developer is used to etch the exposed S1813 and AZ351B developer is used to etch the exposed LOR. Here LOR is used to create undercut, which is useful in metal liftoff process.

Cr [20 nm]/Au [200 nm] is deposited using the DC Sputtering PVD process with 101.68 W power for Cr, 28.36 W power for Au. The deposition is done at room temperature, with deposition rate of 4 A/s for Cr and Au. After metal deposition CPW and actuation lines are

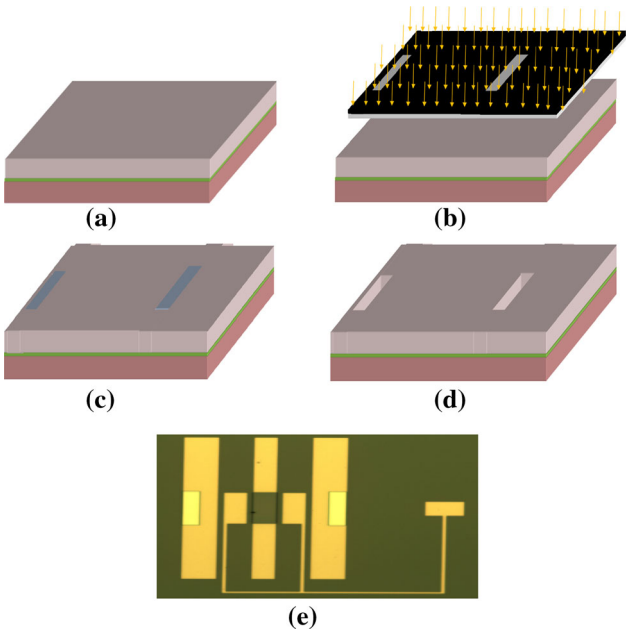

Fig. 15 Lithography using Mask-3, **a** S1813 sacrificial layer deposition using spincoat **b** UV exposure, **c** exposed sacrificial layer, **d** after etching of exposed sacrificial layer using MF26A, **e** microscope image: after etching of sacrificial layer

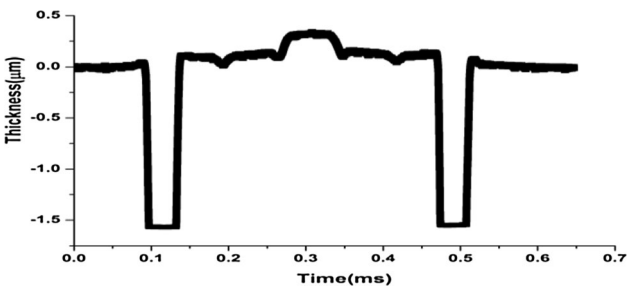

Fig. 16 Trench depth is 1.8 µm measured with dektak

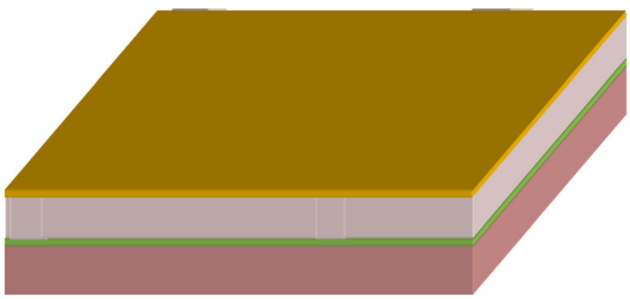

Fig. 17 Membrane material (Au) deposition using DC sputtering PVD process at 90 °C

patterned by doing liftoff process using PG remover as shown in Fig. 11.

AlN dielectric thin film with ε_r = 9.8, 50 nm thickness is deposited using DC Sputtering PVD process at 100 W power (Fig. 12).

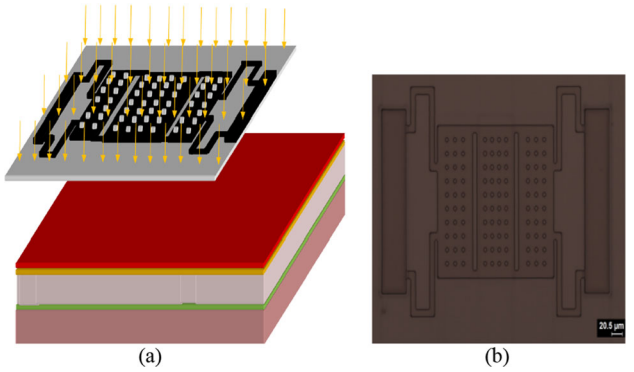

Fig. 18 Lithography using Mask-4, **a** UV exposure, **b** microscope image: after etching of exposed PR

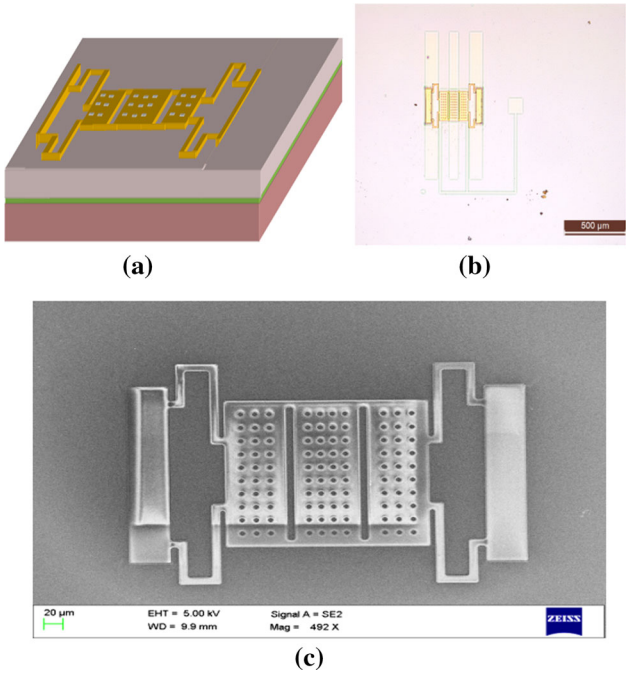

Fig. 19 Patterning of perforated serpentine membrane, **a** exposed Au etching using KI:I_2:H_2O developer in 4:01:40 ratio, **b** microscope image, **c** SEM image

UV lithography with Mask-2 is done in vacuum for 8 s using S1813 as a PR to pattern AlN dielectric layer. After lithography exposed PR is etched using MF26A developer as shown in Fig. 13.

The exposed 100 nm thickness AlN is etched using Reactive Ion Etching (RIE), and it is done using Cl_2 gas at 1800 W-ICP/200RF. At the end the PR is etched using acetone (Figs. 14, 15, 16, 17, 18, 19, 20 and 21).

The required gap between the membrane and the dielectric is 1.8 µm so before depositing the membrane metal (Au) a Sacrificial layer (S1813) is deposited. To achieve the 1.8 µm thickness we did the spin coat at 2000 RPM for 40 s (Figs. 22, 23, 24 and 25).

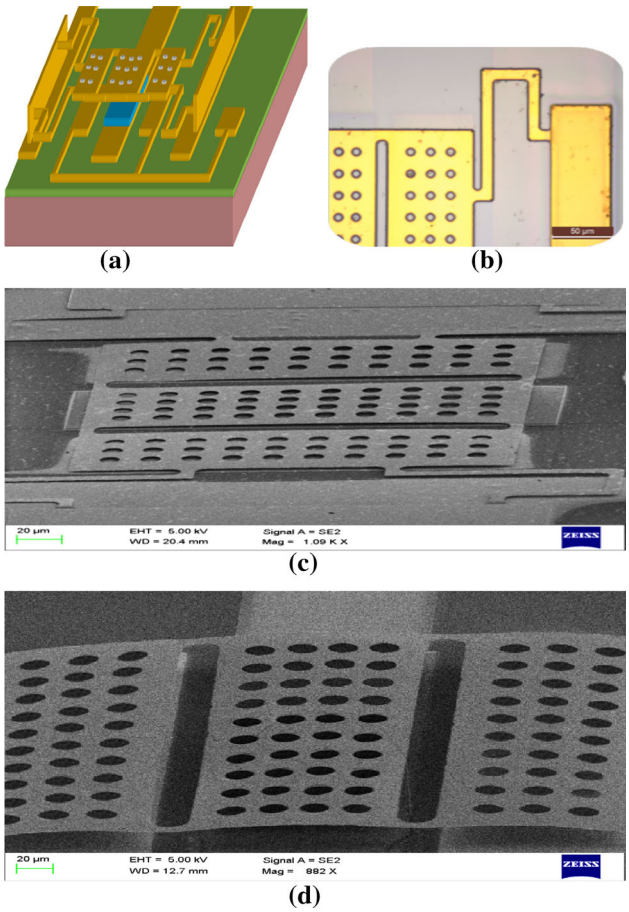

Fig. 20 Membrane release **a** piranha, IPA cleaning and CPD, **b** microscope image, **c** SEM image top view, **d** SEM image side view

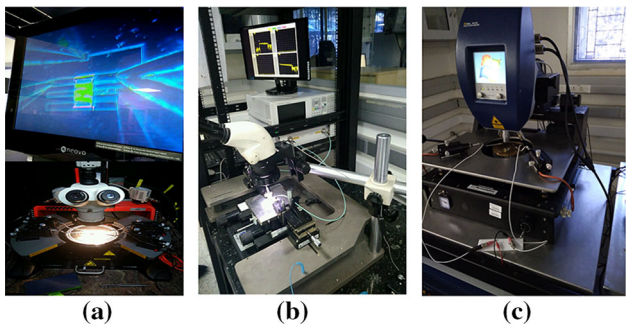

Fig. 21 Characterization setup, **a** DC probe station, **b** RF probe station, **c** MSA

By using Mask-3 lithography is done to form two trenches, later these trenches are helpful to form the anchors for the membrane. Here we did the oven baking for 20 min before lithography and 30 min after lithography which will make PR(S1813) hard.

Here Au is used for membrane, so by using DC Sputtering Au is deposited on the top of sacrificial layer with 500 nm thickness as target. Deposition is done at 90 °C

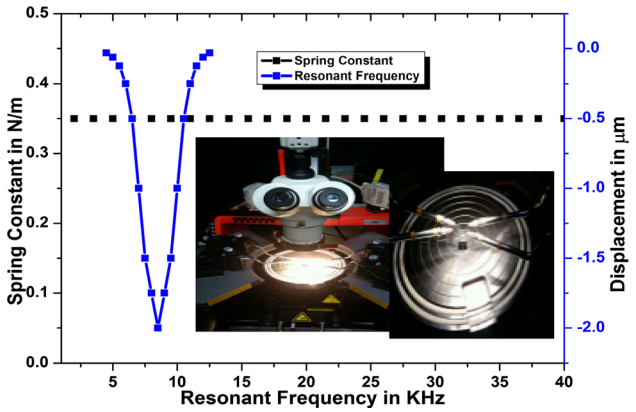

Fig. 22 Switch resonant frequency vs spring constant

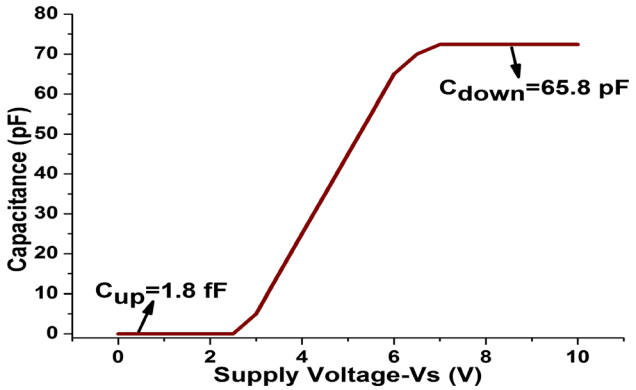

Fig. 23 Switch upstate and downstate capacitances

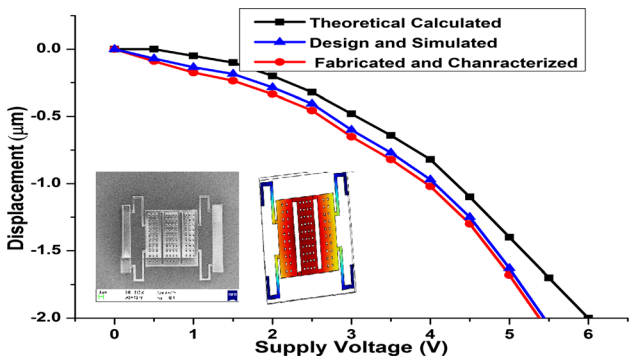

Fig. 24 Electrostatic actuation, displacement (Vs) applied voltage

which will help to develop stress in the membrane, because of this the switch reliability will improve.

Final lithography is done using mask-4, to pattern the membrane using S1813 as PR. And the exposed Au is

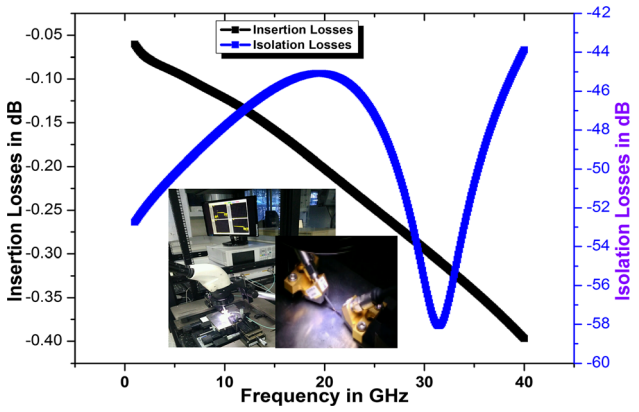

Fig. 25 Insertion losses S_{21} (membrane is in upstate), isolation losses S_{21} (membrane is in downstate)

etched using KI:I_2:H_2O developer solution in 4:01:40 ratio. The etching rate of the KI:I_2:H_2O is 240 nm per second.

In any MEMS devices fabrication, releasing of MEMS structure (membrane) is tricky and difficult. We released the MEMS structure using chemical process, in this first we placed the wafer in Piranha solution for 5 min, after this we placed the wafer in DI water required for further IPA process finally the wafer is placed in critical point drying (CPD). The critical point we observed is Pressure: 1260 Psi, Temperature: 31 °C.

At critical point the liquid carbon dioxide is changed to gaseous state. Because of the CPD we can avoid the stiction like major problem in RF MEMS switch. In the entire fabrication UV explosion in lithography process is done using MJB4. After fabrication we inspected the switch using scanning electron microscopy (SEM) with energy dispersive spectroscopy (EDS).

4 Characterization

The fabricated switch mechanical properties line resonant frequency is analyzed using Micro System Analyzer (MSA). The Au non-uniform meander serpentine structure has 0.35 N/m spring constant and it is resonating at 8.5 kHz. The switch radio frequency (RF) properties are analyzed using RF Probe station, the switch is offering isolation of − 58.5 dB @ 31.5 GHz with 50 nm thickness AlN dielectric material which has 9.8 dielectric constant. The insertion loss of the switch is − 0.4 dB. The switch C–V characteristics are analyzed using DC Probe station. The switch upstate capacitance is 1.8 fF and the switch down state capacitance is 65.8 pF.

Overall the fabricated switch is giving best performance when compared with the literature, based on switch performance it is concluded that the switch can be useful in satellite communication, GPS, cell phones, UHF TV's.

5 Conclusion

In this work, we have fabricated and characterized shunt capacitive RF MEMS switch using surface micromachining. The switch is mechanical properties are analyzed using micro system analyzer, in this we observed that the switch is requiring 4.5 V actuation voltage. The switch radio frequency properties are analyzed using RF Probe station, the switch is offering isolation of − 58.5 dB @ 31.5 GHz with 50 nm thickness AlN dielectric material which has 9.8 dielectric constant. The insertion loss of the switch is − 0.4 dB @ 31.5 GHz. The optimized switch designed in this paper is offering the best performance at 31.5 GHz, so this switch can be use full in GPS, Cell Phones, UHF TV's.

Acknowledgements This Research was performed using the facilities at CeNSE, Indian Institute of Science, Bangalore, Funded by Ministry of Electronics and Information Technology (MeitY), Govt. of India.

References

Agarwal S, Kashyap R, Guha K, Baishya S (2016a) Modeling and analysis of capacitance in consideration of the deformation in RF MEMS shunt switch. Super Lattices Microstruct. https://doi.org/10.1016/j.spmi.2016.10.022

Agarwal S, Kashyap R, Guha K, Baishya S (2016b) Modeling and analysis of capacitance in consideration of the deformation in RF MEMS shunt switch. Super Lattices Microstruct. https://doi.org/10.1016/j.spmi.2016.10.022

Alastalo AT, Mattila T, Seppä H (2003) Analysis of a MEMS transmission line. IEEE Trans Microw Theory Tech 51(8):1977–1981

Badía MF-B, Buitrago E, Ionescu AM (2012) RF MEMS shunt capacitive switches using AlN compared to Si3N4 dielectric. J Micro Electro Mech Syst 21(5):1229–1240

Chawla P, Khanna R (2014) Design, analysis and comparison of various MEMS switches for reconfigurable planar antenna. Acta Polytech Hung 11:21–40

Demirel K, Yazgan E, Demir S, Akın T (2016) A new temperature-tolerant RF MEMS switch structure design and fabrication for Ka-band. J Microelectromech Syst 25(1):60–68

Dragoman M, Aldrigo M, Adam G (2017) Phased antenna arrays based on non-volatile resistive switches. IET Microw Antennas Propag 11(8):1169–1173. https://doi.org/10.1049/iet-map.2016.0974

Dussopt L, Rebeiz GM (2003) Intermodulation distortion and power handling in RF mems switches, varactors, and tunable filters. IEEE Trans Microw Theory Tech 51(4):1247–1256

Fouladi S, Mansour RR (2010) Capacitive RF MEMS switches fabricated in standard 0.35-µm CMOS technology. IEEE Trans Microw Theory Tech 58(2):478–486

Guha K, Kumar M, Parmar A, Baishya S (2016) Performance analysis of RF MEMS capacitive switch with non-uniform meandering technique. Microsyst Technol 22:2633–2640

Guha K, Laskar NM, Gogoi HJ, Borah AK, Baishnab KL, Baishya S (2017) Novel analytical model for optimizing the pull-in voltage in a flexured MEMS switch incorporating beam perforation effect. Solid State Electron 137:85–94

Hijazi YS, Vlasov YA, Larkins GL Jr (2003a) Design of a superconducting MEM shunt switch for RF applications. IEEE Trans Appl Supercond 13(2):696–699

Hijazi YS, Hanna D, Fairweather D, Vlasov YA, Larkins GL Jr (2003b) Fabrication of a superconducting mem shunt switch for RF applications. IEEE Trans Appl Supercond 13(2):700–703

Jensen BD, Saitou K, Volakis JL, Kurabayashi K (2003) Fully integrated electrothermal multidomain modeling of RF MEMS switches. IEEE Microw Wirel Compon Lett 13(9):364–366

Kolis P, Bajaj AK, Koslowski M (2017) Quantification of uncertainty in creep failure of RF-MEMS Switches. J Microelectromech Syst 26(1):1–12

Koutsoureli M, Michalas L, Papandreou E, Papaioannou G (2017) Dielectric charging asymmetry in SiN films used in RF MEMS capacitive switches. IEEE Trans Device Mater Reliab 17(1):1

Li M, Zhao J, You Z, Zhao G (2016a) Design and fabrication of a low insertion loss capacitive RF MEMS switch with novel microstructures for actuation. Solid State Electron. https://doi.org/10.1016/j.sse.2016.10.004

Li M, Zhao J, You Z, Zhao G (2016b) Design and fabrication of a low insertion loss capacitive RF MEMS switch with novel microstructures for actuation. Solid State Electron. https://doi.org/10.1016/j.sse.2016.10.004

Liu Y, Bey Y, Liu X (2016) Extension of the hot-switching reliability of RF-MEMS switches using a series contact protection technique. IEEE Trans Microw Theory Tech 64(10):3151–3162

Liu Y, Bey Y, Liu X (2017) High-power high-isolation RF-MEMS switches with enhanced hot-switching reliability using a shunt protection technique. IEEE Trans Microw Theory Tech 65(9):1–12

Mardivirin D, Pothier A, Crunteanu A, Vialle B, Blondy P (2009) Charging in dielectricless capacitive RF-MEMS switches. IEEE Trans Microw Theory Tech 57(1):231–236

Mercado LL, Lee T-YT, Kuo S-M, Hause V, Amrine C (2003) Thermal solutions for discrete and wafer-level RF MEMS switch. IEEE Trans Adv Packag 26(3):318–326

Molaei S, Ganji BA (2016) Design and simulation of a novel RF MEMS shunt capacitive switch with low actuation voltage and high isolation. Microsyst Technol. https://doi.org/10.1007/s00542-016-2923-2

Mulloni V, Margesin B, Farinelli P, Marcelli R, Lucibello A, De Angelis G (2015) Cycling reliability of RF-MEMS switches with Gold-Platinum multilayers as contact material. Microsyst Technol 23:3843–3850. https://doi.org/10.1007/s00542-015-2782-2

Nejad AG, Hasani JY (2016) Effects of contact roughness and trapped free space on characteristics of RF-MEMS capacitive shunt switches. Can J Electr Comput Eng 39(2):132–140

Ok SJ, Kim C, Baldwin DF (2003) High density, high aspect ratio through-wafer electrical interconnect vias for mems packaging. IEEE Trans Adv Packag 26(3):302–309

Pal J, Zhu Y, Lu J, Dao D, Khan F (2016) High power and reliable SPST/SP3T RF MEMS switches for wireless applications. IEEE Electron Device Lett 37(9):1

Park J, Shim ES, Choi W, Kim Y, Kwon Y, Cho D (2009) A non-contact-type RF MEMS switch for 24-GHz radar applications. J Micro Electro Mech Syst 18(1):163–173

Peroulis D, Pacheco SP, Sarabandi K, Katehi LPB (2003) Electromechanical considerations in developing low-voltage RF MEMS. IEEE Trans Microw Theory Tech 51(1):259–270

Persano A, Cola A, De Angelis G, Taurino A, Siciliano P, Quaranta F (2011) Capacitive RF MEMS switches with tantalum-based materials. J Microelectromech Syst 20(2):365–370

Philippine MA, Zareie H, Sigmund O, Rebeiz GM, Kenny TW (2013) Experimental validation of topology optimization for RF MEMS capacitive switch design. J Microelectromech Syst 22(6):1296–1309

Puyal V, Dragomirescu D, Villeneuve C, Ruan J, Pons P, Plana R (2009) Frequency scalable model for MEMS capacitive shunt switches at millimeter-wave frequencies. IEEE Trans Microw Theory Tech 57(11):2824–2833

Ramadoss R, Lee S, Lee YC, Bright VM, Gupta KC (2003) Fabrication, assembly, and testing of RF MEMS capacitive switches using flexible printed circuit technology. IEEE Trans Adv Packag 26(3):248–254

Rebeiz GM, Muldavin JB (2001) RF MEMS switches and switch circuits. IEEE Microw Mag 2:59–71

Rizk JB, Rebeiz GM (2003) W-Band CPW RF MEMS circuits on quartz substrates. IEEE Trans Microw Theory Tech 51(7):1857–1862

Saias D, Robert P, Boret S, Billard C, Bouche G, Belot D, Ancey P (2003) An above IC MEMS RF Switch. IEEE J Solid State Circuits 38(12):2318–2324

Sharma P, Perruisseau-Carrier J, Moldovan C, Ionescu AM (2014) Electromagnetic performance of RF NEMS graphene capacitive switches. IEEE Trans Nanotechnol. https://doi.org/10.1109/TNANO.2013.2290945

Sharma U, Kumar M, Sharma R, Saha T, Jain KK, Dutta S, Sharma EK (2017) Fabrication process induced changes in scattering parameters of meander type RFMEMS shunt switch. Microsyst Technol 12:5561–5570. https://doi.org/10.1007/s00542-017-3314-z

Shekhar S, Vinoy KJ, Suresh GKA (2017) Surface-micromachined capacitive RF switches with low actuation voltage and steady contact. J Micro Electro Mech Syst 26:1–11. https://doi.org/10.1109/jmems.2017.2688519

Stefanini R, Chatras M, Blondy P, Rebeiz GM (2011) Miniature MEMS switches for RF applications. J Microelectromech Syst 20(6):1324–1335

Wang J, Bielen J, Salm C, Krijnen G, Schmitz J (2016) On the small-signal capacitance of RF MEMS switches at very low frequencies. J Electron Devices Soc 4(6):1

Yang H-H, Han C-H, Choi S-J, Choi D-H, Yoon J-B (2015a) Signal power-insensitive analog MEMS tunable capacitor by immobilizing the movable plates. J Microelectromech Syst. https://doi.org/10.1109/JMEMS.2015.2420121

Yang H-H, Han C-H, Choi S-J, Choi D-H, Yoon J-B (2015b) Signal power-insensitive analog MEMS tunable capacitor by immobilizing the movable plates. J Microelectromech Syst. https://doi.org/10.1109/JMEMS.2015.2420121

Zhang S, Su W, Zaghloul M, Thibeault B (2008) Wideband CMOS compatible capacitive MEMS switch for RF applications. IEEE Microw Wirel Compon Lett 18(9):599–601

Zhang N, Mei L, Wang C, Deng Z, Yang J, Guo Q (2017) A switchable band pass filter employing RF MEMS switches and open-ring resonators. IEEE Trans Electron Devices 64(8):1–7

Zohur A, Mopidevi H, RodrigoM D, Unlu L, Jofre L, Cetiner BA (2013) RF MEMS reconfigurable two-band antenna. IEEE Antennas Wirel Propag Lett 12:72–75

Materials Today: Proceedings xxx (xxxx) xxx

Contents lists available at ScienceDirect

Materials Today: Proceedings

journal homepage: www.elsevier.com/locate/matpr

Preparation and characterization of nanocrystalline tungsten oxide thin films for electrochromic devices: Effect of deposition parameters

K. Pandurangarao [a,b,*], V. Ravi Kumar [a,*]

[a] Department of Physics, Acharya Nagarjuna University, Guntur 522510, Andhrapradesh, India
[b] Andhraloyola Institute of Engineering and Technology, Vijayawada 520008, Andhrapradesh, India

ARTICLE INFO

Article history:
Received 23 July 2019
Received in revised form 27 September 2019
Accepted 17 October 2019
Available online xxxx

Keywords:
WO_3
DC magnetron sputtering
UV–VIS spectrometer
XRD
SEM-EDS
Cyclicvoltammetry and coloration efficiency

ABSTRACT

In the present work, we have reported on deposition of tungsten oxide thin films by DC magnetron sputtering for the fabrication of electrochromic device and the effect of deposition parameters like oxygen partial pressure and substrate temperature on optical, structural, morphological and electrochromic properties of the films. The films were deposited on to Silicon, Quartz and ITO coated glass plates to characterize the properties of the films. The thickness of the films was measured from stylus profilometry and it is 350 nm and the optical transmittance of the films was in the range of 53–75% in the visible region, measured from UV–Visible spectrometer. The films are nanocrystalline in nature and crystallinity improved by increasing the substrate temperature analyzed from X-Ray diffraction. The morphology and composition of the films was determined from SEM, AFM and EDS and the films are nanocrystalline in nature of the size 38 nm and stoichiometric. The phase composition and bonding in the films were investigated from FTIR and Micro-Raman studies. The diffusion coefficient and coloration efficiency of the films were measured from cyclicvoltammetry studies and the values are 3.61×10^{-18} cm^2/s and 34.35 cm^2/C at 550 nm.

Selection and peer-review under responsibility of the scientific committee of the National conference on Functionality of Advanced Materials.

1. Introduction

In the recent times, material science plays a key role in building a nation, especially to combat environmental challenges like green house gases, global warming and other problems. Many researchers developed new materials in that direction. Transition metal oxides are important class of materials, they were used in the fabrication of chromogenic devices and gas sensors. Tungsten oxide is important among the transition metal oxides which are used in the fabrication of smart windows. They alter the transmittance of solar radiation and create energy efficient environment in indoor buildings. WO_3 is n-type semiconductor with band gap of 3.20 eV [1]. The structure is temperature dependent and it exhibits different structures from monoclinic, triclinic, hexagonal and orthorhombic as the temperature changes [2]. The crystalline and amorphous tungsten oxide films shows electrochromism and amorphous films were extensively studied for electrochromism where as crystalline films were studied limitedly in this regard. In the present work, we have comprehensively studied the effect of deposition parameters like sputtering pressure and substrate temperature on optical, structural and electrochromic properties of the films. A small pulse of electric field changes the films from virgin to coloured and to bleached states through reduction reaction mechanism given by the following equation [3].

$WO_3 + xM^+ + xe^{-1} \Leftrightarrow M_xWO_3$

(Transparent)(Blue)where M^+ is alkali metal ions such as H^+, Li^+, K^+ and Na^+.

There are many physical methods like Thermal evaporation [2], Electron beam evaporation [4], Sputtering [5] and chemical methods like, sol-gel [6] spray pyrolysis [7] and Chemical vapor deposition [8] for preparation of the tungsten oxide films. Because of better reproducibility and good adhesion of the film to the substrate, in the present study all the coatings were done with DC magnetron sputtering.

* Corresponding authors at: Department of Physics, Acharya Nagarjuna University, Guntur 522510, Andhrapradesh, India (K. Pandurangarao).
E-mail addresses: pandurangaraokankanala@gmail.com (K. Pandurangarao), vrksurya@rediffmail.com (V. Ravi Kumar).

https://doi.org/10.1016/j.matpr.2019.10.093
2214-7853/
Selection and peer-review under responsibility of the scientific committee of the National conference on Functionality of Advanced Materials.

2. Film preparation and characterization

2.1. DC magnetron sputtering

The films of tungsten oxide were deposited using magnetron sputtering unit (HIND Vacuum). Initially, the sputtering chamber is evacuated to the base pressure of 4×10^{-6} mbar using diffusion and turbo molecular pump. The substrates were cleaned in ultrasonic bath for ten minutes and then using isopropyl alcohol, hydrogen fluoride and acetone to remove any contamination and any other dust particles on the surface and finally mounted on a substrate holder. Siliconwafer, optically flat Quartz glass plates and ITO coated glasses were used as substrates for deposition for different characterizations. Tungsten metal target of one inch diameter used for all coatings. The distance between the target and substrate was 50 mm. Prior to the deposition, argon gas was released into the chamber using mass flow controller to remove the oxide layers on the target and then released reacting gas oxygen using mass flow controller to form tungsten oxide films [9,10]. During the deposition, the substrate holder is rotated through 360° to attain uniform deposition. Sputtering power density was 4.5 W/cm^2 and time of deposition was 20 min for all depositions. The total sputtering pressure was 0.05 mbar and 0.1 mbar measured using penning and pirani gauges with substrate temperatures 300 K–600 K. The deposition parameters were listed in Table 1.

The thickness and roughness of the films were calculated from stylus profilometry and the optical properties were carried out in the wavelength range 300–1100 nm range using shimadzu UV-1800 double beam spectrometer.

A Rigaku samart lab X-Ray diffractometer was employed for diffraction measurements. A CuK_α ($\lambda = 1.540593$ Å) X-Ray source is used by the smart lab diffractometer. Diffraction measurements were made on a 2θ scale in the range of 20–80° with a step size and scan speed of 0.05° and 2° per minute respectively.

Raman spectra were recorded at room temperature from micro-Raman spectrometer (STR-300) with a 540 nm line of Ar^+ laser was used for off resonance excitation.

The surface morphology, composition and surface topography were analyzed from FE-SEM, EDS and AFM.

The electrochemical studies of the samples was analyzed using a standard three electrode electrochemical cell, composed of tungsten oxide films as working electrode, Platinum wire as counter electrode and Ag/AgCl as the reference electrode. A 0.2 M $LiClO_4$ + propylene carbonate was used as the electrolyte. CyclicVoltammograms were recorded with linear sweep potential between −2.50 to +2.50 Volts (versus) Ag/AgCl at different scan rates 100, 200 and 300 mV/s, Chrono Amperometric and Chrono coulometric studies using programmable electrochemical work station (CHI Instruments-Auto 50436).

The performance of any electro chromic device is mostly dependent on its optical, structural properties and morphological properties and how these properties are influenced by deposition parameters were presented.

Table 1
Deposition parameters.

Target	Tungsten (metal)
Substrates	Siwafer, Quartz and ITO glass
Base pressure	4×10^{-6} mbar
Target-Substrate distance	50 mm
Ar:O_2	20:10 sccm
Sputtering pressure	0.05 & 0.1 mbar
Sputtering power density	4.5 W/cm^2
Time of Deposition	20 min

3. Results and discussion

3.1. Thickness and roughness measurement

The thickness of the film plays very important role in optical and electrochromic properties of the film. The thickness of the films were measured using stylus profilometry and thickness of the most of the films were found to be 350 nm and moreover the roughness of the films were are also evaluated, the average roughness of the films were found to be 1.5 nm and Root Mean Square roughness was 2.8 nm.

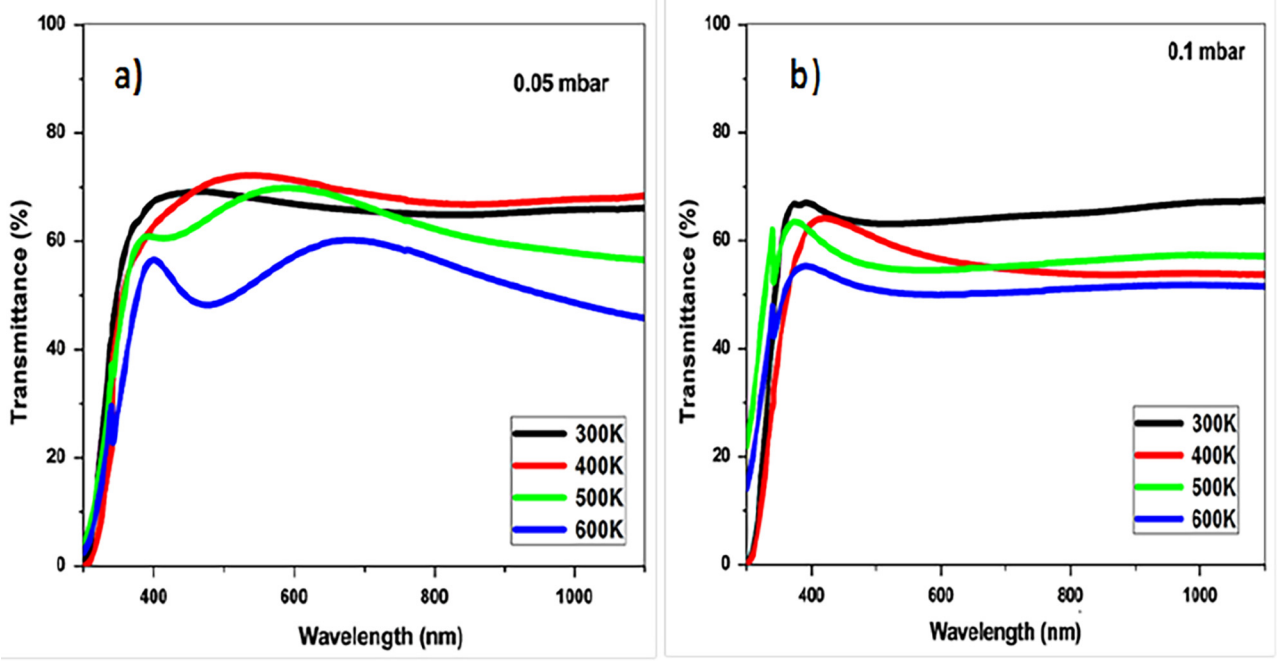

Fig. 1. The optical transmittance spectra of tungsten oxide thin films deposited at different substrate temperatures keeping oxygen partial pressure at a) 0.05 and b) 0.1 mbar.

Please cite this article as: K. Pandurangarao and V. Ravi Kumar, Preparation and characterization of nanocrystalline tungsten oxide thin films for electrochromic devices: Effect of deposition parameters, Materials Today: Proceedings, https://doi.org/10.1016/j.matpr.2019.10.093

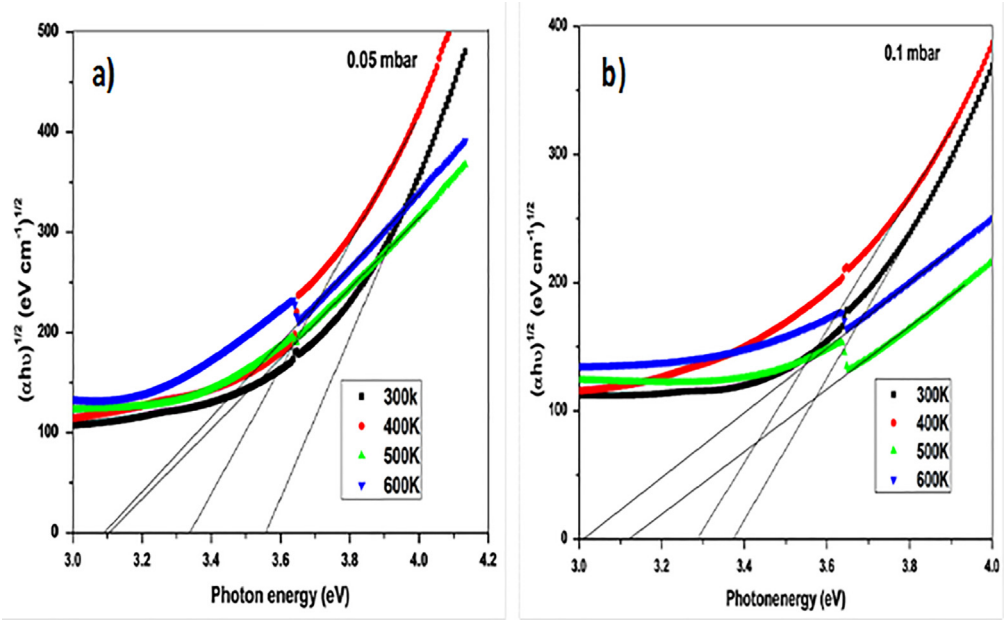

Fig. 2. $(\alpha h\nu)^{1/2}$ vs. hν plots for the films deposited at a) 0.05 mbar b) 0.1 mbar.

3.2. Optical characterization by UV–VIS spectrophotometer

The optical studies like transmittance and optical band gap of WO_3 films have been recorded in the wavelength range 300–1100 nm by using UV–VIS spectrometer. The effect of sputtering pressure and substrate temperature on the optical properties, including percentage of transmittance (%T), and the energy band gap (Eg) were presented in detail. Fig. 1 shows optical transmittance spectra of WO_3 thin films prepared at different substrate temperatures 300–600 K. The optical transmittance of the films observed is in the range of 56–73%. At both partial pressures, the transmittance decreases with increase of substrate temperatures, this is attributed to increase of crystalline nature at higher substrate temperatures and moreover at higher partial pressure the deposition rate decreases and reduces the crystallinity of the films [11,12]. The absorption edge of the films shift towards shorter wavelength side as a result the size of the particle reduces and confirms that the films are nano-crystalline in nature. The optical band gap of the films is evaluated from Tauc's plots by taking graph between $(\alpha h\nu)^{1/2}$ and hν. The extrapolation of the each line on to the X-axis gives the indirect band gap nature of the films and the optical band gap of the films decreases from 3.56 eV to 3.09 eV at 0.05 mbar and 3.38 to 3.01 at 0.1 mbar as the substrate temperature increases as shown in Fig. 2 [13]. The optical band gap Eg was evaluated from absorption coefficient (α) using the relationship for indirect allowed transitions.

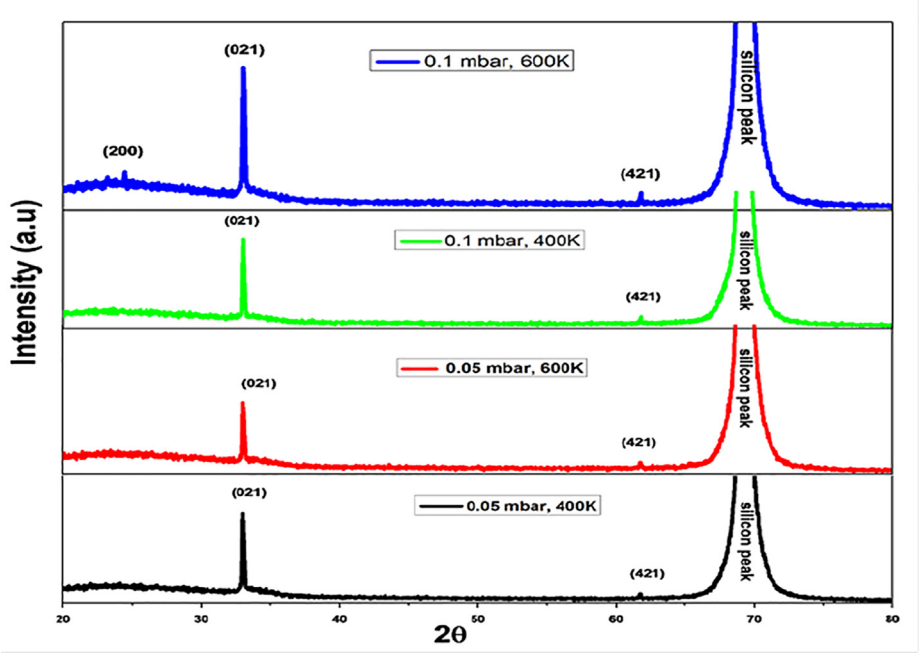

Fig. 3. XRD patterns of the tungsten oxide thin films.

Please cite this article as: K. Pandurangarao and V. Ravi Kumar, Preparation and characterization of nanocrystalline tungsten oxide thin films for electrochromic devices: Effect of deposition parameters, Materials Today: Proceedings, https://doi.org/10.1016/j.matpr.2019.10.093

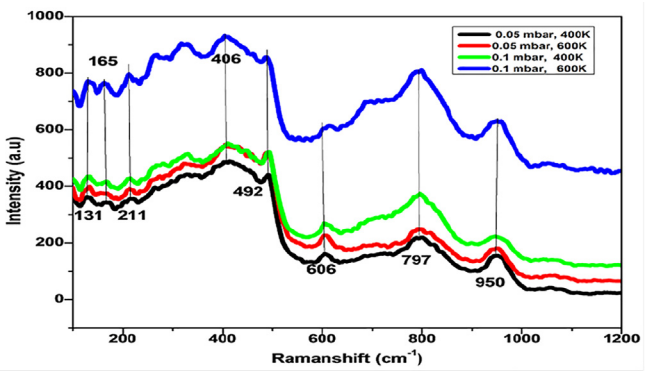

Fig. 4. Micro-Raman spectrum of tungsten oxide thin films.

$$(\alpha h\upsilon)^{1/2} = A(h\upsilon - E_g)$$

where A, hυ and Eg are a constant of proportionality, incident photon energy and optical energy band gap, respectively.

3.3. Structural characterization

The structural characterization of the films was analyzed using a Rigaku samart lab X-Ray diffractometer. For all the films the measurements were taken in the 20–80° range as shown in Fig. 3. From structural studies, all the films have crystalline in nature and having orientations of (0 2 1) and (4 2 1) and additional orientation (2 0 0) was also observed at 0.1 mbar sputtering pressure and substrate temperature of 600 K (JCPDS No. 43-1035). As the substrate temperature increases the crystallinity improves in the films and crystallizes in monoclinic structure [14,15]. From FWHM, we have measured the size of the crystal using Debye-Scherrer's formula and the size of the crystals in the films are nanocrystals and are in the range of 10–40 nm. Clearly we observed that as the substrate temperature increases, the crystallinity improves in the films. The Debye-Scherrer's formula is given by

$$d = 0.9\lambda/\beta\cos\theta$$

where λ is the wave length of X-Ray source (1.5406 Å) and β is Full Width Half Maxima measured graph and θ is the angle of diffraction.

3.4. Micro Raman studies

In present study micro-Raman spectroscopy is used to identify the phase transitions, bonding and disorder in metal oxide thin films and it is one of the non-destructive techniques to characterize the samples. For our samples, we got different peaks in the Raman spectrum as shown in Fig. 4. The peaks, which appear at lower wave numbers (<200 cm^{-1}), are associated with lattice modes and in the medium range wave numbers (range 200–600 cm^{-1}) show O—W—O bending mode features and the wave numbers in the high range (600–1000 cm^{-1}) are related to W—O stretching modes [16]. The peaks at 131 and 165 cm^{-1} are associated with lattice modes of the tungsten oxide molecule. The peaks at 211,406 and 492 cm^{-1} are associated with O—W—O bending mode. Similarly, the sharp peaks 797 and 950 cm^{-1} are associated with stretching mode of W=O double bonds reported earlier in [17]. Commonly, amorphous and nanostructure tungsten oxide films are composed of O—W—O units, reminding the WO_6 octahedral of the bulk crystal with terminal W=O bonds. The intensity of the peaks increases with substrate temperature and the peaks are broad at low substrate temperatures. This indicates that the crystallinity of the films changes with temperature and sputtering pressure confirmed by XRD studies.

3.5. FTIR spectroscopy

In the present case, we have characterized the samples to know the information about phase composition as well as the way oxygen bound to the metal ions (M-O structure). The spectra were taken in the range of 200–2000 cm^{-1} in the transmission mode for all the samples as shown in Fig. 5. The sharp peaks are at 734, 906 and 1106 cm^{-1} with other small peaks at 665, 820 and 1642 cm^{-1}. The peaks at 665 and 734 cm^{-1} are associated with O—W—O bending modes of vibrations and at 820 and 906 cm^{-1} are attributed to W—O—W stretching modes of the films [18]. The wave numbers at 1106 cm^{-1} was due to the presence of the

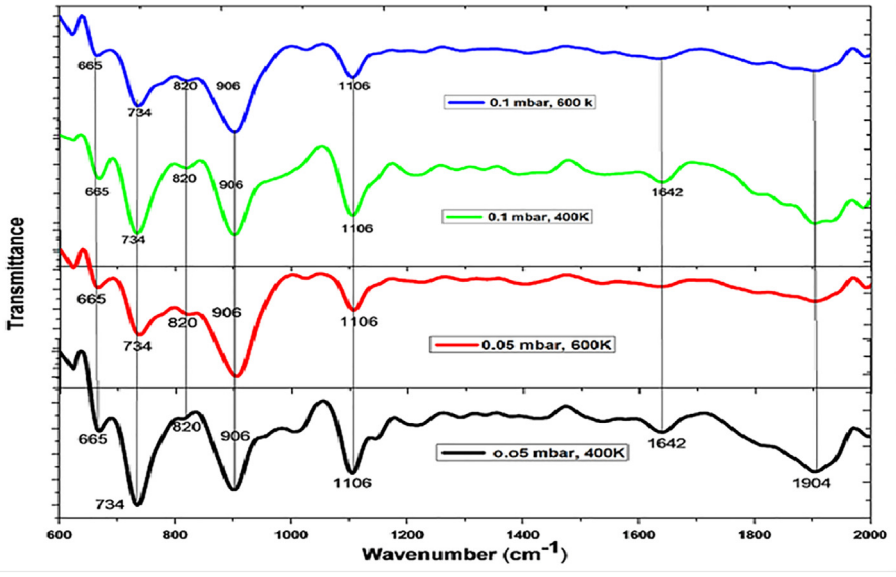

Fig. 5. FTIR spectrum of tungsten oxide thin films.

Please cite this article as: K. Pandurangarao and V. Ravi Kumar, Preparation and characterization of nanocrystalline tungsten oxide thin films for electrochromic devices: Effect of deposition parameters, Materials Today: Proceedings, https://doi.org/10.1016/j.matpr.2019.10.093

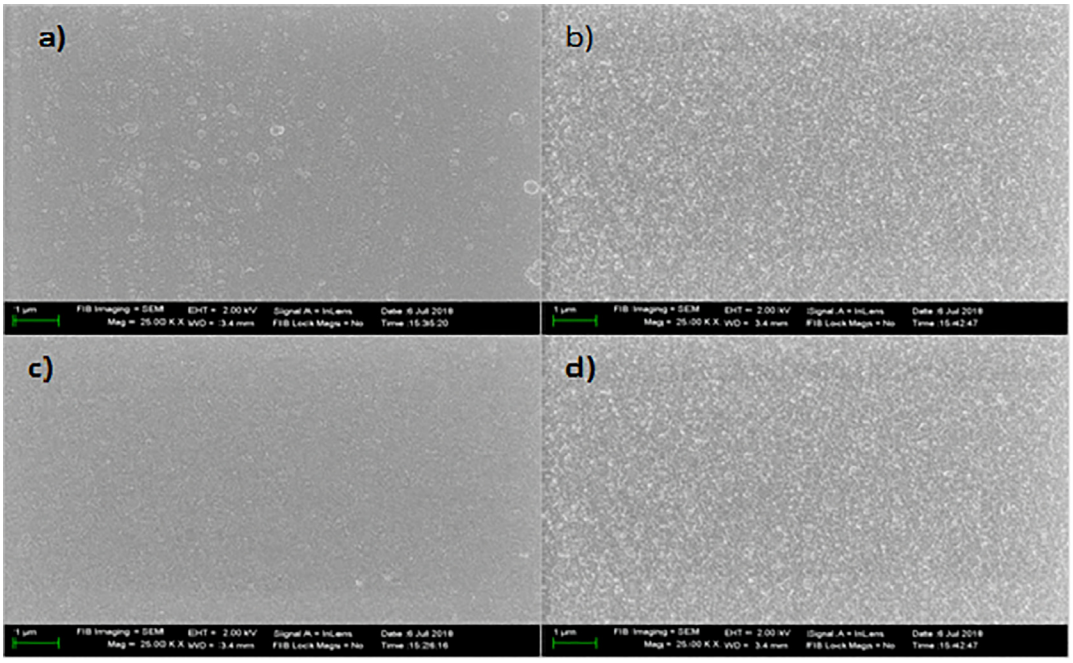

Fig. 6. FE-SEM images of the tungsten oxide thin films deposited at different sputtering pressures and substrate temperatures a) 0.05 mbar, 400 K, b) 0.05 mbar, 600 K, c) 0.1 mbar 400 K and d) 0.1 mbar, 600 K.

silicon oxide bond present on the silicon substrate. The peaks at 1634 cm^{-1} were due to weakly bounded water when the films are exposed to ambient air.

3.6. Morphological studies

The morphological characterization of the films were done with FE-SEM as shown in Fig. 6, and all the films have nano-metric dimensions. It was observed that at 400 K, the films have nanoparticles and distributed randomly with some pores at 0.05 and 0.1 mbar partial pressures. But at 600 K, the films have coarse morphology and the size of the particle increases and all the particles agglomerated and forms nano clusters on the surface of the films at both the partial pressures, which is best suited for insertion or extractions of ions into the films [19].

The composition of the films were analyzed from Energy Dispersive Spectroscopy as shown in Fig. 7. All the films are stoichiometric, the ratio of atomic percentage of the oxygen to tungsten

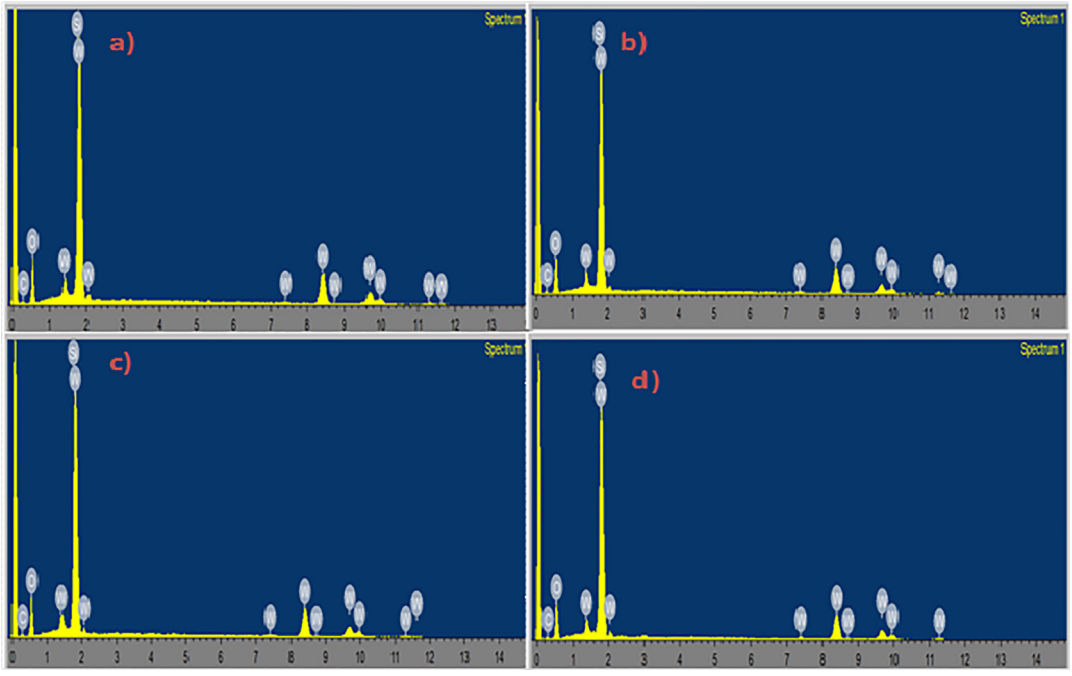

Fig. 7. EDS spectrum of the tungsten oxide thin films deposited at different sputtering pressures and substrate temperatures a) 0.05 mbar, 400 K, b) 0.05 mbar, 600 K, c) 0.1 mbar 400 K and d) 0.1 mbar, 600 K.

Please cite this article as: K. Pandurangarao and V. Ravi Kumar, Preparation and characterization of nanocrystalline tungsten oxide thin films for electrochromic devices: Effect of deposition parameters, Materials Today: Proceedings, https://doi.org/10.1016/j.matpr.2019.10.093

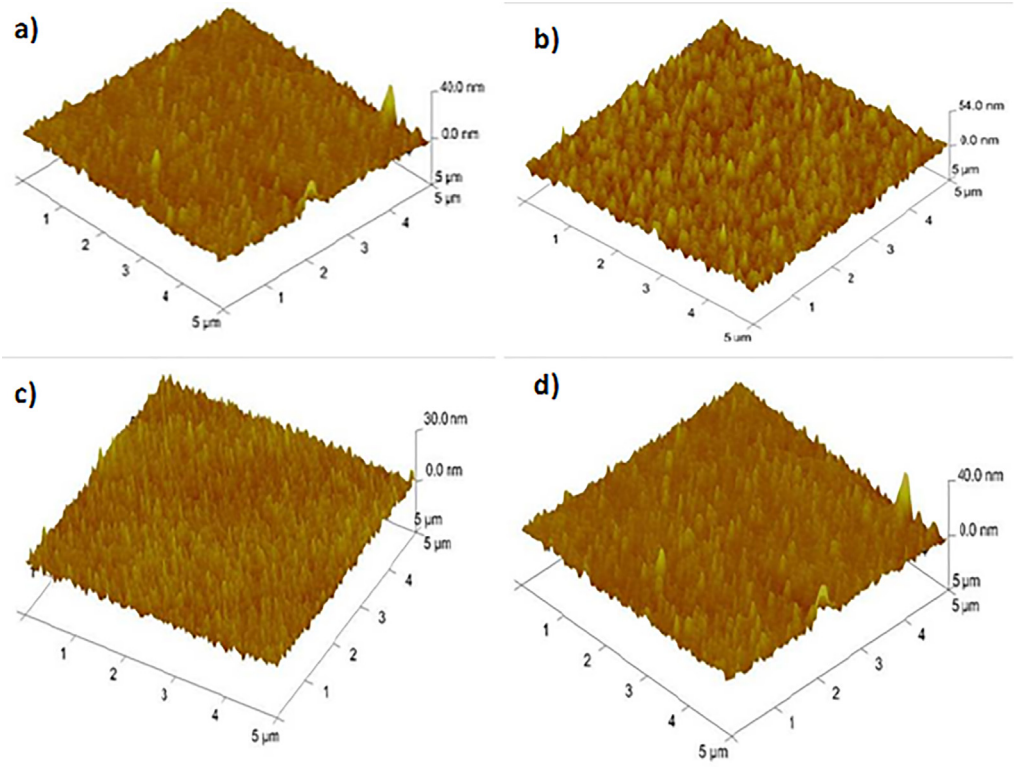

Fig. 8. AFM 3D images of the tungsten oxide thin films deposited at different sputtering pressures and substrate temperatures a) 0.05 mbar, 400 K, b) 0.05 mbar, 600 K, c) 0.1 mbar 400 K and d) 0.1 mbar, 600 K.

was three. Some percentage of silicon and carbon was also observed. This is due to the films coated on silicon substrates was used for the analysis and exposure of the films into atmosphere during analysis.

The topographical studies of the films were characterized using Atomic Force Microscopy and all the images were recorded on 5 μm × 5 μm scale in three dimensions as shown in Fig. 8. All the films have columnar structure with needle like nano grains and the grains are sparsely distributed at lower substrate temperatures and the grain size increases and are agglomerated as the substrate temperature increases at 0.05 mbar. At 0.1 mbar, 400 K the grains are needle like structure and the grains are distributed in compact manner and at 600 K, the grains are sparsely distributed.

3.7. Electrochemical studies

The electrochemical properties of the tungsten oxide films deposited on ITO coated glass were studied using a standard three electrode chemical cell in which the film (WO_3) is used as working electrode, platinum wire is used as counter electrode and Ag/AgCl was used as reference electrode. The 0.2 M $LiClO_4$-Propylenecarbonate (anhydrous) used as electrolyte. The mobility of the Li^+ ion depends upon the viscosity and dielectric constant of the electrolyte and more over the mobility of the Li^+ ion is easy compared to other alkali metal ions into the film. For better understanding of electro chromic properties of the tungsten oxide films, Cyclicvoltammetry (CV), Chronoamperometry (CA) and Chronocoulmetry (CC) measurements were performed [3].

The cyclicvoltammograms of the films recorded at the scan rates 100, 200 and 300 mV/s in 0.2 M $LiClO_4$-PC electrolyte are done with linear potential sweep between −2.50 V to +2.50 V versus Ag/AgCl as shown in Fig. 9. The intercalation and deintercalation of Li^+ ion into the tungsten bronze by oxidation and reduction mechanism of the films is given by the above equation.

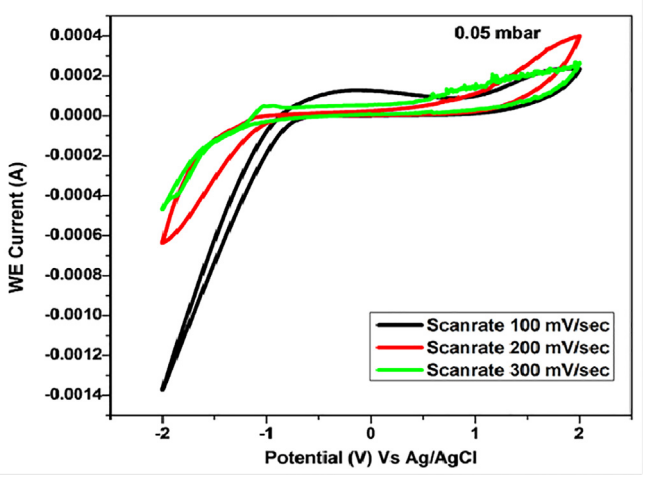

Fig. 9. Cyclic Voltammograms of Tungsten oxide thin films deposited at various sputtering pressure 0.05 mbar and substrate temperature 600 K. The applied potential varies between −2.5 V to +2.5 V at different scan rates.

For each cycle of scanning, the charge insertion/extraction of electrons and lithium ions in the tungsten oxide films occurs. The area of the hysteresis curves and height and position of anodic and cathodic peaks closely related to electrochemical processing occur in the electro chromic films. The cyclicvoltammetry curves of the films deposited at 0.05 mbar and 600 K as shown in fig and other films did not show these studies significantly. From the graph, the area of the hysteresis curve at the scan rate 100 mV/s is more than that of other two scan rates, this is due to the mobility of the ions which is less in the films at these scan rates. From the curves, the diffusion coefficient of the Li^+ ions was estimated from Randle-Sevcik equation give below [20,21]

Please cite this article as: K. Pandurangarao and V. Ravi Kumar, Preparation and characterization of nanocrystalline tungsten oxide thin films for electrochromic devices: Effect of deposition parameters, Materials Today: Proceedings, https://doi.org/10.1016/j.matpr.2019.10.093

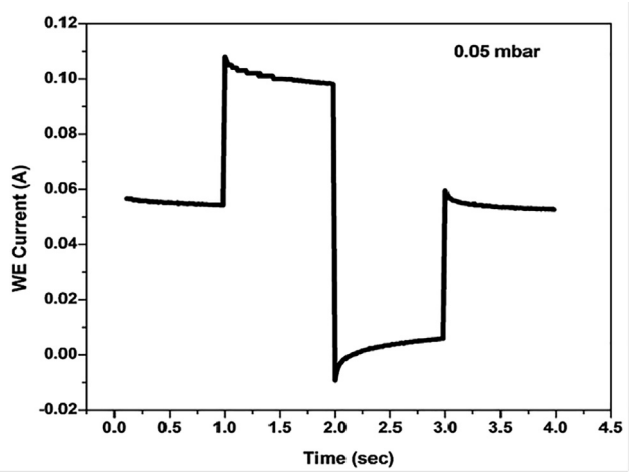

Fig. 10. Chrono Amperometric curve of tungsten oxide thin films at 0.05 mbar, 600 K.

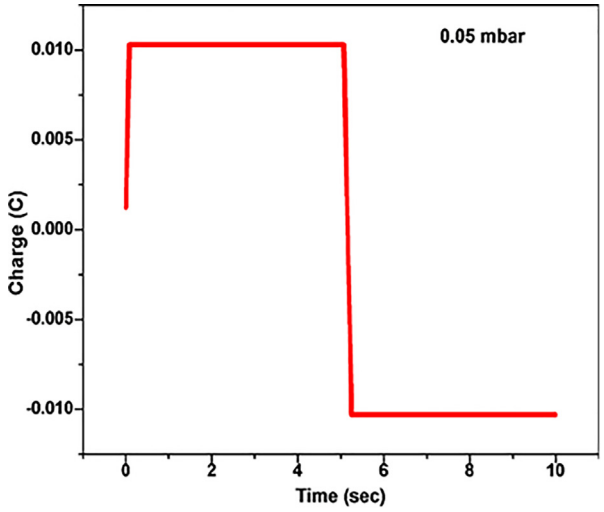

Fig. 11. Chrono Coulometric curve of tungsten oxide thin films at 0.05 mbar, 600 K.

$$i_p = 2.72 \times 10^5 \times n^{3/2} \times D^{1/2} \times C_0 \times v^{1/2}$$

where i_p is the peak current, D is diffusion coefficient, C_0 is the concentration of active metal ions in the electrolyte, v is the scan rate and n = 3 is the number of electrons involved in the process and the values of D are 3.61×10^{-18} cm^2/s, 0.14×10^{-18} cm^2/s and 0.45×10^{-18} cm^2/s at the given scan rates which higher than the reported values earlier.

The chronoamperometry fast is also another important electrochemical tool which gives the time for oxidation (Coloration) and reduction (Bleaching) of the ions in the process. In the present case, the chronoamperomertic curves were taken for step of 5 s between the potential −2.5 V to +2.5 V as shown in Fig. 10. From the graphs the times for coloration and bleaching was t_c = 1.1 s and t_b = 0.8 s.

The amount of charge intercalated and deintercalated was measured from Chronocoulmetric fast studies. These studies were taken for step of 10 s between the potential −2.0 V to +2.0 V as shown in Fig. 11a and the amount of charge intercalated in the films was 9.08 mC and deintercalated was 7.02 mC [22].

The Transmittance spectra of Coloured and Bleached films in the wave length range 300–1100 nm as shown Fig. 12.

Coloration Efficiency is the important parameter for the given electro chromic device and is given by [23]

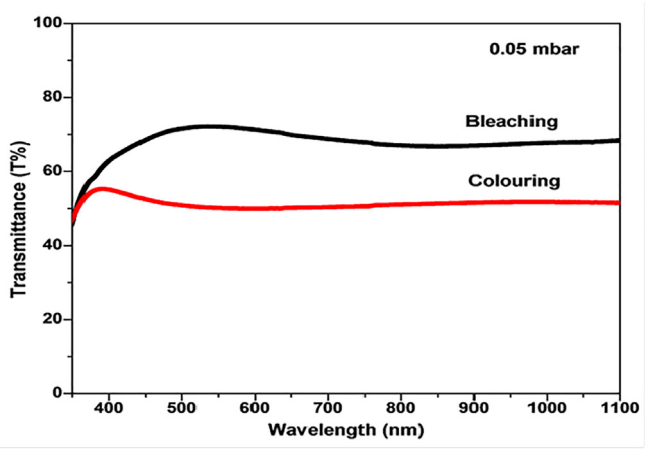

Fig. 12. Optical Transmittance of the Tungsten oxide thin films in colored and bleached states at 0.05 mbar, 600 K.

$$\eta = [\log(t_b/t_c)/q/A]_{\lambda=550\ nm}$$

where t_b and t_c are the transmittance in bleached and coloured states of the films and q/A is the charge density is given by 5.04 C/cm^2. In the present case, the coloration efficiency of our films at 550 nm was 34.35 cm^2/C which is higher than the value reported earlier. Wang et al. reported the coloration efficiency of the tungsten oxide thin films and it was in the range of 5.74 to 11.2 cm^2/C at 632 nm [24].

4. Conclusions

In this investigation, we have made comprehensive studies on the effect of sputtering pressure and substrate temperature on the optical, structural and electro chromic properties of nanocrystalline tungsten oxide thin films. The films exhibited good optical transmittance in visible region and it is observed to change, as the sputtering pressure and substrate temperature are varied. The structural properties of the films conformed that the films have monoclinic structure with nanocrystalline films and the crystallinity is improved as the substrate temperature is increased. The morphology studies of the films indicated nano scale dimension and the films have some pores with nano particle at lower substrate temperatures and at higher temperature the size of the nano particles is observed to increase; the films are observed to have coarse morphology which makes them to be highly suitable for ion intercalation into the films due to the large surface area to volume ratio. The topographical studies indicating all the films have columnar structure with needle like grains and the distribution of the grains is observed to change as the sputtering pressure and substrate temperature changes. The films exhibit good redox reaction mechanism and the diffusion coefficients of the films are estimated to be 3.61×10^{-18} cm^2/s, 0.14×10^{-18} cm^2/s and 0.45×10^{-18} cm^2/s. The coloration efficiency of the films at 550 nm was calculated to be34.35 cm^2/C. The films that are deposited using DC magnetron sputtering at the sputtering pressure of 0.05 and 0.1 mbar and substrate temperature of 400 K and 600 K are the best suited for achieving electrochromism.

Acknowledgements

I take this opportunity to express my sincere thanks to VFSTR Deemed to be University for allowing me to utilize the facilities at the centre and Dr. Pradeep kumar Brahman of KL Deemed to

Please cite this article as: K. Pandurangarao and V. Ravi Kumar, Preparation and characterization of nanocrystalline tungsten oxide thin films for electrochromic devices: Effect of deposition parameters, Materials Today: Proceedings, https://doi.org/10.1016/j.matpr.2019.10.093

be University for providing the lab facility to study electrochemical studies of the films.

References

[1] H. Simchi, B.E. McCandless, T. Meng, W.N. Sharman, Structural, optical, and surfaceproperties of WO_3 thin films for solar cells, J. Alloys Compd. 617 (2014) 609–615.
[2] K.J. Patel, C.J. Panchal, V.A. Kheraj, M.S. Desai, Growth, structural, electrical and opticalproperties of thermally evaporated tungsten trioxide (WO_3) thin films, Mater. Chem. Phys. 114 (2014) 475–478.
[3] C.G. Granquist, Handbook of Inorganic Electrochromic Materials, Amsterdam, Elsevier, 1995.
[4] R. Sivakumar, M. Jayachandran, C. Sanjeeviraja, Studies on the effect of substrate temperature on (VI–VI) textured]tungsten oxide (WO_3) thin films on glass, SnO2:F substrates by PVD:EBE technique for electrochromic devices, Mater. Chem. Phys. 87 (2004) 439.
[5] Masashi Miyakawa, Ken-ichi Kawamura, Hideo Hosono, Hiroshi Kawazoe, Large electrical conductivity enhancement of WO_3 thin films produced by ion implantation, J. Appl. Phys. 84 (1998) 5610.
[6] A. Schmitt, M.A. Agerter, Electrochromic properties of pure and doped Nb_2O_5 coatings and devices, Electrochem. Acta 46 (2001) 2105–12011.
[7] R. Sivakumar, A. Moses Ezhil Raj, B. Subramanian, M. Jayachandran, D.C. Trivedi, C. Sanjeeviraja, Preparation and characterization of spray deposited n-type WO3 thin films for electrochromic devices, Mater. Res. Bull. 39 (2004) 1479–1489.
[8] M.T. Duffy, C.G. Wang, A. Waxman, K.H. Zaininger, Preparation, optical and dielectric properties of vapour deposited niobium oxide thin films, J. Electrochem. Soc. 116 (1969).
[9] A. Subrahmanyam, A. Karuppasamy, Optical and electrochromic properties of oxygen sputtered tungsten oxide (WO_3) thin films, Solar Energy Mater. Solar Cells 91 (2007) 266–274.
[10] K. Salamon, O. Milat, N. Radic, P. Dubcek, M. Jercinovic, S. Bernstorff, Structure and morphology of magnetron sputtered W films studied by x-ray methods, J. Phys. D: Appl. Phys. 46 (2013) 095304.
[11] R. Sivakumar, R. Gopalakrishnan, M. Jayachandran, C. Sanjeeviraja, Preparation and characterization of electron beam evaporated WO3 thin films, Opt. Mater. 29 (2007) 679–687.
[12] I. Castro-Hurtado, T. Tavera, P. Yurrita, N. Pérez, A. Rodriguez, G.G. Mandayo, E. Castano, Structural and optical properties of WO3 sputtered thin films nanostructured by laser interference lithography, Appl. Surf. Sci. 276 (2013) 229–235.
[13] K.J. Patel, C.J. Panchal, V.A. Kheraj, M.S. Desai, Growth, structural, electrical and optical properties of the thermally evaporated tungsten trioxide (WO3) thin films, Mater. Chem. Phys. 114 (2009) 475–478.
[14] A. Karuppasamy, Electrochromism in surface modified crystalline WO3 thin films grown by reactive DC magnetron sputtering, Appl. Surf. Sci. 282 (2013) 77–83.
[15] Samik Roy Moulik, Sudeshna Samanta, Barnali Ghosh, Photoresponse in thin films of WO3 grown by pulsed laser deposition, Appl. Phys. Lett. 104 (2014) 232107.
[16] K. Hari Krishna, O.M. Hussain, C.M. Julien, Electrochromic properties of nanocrystalline WO3thin films grown on flexible substrates by plasma-assisted evaporation technique, Appl. Phys. A 99 (2010) 921–929.
[17] Y.S. Huang, Y.Z. Zhang, X.T. Zeng, X.F. Hu, Study on Raman spectra of electrochromic c-WO3films and their infrared emittance modulation characteristics, Appl. Surf. Sci. 202 (2002) 104–109.
[18] M. Deepa, M. Kar, S.A. Agnihotry, Electrodeposited tungsten oxide films: annealing effects on structure and electrochromic performance, Thin Solid Films 468 (1–2) (2004) 32–42.
[19] F. Di Fonzo, A. Bailini, V. Russo, A. Baserga, D. Cattaneo, M.G. Beghi, P.M. Ossi, C. S. Casari, A. Li Bassi, C.E. Bottani, Synthesis and characterization of tungsten and tungsten oxide nanostructured films, Catal. Today 116 (2006) 69–73.
[20] A. Siva Kumar, K. Shanthakumari, A. Thayumanavan, M. Jayachandran, C. Sanjeeviraja, Coloration and bleaching mechanism of tungsten oxide thinfilms in different electrolytes, Surf. Eng. 23 (2007) 373–379.
[21] K. Punitha, R. Sivakumar, C. Sanjeeviraja, Enhanced coloration efficiency of pulsed DC magnetron sputtered WO_3 films cycled in H_2SO_4 electrolyte solution, Smart Mater. Res. (2014) 151732.
[22] K.S. Usha, R. Sivakmar, C. Sanjeeviraja, Vasanth Sathe, V. Ganesan, T.Y. Wang, Improved electro chromic performance of a radio frequency magnetron sputtered NiO thin film with high optical switching speed, RSC Adv. 6 (2016) 79668–79680.
[23] A. Karuppasamy, Electrochromism in surface modified crystalline WO_3 thin films grown by reactive DC magnetron sputtering, Appl. Surf. Eng. 282 (2013) 77–83.
[24] Shalong Wang, Kang Dou, Yousheng Zou, Yuhang Dong, Jubin Li, Ju. Dan, Haibo Zeng, Assembling tungsten oxide hydrated nanocrystal colloids formed by laser abalation in liquid into fast response electrochromic thinfilms, J. Colloid Interface Sci. 489 (2017) 85–91.

Please cite this article as: K. Pandurangarao and V. Ravi Kumar, Preparation and characterization of nanocrystalline tungsten oxide thin films for electrochromic devices: Effect of deposition parameters, Materials Today: Proceedings, https://doi.org/10.1016/j.matpr.2019.10.093

Optical Materials 101 (2020) 109791

Contents lists available at ScienceDirect

Optical Materials

journal homepage: http://www.elsevier.com/locate/optmat

Studies on magnetron sputtered deposited nanocrystalline tungsten oxide films useful for electrochromic devices

K. Pandurangarao [a,b], N. Purnachand [c], V. Ravi Kumar [a,*]

[a] Department of Physics, Acharya Nagarjuna University, Nagarjuna Nagar, 522 510, India
[b] Department of Physics, Andhra Loyola Institute of Engineering and Technology, 520008, India
[c] School of Electronics Engineering, VIT-AP University, Inavolu, 522237, A.P., India

ARTICLE INFO

Keywords:
WO_3 films
UV-VIS transmittance spectra
Electrochromism
Cyclicvoltammetry

ABSTRACT

WO_3 thin films were sputtered on to different substrates (viz., Si, quartz and ITO coated glasses) at different temperatures and partial pressures using DC magnetron sputtering. The influences partial pressures of O_2 and Ar and substrate temperature (at constant sputtering power) on different characteristics viz., optical, structural, morphological, compositional and electrochromism of the films have been investigated. These characteristics were observed to be strongly reliant on deposition conditions. Thickness and roughness (r.m.s.) of the films were found to be in the ranges of 700–918 nm and 3.18–8.4 nm, respectively. The transmittance in the visible wavelength region of these films was found to in the range of 33–80% depending upon the deposition conditions and optical band gap is found to decrease with increase of substrate temperature from 400 K to 600 K at 16.3 mTorr. The X-Ray diffractogram of the films (deposited at 400 K at 16.3 mTorr) exhibited sharp peaks from the reflections of (0 2 1) and (4 2 1) planes of monoclinic crystalline phase of WO_3 indicating the prepared films are of crystalline in nature. The structural arrangement of WO_3 molecules in the films were analyzed using micro-Raman studies. The morphology studies (using FE-SEM, AFM and EDS techniques) of the films indicated reasonably good stoichiometry of WO_3 films; these results further indicated that the films consist of nanoparticles of with sizes varying upon the deposition conditions. For studying the electrochromism of the films, they were immersed in an anhydrous electrolyte (mixture of 0.2 M lithium perchlorate and 50 ml propylene carbonate); coefficient of diffusion of Li^+ ions and coloration efficiency were measured by cyclic voltammetry and chrono-coulometry methods, respectively. The partial oxygen pressure and substrate temperature used during deposition were found to influence the above mentioned parameters of the films to a larger extent.

1. Introduction

Thin films of transition metal oxides are highly useful in displays, smart windows and other optically operated devices. Out of these, smart windows control the incoming solar radiation and visible radiation and maintain comfortable indoor environment. Electrochromism is an optical phenomenon in which there is a reversible variation in optical features of the films by applying of electric potential of small pulses. In this process there will be insertion of ions/electrons into the films or extraction of charge carriers from the films. Both crystalline and amorphous films do exhibit this phenomenon; in amorphous films it is caused by small polaron hopping, whereas in crystalline films this property was explained using Drude model by several authors [1–5]. WO_3 thin films are being extensively used in the design and fabrication of electrochromic/smart window due to their structural sensitivity. In addition, these are also being used as efficient films for electrochromic applications such as electrochromic mirrors and display devices by optimizing their optical modulation, coloration efficiency and switching time of the films. Besides these, electrochromic WO_3 thin films are being widely used as photochromic and gas sensing materials. In fact, these materials exhibit different structures at different temperatures. The durability of the electrochromic window is however, reliant on structural aspects of the films, deposition conditions and methods adopted for coating the films [6,7]. Thermal evaporation [8], electron beam evaporation [9], pulsed laser deposition [10], sputtering [11] and chemical approaches (like chemical vapour deposition [12], spray pyrolysis [13], sol-gel method [14] etc.) are the some of the methods being used for coating the films. In this study, we have deposited WO_3 films using DC

* Corresponding author.
E-mail address: vrksurya@rediffmail.com (V. Ravi Kumar).

https://doi.org/10.1016/j.optmat.2020.109791
Received 30 January 2020; Received in revised form 24 February 2020; Accepted 24 February 2020

Table 1
Deposition parameters.

Target	Tungsten metal 2″ Diameter and 5 mm thickness
Substrates	Si(100), Quartz glass and ITO coated glass
Base pressure	4×10^{-6} mbar
Target substrate distance	60 mm
Sputtering pressure	16.3 and 17.6 mTorr
Substrate temperature	400 K and 600 K
Argon: Oxygen Flow rate	20:10 and 20:7.5 sccm
Sputtering power	100 W
Deposition time	20 min

reactive magnetron sputtering technique at various substrate temperatures and sputtering pressures and studied their electrochromic properties viz., cyclic voltammetry, chronoamperometry, chronocoulometry and optical transmittance in detail. Even though studies related to these properties were reported by some authors, the studies as such on these films fabricated by DC reactive magnetron sputtering technique could hardly be found in the literature. This method is as an advantageous over the other methods mentioned above by several aspects. For example, it is the most efficient method for obtaining good optical quality films of large surface areas with reasonably uniform thickness and good adhesion with the substrate. Further, this method requires only low processing temperature for the deposition of the films. Moreover, it has the large ability to keep the stoichiometry of the original target composition that gets deposited on the substrate with improved coloration efficiency.

2. Experimental and characterization

Initially, the substrates were cleaned with isopropyl alcohol for 2 min and then were subjected to ultrasonification for about 10 min; later they were successively gutted with acetone and de-ionized for 2 min. Finally, all the substrates were dried and once again cleaned with acetone before mounting on substrate holder in the sputtering chamber. To sputter WO_3 films on a substrate, PLASSYS BESTEK SAS, FRANCE& Model- MP300 sputtering coating unit was used. Tungsten target of thickness 5 mm with sputtering gun of diameter 2 inch were mounted on the substrate holder that can be rotated through 360° so as to get the homogenously deposited films. Before deposition of the films is started, the sputtering chamber is evacuated to the base pressure of 4×10^{-6} mbar [15,16]. The films were deposited on substrate at T = 400 K and 600 K in the chamber. The target and the substrate distance was maintained as 60 mm. Before the process of deposition was started Ar gas was allowed to pass through mass flow controller for 10 min into the chamber to wipe out oxide layers upon the target; during this course, a shutter was used between the target and substrate. Later, the shutter was opened and the reacting oxygen gas was freed into the chamber with a mass flow controller. Deposition has been carried out with two different Ar/O_2 pressure ratios viz., 2:1 and 3:1 with the combined pressures of Ar and O_2 as 17.6 and 16.3 mTorr, respectively. For all the depositions the applied DC power was 100 W. The deposition time was about 20 min. The pertinent data on deposition parameters are furnished in Table 1.

The films were characterized by A Rigaku X-Ray diffractometer. A Bruker- DXT-15-1022 stylus profilometer was used to measure the thickness and roughness of the films. Optical transmission spectra were recorded on SHIMAZDU UV-1800 UV–vis spectrometer in the spectral region of 300–1100 nm. Refractive index of these films was measured from spectroscopic ellipsometry with J.A. Woollam Model: M2000X in the wavelength range of 500–1000 nm. Raman spectral studies of the films were performed on Micro-Raman spectrometer (Model: STR-300). Surface morphology of the films was investigated with FE- Scanning Electron Microscope (Carl Ziess Model: Neon-40) was used for surface morphology studies. Atomic Force Microscope (Veeco Model: Dimension V SPM) was used for topography studies of the films.

The electrochemical studies of the deposited films were performed with a standard three electrode electrochemical work station (CHI Instruments-Auto 50436) where in Ag/AgCl (reference electrode), platinum wire (counter electrode) and the film deposited on ITO coated glass (as working electrode) were used. The current across the working electrode (WO_3 film) was measured with three scanning rates of the applied voltage (viz.,100, 200 and 300 mV/s) in the range −2.0 to +2.0 V. Diffusion coefficients were evaluated with these cyclic voltammograms of the films. The time for coloration and the time for bleaching of the films were obtained from chronoamperometric studies and the quantity of charge intercalated and de-intercalated into the films was measured from chronocoulometric studies.

Table 2
Thickness and Roughness of the films.

Sputtering pressure (mTorr)	Substrate temperature (K)	Thickness (nm)	Roughness (nm)
16.3	400	770	4.19
	600	900	4.4
17.6	400	884	3.18
	600	918	8.4

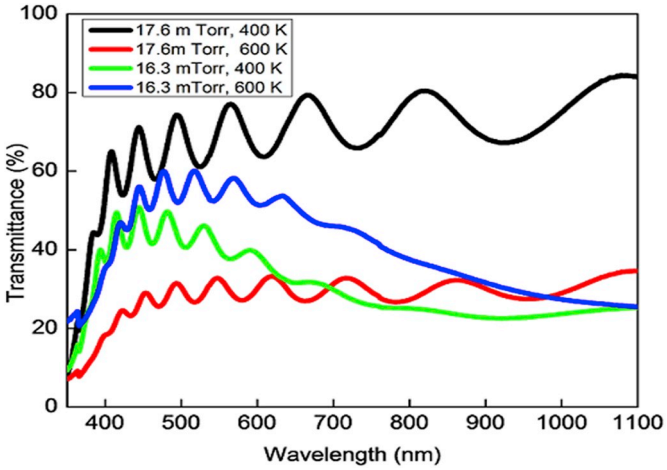

Fig. 1. Optical transmittance spectra of WO_3 thin films.

3. Results and discussion

3.1. Thickness and roughness measurements

Thickness and roughness play very important role in physical characteristics of the films. These parameters are primarily dependent on the deposition conditions e.g., sputtering pressure and substrate temperature. In this study, roughness of the films is observed to be larger for the films sputtered at high sputtering pressures and substrate temperature (Table 2).

3.2. Optical transmittance studies

All the samples have exhibited a reasonably good transmittance in the spectral region 350–1100 nm. To be specific, the films deposited at 17.6 mTorr and 400 K have exhibited transmittance of 84%. A remarkable decrease (35%) in the transmittance of these films is visualized with the hike of the deposition temperature from 400 to 600 K at the same sputtering pressure (Fig. 1). This decrement is presumed to be due to increase in the degree of crystallinity of the samples as has been indicated by FE-SEM, AFM and XRD patterns described later in the manuscript. The sputtering pressure is also observed to play a crucial role on the transmittance of these films. When sputtering pressure is decreased from 17.6 mTorr to 16.3 mTorr, the transmittance of the films (deposited at 400 K) is found to be decreased from 84% to 46%.

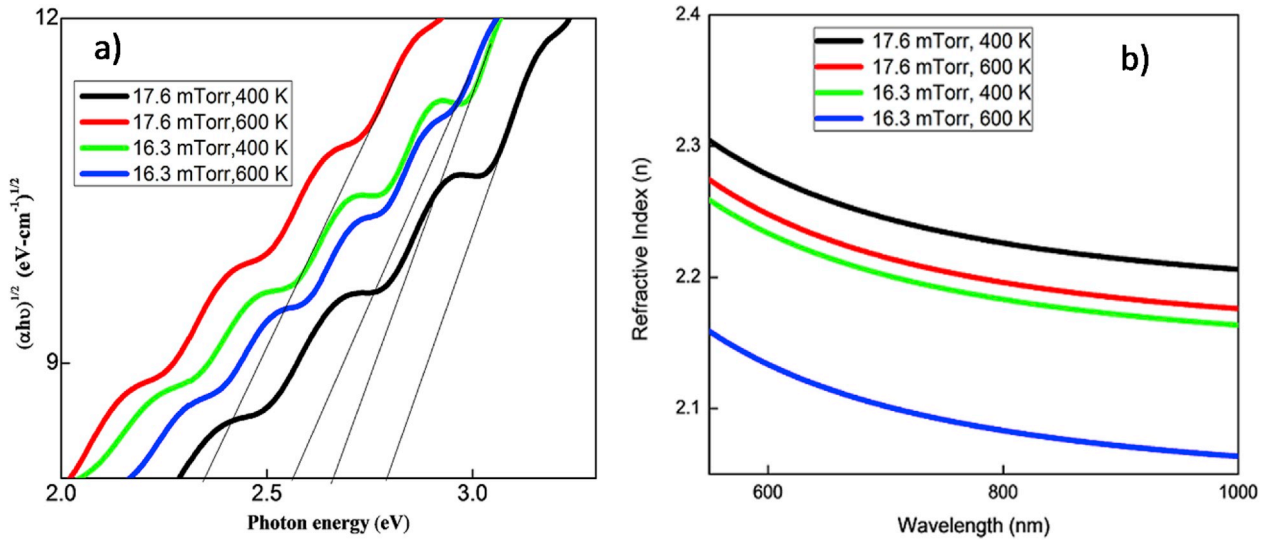

Fig. 2. (a) Tauc plots for evaluating optical band gap of the WO_3 thin films **(b)** Variation of refractive index with the wavelength of the WO_3 thin films prepared under different conditions.

Table 3
Optical characteristics of the films.

Sputtering pressure (m Torr)	Substrate temperature (K)	Transmittance (%)	Optical bandgap (eV)	Refractive Index (at λ = 550 nm)
16.3	400	46	2.65 (t = 770 nm)	2.37
	600	61	2.56 (t = 900 nm)	2.29
17.6	400	84	2.79 (t = 884 nm)	2.34
	600	35	2.35 (t = 918 nm)	2.31

However, at the high substrate temperature viz., 600 K, the decrease of pressure from 17.6 mTorr to 16.3 mTorr, caused an increase in the transmittance of the films from 35% to 61%. The increased transmittance due to decreased sputtering pressure (for the films deposited at higher temperature, viz., 600 K) indicates that the films are of sub-stoichiometric at lower oxygen partial pressures and at higher substrate temperature [17]. Cut-off edge for the films deposited under different conditions was observed to be in the range of wavelength 340–375 nm. However, the spectral position of the edge is observed to be reliant on sputtering pressure and substrate temperature. To elaborate more, either with rise of pressure (at constant T) or with rise of T (at constant P) from 400 K to 600 K the edge shifted towards longer wavelength region (Fig. 1) [18]. Indirect optical band gap (E_g) of the films was estimated by plotting $(\alpha h\nu)^{1/2}$ vs $h\nu$ (Tauc plots, Fig. 2a); by extending linear portions of these curves to the X-axis, value of E_g is estimated and furnished in Table 3. E_g is observed to decrease with rise of substrate temperature; such dependence of E_g on temperature indicates increased crystallinity of the films with substrate temperature. Further, we have also noticed that E_g is dependent on the film thickness; as t increases E_g is observed to increase as has been reported for a number of other films [19,20]. Refractive index (n) of the films is observed to decreases with increase of wavelength (Fig. 2 (b)). Further, n is observed to be high for the films coated at low substrate temperatures and found to decrease with increased temperature of the substrate. Such decrease suggests the increased fraction of crystal grains in the films with increase of substrate temperature [21]. We have also noticed decrease of n as the thickness of the films is increased similar to optical bandgap.

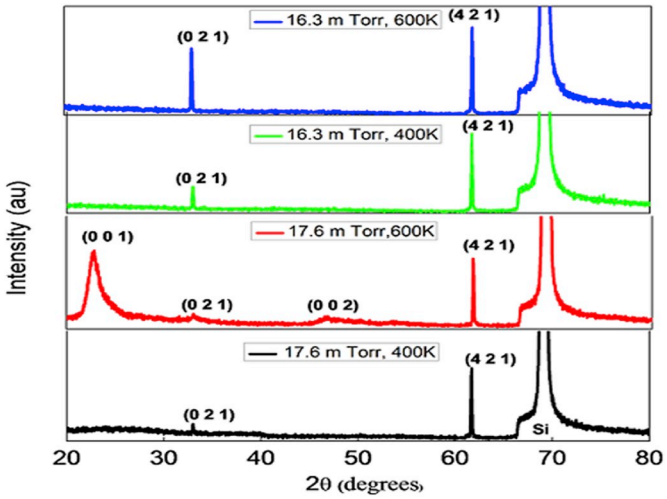

Fig. 3. XRD profiles of WO_3 thin films.

3.3. Structural analysis

3.3.1. X-ray diffraction studies

The X-ray diffractograms of the films (Fig. 3) deposited on silicon substrate (at 400 K and at sputtering pressure 16.3 mTorr) exhibited peaks from reflections of (0 2 1) and (4 2 1) planes of monoclinic WO_3 crystalline phase (JCPDS card No-24-0747). The diffractograms of the films sputtered at T = 600 K and at sputtering pressure 17.6 mTorr exhibited additional peaks due to reflections from (0 0 1) and (0 0 2) planes. This observation suggests increased fraction of crystallites in the films as temperature of the substrate is increased [22–24]. Average crystallite size was calculated from the diffractograms using

Table 4
Crystallite sizes from XRD studies.

Sputtering Pressure (mTorr)	Substrate Temperature (K)	Crystallite size (nm)
16.3	400	60
	600	76
17.6	400	56
	600	40

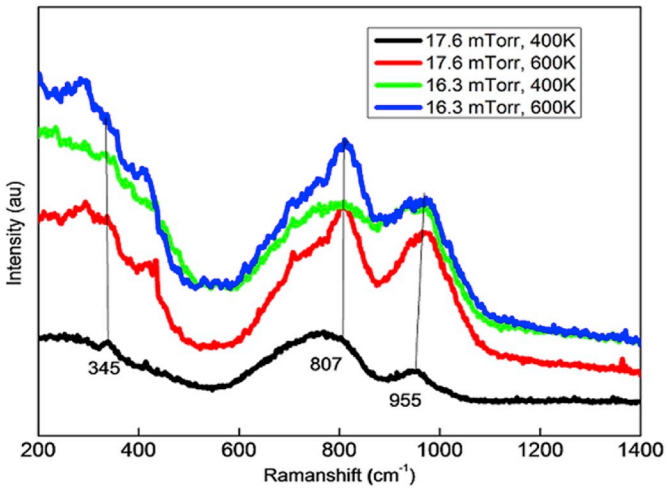

Fig. 4. Micro-Raman spectra of WO_3 thin films.

Debye-scherrer formula and it is found to be in the range of 38–60 nm (Table 4).

3.3.2. *Raman spectra*

Raman spectra of these films (Fig. 4) exhibited two prominent vibrational bands at 808 and 955 cm^{-1} and a feeble kink at 345 cm^{-1}. Tungsten ions occupy T_d and O_h positions in WO_3 films. Weak vibrational band observed at low energy side viz., 345 cm^{-1}, represents the bending vibrations of WO_6 structural units, whereas the bands located at 807 and 955 cm^{-1} are attributed to asymmetric stretchings of W–O and W═O bonds of WO_4 structural units, respectively [20,24,25]. As the temperature of the substrate is raised from 400 K to 600 K (at a fixed sputtering pressure viz., 17.6 mTorr) the intensity of asymmetrical vibrational bands observed at 808 and 955 cm^{-1} is observed to increase. A similar variations in the intensity of these bands is visualized with the rise of sputtering pressure from 16.3 mTorr to 17.6 mTorr at a fixed substrate temperature. This observation suggests the substrate temperature plays a dominent role in increasing the structural disorder of the films which facilitate the increase of electrochromism.

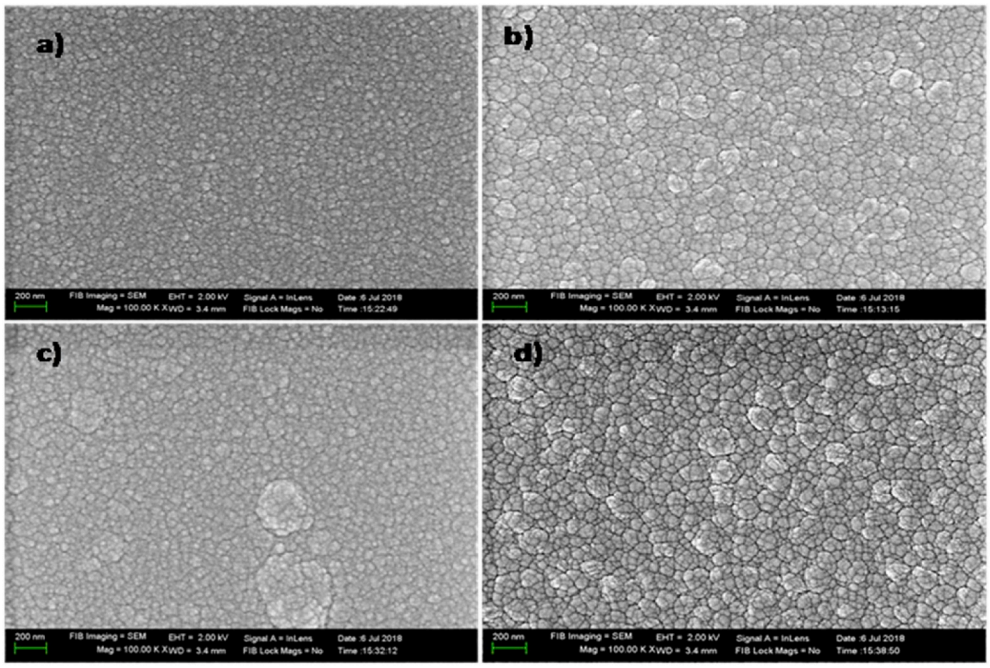

Fig. 5. FE-SEM images of WO_3 thin films a) 16.3 mTorr, 400 K and b) 16.3 mTorr, 600 K c) 17.6 mTorr, 400 K and d) 600 K.

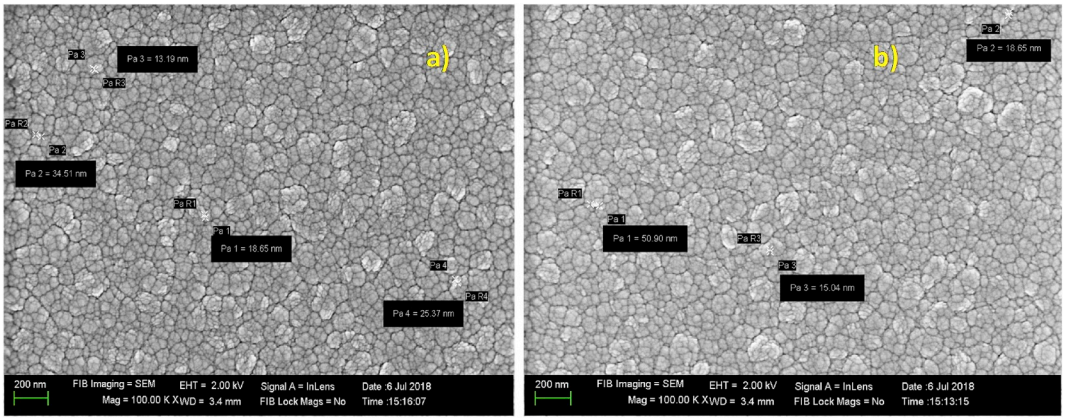

Fig. 6. Particle sizes from FE-SEM images at 600K a) 16.3 mTorr, b) 17.6 mTorr.

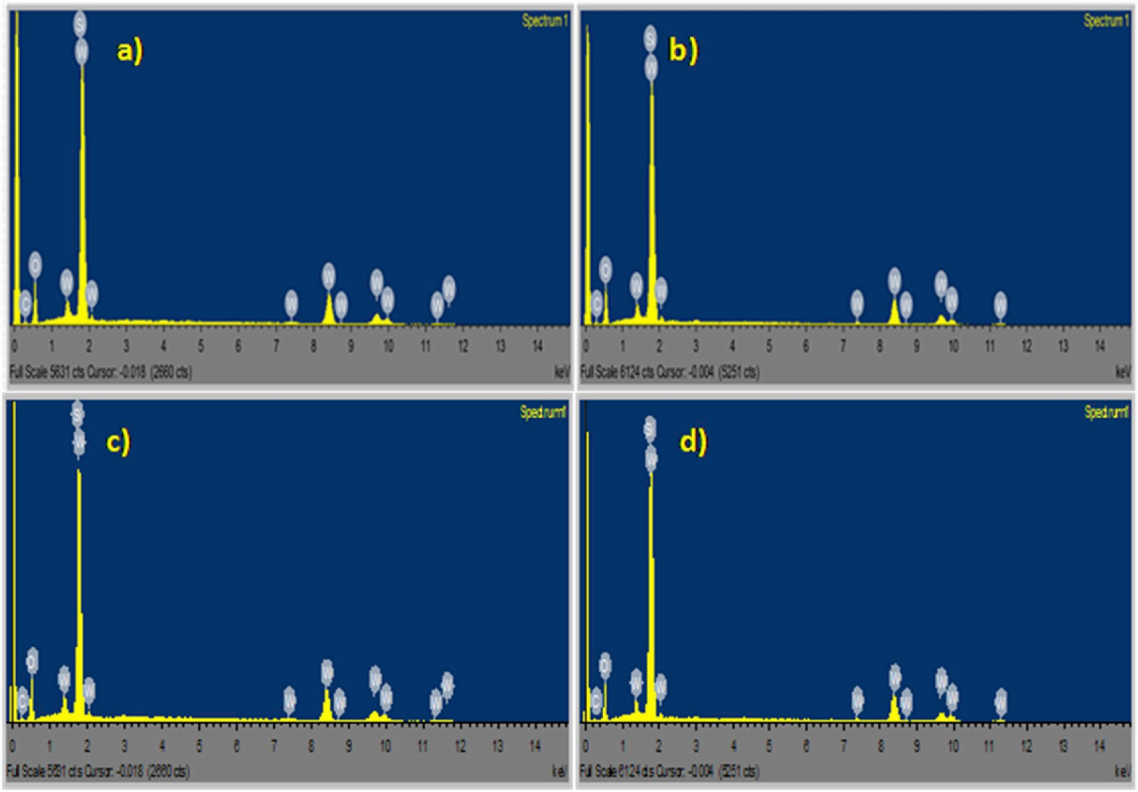

Fig. 7. Energy dispersive spectra of WO_3 thin films deposited a) at 16.3 mTorr, 400 K and b) at 16.3 mTorr, 600 K, c) at 17.6 mTorr, 400 K and d) 17.6 mTorr, 600 K.

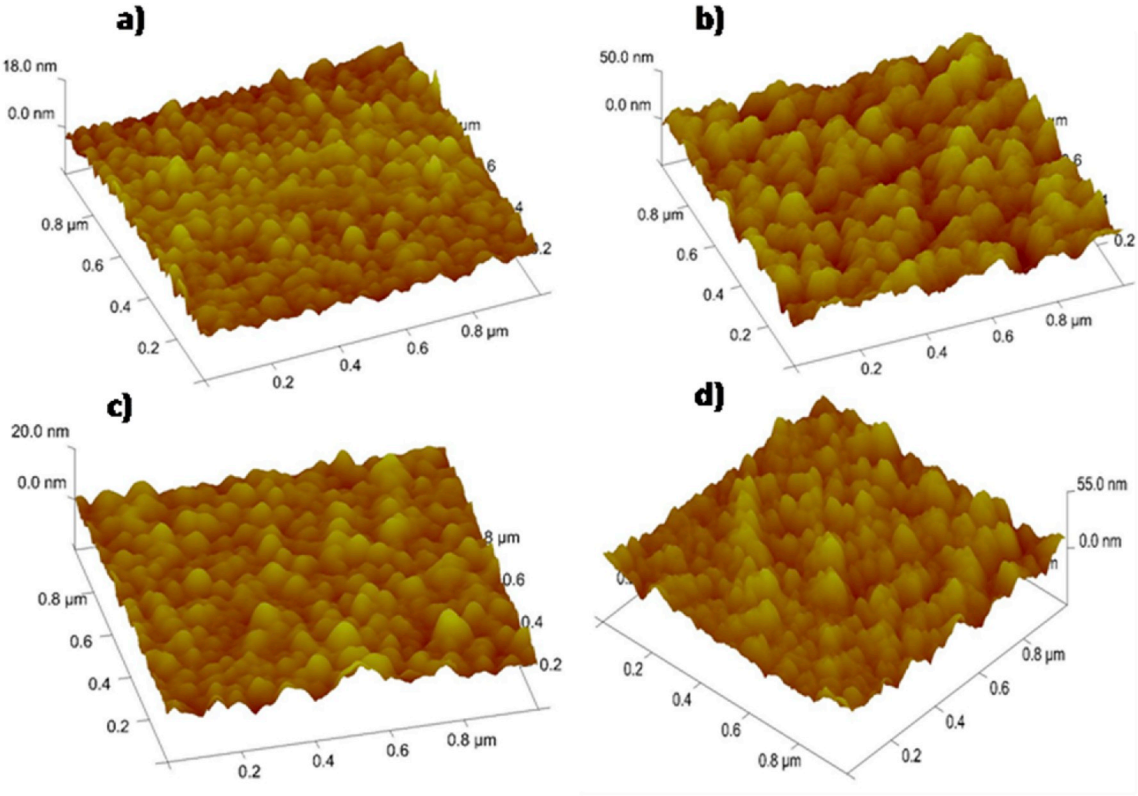

Fig. 8. Surface topography of the films in 3D prepared at a) 16.3 mTorr, 400 K, b) 16.3 mTorr, 600 K, c) 17.6 mTorr, 400 K and d) 17.6 mTorr, 600 K.

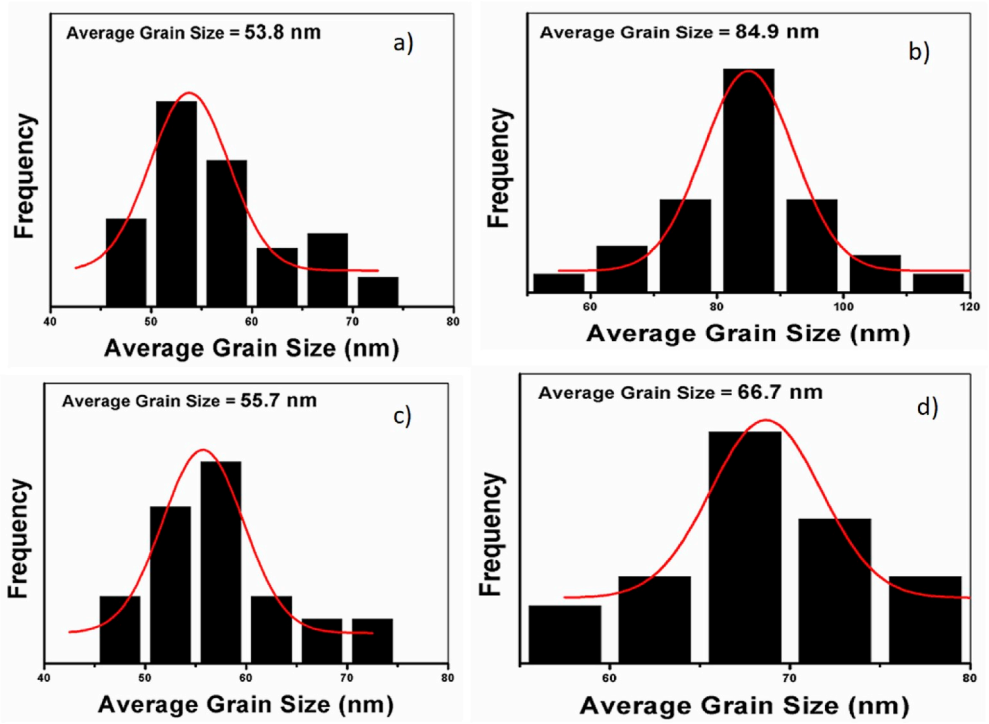

Fig. 9. Average grain size distribution curves of the WO_3 thin films prepared at a) 16.3 mTorr, 400 K b) 16.3 mTorr, 600 K, c) 17.6 mTorr, 400 K and d) 17.6 mTorr, 600 K.

3.3.3. *Surface morphology and composition*

In Fig. 5 FE-SEM images of WO_3 films are shown; images indicate, the films consist of nano sized particles dispersed randomly over the surface. The size of these particles is observed to be reliant strongly on temperature of the substrate and sputtering pressure. To be more specific, the films deposited at 400 K substrate temperature (at sputtering pressure

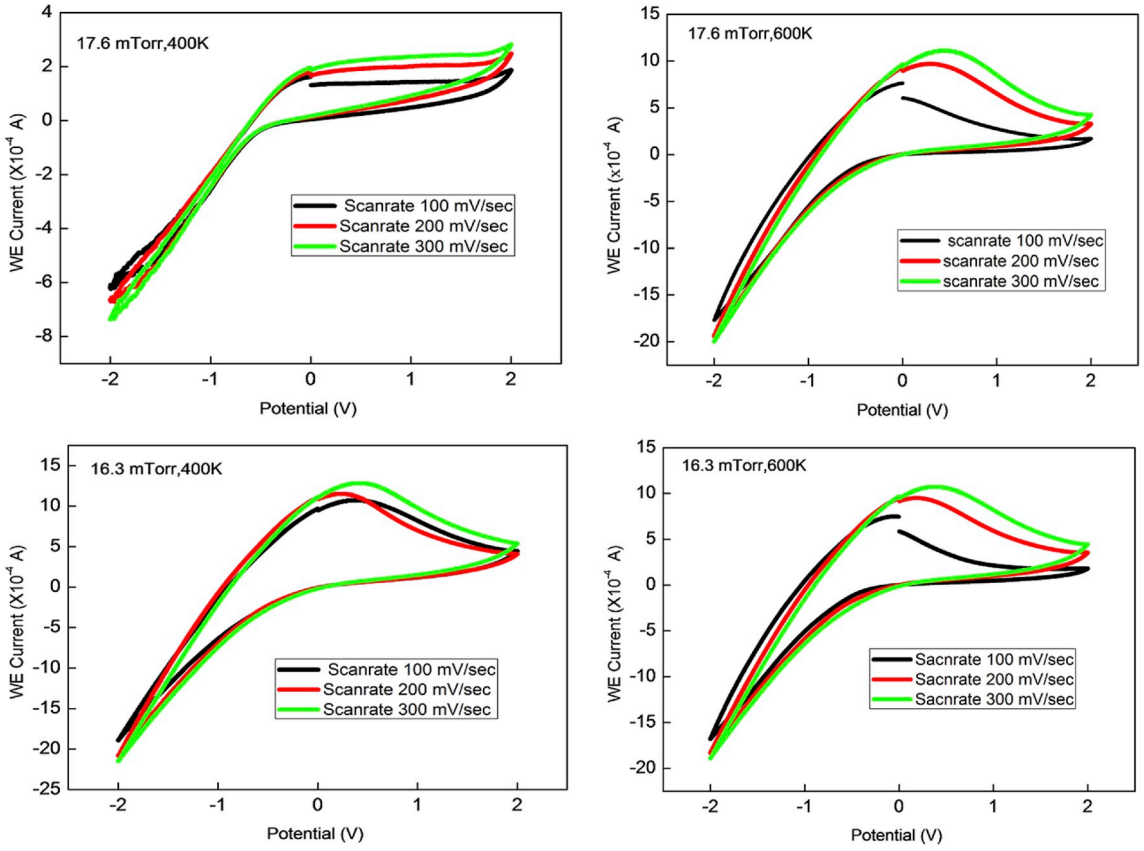

Fig. 10. Cyclic voltammograms of WO_3 thin films swept between −2.0 V and +2.0 V with Ag/AgCl as reference electrode measured at different scan rates.

Table 5
Diffusion coefficients of lithium ions.

Sputtering pressure (mTorr)	Substrate temp. (K)	Diffusion coefficient of Li^+ ions cm^2/sec at different scan rates		
		100 (mV/sec)	200 (mV/sec)	300 (mV/sec)
16.3	400	1.69×10^{-16}	4.09×10^{-17}	2.11×10^{-17}
	600	7.51×10^{-17}	2.70×10^{-17}	1.44×10^{-17}
17.6	400	7.86×10^{-17}	2.82×10^{-17}	1.68×10^{-17}
	600	3.20×10^{-18}	0.79×10^{-18}	0.68×10^{-18}

16.3 mTorr) found to be consisting of the particles of the size varied between 13.19 and 34.51 nm and when substrate temperature is raised to 600 K, size of these particles is found to increase and it is in the range of 15.04–50.90 nm (Fig. 6). However, sputtering pressure seemed to have little influence on the size of the particles. In addition, an increased fraction of the crystal grains is also observed in these films with increase of substrate temperature; such increase makes films more suitable for electrochromic devices since such films are more conducive for easy migration of ions [24,26,27]. The chemical composition of the films was analyzed using EDS spectra. The spectra of the films (Fig. 7) suggested the stoichiometry of tungsten and oxygen are within the expected ratio (viz., 1:3).

The topography (AFM images) of these films is found to have columnar structure (Fig. 8) with uneven distribution of nano crystallites; images of these films (sputtered at substrate temperature 400 K) and at both sputtering pressures, the size of the crystal grains is observed relatively low when compared with that in the films, sputtered at the substrate temperature 600 K. Moreover, in the films sputtered at T = 600 K, a coagulation of the grains with some voids is visualized on the surface of these films. Average size of the grains estimated from these images is found to be nearly the same as that observed from FE-SEM images (Fig. 9).

3.4. Electrochemical studies

3.4.1. Cyclicvoltammetry

The working electrode (tungsten oxide films coated on ITO substrate) current is measured in an electrolyte (a mixture of $LiClO_4$ and propylene carbonate) in the range of potential swept between −2.0 and +2.0 V at different scan rates (100 mV/s, 200 mV/s and 300 mV/s) and presented in Fig. 10. The current (due to the diffusion of Li^+) across the working electrode is observed to increase with increase of scan rate.

We have observed a gradual color change of the tungsten bronze (from light blue to dark blue) during the negative potential scan (−2 to 0 V); this is obviously because of reduction of W^{6+} into W^{5+} ions in the films due to the diffusion of electrons. During the positive voltage scan (0–2 V), the color of the films appeared to be gradually colorless (bleaching process); this is because during this cycle, the electrons ($W^{5+} \rightarrow W^{6+} + e^-$) and even Li^+ get ejected from the films. Such ejection of charge carriers accounts for the observed decrease in the current during this scan (Fig. 10). When these measurements were repeated in the reverse direction we have obtained a hysteresis loop (instead of getting a retraced curve). Such loop indicates a complete reduction-oxidation reaction process (electrochemical process) [28].

Diffusion of Li^+ ions into the film is calculated using well known Randell- Sevcik equation

$$i_p = 2.72 \times 10^5 \, D^{1/2} \, n^{3/2} \, C_o \, v^{1/2}. \quad (1)$$

In Eq. (1), i_p represents peak value of cathodic current (amp), n stands for No. of ions participated in the reaction, D is the coefficient of diffusion (cm^2/sec), C_o represents electrolyte concentration (M) and v represents rate of voltage scan in mV/sec.

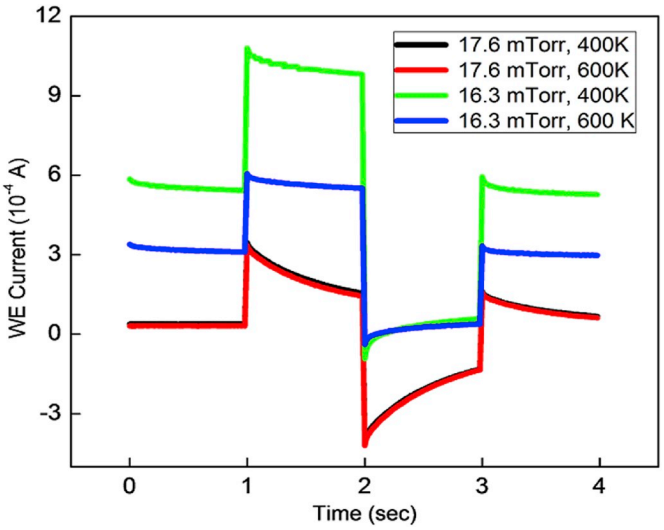

Fig. 11. Chronoamperometry curves of WO_3 thin films prepared at different conditions.

Diffusion coefficients were evaluated as per Eq. (1) for the films deposited under different conditions and tabulated in Table 5. D is found to be relatively larger than those reported earlier in several other films [1,2,26,29]. This is mainly due to the variations in the morphology of the films in the current study.

3.4.2. Chronoamperometry (CA)

Chronoamperometry fast is a step potential technique used for measuring processes of coloration and bleaching response time of the films. The process consists of stepping the working electrode (WE) potential from a value at which no faradaic reaction occurs to the potential up to which there is no detectable electroactive species' in the electrolyte. In Fig. 11, we have shown switching response of the current under step voltage application. During measurement, the potential raised from −0.5 V to +0.5V for 5 s. During the process of bleaching, the higher current arises due to the diffusion of Li ions (from electrolyte) to tungsten bronze and the fast decay of current occurs because of ejection of Li ions from Li_xWO_3 as per the chemical process $WO_3 \leftrightarrow Li_xWO_3$. Whereas in the transition of insulator to conductor behaviour the coloration is sluggish [30]. Response time for the process of coloration (t_c) and bleaching (t_b) were evaluated using current transient time data (Fig. 11)

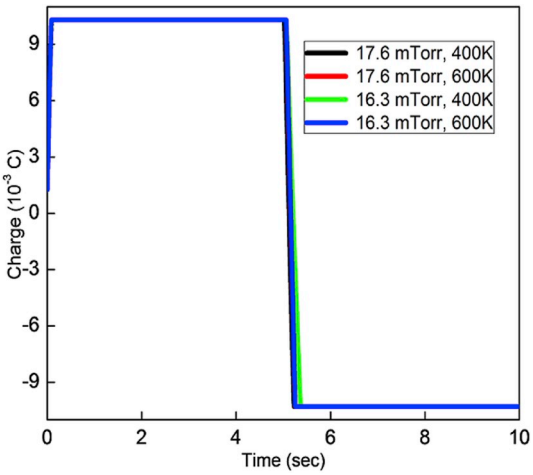

Fig. 12. Chronocoulometry curves of WO_3 thin films prepared at different conditions.

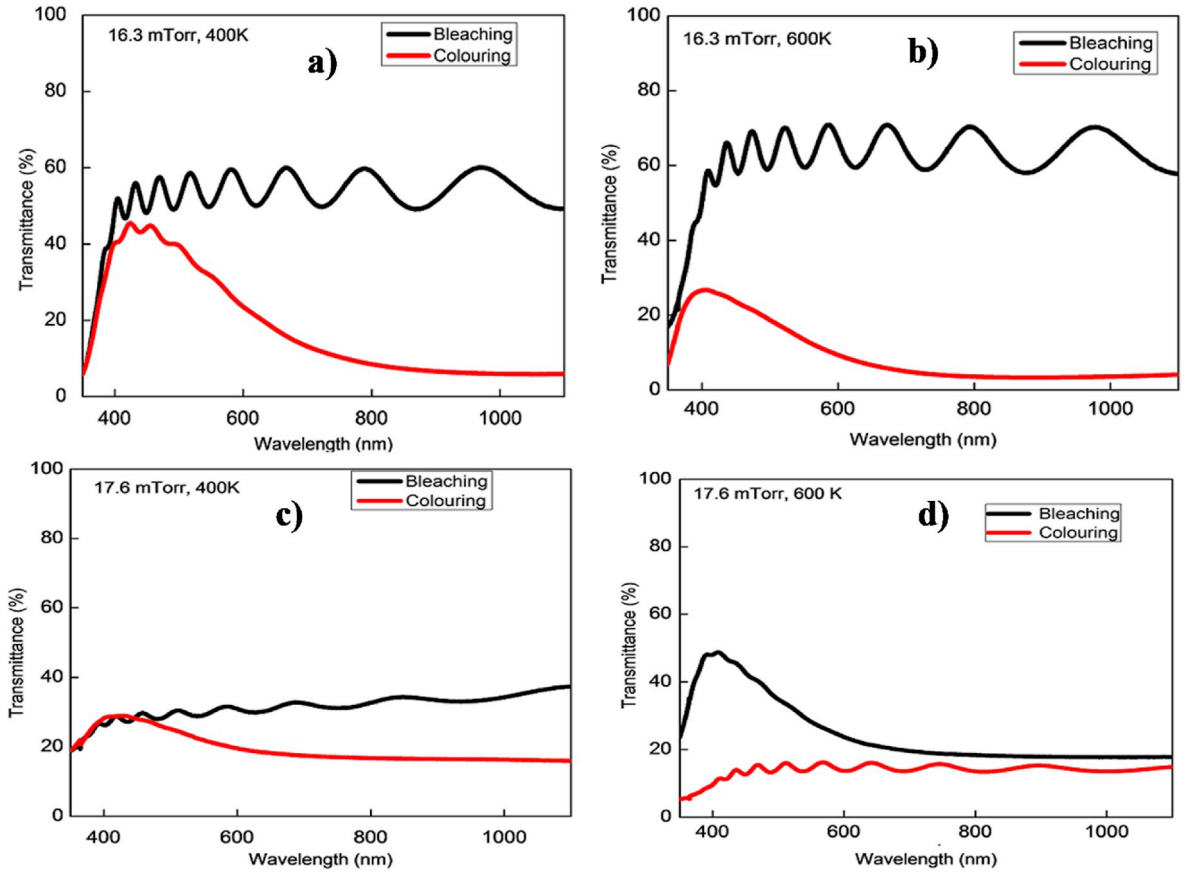

Fig. 13. Transmittance spectra of WO_3 thin films recorded in coloring and bleaching states.

and were found to be t_c ~0.45 s and that of t_b ~0.25 s. Such low values t_c and t_b suggest fast color-bleach kinetics. Further, the comparison of these two values indicate, bleaching process is quicker than the coloring rate regardless of the nature of mechanisms that are controlling these two processes. To elaborate more on these phenomenon, the bleaching speed is controlled by space charge limited current flow of cations across the film, whereas during coloring, potential barrier at the WO_3 – electrolyte interface and the number of Li^+ ions that are diffused into the film, play a major role. Values of t_c and t_b obtained in the current study are found to be lower when compared to those reported for various other films by different researchers earlier [28].

3.4.3. Chronocoulometry (CC)

The concentration of Li^+ ions intercalation and deintercalation with respect to time was performed by using chronocoulometry for the films in the interval of potential from – 0.5 V to + 0.5 V for a time interval of 10 s. Fig. 12 represents, the plot of intercalated charge *vs* time transient for WO_3 film. In the positive scan the charges are intercalated into the film through diffusion and the coloration of the films takes place due to reducing of tungsten ion from hexavalent to pentavalent state. In the backward scan, intercalated charge is ejected by the film and the W^{5+} ions oxidized to W^{6+} state and as a result the process of bleaching takes place [28]. Reversibility factor of these films is evaluated using the fraction of charge deintercalated (Q_{di}) to the intercalated charge (Q_i). Values of Qi and Q_{di} are found to be 8.7 mC and 8.0 mC, respectively, for all the films and the corresponding intercalated charge density was found to be 6.96 mC/cm^2. The reversibility (Q_{di}/Q_i) of the films prepared under different conditions is found to be 91%. This result suggests the substrate temperatures and sputtering pressures are optimal values for obtaining such a superior value of reversibility.

Table 6
Coloration efficiency of the films.

Sputtering Pressure (mTorr)	Substrate temp. (K)	Optical density, Δ	Coloration efficiency, η (cm^2/C) at λ = 650 nm
16.3	400	0.249	35.90
	600	0.126	18.11
17.6	400	0.508	73
	600	1.047	150.05

3.4.4. Optical transmittance of films after coloring and bleaching

Optical transmission of the films in the bleached and colored conditions of WO_3 films was registered in the spectral region of 300–1100 nm and shown in Fig. 13. As expected, transmittance of the films was found to be decreased after coloration. However, optical modulation is observed to be higher for the films sputtered at higher oxygen partial pressure; this attributed to increased crystallinity of the films at higher pressure.

Coloration efficiency η of WO_3 thin films at a fixed wavelength can be correlated with the optical contrast (i.e., the change in optical density, ΔOD and with charges intercalated Qi = q/A, where A stands for electrode area) by the relation [31].

$$\eta = \Delta OD \,/\, Q_i = \log (T_b/T_c) \,/\, (q/A). \quad (2)$$

In Eq. (2), T_b and T_c represents transmittance of the films during bleaching and coloring modes, respectively. Coloration efficiency of the films is found to varied between 35.90 and 150.05 cm^2/C with deposition parameters adopted and it is found to be larger than the values reported earlier for these films [32]. A brief summary of the data optical transmittance and other related parameters of the studied films is tabulated in Table 6.

4. Conclusions

Thin films of WO_3 were prepared at two sputtering pressures and substrate temperatures by DC Magnetron sputtering on to silicon wafer, quartz glass and indium doped tin oxide coated glass (ITO). Thickness and roughness of these films (which affect the physical characteristics of the films) were observed to be dependent on the conditions of deposition. The optical properties revealed that transmittance of the films in the visible region is ~84%. The XRD, FE-SEM and AFM studies have indicated the films embedded with crystal grains and the degree of crystallinity is observed to increase with increasing of substrate temperature. XRD studies further confirmed that the crystal grains entrenched in the films possess the monoclinic structure. The structural analysis of the films is further evaluated by Raman spectral studies; these spectra have exhibited both bending and stretching vibrational modes of W–O linkages in WO_3 crystallites. Morphological studies indicated that as substrate temperature is increased the size of the particle increases and coagulation of particles also takes place. The energy dispersive spectra of confirmed stoichiometry of the films. Coloration efficiency and response time for coloring and bleaching of the films are found to be dependent on sputtering pressure and substrate temperature. Coloration efficiency of WO_3 films prepared with the optimal conditions in the current study is found to be higher than that reported earlier by several other authors. Hence the films coated by using DC Magnetron sputtering at the mentioned substrate temperature and sputtering pressure are the optimal values for fabrication of electro chromic device with high coloration efficiency.

Author statement

All the authors equally contributed for this work.

Declaration of competing interest

The authors declare that they have no known competing financial interests or personal relationships that could have appeared to influence the work reported in this paper.

Acknowledgements

We express our sincere thanks to Gobi Saravanan, Karthick, Suresh and Durai Nayak of Sathyabama university (Deemed) for their help in the preparation and characterization of the films. The help rendered by Dr. Pradeep Kumar Brahman of KL University (Deemed) in some of the measurements presented in this work is also gratefully acknowledged.

References

[1] C.G. Granqvist, Handbook of Inorganic Electrochromic Materials, Elsevier, Amsterdam, 1995.
[2] P.M.S. Monk, R.J. Mortimer, D.R. Rosseinsky, Electrochromism:Fundamentals and Applications, VCH, Weinheim, 1995.
[3] A. Gunnar, Niklasson, G. Claes, Granqvist Electrochromics for smart windows: thin films of tungsten oxide and nickel oxide, and device based on these, J. Mater. Chem. 17 (2007) 127–156.
[4] C.G. Granqvist, Electrochromics for smart windows: oxide based thin films and devices, Thin Solid Films 564 (2014) 1–38.
[5] K. Thummavichai, Y. Xia, Y. Zhu, Recent progress in chromogenic research of tungsten oxides towards energy- related applications, Prog. Mater. Sci. 88 (2017) 281–324.
[6] P.M. Woodword, A.W. Sleight, T. Vogt, Ferroelectric tungsten trioxide, J. Solid State Chem. 131 (1997) 9–17.
[7] S.S. Kalagi, S.S. Mali, D.S. Devi, A.I. Inamdar, H. Im, P.S. Patil, Transmission attenuation and chromic contrast characterization of R.F. sputtered WO3 thin films for electrochromic device applications, Electrochim. Acta 85 (2012) 501–508.
[8] A. Antonaia, T. polichetti, M.L. Addonizio, S. Aprea, C. Minarini, A. Rubino, Modification of vapor deposited WO_3 electrochromic films by oxygen backfilling, Thin Solid Films 354 (1999) 73–81.
[9] A.A. Joraid, S.N. Almari, Effect of annealing on structural and optical properties of WO3 thin films prepared by electron beam coating, Physica B: Phys. Condens. Matter 391 (2007) 199–205.
[10] Y.W. Sun, Y.Y. Tsui, Production of porous nanostructured zinc oxide thin films by pulsed laser deposition, Opt. Mater. 29 (2007) 1111–1114.
[11] F. Anjum, M.F. David, J. Gold, A. Riaz, D.C. Robert, P.K. Nobuhiko, Study of optical and structural properties of sputtered aluminum nitride films with controlled oxygen content to fabricate Distributed Bragg Reflectors for ultraviolet A, Opt. Mater. 98 (2019) 109405.
[12] P. Tagtstrom, U. Jansson, Chemical vapour deposition of epitaxial WO_3 films, Thin Solid Films 352 (1999) 107–113.
[13] L. Boudoud, L. Benramdane, R. Desfeux, B. Khelifa, C. Mathieu, Structural and optical properties of MoO3 and V2O5 thin films prepared by Spray Pyrolysis, Catal. Today 113 (2006) 1327.
[14] R. Pena-Garcia, Y. Guerra, R. Milani, D.M. Oliveira, F.R. de Souza, E. Padron-Hernandez, Influence of Ni and Sr on the structural, morphological and optical properties of ZnO synthesized by sol gel, Opt. Mater. 98 (2019) 109427.
[15] A. Subrahmanyam, A. Karuppasamy, Optical and electrochromic properties of oxygen sputtered tungsten oxide (WO3) thinfilms, Sol. Energy Mater. Sol. Cells 91 (2007) 266–274.
[16] K. Salamon, O. Milat, N. Radic, P. Dubcek, M. Jercinovic, S. Bernstorff, Structure and morphology of magnetron sputtered W films studied by x-ray methods, J. Phys. D Appl. Phys. 46 (2013), 095304.
[17] V. Nirupama, K.R.M. Gunasekhar, B. Sreedhar, S. Uthana, Effect of Oxygen partial pressure on the structural and optical properties of dc reactive magnetron sputtered molybdenum oxide films, Curr. Appl. Phys. 10 (2010) 272–278.
[18] A. Karuppasamy, Electrochromism in surface modified crystalline WO3 thin films grown by reactive DC magnetron sputtering, Appl. Surf. Sci. 282 (2013) 77–83.
[19] K.J. Lethy, D. Beena, R.V. Kumar, V.P.M. Pillai, Structural, Optical and Morphological studies on laser ablated nano structured WO3 thin films, Appl. Surf. Sci. 254 (2008) 2369–2376.
[20] G. Merhan Muglu, E. Giir, Oxygen partial pressure effects on the magnetron sputtered WO3 films, J. Phys.: Conf. Ser. 707 (2016), 012009.
[21] D. Green, Optical constants of sputtered WO_3 thin films, Appl. Optic. 29 (1990) 4547–4549.
[22] Y. Yamada, K. Tabata, T. Yashima, The character of WO3 films prepared with RF sputtering, Sol. Energy Mater. Sol. Cells 91 (2007) 29–37.
[23] H. Kalhori, B.P. Stephen, A.S. Esmaeily, M. Coey, M. Ranjbar, H. Salamati, Morphology and structural studies of WO_3 films deposited on $SrTiO_3$ by pulsed laser deposition, Appl. Surf. Sci. 390 (2016) 43–49.
[24] M. Mai, X. Ma, H. Zhou, M. Ye, T. Li, K. Shanming, P. Lin, X. Zeng, Effect of oxygen pressure on pulsed laser deposited WO_3 thin films for photoelectrochemical water splitting, J. Alloys Compd. 722 (2017) 913–919.
[25] Z. Feng, W. Hai-Qia, W. Song, W. Jing-Yan, Z. Zhi-Cheng, J. Ye, Structures and optical properties of tungsten oxide thin films deposited by magnetron sputtering of WO_3 bulk; Effects of annealing temperatures, Chin. Phys. B 23 (2014), 098105.
[26] A. Baserga, V. Russo, F. Di Fonzo, A. Bailini, D. Cattaneo, C.S. Casari, A. Li Bassi, C. E. Bottani, Nanostructured tungsten oxide with controlled properties: synthesis and Raman characterization, Thin Solid Films 515 (2007) 6465–6469.
[27] K.J. Lethy, D. Beena, R. vinod kumar, V.P. Mahadevan pillai, V. Ganesan, V. Sathe, D.M. phase, Nanostructured tungsten oxide thin films by the reactive pulsed laser deposition technique, Appl. Phys. A 91 (2008) 637–649.
[28] P.M. Kadam, N.L. Tarwal, P.S. Shinde, R.S. Patil, H.P. Deshmukh, P.S. Patil, From beads – to wires-to-fibers of tungsten oxide Electrochromic response, Appl. Phys. A 97 (2014) 323–330.
[29] F. Di Fonzo, A. Bailini, V. Russo, A. Baserga, D. Cattaneo, M.G. Beghi, P.M. Ossi, C. S. Casari, A. Li Bassi, C.E. Bottani, Synthesis and characterization of tungsten and tungsten oxide nanostructured films, Catal. Today 116 (2006) 69–73.
[30] R. Sivakumar, K. Shanthakumari, A. Thayumanvan, M. Jayachandran, C. Sanjeeviraja, Coloration and bleaching mechanism of tungsten oxide thin films in different electrolytes, Surf. Eng. 23 (2007) 373–379.
[31] M. Meenakshi, R. Sivakumar, A. Sivanantharaja, C. Sanjeeviraja, Electrochromic performance of RF sputtered WO3 thin films by Li ion intercalation and de-intercalation, AIP Conf. Proc. 1832 (2017), 080003.
[32] M. Deepa, A.K. Srivastava, M. Kar, S.A. Agnihotry, A case study of optical properties and structure of sol-gel derived nanocrystalline WO3 thin films, J. Phys. D 39 (2006) 1885–1893.

Journal of Critical Reviews

ISSN- 2394-5125 Vol 7, Issue 11, 2020

DOMINATION IN REGULAR AND IRREGULAR BIPOLAR FUZZY GRAPHS

Abdul Muneera[1*], Dr.T. Nageswara Rao[2], Dr.J. Venkateswara Rao[3], Dr.R.V.N. Srinivasa Rao[4]

[1*]Research Scholar, Department of Mathematics, Koneru Lakshmaiah Education Foundation, Green Fields, Vaddeswaram, Guntur District, Andhra Pradesh, India.
[2]Department of Mathematics, Koneru Lakshmaiah Education Foundation, Green Fields, Vaddeswaram, Guntur District, Andhra Pradesh, India.
[3]Department of Mathematics, School of Science & Technology, United States International University, USIU- Africa.
[4]Department of Mathematics, Wollega University, NEKEMTE, ETHOPIA.

Received: 12.04.2020 *Revised: 19.05.2020* *Accepted: 10.06.2020*

Abstract
The aim of this article is to take a broad view of dominations in bipolar fuzzy graphs(or) f-graphs. A set S⊆ V is assumed to be fuzzy dominating set of a f-graph G= (σ, μ), if for each v ϵ V – S ∃ u ϵ S ∋ u dominates v. we discuss the perception of domination in regular bipolar f-graphs (γ_{rbf}) and overall domination in regular bipolar f-graphs. We extended our study to dominations in Irregular bipolar f-graph (γ_{Irbf})and total domination in Irregular bipolar f- graphs. Establish the relation between the neighborly irregular f-graphs and highly irregular bipolar f-graphs. We studied properties of regular bipolar f-graphs and irregular bipolar f-graphs. Some results are derived related to various dominations in bipolar fuzzy graphs or f-graphs.

Keywords: Bipolar f-graphs (BFG), Domination in Regular Bipolar f- graphs, Total Dominations in Irregular Bipolar f-graphs, Neighborly Irregular Bipolar f-graphs, Regular Bipolar f-graphs (RBFG), Irregular Bipolar f-graphs (IRBFG).

DOI: http://dx.doi.org/10.31838/jcr.07.11.141

INTRODUCTION

To study many real world problems Graph theory is a helpful tool. Nowadays, graphs do not represent many real world problems due to uncertainty of the parameters of systems. The work [1] introduced a fuzzy set idea after that Rosenfeld initiated fuzzy graphs. In various disciplines fuzzy set theory become a dynamic part of research like as signal processing, artificial intelligence, computer networks, life sciences, robotics, automata theory, medical sciences etc. The ides of "bipolar fuzzy sets (BFSs)" was presented by [5] in 1994 with the innovation of membership values to the components of universal set varies from -1 to 1.According to the classification of a BFS, if the part is inappropriate to the consequent possessions the membership significance of that element is 0.The membership range (0, 1] of a component shows that the component rather fulfills the possessions, & membership range [-1, 0) of a component indicates that the component rather fulfills the hidden counter property. Non negative data signifies what is approved to be likely, while negative data signifies what is measured to be impossible. The work [6] presented "regular f- graphs and totally regular f-graphs". In 2011, Akram [7] [8] defined bipolar fuzzy graphs (BFG). Come to of graph theorists numerous authors have accomplished exceptionally intriguing work with regards to the domination related themes. In this article we develop domination in "regular bipolar fuzzy graphs" (γ_{rbf}), domination in IRBFG (γ_{Irbf}), and dominations in totally IRBFG. We discussed various applications on bipolar fuzzy graphs (or) f-graphs.

PRELIMINARIES

Let S bean Universal set. Consider Fuzzy set B in S is signified by B = {(p, $\mu_B(p)$): $\mu_B(p) > 0$, pϵ S}, where the functionμ_B: S→ [0, 1] be the membership value of element p in fuzzy set B. Consider a f-graph $G=(V,\sigma,\mu)$ be the non-empty set V together with a pair of functions $\sigma: V \to [0,1]$and $\mu: V\times V \to [0,1] \forall x,y \in V, \mu(x,y) \le \min\{\sigma(x),\sigma(y)\}$. If $\mu(x,y)=\min\{\sigma(x),\sigma(y)\}\ \forall x,y\in V$, then the fuzzy graph is assumed to be complete. The degree of vertex x is d (x) = $\sum_{(x,y)\epsilon\xi}\mu(x,y)$.The minimum &maximum degree of the FG is $G=(V,\sigma,\mu)$ is given byδ(G) = ∧ {d (x)/x ϵV}, Δ(G)=∨ {d (x)/ xϵ V}respectively. td(x) = d(x) + σ (x) is assumed to be total degree of a node x which is belongs to V. Fuzzy graph G = (V, σ, μ) is assumed to be k-regular [6], if degree of each vertex (or) node is k. i.e. d(v) = k, +ve real number, ∀ v ϵ V. If for every node of G, it has identical total degree k, then G is assumed to be a "k-totally regular fuzzy graph" or f- graph. An f-graph (FG) is said to be irregular f-graph if any two neighboring nodes of f-graph having different degrees. The FG is said to be neighborly irregular, if each two neighboring nodes of graph have distinct degrees. The FG is said to be totally irregular, if there will be a node that is adjacent to nodes with separate total degrees. And also a FG is assumed to be neighborly total irregular, if every 2 adjacent nodes have different total degrees. And also a FG is named highly irregular [14],if each node of G is neighboring to nodes with different degrees.

Definition 2.1: Deliberate ψ be a non-void set.βis a BFS in the form {(m, $\mu_\beta^+(m)$, $\mu_\beta^-(m)$) / m ϵ ψ} where $\mu_\beta^+ : \psi \to [0,1]$ &$\mu_\beta^-: \psi \to [-1,0]$ are mappings. Here$\mu_\beta^+(\psi)$ Is used to symbolize the non-negative membership degree of component m, negative membership degree is denoted by $\mu_\beta^-(\psi)$ of a component m. If $\mu_\beta^+(m) \neq 0$ as well as$\mu_\beta^-(m) = 0$, it means that m is having just +ve fulfillment for β. If $\mu_\beta^+(m) = 0$ &$\mu_\beta^-(m) \neq 0$ it means the condition that m does not fulfill the property β, but fulfills the contradict property of β.
A bipolar f- graph ξ = (V, α, β) where α = (μ_α^+,μ_α^-) is a BFS in V and β = (μ_β^+,μ_β^-) is a BFS in S⊆ V X V, ∋ μ_β^+ ({m,n}) ≤ min ((μ_α^+(m), μ_α^+(n)) and,μ_β^- ({m,n}) ≥ max ((μ_α^-(m), μ_α^-(n)), ∀ {m,n} ϵS. Hereα is the bipolar f- node set of V, and β be the bipolar f- edge set of S.

Definition 2.2: Let ξ = (V,α, β) be a BFG. If entire nodes having equivalent open neighborhood degree k, at that point G is specified as k-RBFG. The "open neighborhood degree" of a node m in ξ is determined by deg(m)or simplyd (m)=((d$^+$(m),d$^-$(m)) whereasd$^+$(m)=$\sum_{x\epsilon V}\mu_\alpha^+(m)$ andd$^-$(m)=$\sum_{x\epsilon V}\mu_\alpha^-(m)$.

Definition 2.3: Let ξ = (V,α, β) be a RBFG. The order of a RBFG is ξO (ξ)= $(\sum_{x\epsilon V} \mu_{\alpha}^{+}(m), \sum_{x\epsilon V} \mu_{\alpha}^{-}(m))$. The size of a RBFG ξ is S (ξ) = $(\sum_{pq\epsilon S} \mu_{\beta}^{+}(mn), \sum_{pq\epsilon S} \mu_{\beta}^{-}(mn))$.

Definition 2.4: Letξ = (V,α, β) be a BFG. If every node of ξhas equal closed neighborhood degree p, then ξ is said to bep-totally RBFG. The "closed neighborhood degree" of a node p is distinct by $d^{+}[m] = d^{+}(m) + \mu_{\alpha}^{+}(m)$, $d^{-}[m] = d^{-}(m) + \mu_{\alpha}^{-}(m)$.

Definition 2.5: Consider a BFG ξ = (V,α, β) whose arc is termed effective if $\mu^{+}(m\ n) = \min\{\mu^{+}(m), \mu^{+}(n)\}$, and $\mu^{-}(m\ n) = \max\{\mu^{-}(m), \mu^{-}(n)\}$, ∀ m n ϵ S. It is denoted by $\mu_S(m\ n) = (\mu_S{}^{+}(m\ n), \mu_S{}^{-}(m\ n))$. The effective degree of a node v in BFG ξ, signified by $d_S(v)$ is distinct as $d_S(v) = \sum_{m\ n\epsilon S} (\mu_S{}^{+}(m\ n), \mu_S{}^{-}(m\ n))$.

Definition 2.6: Consider a BFG ξ = (V,α, β). Degree of a node in BFG ξ, signified by d(v) is distinct as $d(v) = \sum_{mn\epsilon S} (\mu^{+}(m\ n), \mu^{-}(m\ n))$.

Proposition 2.7: In a RBFG ξ = (V,α, β), Order O(ξ) and S(ξ) Size of a BFG are equivalent & i.e., also equal to closed neighborhood degree of a Bipolar f- graph.

Proof: Given ξ is a RBFG.
This means all nodes are having equal level (or) degree.
It is possible only when the membership values for all nodes is same and nodes are connected to each other.

We have $d_N[p] = O(\xi), \forall p\in V$ .....(1)
And also we know that $S(\xi) = (\sum_{pq\epsilon S} \mu_{\beta}^{+}(pq), \sum_{pq\epsilon S} \mu_{\beta}^{-}(pq))$
$= (\sum_{p\epsilon V} \mu_{\alpha}^{+}(p), \sum_{p\epsilon V} \mu_{\alpha}^{-}(p)) = O(\xi)\ \forall p\in V$ .....(2)
From (1) and (2) we get $d_N[p] = O(\xi) = S(\xi). \forall p\in V$.

Proposition 2.8: In a RBFG ξ = (V,α, β)neighborhood degrees, effective degrees and degrees are the same for any node in ξ.
i.e.$d(m) = d_S(m) = d_N(m), \forall m\in V$

Proposition 2.9: The size S (ξ) of a p-RBFGξ is $\frac{pk}{2}$, where cardinality of v is k. i.e.;|V|=k.

Proposition 2.10: If ξbe a q-totally RBFG, then 2S(ξ) + O(ξ) = qk, cardinality of v is k. i.e.; where |V|=k.

Proposition 2.11: If ξbe the both "p-regular &q-totally regular bipolar f- graph (FG)", then the order of ξ is distinct byO (ξ) = K (q - p), where cardinality of v is k. i.e.;|V|=k.

Properties 2.12: For a bipolar fuzzy graph
(i). $O(\xi) - \Delta_E{}^{+} \le O(\xi) - \delta_E{}^{+}$
(ii). $O(\xi) - \Delta_N{}^{+} \le O(\xi) - \delta_N{}^{+}$

Definition 2.13: Consider a BFG ξ= (V, α,β), where $\alpha = (\mu_{\alpha}^{+}, \mu_{\alpha}^{-})$ and $\beta = (\mu_{\beta}^{+}, \mu_{\beta}^{-})$ be 2BFSson a non-void finite set V & S⊆ V x V correspondingly. ξis known as IRBFG if there exists a node that is adjacent to a node with different levels.ξis supposed to be totally IRBFG if ∃ a node that is adjacent to a node with different total degrees.

Definition 2.14: The cardinality of V, i.e.; amount of nodes is termed as the order of a BFG ξ = (V,αβ) and is signified by | V| (or O (ξ)), and determined by $O(\xi) = |V| = \sum_{m\in V} \frac{1+\mu_{\alpha}^{+}(m)+\mu_{\alpha}^{-}(m)}{2}$, the no. of elements in a set of S, i.e.; amount of edges is termed as size of BFG ξ = (V,αβ) and is signified by |S| (or S(ξ)), and described as $S(\xi) = |S| = \sum_{m\in V} \frac{1+\mu_{\beta}^{+}(mn)+\mu_{\beta}^{-}(mn)}{2}$.

Definition 2.15: Let ξ = (V,αβ) be a connected BFG. ξis called neighborly irregular f-graph if degree of each two adjacent nodes ofξ is different. ξis named neighborly totally IRBFG if for each 2 adjacent nodes of G having separate total degrees.

DOMINATIONS IN BIPOLAR FUZZY GRAPHS

Definition 3.1: The strength of connectedness between two nodes a & b is $\mu^{\infty}(a, b) = \sup\{\mu^{k}(a, b) / k = 1, 2,.....\}$ whereas$\mu^{k}(a, b) = \sup\{\mu(aa_1) \wedge \mu(a_1a_2) ..... \wedge \mu(a_{k-1}b) / a_1 .....a_{k-1} \epsilon V\}$.

Definition 3.2 : An arc (a, b) is said to be strong edge in a BFG, ξ = (V, E) if $\mu_2^{+}(a, b) \ge (\mu_2^{+})\infty(a,b)$ &$\mu_2^{-}(a, b) \ge (\mu_2^{-})\infty(a,b)$ whereas $(\mu_2^{+})\infty(a,b) = \max\{(\mu_2^{+})^{k}(a, b) / k = 1,2,....n\}$ and $(\mu_2^{-})\infty(a,b) = \min\{(\mu_2^{-})^{k}(a, b) / k = 1,2,3,....n\}$.

Definition 3.3: A subset S of V is said to be a dominating set in ξ if ∀v ϵ V – S, ∃ u ϵ S ∋ u dominates v. A dominating set S of a bipolar f- graph (BFG) is known to be "minimal dominating set" if no appropriate subset of S is a dominating set. The minimum cardinality between all minimal dominating set is named lower domination number of ξ, and is signified by $d_B(\xi)$. The maximum cardinality between all "maximal dominating set" is said to be upper domination number of ξ, and is signified by $D_B(\xi)$.

Definition 3.4: Let ξ be a BFG on G*. If there is a node that is neighboring to node with different neighborhood degrees, then ξ is said to be an IRBFG. i.e.,deg (m) ≠ n ∀ m ϵ V.

Definition 3.5: A Dominating set D of a BFG ξis known Domination in IRBFG, if ξ is an IRBFG.

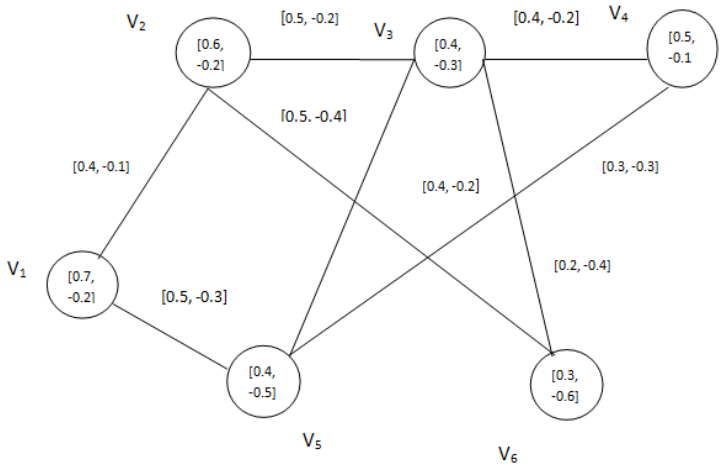

Fig. 1

In Fig 1, deg(V_1) = (0.9,-0.4), deg(V_2) = (1.4,-0.7), deg(V_3) = (1.6,-0.9), deg(V_4) = (0.6,-0.6), deg(V_5) = (1.1,-0.9), deg(V_6) = (0.8,-0.7)
The vertex cardinality of FG in Fig 1 is
0.75+0.7+0.55+0.7+0.35+0.45=3.5
That is the order of the IRBFG is O (ξ) = 3.5.
The Edge cardinality of FG in Fig 1 is
0.65+0.65+0.6+0.6+0.55+0.6+0.5+0.4 = 4.55.
That is the size of IRBFG is S (ξ) = 4.55
Here Domination set D is {V_2, V_4}.
Minimum fuzzy cardinality is γ_{irbf} = (1.1, -0.3)

Definition 3.6: A Dominating set S of a BFGξ is known Domination in RBFG, if ξ is a regular bipolar f- graph (RBFG).

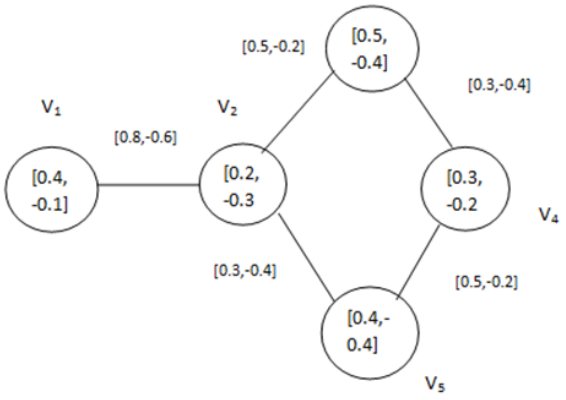

Figure 2

deg (V_1) = (0.8, -0.6), deg (V_2) = (0.8, -0.6), deg(V_3) = (0.8, -0.6), deg(V_4) = (0.8, -0.6), deg(V_5) = (0.8, -0.6).Since the degrees are equal, it is a RBFG. Domination set is {V_2, V_4}. Minimum fuzzy cardinality is γ_{rbf} = (0.5, -0.5)

Definition 3.7: Let ξbe a BFG without isolated nodes. If for every node v ϵV, ∃ a node u ϵ S, u ≠v ∋ udominates v then set S is named a Total domination set of bipolar fuzzy graph ξ = (V, α, β).

Definition 3.8: If there will be no appropriate subset of S is a "total dominating set" of a bipolar f- graph G is said to be minimal total dominating set.

Definition 3.9:A lower total dominating number of ξ is distinct as the "minimum cardinality of a minimal total dominating set" ξ, and it is signified by $t_B(\xi)$.

Definition 3.10: The "maximum cardinality of a minimal total dominating set" is known as upper total dominating number of ξ, and it is signified by $T_B(\xi)$.

Corollary 3.11: For any BFG, ξ = (V,αβ) without isolated nodes, $d_B(\xi) = O(\xi)/2$ and $d_B(\xi) \le O(\xi) - \Delta$.

Corollary: In a RBFG, $O^P(\xi) = S^P(\xi)$;
and $O^N(\xi) = S^N(\xi)$.

Theorem3.12: For a BFG, $t_B(\xi) = O_B(\xi)$ iff each node of ξhas a only one neighbor.

Proof: Suppose each node of ξhas a single neighbor, then node set v be the only "total dominating set" of G then $t_B(\xi) = O_B(\xi)$.
Conversely, assume that $t_B(\xi) = O_B(\xi)$.
If ∃ a node a with neighbor b and c then b– {a} is "total dominating set" of ξSo that $t_B(\xi) \le O_B(\xi)$ which prompts logical inconsistency. Hence each node of ξ has single neighbor.

Theorem 3.13: Every complete BFG is a totally RBFG.

Theorem 3.14: Let ξ = (V,α, β) be a BFG. Then $\alpha = (\mu_\alpha^+, \mu_\alpha^-)$ is a constant function iff the next are the same.
(a). ξ is a RBFG
(b). ξ is a totally RBFG

Proof: Assume that $\alpha = (\mu_\alpha^+, \mu_\alpha^-)$ is a constant function. Let $\mu_\alpha^+(m) = C_1$ and $\mu_\alpha^-(m) = C_2 \forall\ m \in V$.
(a) ⇒(b); suppose that ξ is n-RBFG, then $deg^+(m) = n_1$ and $deg^-(m) = n_2 \forall m \in V$. So
$deg^+[m] = deg^+(m) + \mu_\alpha^+(m)$,
$deg^-[m] = deg^-(m) + \mu_\alpha^-(m) \forall\ m \in V$.
Thus $deg^+[m] = n_1 + C_1$, $deg^-[m] = n_2 + C_2 \forall\ m \in V$.
Hence ξ is totally RBFG.
(b)⇒(a); presume that ξ is a totally RBFG, then
$deg^+[m] = K_1$, $deg^-[m] = K_2 \forall\ p \in V$.
Thus ξ is a RBFG.

Theorem 3.15: Let us considerξ be a BFG.ξis highly IRBFG& neighborly IRBFG, iff the levels of all nodes of ξ are different.

Proof: Let ξ = (V,αβ) be a BFG where $\alpha = (m_1^+, m_1^-)$ and $\beta = (m2^+, m_2^-)$ be two BFSs on a non-void finite set V and V×Vcorrespondingly. Let V={v_1, v_2 …v_n}. We suppose that ξ is highly irregular and neighborly IRBFG. Let the adjacent nodes of u_1 be u_2, u_3, …u_n with degrees (k_2^+, k_2^-), (k_3^+, k_3^-), (k_4^+, k_4^-)……(k_n^+, k_n^-) correspondingly. As ξ is highly and neighborly irregular, $d(u_1) \ne d(u_2) \ne d(u_3) \ne \ldots\ldots d(u_n)$. So it is understandable that all nodes are of separate degrees.
On the contrary presume that the degree of every nodes of G is different. This implies that each two neighboring nodes take different levels & to each node the adjacent nodes have separate degrees. Thus G is highly irregular &neighborly irregular f-graphs.

Theorem 3.16: If a BFGξ is both totally regular&regular, then $\alpha = (\mu_\alpha^+, \mu_\alpha^-)$ is a constant function.
Proof: Let ξbe a RBFG and also totally RBFG, then
$deg^+(m) = n_1$, $deg^-(m) = n_2 \forall\ m \in v$, $deg^+[m] = K_1$, $deg^-[m] = K_2 \forall\ m \in V$. Now
$deg^+[m] = K_1$
$\Rightarrow deg^+(m) + \mu_\alpha^+(m) = K_1$
$\Rightarrow n_1 + \mu_\alpha^+(m) = K_1$
$\mu_\alpha^+(m) = K_1 - n_1 \forall\ m \in V$
Similarly $\mu_\alpha^-(m) = K_2 - n_2 \forall\ m \in V$
Hence $\alpha = (\mu_\alpha^+, \mu_\alpha^-)$ is a constant function.

Theorem 3.17: A BFGξ of G*, whereas G*be the cycle with nodes 3 is highly IRBFG &neighborly irregular, iff every pair of nodes having distinct positive as well as negative membership values.

Proof: Assume that nodes of BFGξhaving distinct positive membership and negative membership values.
Let V_i, Vj, Vk ϵ V. Given that, $\mu_\alpha^+(V_i) \ne \mu_\alpha^+(V_j) \ne \mu_\alpha^+(V_k)$ and, $\mu_\alpha^-(V_i) \ne \mu_\alpha^-(V_j) \ne \mu_\alpha^-(V_k)$, which implies that
$\sum_{x\epsilon N(x)} \mu_\alpha^+(V_i) \ne \sum_{x\epsilon N(x)} \mu_\alpha^+(V_j) \ne \sum_{x\epsilon N(x)} \mu_\alpha^+(V_k)$ and $\sum_{x\epsilon N(x)} \mu_\alpha^-(V_i) \ne \sum_{x\epsilon N(x)} \mu_\alpha^-(V_j) \ne \sum_{x\epsilon N(x)} \mu_\alpha^-(V_k)$. That is deg ($v_i$) ≠ deg ($v_j$) ≠ deg ($v_k$) Therefore G = (V, σ, μ) is neighborly irregular & highly IRBFG.
On the contrary, suppose that G is highly irregular &neighborly irregular.
Let deg (V_i = (K_i, l_i), I = 1,2,…,n.
Assume that +ve& -ve membership value of any 2 nodes are equal.
Let $V_1, V_2 \epsilon V$. Let $\mu_A^P(V_1) = \mu_A^P(V_2)$ and $\mu_A^N(V_1) = \mu_A^N(V_2)$.
Then deg (V_1) = deg (V_2), seeing as G^* bea cycle that is a disagreement to fact that G=(V, σ, μ) is neighborly irregular & highly IRBFG. Therefore +ve& -ve value of nodes are all dissimilar.

Definition 3.18: A BFG ξ is said to be neighborly totally IRBFG, if ξ is neighborly IRBFG&(μ_α^+ ,μ_α^-) is a constant function.

Theorem 3.19: Consider a dominating set S of a BFG, ξ = (V,α, β).Sis said to be a minimal dominating set, iff∀ s ϵ S any one of the subsequent conditions holds.
(i). s is not a strong neighbor of any node in S.
(ii). There is a node v ϵ V – S∋N(v) ∩ S = s.

Proof: suppose that S be the "minimal dominating set" ofξ. At that time for each node s ϵ S, S - s is not a dominating set. Thus ∃v ϵ V - (S – {s}) that is not dominated by any node in S – {s}. If v= s, then v is not strong neighbor of any node in S.
If v ≠s, v is not dominated by S – {v}, however dominated by S, then node v is a strong neighbor only to s in S. That is N(v) ∩ S = s.
On other hand suppose that Swill be a dominating set & for every node s ϵ S, one of the given 2 conditions holds. Presume S is not a "minimal dominating set", then ∃ a node s ϵS, S – {s} is a dominating set.
Therefore s is a strong neighbor to at least one node in S – {s}, the first condition one does not hold.
If S – {s} is a dominating set then each node in v - S is strong neighbor to at least one node in S -{s}, the 2nd condition does not hold that contradicts our supposition that at least one of the conditions hold. Hence S is a "minimal dominating set".

APPLICATIONS

Suppose, in a city planning, city routes are to be so designed that the member of accidents should be minimized. Now, the number of accidents depends on many factors, like traffic system, road conditions, number of crossing between routes, etc. To solve this route planning problem, keeping in mind these factors, in a mathematical way, we convert the problem into a bipolar f-graph model. In this bipolar f- graph consider routes as edges and nodes are the transporting points. As the transporting points have no contribution to this problem, the membership values for all the nodes are taken as [-1, 1]. The +ve membership values of arcs on chances of accidents in the corresponding route. The -ve membership values of arcs are assigned some grade between -1 and 0 depending on traffic system available for that route. The gradation corresponding to traffic system is conceptually taken as negative since a better traffic system can decrease the chances of accidents.

CONCLUSION

Fuzzy graph theory is tremendously applied in Software Engineering applications. In this article explicit sorts of BFGs have been discussed. We discussed IRBFG, neighborly irregular, totally & highly IRBFGs. We have initiated the ideas of dominations in regular bipolar f- graphs and domination in IRBFGs. The expansion of this explore work is related with neural networks, roughness in graphs, geographical data system, soft graphs and soft hyper graphs**.**

REFERENCES

1. L.A. Zadeh, Fuzzy sets, Information and Control, 8 (197=65) 338 -353.
2. A. Rosenfeld, Fuzzy graphs, ln: L.A. Zadeh, K.S. Fu and M. Shimura Eds, Fuzzy sets and their applications, Academic Press, New York,(1975)77-95.
3. Vijaya Prasad, S., Peter Praveen, J., Tiwari, A., Prasad, K.Bindu, P., Donthi, R., &Mahaboob, B. (2018).An Application of LPP – graphical method for solving multi server queuing model. International Journal of Mechanical Engineering and Technology, 9 (1066-1069), Retrieved from www.scopus.com
4. NageswaraRao, B., Ramakrishana, N., &Eswarlal, T. (2016). Application of translates of vague sets in carier decision making. International journal of chemical sciences, 14(1), 372-380. Retrieved from www.scopus.com
5. Zhang W-R (1994) Bipolar fuzzy sets and relations: a computational framework for cognitive modeling and multi agent decision analysis, Proceedings of IEEE conference, pp 305–309.
6. Nagoor Gani. A and Radha. K, (2008). On Regular fuzzy Graphs. Journal of Physical sciences, Vol 12, 2008,33-40.
7. Haynes, T.W., Hedetniemi S.T. and Slater P.J. (1998). Fundamentals of domination in graphs, Marcel Dekker Inc. New York, U.S.A.
8. Akram M (2011) Bipolar fuzzy graphs. InfSci 181:5548–5564
9. Srinivasa Rao, T., Suresh Kumar, G., Vasavi, C., & Murthy, M.S.N. (2016). Observability of fuzzy difference control systems. International Journal of Chemical Sciences, 14(4), 2516-2526. Retrieved from www.scopus.com
10. Sovan Samanta and Madhumangal Pal, Irregular Bipolar Fuzzy Grphs, International journal of Applications of Fuzzy sets, Fol.2 (2012), 91-102.
11. V.R. Kulli and L.S.C. Sigarkanti, Inverse domination in graphs, Nat. Acad. Sci. Ltt. 14(1991)473-475.
12. Basheer Ahmad Mohideen, Types of Degrees in Bipolar Fuzzy Graphs, Applied Mathematical Sciences, Vol.7, 2013, n0.98, 4857-4866.
13. A. Muneera, R.V.N. Srinivas Rao (2017), On Domination of fuzzy graphs and fuzzy Trees, International Journal of Pure and applied Mathematics Volume 113 No. 8, 2017, page 210-219.
14. A.N. Gani, S.R. Latha, On irregular fuzzy graphs, Applied Mathematical Sciences 6 (2012) 517–523.
15. A. Muneera, R.V.N. Srinivas Rao (2017), Analogous study of Inverse Dominations in Fuzzy graph and its applications, International Journal of Innovative Research in Sciene, Engineering and Technology, Volume 6, Issue 12, Dec 2017.
16. A. Muneera, T. Nageswara Rao, R.V.N. SrinivasRao, Fuzzy Eulerian and Fuzzy Hamiltonian Graphs with Their Applications, International Journal of Recent Technology and Engineering, Volume 8, Issue 4, November 2019, ISSN 2277-3878.

Study Of Various Dominations In Graph Theory And Its Applications

A. Gayathri, Abdul. Muneera, T. Nageswara Rao, T. Srinivas Rao

Abstract: The aim of the article is to sum up the different dominations on graphs. The following article holds the idea of Domination in Planar graphs, connected graph, edge dominations in Paths, Cycles of related graphs and few properties. Likewise, we broadened our study on inverse dominations on graphs and few applications based on dominations. It incorporates social network, land reviewing, radio broadcasts, computer PC correspondence system, school transport directing, interconnection systems so forth.,

Key words: Domination, Inverse domination, domination in planar graphs and connected graphs.

1. INTRODUCTION

The fundamental thought of graphs was first presented in eighteenth era by Swiss mathematician Leonhard Euler. His endeavors and inevitable answer for the popular Konigsberg bridge problem portrayed is ordinarily cited as root of theory of graph. He wrote an article on seven bridge konigsberg issue which was brought out in 18th century is considered to be the initial article in the former times of theory of graph. Since, 50 years theory of graph has incredible advancements due to its correspondence with and application in couple of locales like Natural Sciences, Technology, Information System Research and so on. The quickest developing region in theory of graph is domination. The analysis of dominating set in theory of graph was initiated by Ore and Berge. Kulli and Patwari analyzed about the total edge domination number of graphs. The issue of choosing two disjoint arrangements of transmitting stations with a goal that one set can give admiration on account of disappointment of portion of the transmitting stations of the other set. This drove them to characterize the Inverse domination number. The Inverse domination was initiated by V.R. Kulli and Sigarkanti.

2. PRELIMINARIES

Definition 2.1: A graph is an ordered pair G (V, E) is a finite arrangement of nodes and arcs, where V is a limited arrangement of nodes and E is a limited assortment of arcs. The arrangement E is having components from union of 1 and 2 component subsets of V. i.e., every arc is either a 1 or 2 component subset of V.

Definition 2.2: Let G= (V, E) be a graph. Two nodes A & B are said to be adjoining if there is an arc e ϵ E so that e = {A, B}. Two arcs e1 and e2 known to be adjoining if there is a node v so that v is a component of e1 and e2.

- *M. Sc Student, Department of Mathematics, Koneru Lakshmaiah Education Foundation, Vaddeshwaram, Guntur, Andhra Pradesh, India. akurathigayathri83@gmail.com*
- *Research Scholar, Department of Mathematics, Koneru Lakshmaiah Education Foundation, Vaddeshwaram, Guntur, Andhra Pradesh, India.Associate Professor, Department of Mathematics, Koneru Lakshmaiah Education Foundation, Vaddeshwaram, Guntur, Andhra Pradesh, India.Associate Professor, Department of Mathematics, Koneru Lakshmaiah Education Foundation, Vaddeshwaram, Guntur, Andhra Pradesh, India.*

Definition 2.3: A digraph is an arrangement of objects that are connected together, where all the arcs are directed from one node to another. In addition, a graph where the arcs are biconditional is known an undirected graph.

Definition 2.4: Number of arcs occurrence with node of a graph with self-loop tallied twice is called Level of node, it is signified by v(x) or degG(x).

Definition 2.5: A simple graph is where there is exactly one arc between each set of distinct nodes is known as complete graph and is usually signified by K_n.

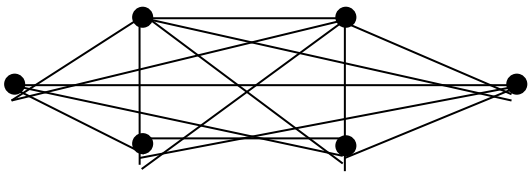

Definition 2.6: A graph G is known as connected if every set of nodes in G are associated.

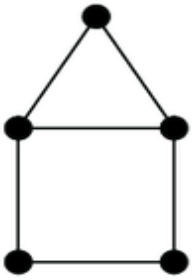

Definition 2.7: Graph that is not associated is said to be disconnected. An arc less graph with two or more nodes is known as disconnected.

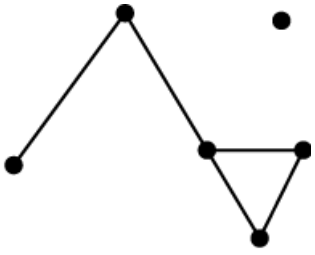

Definition 2.8: In the event that the node V of a Simple Graph G= (V, E) is partitioned into 2 subsets 'u' & 'v' to an

extent that every arc of G associate a node ‘u’ & node ’v’, then G is known as Bipartite Graph.

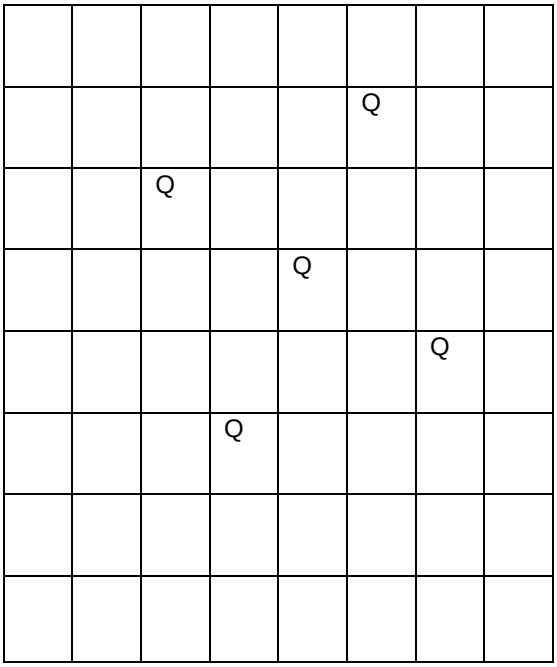

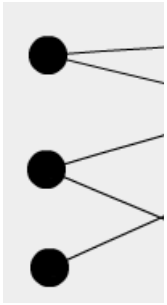

Definition 2.9: If a graph is traced on a plane in a way that no arcs cross each other is known as planar graph.

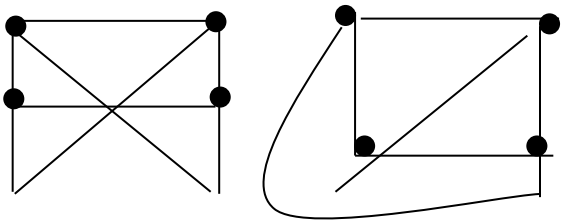

Non – Planar Graph

Remark-1: On the off chance that G = (V, E) be an Undirected Graph with e arcs. At such point the level of degrees of the vertices in an Undirected Graph is even. i.e., $\sum_{v \in V} deg_G$ (V) = 2e, this is called Hand-shaking property.

Remark-2: The utmost numeral of arcs of Simple Graph with ‘n’ nodes is $\frac{n(n-1)}{2}$.

3. DOMINATIONS IN GRAPHS

In 1850, Chess freaks in Europe give thought to issue for finding the least numeral of queens that is set on a chess board with a goal that each one of the blocks are either charged by a queen or inhibited by a queen. The idea of Domination came into existence with this problem. It was found that five queens are enough to tower over all the blocks of (8 ×8) chess board. Here we are showing two of such arrangements of five queens such that all squares are dominated is shown in the following Fig

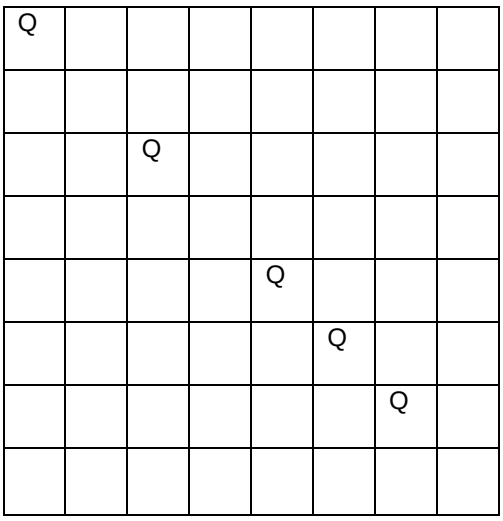

Two arrangements of queens in 8 × 8 checker board in order to occupy every block by Queens.

Definition 3.1: In a Graph G of dominating set S where each node of G is either in S or adjoining to any node in S. The domination number γ = γ (G) is the least cardinality of an arrangement of domination. The Dominating set problem concerns finding a base dominating set.

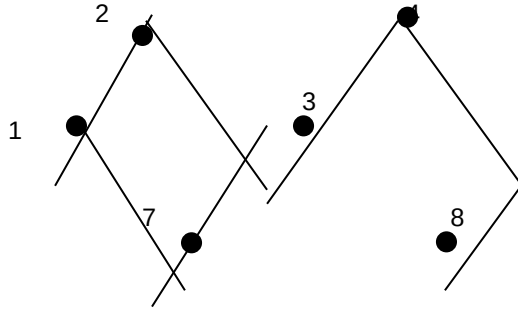

Planar graph

For the graph G in Fig. 3, {1,3,5} is dominating set of cardinalities 3, {3,6,7,8} is a m dominating set of cardinalities four and {2,4,6,7,8} is a dominating set of cardinalities five. Hence the least cardinality is γ (G) = 3.

Definition 3.2: An arrangement S of nodes in a graph G (V, E) is known as Total Dominating set, on the condition that each node v ∈ V is adjoining to a component of S and hence γ_t (G) is Total Domination number. For an application, we contemplate a PC arrangement where a group of servers has capacity to transmit legitimately with each PC outside the core group. Also, each document server is directly connected to in any event one other 'backup' file server where copy data is kept. A small group with this trait is a γt set constituted to the system.

Definition 3.3: In graph of an edge dominating set G= (V, E) is subset S⊆E with the end goal that each arc not in S is adjoining to any one arc in S. An edge dominating set is otherwise known as line dominating set.

Definition 3.4: A connected dominating set of a graph G is a dominating set D whose induced sub graph is also associated.

Definition 3.5: A dominating set S of a graph G is a minimal dominating set of G iff every node v in S fulfills in any of the accompanying two properties:
(i). ∃ node w in V(G) – S ∋ Γ (W) ∩ S = {v}.
(ii). v is adjoining to no node of S.

INVERSE DOMINATIONS IN GRAPHS

The idea of graphs in the area of dominations found its root in 1850's with the enthusiasm of few chess players. Out of the different uses in the theory of domination, the frequently examined is Data bank. Communication system comprises of connections at fixed arrangement of sites. The issue is to choose the small arrangements of destinations at which the senders are set, so that every other site in the system is united by an immediate correspondence connection to the plot, which contains a sender. In other word the issue is to locate a least dominating set in the graph relating to this system. Kulli and Sigarkanti considered the problem of determination two disjoint sets of transmitting stations of the other set. This drove them to characterize the inverse domination number.

Definition 3.6: An arrangement S of nodes in a Graph G is a dominating set if each node not in D is nearby any one node in S. In the event that V-S contains a dominating set say S' of G, at that point S ' is known as inverse dominating set concerning S.
Example: 3.6.1

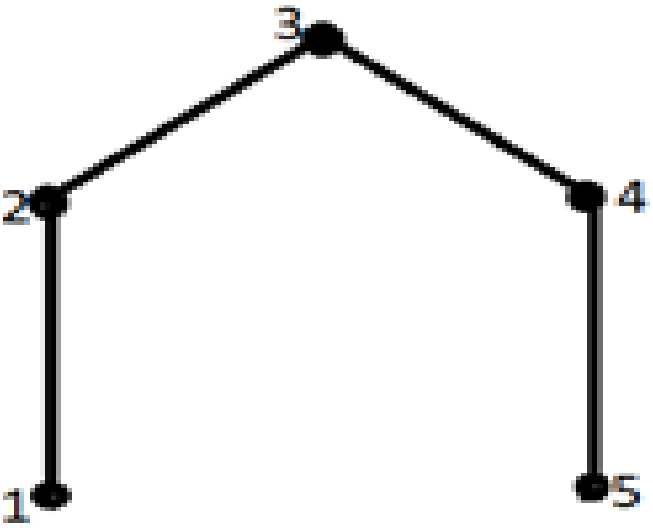

$D_1 = \{2, 4\}$, $D_2 = \{2, 5\}$ and $D_3 = \{1, 4\}$ are the least dominating sets. Their comparing opposite inverse dominating sets are $D_1^* = \{1, 3, 5\}$, $D_2^* = \{1, 4\}$ and $D_3^* = \{2, 5\}$ respectively. Thus, the domination number of G is γ(G) =2 & the inverse domination number of G is $\gamma^{-1}(G) = 2$.
Theorem 3.7: Let d be a positive divisor of a +ve number n. Then ∃ a regular graph G on n nodes, for γ (G) = γ^{-1} (G) = d.
Proof: Assume that d is a +ve number and divides n ≥ 1. i.e.; n = kd.
Let $V = \cup_{i=1}^{k} V_i$, where $V_i = \{v_{i1}, v_{i2}, \ldots\ldots, v_{id}\}$ for $1 \le i \le d$.
Let G be the graph with node set as V and every node of V_i is adjoining precisely to one node of V_j, for $j \neq i$. Then d(v) = k – 1 ∀ v ϵ V, so G is k – 1 regular.
Also, each V_i is a γ – set of G.

Hence γ (G) = $|V_i| = d$, $\gamma^{-1}(G) = |V_j| = d$.

4. APPLICATIONS

Over the most recent three decades, a stupendous development is seen in theory of graph because of its far-reaching scope in algebraic, optimization and computational issues. Graph theoretical ideas are usually utilized in OR. For instance, the travelling sales-man problem, shortest spanning tree in weighted graphs, and finding the most limited way between two vertices of graph. For example, train and plane ways to cover maximum stations with minimum cost included. One of the important applications among domination in graph is school transport routing, most school give school transports to moving kids to and from school and work under specific standards, one of which generally expresses that no student will need to walk more remote than one kilometer to a transport pickup point. Therefore, management ought to develop course to every transport vehicle is available in less than one kilometer of each student in their designated region. Vehicle ride cannot take more than predefined time, likewise, Limit on total number of children that a vehicle. Give us a chance to consider the graph represent the road guide of city, where each link address to a pickup point.

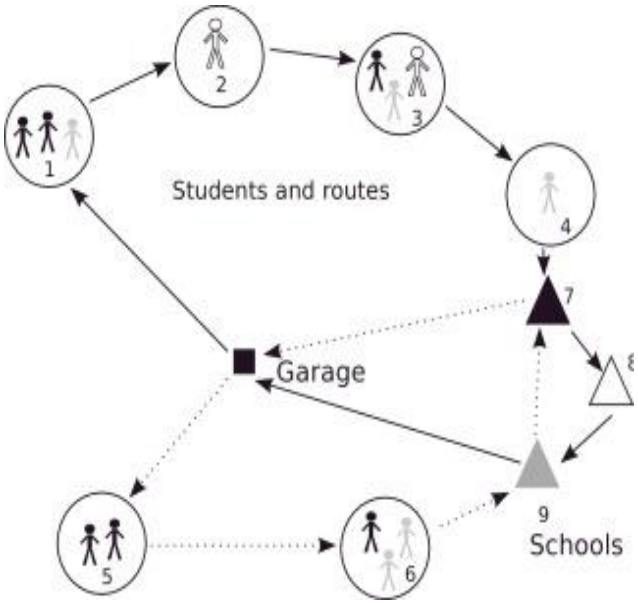

5. CONCLUSION

The standard purpose of the paper is to explain the significance of Graph theory and Dominations in various fields like Sciences and Engineering. We examined the idea of Dominations in planar graphs, connected graphs and arc domination in paths, cycles of related graphs. Also expressed some real-life applications where dominations in graph is used. We extended our study in Inverse Dominations.

REFERENCES

[1]. Ore, O. (1962). Theory of Graphs. American Mathematical Society Colloq. Public, providence
[2]. C. Berge, Graph and hypergraphs, North Holland, Amsterdam in graphs, Networks, Vol.10 (1980), 211 – 215.

[3]. V.R. Kulli, Theory of Domination in Graphs, Vishwa International Publications, Gulbarga. India (2010).
[4]. V.R. Kulli and D.K. Patwari, Total efficient domination number of a graph, Technical Report 1991:01 Department of Mathematics, Gulbarga University, Gulbarga, India (1991).
[5]. V.R. Kulli, Inverse and disjoint neighborhood total dominating sets in graphs, Far East J. of Applied Mathematics, 83(1), 55-65 (2013).
[6]. V.R. Kulli, S.C. Sigarkanti and N.D. Soner, Entire domination in graphs. In V.R. Kulli, ed., Advances in Graph Theory, Vishwa International Publications, Gulbarga, India, 237-243 (1991).
[7]. S.M. Hedetniemi, S.T. Hedenieni, R.C. LAskar, L. Markus and P. J. Slater, Disjoint dominating sets in graphs, Discrete Mathematics, Ram. Math. Soc. Lect. Notes Series 7, Ram. Math. Soc. Mysore 87 – 100 (2008).
[8]. V.R. Kulli, Inverse and disjoint secure total domination in graphs, Annals of Pure and Applied Mathematics, 12(1), 23 – 29, (2016).
[9]. A. sasirekha, A.H. Nandhu Kishore, Applications of Dominating Set of Graph in Computer Networks, International Journal of Engineering Sciences and Research Technology,3(1) January 2014, 170- 173.
[10]. Wu, Yiwei, Yingshu Li, “Connected Dominating Sets.”, In Handbook of Ad Hoc and Sensor Wireless Networks: Architectures, Algorithms and Protocols: pp. 19–39, 2009

Fuzzy Eulerian and Fuzzy Hamiltonian Graphs with Their Applications

Abdul. Muneera, T. Nageswara Rao, R.V.N.Srinivasa Rao

Abstract: ***In this article we discussed prominence of Fuzzy Eulerian and Fuzzy Hamiltonian graphs. Fuzzy logic is introduced to study the uncertainty of the event. In Fuzzy set theory we assign a membership value to each element of the set which ranges from 0 to 1. The earnest efforts of the researchers are perceivable in the relevant establishment of the subject integrating coherent practicality and reality. Fuzzy graphs found an escalating number of applications in day to day life system where the information intrinsic in the system varies with different levels of accuracy. In this article we initiated the model of fuzzy Euler graphs (FEG) and also fuzzy Hamiltonian graphs (FHG). We explored about fuzzy walk, fuzzy path, fuzzy bridge, fuzzy cut node, fuzzy tree, fuzzy blocks, fuzzy Eulerian circuit and fuzzy Hamiltonian cycle. Here we studied some applications of Fuzzy Eulerian graphs and fuzzy Hamiltonian graphs in real life.***

Key Words: Fuzzy walk, Fuzzy path, Fuzzy Bridge, Fuzzy block, Fuzzy Euler graph, Fuzzy Eulerian circuit, Fuzzy Hamiltonian cycle.

I. INTRODUCTION

The river Pregl was crossed 7 bridges which connected 2 islands on the river with each other and with opposite banks. Euler thought that to have a walk along all the seven bridges exactly once by starting from any of the four land areas and return to the same starting point. While proving this problem Euler replaced each land area by nodes A, B, C, D and all the bridges by an edge joining the corresponding nodes. Using this Euler proved that such a route over the bridges of Konigsberg is impossible. This method used by Euler in solving this problem gave rise to the notion of graph theory. To study the relationship between objects, Graph is a convenient way. In this graph theory objects are represented by nodes and the line joining the nodes shows the relation between them known as edges. The idea of fuzziness is one of enrichment, not of replacement. To describe vagueness in the objects (or) relations (or) in both fuzzy graphs plays a vital role. Consider the set S = {Apple, Banana, Guava, Orange} to study the eating habits of fruits. One cannot decide that to like (or) dislike the set S because both things are there. To deal these types of uncertainty fuzzy set theory came into existence in 1965, which was introduced by [1] Lotfi A. Zadeh. In fuzzy sets and fuzzy relations elements are assigned by the membership values in the range from 0 to 1. i.e., the above set S defined in fuzzy set as S = {Apple/ {0.4}, Banana/ {0.6, Guava / {0.3}, Orange/ {0.9}}.

Kaufmann [3] introduced the definition of fuzzy graph; Rosenfield [2] defined elaborated definition of fuzzy node and fuzzy edge. H.J. Zimmermann thoroughly studied the conceptual phenomena of fuzzy set theory in 2010. Rosenfeld [3] has explained various concepts of fuzzy graph. An Eulerian trail of a certain fuzzy graph (FG) is open trail of fuzzy graph containing all the edges of fuzzy graph exactly once, which began and ends on different nodes. This kind of graph is said to be passable. We call Eulerian trail as an Eulerian circuit if it begins and ends on the same node. A fuzzy graph containing an Euler line is named as fuzzy Euler graph. If an edge set of connected fuzzy graph can be partitioned into cycles, then such a fuzzy graph is called Eulerian fuzzy graph. This condition is necessary and sufficient also. Hamiltonian graphs were introduced by great Irish mathematician Sir William Rowan Hamilton in nineteenth century (i.e, 1805-1865). A closed path that visits every node only once is a fuzzy Hamiltonian circuit.

If each node in a fuzzy graph visited exactly once excluding beginning vertex where as edges may repeat then such a circuit it called Hamiltonian circuit. A fuzzy graph which is having Hamiltonian circuit is called fuzzy Hamiltonian graph. In the same way a circuit which traverses every edge exactly once in a fuzzy graph where as nodes may repeat such a circuit is called fuzzy Eulerian circuit.

II. PRELIMINARIES

The definitions and theorems in the preliminaries are in the Rosenfeld [2]

Definition 2.1: Let V be a finite non empty set and E be the collection of two element subset of V. A fuzzy graph $G(\sigma, \mu)$ is a pair of functions, where $\sigma : V \rightarrow [0, 1]$ and $\mu: E \rightarrow [0, 1]$, such that $\mu(xy) \leq (\sigma(x) \wedge \sigma(y))$ for all $x, y \in V$.

Example: Let a, b, c be the vertices. i.e., V = {a, b, c}. Consider the fuzzy set σ on V by membership values as σ (a) = 0.7, σ (b) = 0.2, σ (c) = 0.4 .Define a fuzzy set μ of E such that μ (ab) = 0.2, μ (bc) = 0.2, μ (ac) = 0.4. Thus the graph G (σ, μ) is a fuzzy graph (FG).

Definition 2.2: Let G (σ, μ) be a fuzzy graph. Sum of the membership values of the edges incident on the node v is called the degree of v, labeled as $d(v) = \sum_{u \neq v} \mu(u, v)$.

$\delta(G) = \wedge \{ d(v)/ v \in V\}$ is the minimum degree of fuzzy graph G and

$\Delta(G) = \vee \{d(v)/ v \in V\}$ is the maximum degree of fuzzy graph G.

Revised Manuscript Received on November 19, 2019

Abdul. Muneera , Scholar, Koneru Lakshmaiah Education Foundation , Vaddeswaram, Guntur, Andhra Pradesh, India and Lecturer, Department of Mathematics , Andhra Loyola Institute of Engineering and Technology, Vijayawada, Andhra Pradesh, India.

T. Nageswara Rao, Dept of Mathematics , Koneru Lakshmaiah Education Foundation , Vaddeswaram, Guntur, Andhra Pradesh, India.

R.V.N.Srinivas Rao, Department of Mathematics, Wollega University Ethopia.

Definition 2.3: A Path P in a fuzzy graph (FG) G (σ, μ) is a sequence of different nodes $x_0, x_1, \ldots, x_n$ such that $\mu(x_{i-1}, x_i) > 0, i = 1,2,\ldots n$. Here the length of the path is n. The alternate pairs are called the edges (or) arcs of the path. Weight of the weak edge is the Strength of the path .Suppose if we want to check the strength of chain which is having some links then its strength depends upon the weakest connection of that chain. The strength of connectedness $\mu^{\infty}(x, y)$ is denoted by $CONN_G(x, y)$. A fuzzy graph is connected if $CONN_G(x, y) > 0$ for every pair of nodes $x,y \in \sigma$ *.

Definition 2.4: A fuzzy walk W of the fuzzy graph (FG) in fig 1. a μ(a, b) b μ(b, c) c μ(c, d) d μ(d, e) e which started with the initial node a and the terminal node is e. The length of the fuzzy walk W is min $\mu(x_i, x_{i+1})$ for all nodes contained in the fuzzy walk. Length of the fuzzy walk in fuzzy graph (FG) in fig1 is 0.3.

Definition 2.5: If initial and terminal nodes of a fuzzy walk W with $\mu(x_i, x_{i+1}) \geq 0$ are distinct then that walk is called open fuzzy walk otherwise it is called a closed fuzzy walk.

Definition 2.6: Trail is a fuzzy walk in a fuzzy graph (FG) where the edge $\mu(x_i, x_{i+1}) \geq 0$ is not repeated. A fuzzy walk with distinct initial and terminal nodes is called open fuzzy walk otherwise it is closed fuzzy walk.

Example: (i). a μ(a, b) b μ(b, d) d μ(d, a) a μ(a, e) e is a trail in fuzzy graph (FG) in fig 1. (ii). b μ(b, c) c μ(c, d) d μ(d, a) a μ(a, e) e is a fuzzy path in the fuzzy graph (FG) in fig 1.

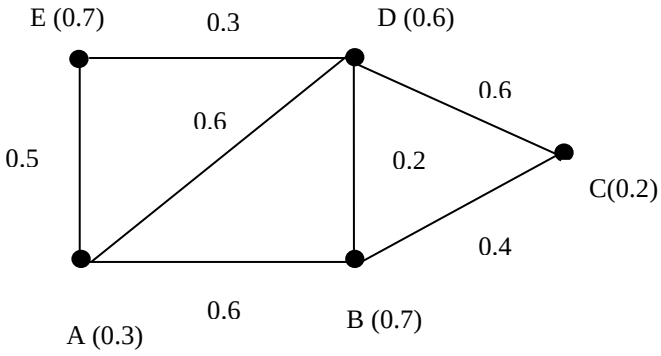

Fig.1. Fuzzy Graph (FG)

Definition 2.7: min $\mu(x_i, x_{i+1})$ for all nodes contained in the fuzzy walk is called the strength of the fuzzy path and the length of a fuzzy path n > 0 is the number of nodes contained in the fuzzy path and is a sum of the membership values.

Example: Strength of the above defined fuzzy path is 0.4 and the length is 2.3.

Definition 2.8: In a fuzzy graph G , if removal of a node reduces the strength of connectedness $\mu^{\infty}(x, y)$ between some other pair of nodes then such a node is called fuzzy cut vertex (or) fuzzy cut node of a fuzzy graph (FG) G(σ, μ).

Definition 2.9: In a fuzzy graph G , if removal of an edge (u, v) reduces the strength of connectedness $\mu^{\infty}(x, y)$ between some other pair of nodes then such an edge (or) arc (u, v) is called a fuzzy bridge of G(σ, μ).

Theorem 2.10: If (u, v) is a fuzzy bridge, then $\mu^{\infty}(u, v) = \mu(u, v)$.

Theorem 2.11: In a fuzzy graph G, every fuzzy bridge is strong.

Proof: Let xy be the fuzzy bridge of fuzzy graph (FG), G = (σ, μ).

Let us suppose that edge xy is not strong. Then $\mu(xy) < CONN_{G-xy}(x,y)$. The strongest path in fuzzy graph G from x to y is p. Then the strength of this path p is $CONN_{G-xy}(x,y)$. If we adjoin edge xy to p to obtain a cycle, then xy becomes the weakest edge of this cycle. By known property the edge xy is not a fuzzy bridge of G. Hence clearly it proves that a fuzzy bridge must be strong.

Theorem 2.12: An edge xy in a fuzzy graph G is strong if and only if $\mu(xy) = CONN_G(x, y)$.

Definition 2.13: A fuzzy graph is said to be a block if it is connected and has no fuzzy cut nodes. Note that in a graph, a block cannot have bridges. But in fuzzy graphs, a block may have fuzzy bridges.

Note: **A** complete fuzzy graph with n vertices is denoted by K_n

Example:

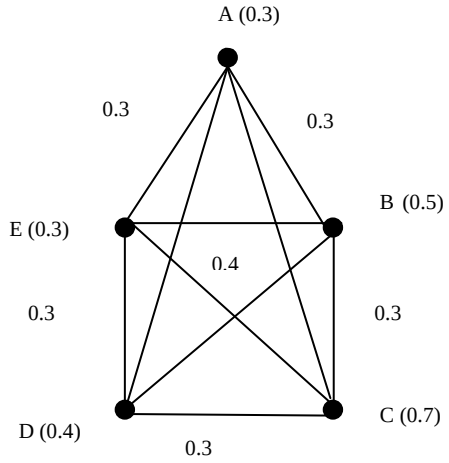

Figure 2 is the example of complete fuzzy graph with 5 vertices (K_5) which has two Hamiltonian fuzzy cycles 123451, 135241.All the membership values are greater than zero**.**

Definition 2.14: If all the arcs of a fuzzy cycle are strong then such a cycle is called strong fuzzy cycle.

Definition 2.15: The strength of a cycle C in an f-graph is defined as the weight of a weakest arc in C. In graphs, any two nodes of a block belong to a cycle and conversely.

Theorem 2.16: Let G be a connected fuzzy graph. If there is at most one strongest path between any two nodes of G, then G is a fuzzy tree.

Theorem 2.17:

G= (σ, μ) is a fuzzy tree if and only if the following are equivalent.

(1). (u, v) is a fuzzy bridge.

(2). $\mu^{\infty}(u,v) = \mu(u,v)$

Result 2.18: A connected fuzzy graph (FG), G (σ, μ) with n nodes has at most n-1 fuzzy bridges.

III. FUZZY EULERIAN AND FUZZY HAMILTONIAN GRAPHS

In the Fig . 3 has an Euler circuit but Fig. 4 is not having Euler circuit. In Euler graph each node should have an even number of neighborhood nodes.

But both the above figures are having Hamiltonian paths but not Hamiltonian circuits. In Fig. 3 Hamiltonian paths is A –F-E-D-B-C and in Fig 4. Hamiltonian path is A – E-D-C-B-F.

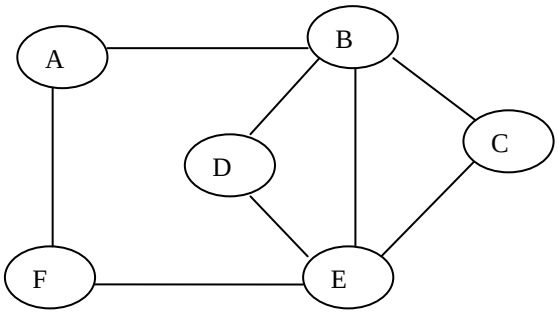

Fig. 3

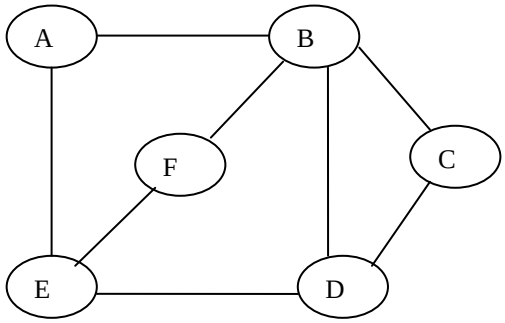

Fig. 4

Definition 3.1: A connected fuzzy graph G (σ, μ) is said to be a fuzzy Eulerian graph if there exists a circuit which includes every edge of G(σ, μ) exactly once which starts and ends with different nodes.

Note: The dual of dual fuzzy graph (FG) is the fuzzy graph itself, Eulerian fuzzy graph can be obtained by considering the dual of a bipartite fuzzy graph (FG).

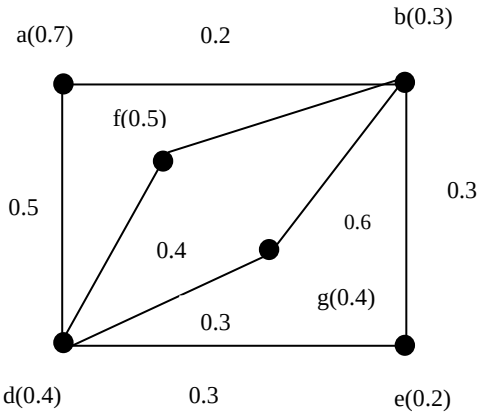

Fig. 5. Eulerian but Not Hamiltonian fuzzy graph

Definition 3.2: A connected fuzzy graph G (σ, μ) is said to be a fuzzy Hamiltonian graph if there exists a fuzzy cycle which covers all the nodes of fuzzy graph G (σ, μ) exactly once except the terminal nodes.

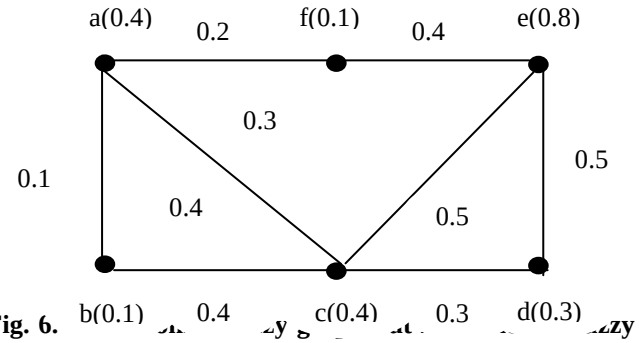

Fig. 6. graph.

Definition 3.3: A cycle C in an fuzzy graph (FG), G(σ, μ) is called a strongest strong cycle (SSC) if C is the union of two strongest strong u − v paths for every pair of nodes u and v in C except when (u, v) is an fuzzy bridge of G in C.

Definition 3.4: A disconnection of a fuzzy graph G: (σ, μ) is a node set D whose removal results in a disconnected or a single vertex graph. The weight of D is defined to be $\Sigma\, v \in D \{\min \mu (v, u) \mid \mu (v, u) \neq 0\}$.

Definition 3.5: In a fuzzy graph (FG), G: (σ, μ) the node connectivity is defined to be the minimum weight of a disconnection in G and is denoted by Ω (G).

Definition 3.6: The node set of a fuzzy graph (FG), be partitioned into two sets $\{V_1, V_2\}$. The set of edges joining nodes of V_1 and nodes of V_2 is called a cut- set of fuzzy graph G, denoted by (V1, V2) relative to the partition $\{V_1, V_2\}$. The weight of the cut-set (V_1, V_2) is defined as $\Sigma\, \mu (u, v)$ where $u \in V_1$ and $v \in V_2$.

Definition 3.7: Let G be a fuzzy graph. The edge connectivity of G denoted by λ (G) is defined to be the minimum weight of cut-sets of G.

Theorem 3.8: Let G (σ, μ) be a connected fuzzy graph (FG), The relations between node connectivity Ω (G), edge connectivity λ (G) and minimum degree is given as $\delta (G) \geq \lambda (G) \geq \Omega (G)$.

Theorem 3.9: An Eulerian fuzzy graph (FG) is a graph obtained from the dual of a fuzzy bipartite graph.

Proof: Consider G (σ, μ), a maximal fuzzy bipartite graph (FBG),

Suppose the degree of the membership for the vertices is σ(v), degree of the membership for the edges is μ(e) and the degree of membership of faces is λ(f) respectively.

It is a maximal fuzzy bipartite planar graph so each cycle's length is even, such that every face f in FG has even lengths. So the dual of these faces f_i for all I =1,2,….k obtained a vertices v_i* of even degree. We know that "A given connected graph G is an Eulerian Graph if and only if all vertices of G are of even degree".

Hence the dual graph is Eulerian fuzzy graph with the degree of membership

σ(v*) = λ(f), μ(e*)= μ(e) and λ(f*)= σ(v).

Theorem 3.10: If every node of a fuzzy graph (FG) has exactly two adjacent nodes, then there exists a fuzzy Hamiltonian cycle.

Proof: Let us Consider a fuzzy graph (FG), G(σ, μ) with n nodes $x_1, x_2, \ldots . x_n$.

Suppose that each node of fuzzy graph (FG) has exactly two adjacent nodes.

Suppose any edge between any two nodes is removed. Say μ (x_1, x_2).

Now if we begin to find a path starting with the vertex x_1 (or) x_2 and end with x_2 (or) x_1 by covering all the nodes of fuzzy graph (FG). In this case it is not possible to reach to the staring node, so can't get a Hamiltonian cycle.

Suppose any node x_i is removed, either it takes the path x_{i-1}, x_{i-2}, …. and end with x_1 or end with x_2, excluding some nodes of fuzzy graph (FG), in this case also we won't get Hamiltonian cycle.

Hence it is necessary in fuzzy Hamiltonian cycle that each vertex of (FG) has exactly two adjacent nodes.

IV. APPLICATIONS

Fuzzy set theory is the modern mathematical apparatus that enables considering the initial information uncertainty. Eulerian graphs are used to resolve various practical problems. Many applications ask for a path or circuit that traverses each street in a neighborhood, each connection in a utility grid, or each link in a communications network exactly once. It is also used for ranking hyperlinks or by GPS to find shortest path home. The existence of the Hamilton's cycle will also allow the design of a programmed test so that once the data is entered and finally the test conditions are created. By using Hamiltonian circuit we can solve the practical problems such as road intersections, pipeline crossings etc.

V. CONCLUSION

The manuscript studied about the importance of fuzzy Eulerian and fuzzy Hamiltonian graphs. Also we established the model of fuzzy Eulerian and fuzzy Hamiltonian graphs. More over it deliberated the some applications of these graphs in real life problems. Fuzzy graph theory is becoming gradually more considerable as it is useful in computers, mathematics, science and technology. We can see the implementation of fuzzy logic in WI FI technology, IOT, GPS map , GSM mobile phone networks, data mining, electronic chip design, web designing, coding etc.

REFERENCES

1. Fuzzy sets by Lotfi.A. Zadeh, *Information and Control*, 8 (1965) 338 – 353.
2. Fuzzy graphs in Fuzzy sets and their applications by A. Rosenfeld, L.A.Zadeh, K.S.Fu and M.Shimura Eds, *Academic Press, New York* (1975) 77-95.
3. Introduction `a la th´eorie des sous-ensembles flous, by A.Kaufmann, vol . 1,El´ementsth´eoriques de base. Paris: Masson et Cie; (1976).
4. Number of Hamiltonian Fuzzy Cycles in Cubic fuzzy graphs with vertices 'n', by M. Vijaya and A. Kannan, *International Journal of Pure and Applied Mathematics*, Volume 117, No.6, 2017 , 91 – 98 , ISSN: 1311 – 8080.
5. Fuzzy walk on a Fuzzy Graph, by S. Vimala and P. Jayalakshmi, *Middle-East Journal of Scientific Research* 25(3): 489-492, 2017 ISSN : 1990-9233.
6. Nayagam, V.L.G., Jeevaraj, S., & Dhanasekaran, P. (2017). An intuitionistic fuzzy multi-criteria decision-making method based on non-hesitance score for interval-valued intuitionistic fuzzy sets. Soft computing, 21(23) ,7077 – 7082 doi:10.1070/s00500-016-2249-0.
7. Rao, T.S., kumar, G.S., Vasavi, C., & Rao, B.V.A. (2017). On the controllability of fuzzy difference control systems. International Journal of Civil Engineering and Technology, 8(27), 723-732. Retrived from www.scopus.com.
8. Nageswara Rao, B., Ramakrishna, N., & Eswarlal, T. (2016). Application of translates of vague sets on electrol democracy model. International journal of Chemical Sciences, 14(2), 762-768. Retrived from www.sscopus.com
9. Bhargavi, Y., & Eswarlal, T. (2016).Application of vague set in medical diagnosis. International Journal of Chemical Sciences, 14(2), 842-846. Retrieved from www.scopus.com
10. Srinivasa Rao, T., Suresh Kumar. G., Vasavi, C., & Murty, M.S.N.(2016). Observability of fuzzy difference control systems. International Journal of Chemical Sciences, 14(4), 2516-2526.Retrived from www.scopus.com
11. On Domination of fuzzy graphs and fuzzy trees by A. Muneera, R.V.N. Srinivasa Rao, International Journal of Pure and Applied Mathematics, Volume 113 ,No. 8, 2017, pafe 210 – 219, ISSN: 1314- 3395.
12. Lakshmana Gomathi Nayagam, V., Jeevaraj, S., & Dhanasekaran, P. (2016). A linear orering on the class of trapezoidal intuitionstic fuzzy numbers. Exper systems with Applications, 60, 269-279.doi:10.1016/j.eswa.2016.05.003
13. Vasavi, C.H., Suresh Kumar, G., & Murty, M.S.N.(2016). Fuzzy dynamic equations on time scales under second type hukuhara delta derivative. International Journal of Chemical Sciences, 14(1), 49-66. Retrieved from www.scopus.com
14. Sobhanbabu, Y., RAo, B. V.A., Rao, T.S., & Prasa, K.A.S.N.V.(2017). Addaptive control and realizability on nable settings. International Journal of Mechanical Engineering and Technology, 8(12), 712-721. Retrived from www.scopus.com
15. Vasavi, C.H., Kumar, G.S., Rao, T.S., & Rao, B.V.A.(2017). Application of fuzzy differential equations for cooling problems. International Journal of Mechanical Engineering and Technology, 8(12), 712-721.Retrieved from www.scopus.com
16. Srinivasa Rao, T., Suresh Kumar, G., Vasavi, C., & Murty, M.S.N.(2016). Observability of fuzzy difference control systems. International Journal of Chemical Sciences, 14(4) 2516-2526. Retrived from www.scopus.com
17. Bhargavi, Y., & Eswarlal, T. (2016). Application on vague set in medical diagnosis. International journal of Chemical Sciences, 14(2), 842-846. Retrieved from www.scopus.com
18. Nageswara Rao, B.,Ramakrisana, N., & Eswarlal, T. (20216). Application of translates of vague sets in career decision making. International journal of Chemical Sciences, 14(1), 372-380. Retrieved from www.scopus.com

AUTHORS PROFILE

A.Muneera, Completed M.Sc. Mathematics from Acharya Nagarjuna University in the year 2004. Presently working as Assistant Professor, Department of Mathematics, Andhra Loyola Institute of Engineering and Technology, Vijayawada. She was Pursuing Ph.D from, K L E F Vaddeswaram, under the guidance of Dr.T.Nageswara Rao . She Published 6 research articles in reputed international journals. Also Participated and presented research articles at National and International conferences.

Dr T Nageswara Rao, working as Associate professor in Dept of Mathematics, K L E F. He completed his M. Tech, Computer science. in 2008 from ANU and completed his Ph. D in 2013 from ANU. He published 20 research papers in different reputed journals. Under his guidance one scholar was awarded by Ph. D in 2019. He has total 20-years teaching experience. His research area includes Lattice theory, Fuzzy and difference theory.

R.V.N. Srinivasa Rao, awarded M.Sc and Ph.D. in Mathematics from Acharya Nagarjuna University, Andhra Pradesh, India. He has 22 years of teaching and research experience. Presently working as a professor at Wollega University Ethopia. He published 16 research articles at Internationally reputed peer reviewed journals. Currently he is supervising Ph.D. students in the area of graph theory and fuzzy graph theory. His research interests include graph theory, fuzzy graph theory, lattice theory, mathematical modeling and related areas.

Reconfigurable Antenna using Micromechanical Actuation Switches for K and Ku-Band Applications

Sathuluri Mallikharjuna Rao, G. Sasikala

Abstract- In this paper, we have proposed a reconfigurable antenna using micro mechanical actuation switches for K and Ku-band applications. Overall two identical cantilever micro mechanical switches (S_1 & S_2) are used to design reconfigurable patch antenna. The switches are working by electrostatic actuation mechanism. With the switches, overall the antenna is offering four resonant frequencies based on the switches ON/OFF condition. The Micro mechanical switches are offering an isolation loss of -18.5dB and an insertion loss of -1dB. The switch requires a DC actuation voltages of 6V. The Proposed reconfigurable antenna is resonating at four different frequencies based on the different switching conditions of RF MEMS switches. If S_1 & S_2 both are ON the antenna is resonating at 16.9GHZ, if S_1 -ON & S_2-OFF the antenna is resonating at 47.3GHZ & 59.1GHZ, if S_1 -OFF & S_2-ON the antenna is resonating at 28.4GHZ, if S_1 -OFF & S_2-OFF the antenna is resonating at 27.9GHZ

Index Terms- Patch antenna, re-configurability, RF MEMS switch, PIN diode, FET, Polarization, bandwidth, gain, directivity.

I INTRODUCTION

The latest communication applications require high speed data transmission with low power consumption, this is the significant research problem. Massive MIMO like systems require array of antennas but it eventually suffers with signal interference problems. To overcome these type of problems, we can use reconfigurable microstrip patch antennas other than the array of antennas. The re-configurability in patch antennas can be achieved with structure like E-shape, but the efficiency is not up to the level, so this approach is not preferable[1-4].

The alternative method to get re-configurability in microstrip patch antenna is by placing switches like PiN diodes or FET transistors and RF MEMS switches. In this RF MEMS switches offering best performance compared with PiN diode and FET transistors in terms of power consumption and offers better linearity[5-9].

Achieving the high isolation, low insertion and low pull-in voltage are the significant research challenges in micromechanical switches.

In this paper, we have designed and verified the performance of reconfigurable antenna using capacitive RF MEMS switches. The antenna is preferable in k-band and ka-band applications.

Revised Manuscript Received on December 15, 2019.

Sathuluri Mallikharjuna Rao, Research Scholar, Department of ECE, Vel Tech University, & Assistant Professor, Dept. of ECE, Andhra Loyola Institute of Engineering and Technology, Andhra Pradesh, India. Email.: smr.aliet@gmail.com.

Dr.G Sasikala, Professor, Department of ECE, Vel Tech University, 400 feet outer ring road, Avadi, Chennai-600062, Tamilnadu, India. Email.: gsasikala@veltech.edu.in.

The eventual reconfigurable microstrip antenna design is done in three steps, as an initial task we have designed an RF MEMS switch suitable in K-band and Ku-band frequency range, in the second level a microstrip patch antenna is designed and which is suitable to place RF MEMS switches, and in the final step the RF MEMS switches are placed in the proposed microstrip antenna structure as shown in figure 9.

II MICROMECHANICAL SWITCH

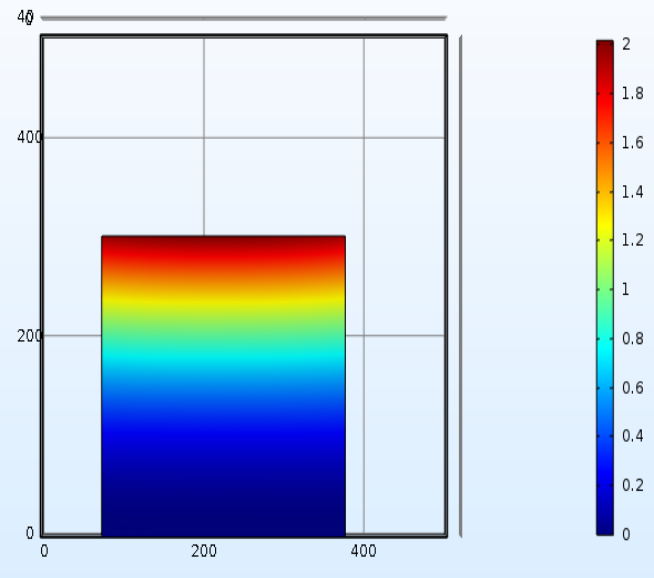

Figure 1: Micromechanical Cantilever shunt capacitve switch electromechanical analysis

The reconfigurable micro strip patch antenna design involves placing of two identical RF MEMS switches. An electrostatic shunt capacitive RF MEMS switches are used. CPW transmission line is used for switch design with dimension 100 µm x100 µm x100 µm.

The working principle of micro mechanical switch is, when the structure is in upstate(OFF), the input radio frequency signal is allowed to the output port with low insertion losses, and if the structure is in downstate(ON) the switch offers a capacitance in the range of pF and the input radio frequency signal is completely isolates and the output is zero. The electrostatic actuation model cantilever based shunt capacitive RF MEMS switch is shown in figure 1.

Table 1: RF MEMS switch materials and dimensions

Parameter	Material	Dimension in µm (Length x width x thickness)
Substrate	Silicon	500 x 500 x 1600
CPW	Gold	100 x 100 x 100
Cantilever	Gold	300 x 300 x 1
Dielectric	Silicon Nitrite (ε_r=7)	320 x 120 x 0.5

Silicon is used as a substrate for RF MEMS switch, CPW lines, cantilever is designed using gold material and silicon nitride (Si3N4) is used as a dielectric material. The shunt capacitive switch is actuated with electrostatic actuation.

The switch is designed and simulated using FEM tools. The cantilever with dimensions 300µm x 300 µm x 1 µm requires an actuation voltage of 6V to displace 2µm as shown in figure 1, is the simulation result.

The pull-in voltage of the cantilever based shunt capacitive RF MEMS switch can be calculate using following mathematical equation[10-12],

$$Pull-in\ \ Voltage = \sqrt{\frac{8kg_0^3}{27A\varepsilon_0}} \quad (1)$$

where, k is the cantilever spring constant, g0 is the switch air gap, A is the electrodes cross sectional area, and εo =8.85 x 10-12 is the free space relative permittivity.

The spring constant (k=(Ewt3)/l3) of gold cantilever structure with 300umx300umx1um dimension, E=70GPa, is theoretically value is 0.77 N/m, the required pull-in voltage for air gap of 2um with actuation electrodes cross sectional area 300umx300um is 4.5V.

The error in the pull-in voltage result is very low that is % of error=((Simulation-Theoretical)/Theoretical)X100 , the error in the pull-in voltage in terms of simulation (6V) and theoretical (4.5V) is approximately 0.33%. It is indicating that simulated one is very close to theoretical result.

The switch Radio frequency behavior is analyzed using HFSS tool. The switch overall performance is simulated in the frequency range 1GHZ to 60GHZ. The insertion losses of the switch is -1dB and the isolation losses of the switch is -18.5dB as shown in figure 3 and 4 respectively.

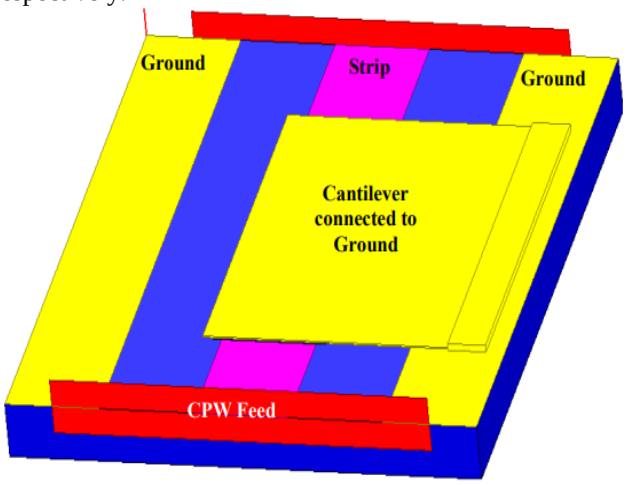

Figure 2: Micromechanical cantilever shunt capacitve switch Radio Frequency analysis.

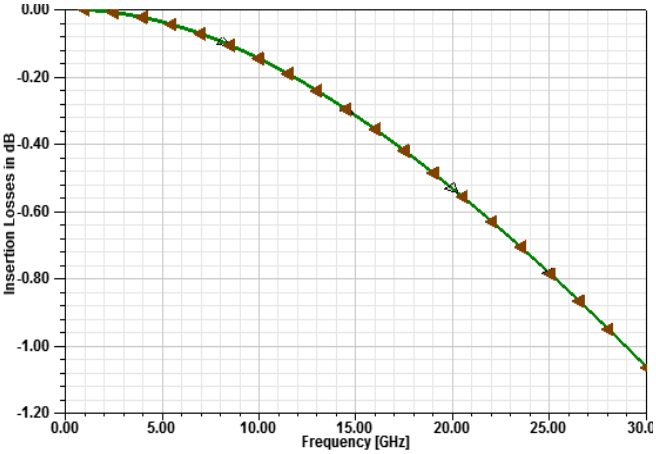

Figure 3: Insertion Losses in dB

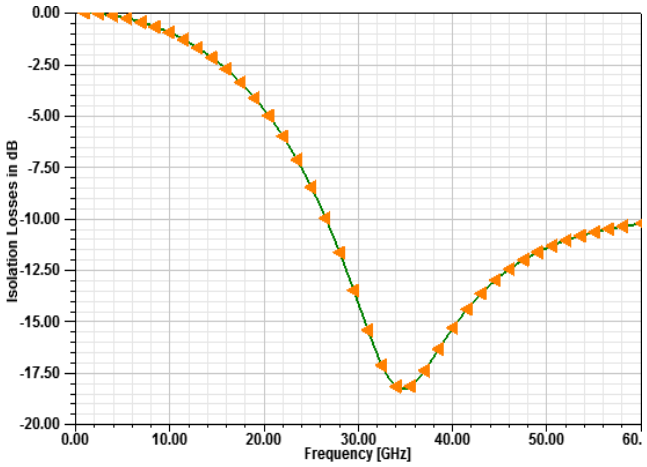

Figure 4: Isolation Losses Losses in dB

III MICROSTRIP PATCH ANTENNA

In this paper we have proposed a rectangular slotted microstrip patch antenna suitable to incorporate the RF MEMS switches as shown in figure 5. CPW feeding is used to feed microstrip antenna with input impedance of 50Ω.

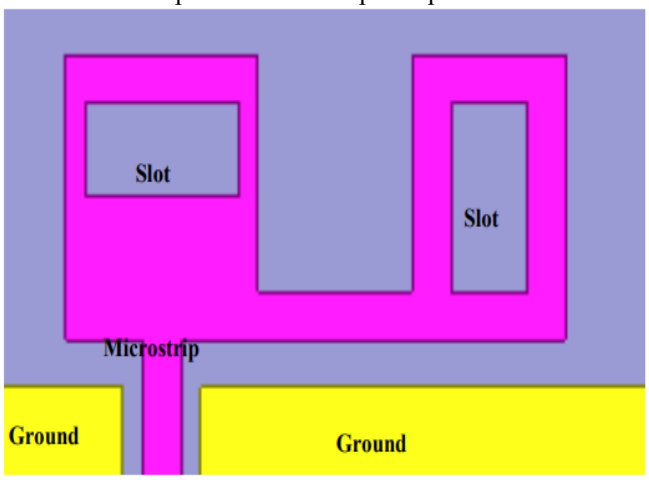

Figure 5: Proposed micro strip patch antenna suitable to incarporate RF MEMS swithes

The operating frequency of reconfigurable antenna is to be aimed in the range k-band and Ku-band, so the basic antenna is also designed in appropriately same band.

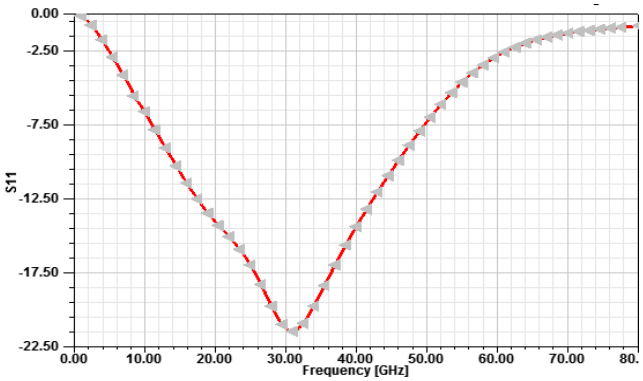

Figure 6: Micromechanical switche in microstrip patch antenna

The antenna without RF MEMS switches is resonating at 30GHZ as shown in figure 6. Here, we have extended out analysis on the performance of antenna with different substrate materials like FR4, Rogers RO3006, Glass and silicon. In this analysis we noticed that as silicon as the substrate antenna is offering best performance.

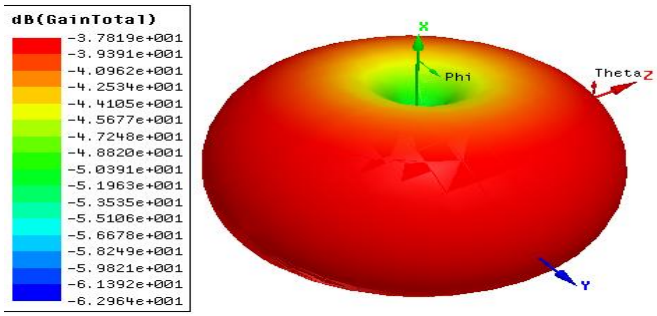

Figure 7: Polar plot of antenna with out RF MEMS switches.

IV PROPOSED RECONFIGURABLE ANTENNA

The eventual reconfigurable microstrip antenna using RF MEMS switches design is discussed in this section. Overall two RF MEMS switches are placed in the proposed microstrip antenna structure which is convenient to place RF MEMS switches. Silicon with 1.6mm thickness is used as a substrate material, microstrip, ground and RF MEMS switches design is done using gold material.

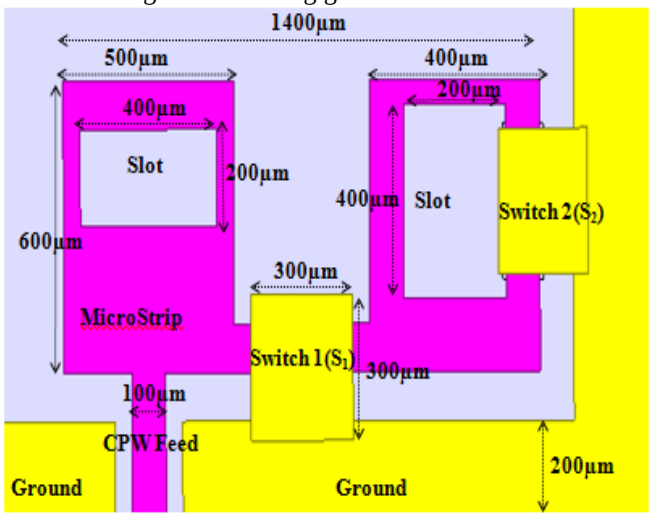

Figure 8: Proposed reconfigurable antenna model-top view

Under different switching condition of RF MEMS switches the antenna resonating in different frequencies. Overall proposed reconfigurable antenna is resonating at four different frequencies.

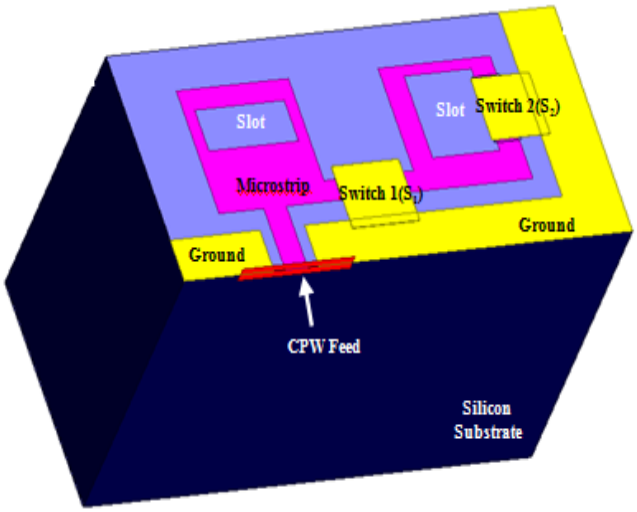

Figure 9: Proposed reconfigurable antenna model- side view

If S1 & S2 both are ON the antenna is resonating at 16.9GHZ, if S1 -ON & S2-OFF the antenna is resonating at 47.3GHZ & 59.1GHZ, if S1 -OFF & S2-ON the antenna is resonating at 28.4GHZ, if S1 -OFF & S2-OFF the antenna is resonating at 27.9GHZ.

The antenna performance is analyzed over the frequency range 1GHZ to 80GHZ using HFSS FEM tool. After observing the frequency response of the reconfigurable antenna we would like to refere the antenna in a wide range of applications in K-band and ka-band range. Other than polarization proposed antenna is switching the operating frequency from one frequency to other frequency.

Table 2: Antenna Resonant Frequencies for different switch conditions

Condition	Resonant Frequency
S_1=*ON*, S_2=*ON*	16.9GHZ
S_1=*ON*, S_2=*OFF*	47.3GHZ & 59.1GHZ
S_1=*OFF*, S_2=*ON*	28.4GHZ
S_1=*OFF*, S_2=*OFF*	27.9GHZ

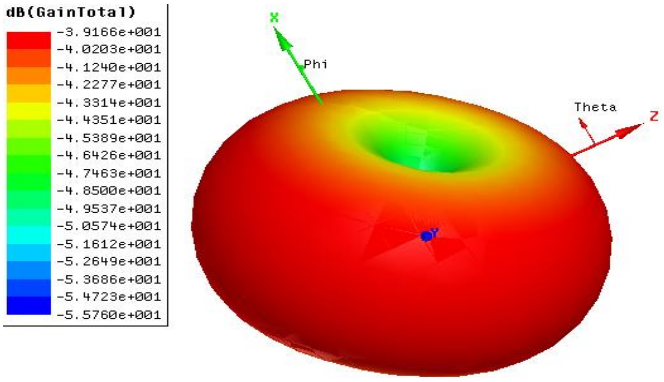

Figure 10: Polar plot of reconfigurable antenna at S_1-ON & S_2-ON

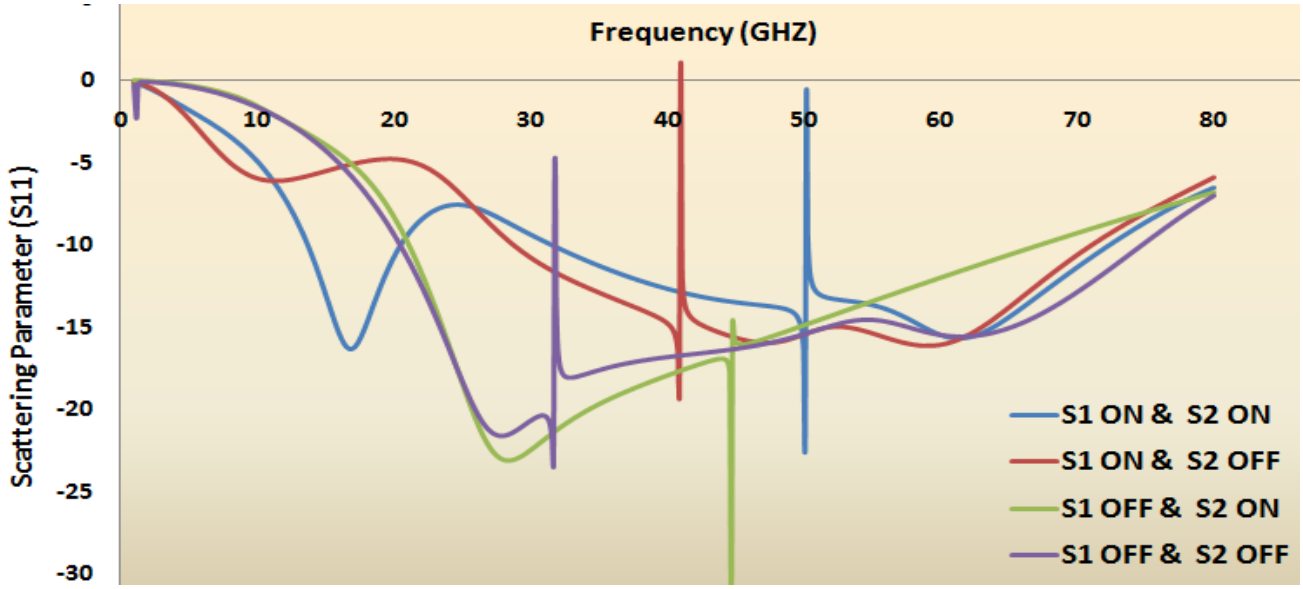

Figure 10: Scattering parameters for different switch states

Table 3:Comparison of the related work with the proposed reconfigurable antenna

Survey Paper	Antenna Shape	Number of switches	Switches	Switches State and Resonant Frequency	Antenna Application
Harish Rajagopalan et al. [13]	E-shape	2	RMSW100HP - SPST, High Power (10 W), DC-12 GHz	S1 & S2 : ON-2-2.6 GHz, S1 & S2 : OFF-2.6-3.2 GHz.	Cognitive Radio
Tony J. Jung et al. [14]	Circle	1	DC contact RF MEMS	S1 :OFF- Circular polarization(17.4 -21.9 GHz), S1 :ON- Linear polarization(16.9-22.5 GHz).	Satellite
Caner Guclu et al.[15]	Split rings	6	Series DC contact RF MEMS switch.	24.4 GHz and 35.5 GHz independently.	K-Band & Ka-Band.
Chih-Chieh Cheng et al. [16]	Programmable Lens-Array Antenna	5	Capacitive RF MEMS switches.	35 GHz	Ka-Band
Proposed	Slotted Rectangular	2	Shunt capacitive cantilever RF MEMS switches	S_1=ON, S_2=ON: 16.9GHZ S_1=ON, S_2=OFF:47.3GHZ & 59.1GHZ S_1=OFF, S_2=ON: 28.4GHZ S_1=OFF, S_2=OFF:27.9GHX	K-Band & Ku-Band

V CONCLUSION

The reconfigurable microstrip antenna design is done in three steps, as an initial task we have designed an RF MEMS switch suitable in K-band and Ku-band frequency range, in the second level a microstrip patch antenna is designed and which is suitable to place RF MEMS switches, and in the final step the RF MEMS switches are placed in the proposed microstrip antenna structure. The RF MEMS capacitive shunt switch is designed with cantilever structure with electrostatic actuation. The switch requires 6v actuation voltage and it offers 1dB insertion and 18.5dB isolation. The microstrip patch antenna suitable to place RF MEMS switches is resonate at 30GHZ frequency before placing RF MEMS switches. Overall two RF MEMS switches are place in the slotted rectangular patch antenna. Under different switching condition of RF MEMS switches the antenna resonating in different frequencies. Overall proposed reconfigurable antenna is resonating at four different frequencies.

ACKNOWLEDGMENT

We would like to thank Department of ECE, K L University, AP, India, for official use of FEM software for designing and simulation.

REFERENCES

1. Nickolas Kingsley, George E. Ponchak, and John Papapolymerou, " RF MEMS Sequentially Reconfigurable Sierpinski Antenna on a Flexible Organic Substrate With Novel DC-Biasing Technique", *IEEE Transactions on Antennas and Propagation*, Vol. 56, No. 1, pp.108-118, January 2008.
2. Y. Tawk, J. Costantine, K. Avery, and C. G. Christodoulou, "Implementation of a cognitive radio front-end using rotatable controlled reconfigurable antennas," *IEEE Trans. Antennas Propag*, vol. 59, no. 5, pp. 1773–1778, May 2011.
3. J. R. Kelly, P. Song, P. S. Hall, and A. L. Borja, "Reconfigurable 460 MHz to 12 GHz antenna with integrated narrowband slot," *Progress in Electromagn. Res. C*, vol. 24, pp. 137–145, 2011.
4. G. T. Wu, R. L. Li, S. Y. Eom, S. S. Myoung, K. Lim, J. Laskar, S. I. Jeon, and M. M. Tentzeris, "Switchable quad-band antennas for cognitive radio base station applications," *IEEE Trans. Antennas Propag.*, vol. 58, no. 5, pp. 14668–1476, May 2010.
5. E. Ebrahimi, J. R. Kelly, and P. S. Hall, "Integrated wide-narrowband antenna for multi-standard radio," *IEEE Trans. Antennas Propag.*, vol. 59, no. 7, pp. 2628–2635, Jul. 2011.
6. J.Guterman, A.Moreira, C. Peixeiro, andY. Rahmat-Samii, "Wrappedmicrostrip antennas for laptop computers," *IEEE Antennas Propag. Mag.*, vol. 51, no. 4, pp. 12–39, Aug. 2009.
7. J. Robinson and Y. Rahmat-Samii, "Particle swarm optimization in electromagnetics," *IEEE Trans. Antennas Propag.*, vol. 52, no. 2, pp.397–407, Feb. 2004.
8. F. Yang, X.-X. Zhang, X. Ye, and Y. Rahmat-Samii, "Wide-band E-shaped patch antennas for wireless communications," *IEEE Trans.Antennas Propag.*, vol. 49, no. 7, pp. 1094–1100, Jul. 2001.
9. N. Jin and Y. Rahmat-Samii, "Parallel particle swarm optimization and finite-difference time-domain (PSO/FDTD) algorithm for multiband and wide-band patch antenna designs," *IEEE Trans. Antennas Propag.*, vol. 53, no. 11, pp. 3459–3468, Nov. 2005.
10. H. Rajagopalan, J. M. Kovitz, and Y. Rahmat-Samii, "Frequency reconfigurable wideband E-shaped patch antenna: Design, optimization, and measurements," in *Proc. IEEE Antennas Propag. Soc. Int. Symp. (APSURSI)*, Jul. 8–14, 2012, pp. 1–2.
11. Y. Rahmat-Samii, J. M. Kovitz, and H. Rajagopalan, "Nature-inspired optimization techniques in communication antenna designs," *Proc. IEEE*, vol. 100, no. 7, pp. 2132–2144, Jul. 2012.
12. G. M. Rebeiz, *RF MEMS: Theory, Design and Technology*. New York, NY, USA: Wiley, 2003.
13. Harish Rajagopalan, Joshua M. Kovitz, and Yahya Rahmat-Samii, " MEMS Reconfigurable Optimized E-Shaped Patch Antenna Design for Cognitive Radio", *IEEE transactions on antennas and propagation*, Vol. 62, NO. 3, pp.1056-1064, March 2014.
14. Tony J. Jung, Ik-Jae Hyeon, Chang-Wook Baek, and Sungjoon Lim, " Circular/Linear Polarization Reconfigurable Antenna on Simplified RF-MEMS Packaging Platform in K-Band", *IEEE transactions on antennas and propagation*, Vol. 60, No. 11, pp.5039-5045, November 2012.
15. Caner Guclu, Julien Perruisseau-Carrier, and Ozlem Aydin Civi," Proof of Concept of a Dual-Band Circularly-Polarized RF MEMS Beam-Switching Reflectarray", *IEEE transactions on antennas and propagation*, Vol. 60, No. 11, pp.5451-5455, November 2012.
16. Chih-Chieh Cheng, Balaji Lakshminarayanan, and Abbas Abbaspour-Tamijani, " A Programmable Lens-Array Antenna With Monolithically Integrated MEMS Switches", *IEEE transactions on microwave theory and techniques*, Vol. 57, No. 8, pp.1874-1884, August 2009.

Predictive Modelling Of Air Pollutionusing Machine Learning Models And Neural Networks

Md. Baig Mohammad, Eswar Prasad Reddy Venna, Chris Peter Pallepogu, Madhu Babu Redapongala

Abstract: Air is the major resource for sustenance of life. Estimating and protecting air quality has become one of the most essential activity in many industrial and urban areas today. The geographical and traffic factors, burning of fossil fuels, and industrial parameters play significant roles in air pollution. The air quality index and associated concentrations of air pollutants (Ozone, Particle Matter $PM_{2.5}$, PM_{10}, Sulphur dioxide SO_2) are predicted using Machine Learning approaches and artificial neural network using MATLAB. The neural network model can appropriately predict the air pollutants and hence Air Quality Index (AQI) with mean square error of 0.744 is obtained in comparison withother regression models like SVR, GPR, Linear, Tree Bagger.

Keywords: Machine Learning (ML), Prediction, Air Quality Index (AQI). Neural Network Predictive Modelling.

1. INTRODUCTION

Pollution is the key issue in the developing countries, rapid growth in population lead to environmental problems such as air pollution, water pollution, noise pollution and many more. Air pollution has direct impact on human health. There has been increased public awareness on the effects of Air Pollution. Precise air quality forecasting can reduce the effect of maximal pollution on the humans and environment. Hence, developing air quality forecasting is essential. Out of the many air pollutants available the major focus is on Particulate Matter ($PM_{2.5}$ & PM_{10}), Carbon Monoxide (CO), Nitrogen Dioxide (NO_2), Sulphur Dioxide (SO_2), Ozone(O_3) and Lead (Pb).

A. Particulate Matter ($PM_{2.5}$ and PM_{10}):

$PM_{2.5}$refers to the atmospheric particulate matter that has the diameter of less than 2.5 microns, which is of about 3% of diameter of human hair. The particles in $PM_{2.5}$ is very small compared to PM_{10} so that they can be detected only by using electronic microscope. PM_{10} are the particles which has the diameter of 10 microns and they are called fine particles.PM_{10} is also known as respirable particulate matter. Particulate matter is a mixture of soot, smoke, metal, nitrates, dust, water and rubber etc. It is mostly generated from smoke from auto mobiles, industries, burning of agricultural waste etc. $PM_{2.5}$ and PM_{10} are directly inhaled into lungs causes several short-term and long-term effects such as infection of lungs, permanent damage of respiratory track, heart diseases and coronary diseases among children, breathing difficulties for infants etc. The natural concentration of $PM_{2.5}$ and PM_{10} in air are 60 $\mu g/m^3$ and 100 $\mu g/m^3$ [1] and that may not be harmful to humans.

B. Carbon monoxide (CO):

Carbon monoxide isair pollutant which is produced during the incomplete combustion of carbon containing fuels such as gasoline, natural gas, oil, coal, wood etc. High levels of CO are harmful to humans and, it cannot detect by human beings because it has no colour and odour, so it cannot detect. The natural concentration of CO in air is about of 0.2 ppm and that may not harmful to humans. Natural sources of carbon monoxide include volcanoes and bushfires. Excessive presence of CO than permissible level can cause headaches, heart diseases and impaired reaction timing.

C. Nitrogen Dioxide (NO_2):

NO_2 is a group of gaseous air pollutants produced as a result of road traffic and the other fossil fuel combustion process. The over exposure to the NO_2causes the Respiratory ailments, inflames the lining of the lungs. The maximum permissible level of NO_2 is 80$\mu g/m^3$ [1]and it is not affected to humans.

D. Sulphur Dioxide (SO_2):

SO_2 is a colourless, bad smelling, toxic gas, is a part of a larger group of chemicals referred to as sulphur oxides(SOx). Especially the SO_2 is emitted by the burning of fossil fuels like coal, oil etc which contains sulphur. SO_2 is also a natural by-product of a volcano activity. Similar to nitrogen dioxide, the SO_2 can create a secondary pollutant once it is released in air. The natural concentration of SO_2 is 80$\mu g/m^3$ [1] which is not harmful to humans. Secondary pollutants produced by SO_2 includes sulphate aerosols, particulate matter, and acid rain.

E. Ozone (O_3):

Ozone is present in the atmosphere although there are concentration peaks at two levels, stratosphere (15 -50) km and troposphere (0-15) km. Stratospheric O_3 is important because it regulates the transmission of UV light to earth surface. Mixing with stratospheric air provides a natural global average background of around 10-20 parts per billion (ppb), though there is some debate about the concentration. Additional quantities of tropospheric O_3 are produced by photochemical reactions from nitrogen oxides (NO_X) and volatile organic compounds (VOCs), which includes various hydrocarbons.

F. Ammonia (NH_3):

Ammonia is a compound of nitrogen and hydrogen with the formula NH3 and its molar mass is 17.031g/mol. Ammonia is a colourless gas with a characteristic pungent smell. Ammonia either directly or indirectlyacts as a building block for the synthesis of many pharmaceutical products and is used in many commercial cleaning products. It is soluble in

chloroform, either, ethanol, methanol. Molecular shape is trigonal pyramid. The immediate effects of ammonia are inhalation, ingestion, skin or eye contact. In inhalation it causes immediate burning of nose, throat and respiratory tract, the skin or eye contact causes the skin burn permanent eye damage or blindness. And ingestion results to corrosive damage to mouth throat and stomach.

G. Lead (Pb):

Lead is an elemental heavy metal found naturally in the environments as well as in manufacturing products. It can be released directly into the air, as suspended particles. The major sources of lead air emissions are motor vehicles and industrial sources. The permissible concentration of Pb is 1.0 which is not harmful to humankind. With the help of phasing out of leaded gasoline the motor vehicle emissions have been reduced, still lead is used in general aviation gasoline for piston engine aircraft.

H. Benzene (C_6H_6):

Benzene is a colourless liquid with a distinctive smell. It can be evaporated easily and highly flammable when it is exposed to flame or heat. It is soluble in water, and it can mix with most organic solvents. Benzene is part of the group of compounds knows as volatile organic compounds. This paper has been organised in V sections. Section I discusses about introduction and motivation. Section II describes the related work. Section III describes the methodology. Section IV describes the results and discussion. Section V describes about conclusion and future scope.

2. RELATED WORK

Various techniques have been proposed to apply data science, data mining to the topic like prediction for Air Pollution control in recent literatures [10]. Chavi srivastha et.al [2] applied linear regression, stochastic gradient descent, random forest, decision tree, support vector, multi-layer perceptron, gradient boosting, adaptive boosting for the prediction of pollutants like PM_{10}, $PM_{2.5}$, O_3, NO_2, CO, SO_2 in the city of New Delhi and observed the R squared quality meter for $PM_{2.5}$ as 0.692 by applying multi-layer perceptron. similarly, PM_{10} as 0.494 by applying random forest regression. Ke hu et.al [3] appliedsupport vector regression, decision tree, random forest, extreme gradient boosting, multilayer perceptron, linear regression, adaptive boosting Models in the city of Metropolitan Sydney for the prediction of concentration of co and obtained Mean Absolute Error value (MAE) values are 0.0493 by applying linear regression. Aditya CR et.al [4] applied Logistic Regression and Auto regression in the city of Beijing in China. For the prediction of future values of $PM_{2.5}$ based on previous $PM_{2.5}$ readings and obtained for Mean Accuracy of 0.998859 for Logistic Regression and Mean Square Error of 27.00 for Auto Regression. Sachit Mahajan et.al [5] employedNeural Network Auto Regression and Auto Regressive Integrated moving average and they also applied Holt-winter model for predicting $PM_{2.5}$ in the city of Tiachung in China and resulted Mean Absolute error for Neural Network Auto Regression is 1.47 and RMSE of 1.58. Jan Kleine Deters et.al [6] employed Neural Network, Linear Support Vector Machine, Binary Tree, CGM for predictingPM2.5 in the city of Belisario, Cotocollao and the obtained results for Neural Network for MSE in Belisario is 26% and in Cotocolla is 40% and for MAPE in Belisario is 22.1 and in Cotocolla is 40.7. V.Duc Le et.al [7] applied Convolutional Neural Network and the combination of Long short- Term Memory for time series data and a Neural Network model for other air pollution impact factors for predicting $PM_{2.5}$ in the city of Daegu city of Korea and the resulted prediction accuracy of 74%. Ping Wang et.al [8] proposed Hybrid Artificial Neural Network and Hybrid Support Vector Machine to enhance the prediction accuracy of traditional ANN and SVM by revising the error terms. For evaluation they used data set of PM10 and concentration of SO2 from different monitoring stations located in Taiyuan of China. The statistical index of MAE comparison for traditional and hybrid ANN is given by 0.049, 0.036. Sachin Bhogite et.al [9] applied the integrated model using Artificial Neural Networks and Gaussian Process Regression to Predict the level of SO_2 pollutant in Mumbai obtained Mean Square Error (MSE) 166.358. Zhongang Qi et.al [11] proposed general and effective approach in Deep Air Learning (DAL). It is an embedding feature selection and semi supervised learning in different layers of Deep Learning networks.

3. METHODOLOGY

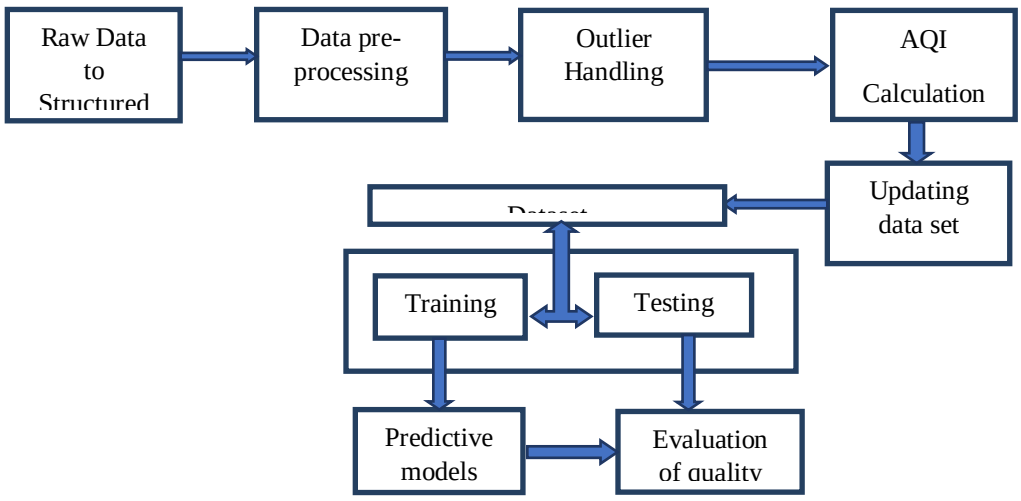

Fig 3.*1: Block Diagram for Predictive Modelling*

In figure 3.1 describes the flow diagram. For prediction of AQI, the first step is to collect the raw data. Authors have obtained raw data from the Pollution Control Board-Vijayawada. In that, sensordata has missing entries, outliers and the anomalies due to human errors, machine errors and experimental errors. Data pre-processing is carried out to handle those missing entries followed by outlier removal. The processed data is ready for statistical analysis. The processed data has been evaluated for AQI in Indian Standards. After calculating AQI, data set hasto be updated with a provision for AQI along with other sensory data. The obtained dataset is divided into training set and testing set. Machine learning models mainly regression and neural networks have been trained on the training set to predict the future samples of the AQI. Several quality metrics like MSE, RMSE, MAE, R^2 error have been evaluated for performance comparison.

4. RESULTS & DISCUSSION

a. DATA SET

The required data of past 5 years has been provided by the Andhra Pradesh Pollution Control Board (APPCB)-Vijayawada, in an unstructuredform. The data set is comprising of 1550 records of pollutant concentration recorded at Municipal Guest House (MGH)-Vijayawada. The dataset has 22 parameters consisting of pollutant concentrations viz. $PM_{2.5}$,PM_{10},NO_2,SO_2,NH_3(Ammonia),NO_X,NO,CO,O_3,Benzene, Toluene, Ethyl Benzene, Meta &Para Xylene, Ortho-Xylene and weather data like Relative Humidity, Temperature, Wind Speed, Wind Direction, Rainfall, Solar radiation, Barometric Pressure, Vertical wind speed.For the estimation of AQI the authors have consideredmajorly nine pollutantconcentrationsofPM_{10},$PM_{2.5}$,SO_2,NO_2,NH_3, CO, O_3, Benzene. Figure 4.1 represents the scatterplot for the concentration of air pollutants.

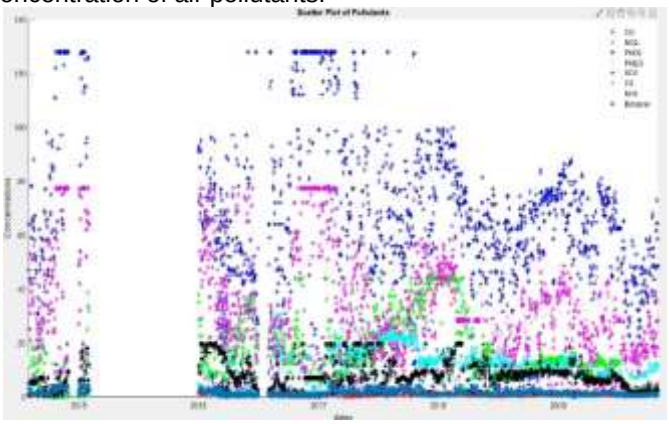

Fig-4.1*: Scatter plot of pollutants*

b. DATA PRE-PROCESSING

The dataset has been found with a large number of missing entries due to sensor faults or human errors. The missing entries are filled up using median value of the data. Outliers are the data points which differs significantly with the other observationsbecause of either experimental errors or the sensory faults. This error has a serious effect in the statistical evaluation. Outlierswhich fall outside 3 standard deviations from the mean value are processed. A statistical evaluation is performed using quartiles for detection of outliers and are replaced with clip method. Quartiles method considers above 75% data and below 25% data as an outlier. Clip method fills the detected outliers with nearest values above and below the threshold. Figure 4.2 represents the plots of various pollutants filled with median of the data for missing entries. Figure 4.3 represents the plots for various pollutants after outlier removal with the nearest threshold value.

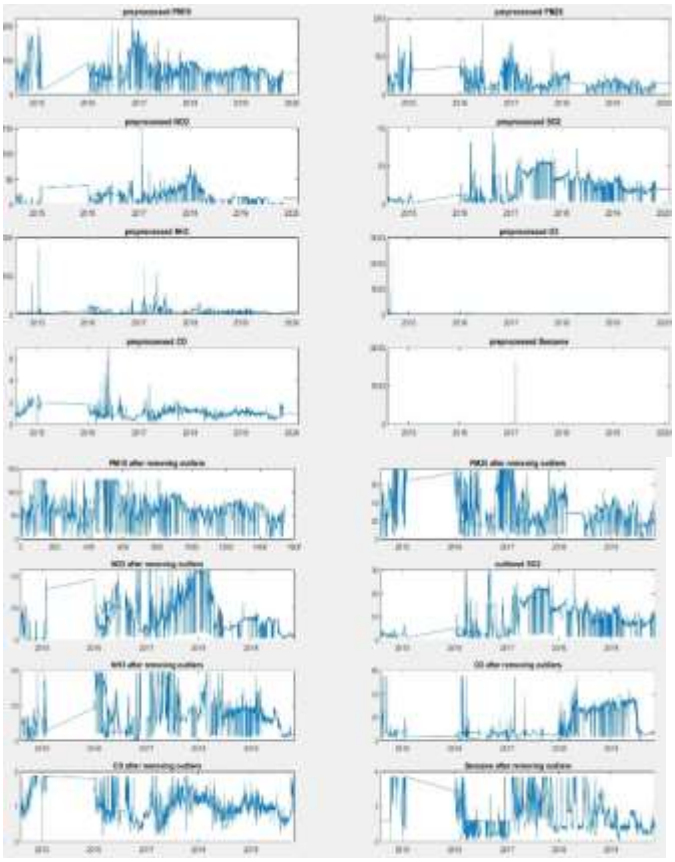

Fig-4.*3: Plots of air pollutants after removal of outliers*

On observing the plots in Figure 4.2 and 4.3 the data have spread accordingly on filling the missing entries and removal of the outlier. On observing the benzene data in the processed data (Fig:4.2) the authors have observed the sudden change in the data point which varied significantly compared to the other data points. Such error points are removed or clipped off in the outlier handling process.

c.

d. AIR QUALITY INDEX (AQI):

The AQI is an index for reporting air quality regularly. It tells how polluted or clean our air is, and what corresponding health effects might be a concern. The AQI focuses on health effect after breathing polluted air. This includes the major 8 pollutants like ground-level ozone, particle pollution (particulate matter), carbon monoxide, sulphur dioxide, nitrogen dioxide. For each of these pollutants, Central Pollution Control Board (CPCB) has established national air quality standards to protect public health. The CPCB had indicated the rate of effect of pollution on human health based on the AQI range. The breakpoint is the point at which the pollution category varies. The Standards breakpoints for each pollutant is laid by the CPCB [1] as shown in table-1.

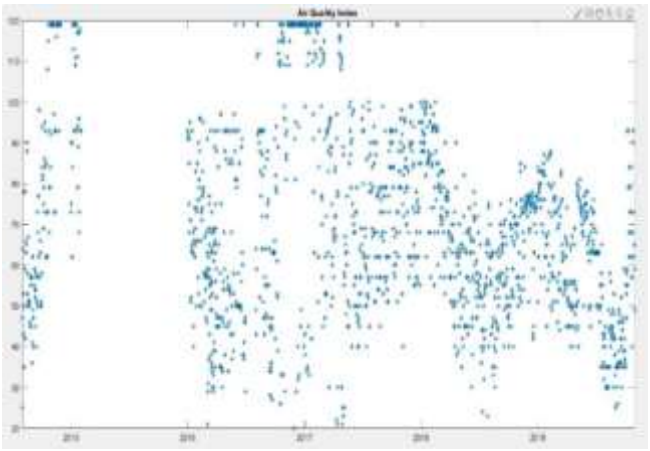

***Fig-4.2**: Plots for pre-processed data*
***Fig-4.4:** Calculated Air Quality Index (AQI) scatter plot*

AQI Category	AQI Range	Break point concentration							
		O_3 (ug/m^3)	NO_2 (ug/m^3)	PM_{10} (ug/m^3)	$PM_{2.5}$ (ug/m^3)	SO_2 (ug/m^3)	CO (mg/m^3)	NH_3 (ug/m^3)	Pb (ug/m^3)
Good	0-50	50	40	50	30	48	1	200	0.5
Satisfactory	51-100	100	80	100	60	80	2	400	1
Moderately Polluted	101-200	200	180	250	90	380	10	800	2
Poor	201-300	265	280	350	150	800	17	1200	3
Very Poor	301-400	748	400	430	250	1600	34	1800	3.5
Severe	401-500	748+	400+	430+	250+	1600+	34+	1800+	3.5+

***Table-1**: Break Point Standards.*

The equation for AQI proposed by Central Pollution Control board for individual pollutants is given by the equation-1[1].

$$AQI = \frac{(AQIhi - AQIlow)}{(Conchi - Conclow)} * (Conc - Conclow) + AQIlow$$

……. (1)

AQIhi = Max Aqi Range
AQIlow = Min Aqi Range
Conchi = Max Break Point concentration
Conclow = Min Break Point concentration
Conc = Current concentration.

After Calculating the individual pollutants AQI the Overall AQI is given by the maximum of the Current day's AQI.

i.e., AQI = Maximum (AQI_1, AQI_2, ……, AQI_n).

…… (2)

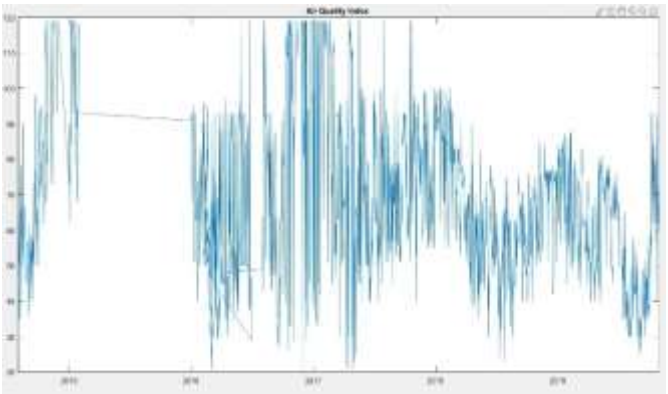

***Fig-4.**5: Calculated Air Quality Index (AQI)*

Figure 4.5 describes the AQI calculated for the pollutant data obtained after pre-processingand outlier removal.

e. PREDICTIVE MODELLING

Predictive modelling is a technique that uses mathematical and computational methods to forecast an event. The mathematical approach uses the equation-based phenomenon. The model parameters help how model inputs effect the output. Where the computational approach involves in the simulation to create a prediction. Regression is a statistical approach used to find the relation between the dependent and independent variables. There are different regression models in order to fit all the data into an equation.

There are total 5 types of regressions techniques are used.

i. Support vector regression
ii. Decision tree regression
iii. Regression Tree
iv. Gaussian Process Regression
v. Linear regression

i. Support vector regression:

It is a supervised machine learning model for regression analysis. It will provide the non-linear mapping function to map a given data set M: {(x1, y1), (x2, y2) …. (xi, yi) to a high dimensional feature space. In that space a command separating hyper plane can be defined which separate the data points with maximal functional margin[3]. The algorithm involved in SVR is presented below,

Step1:Collect a training set T={X,Y}
Step2: Choose a kernel and its parameters as well as any regularization needed.
Step3: Form the correlation matrix, K.
Step4: Train your machine, exactly or approximately to get contraction coefficients, $\alpha = \{\alpha_i\}$.
Step5: Use these coefficients to create your estimator, $f(X, \alpha, x^*) = x^*$

ii. Decision Tree Regression:
It is frequently used machine learning method for regression analysis and classification. It will create a model that can target values by learning decision rules from features. If we want our response variable as categorical then that will work as a classifier, if we want our response variable as numeric then it works as a regression model.[3] The flow involved in Tree bagger is presented below,
Step1: Tree Bagger generates in bag samples by oversampling classes with large misclassification costs and under sampling classes with small misclassification costs.
Step2:consequently out of bag samples have fewer observations from classes with large misclassification costs and more observations from classes with small misclassification costs.
Step3: Tree bagger selects a random subset of predictors to use at each decision split as in the random forest algorithm. By default, tree bagger bags classification trees.

iii. Regression Tree:
Its breakdowns the data into smaller subsets while at the same time an associated decision tree is incrementally developed and represents a decision on the numerical target.it is used the examine the relation between one dependent and one independent variable. It allows input variable to be a mixture of continuous and categorial values. Regression tree is designed to approximate real-valued functions.
Step1: Regression tree breaks the data set in smaller and smaller subsets. And at the same time the associated tree will Incrementally developed. This is basically dividing the points into some groups.
Step2: The tree contains decision nodes and leaf nodes. The decision nodes are those the nodes which represent the value of input variable and it has two or more branches. The leaf nodes contain the decision or output variable. The decision node that corresponds to the best predictor becomes the top most node called the root node.
Step3: The algorithm decides the optimal number of splits and splits the dataset accordingly.

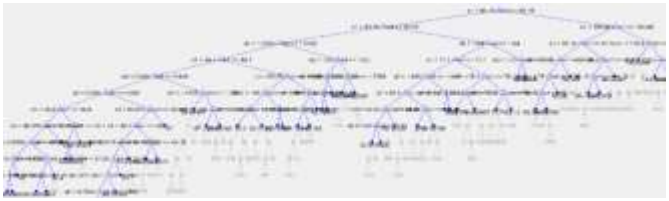

Fig: 4.*6: Plot of Regression Tree*

Figure 4.6 shows the regression tree model with the pruning level of 75 out of 126 levels.

iv. Gaussian Process Regression:
Gaussian process generates data located throughout some domain such that any finite subset of range follows a multivariate gaussian distribution. It is a interpolation method for which the interpolated values are modelled by a gaussian process governed by prior covariance. The prior covariance is specified by passing a kernel object. The procedure involved in GPR is shown below,
Step1: Assume a Gaussian process prior which can be specified using a mean function and covariance function.
Step2: Calculate the probability distribution over all admissible functions that fit the data.
Step3: Calculate the posterior using the training data, and compute the predictive posterior distribution on our points of interest.

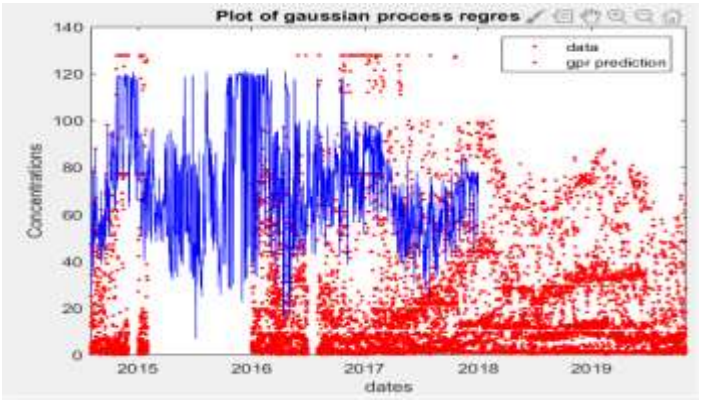

Fig-4.7*: Gaussian Process Regression*

v. Linear Regression:
Linear Regression is used to find the relationship between one or more multiple inputs x and one output y. [3]
Step1: Start with a training set
X is input training data
Y labels the data
When training the model – it fits the best line to predict the value of y for a given value of x. The model gets thebest regression fit line by finding the best θ_1 and θ_2 values.
Step2: Start with parameter with random variables.
Step3:The algorithm learns the line, plane or hyper-plane that best fits the training sample
Step4: Prediction: uses the learning line, plane or hyper-plane to predict the output value for any input sample.

Artificial Neural Network:

It is a machine learning algorithm in which it performs information processing. It consists of multiple layers like input layer, output layer, hidden layer. These layers are made up of multiple nodes which contain an activation function. Artificial neural network can learn the complex data pattern and can be applied in clustering, classification and predicting.[12] In the Neural Network the different algorithms are used for the data division. Authors used random data division algorithm, where the target is divided into three sets using the random indices. For training of the model, the authors have used the Levenberg-Marquardt as the training algorithm. The performance is observed as Mean Square Error (MSE). In ANN here we use the Levenberg- Marquardt training algorithm

Step1: Initialising the training epoch =1
Step2:Initialising network of weights and biases with uniform distribution values
Step3: Calculate actual output of actual units and hidden units
Step4: Calculate error.

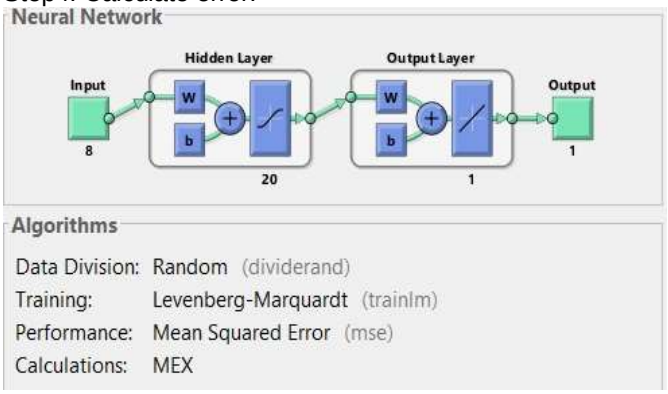

***Fig 4.8**: Neural network layers*

The performance plot and the train state plots for the neural network algorithm that used for training a model, Levenberg-Marquardt is as shown below in figure 4.9

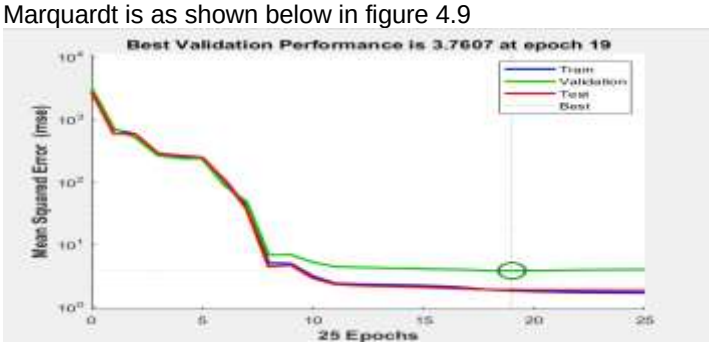

***Fig. 4.9**: Performance plot*

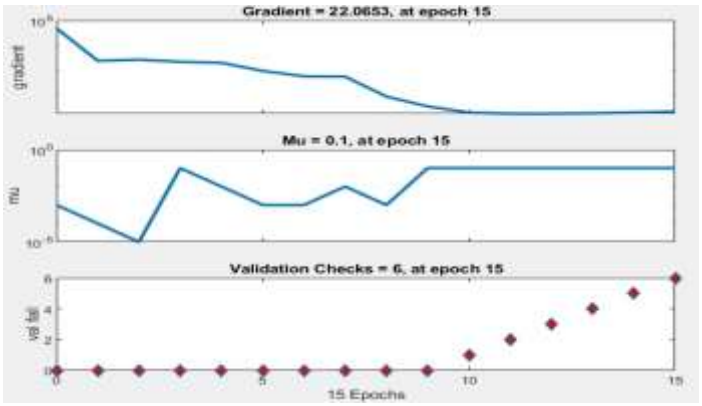

***Fig.4.10:** Training State Plot.*

In this Model we set the Target as AQI and all the other parameters like PM10, PM2.5, O3, etc. as the input vector. For employing the regression model to the data set, the data splitsinto two partitions. The first one is for training the model and other set for testing. Data before Jan-2019 for training and after Jan-2019 for testing the model. The Quality metrics or performance features like Mean Square Error, Mean Absolute Error, Root Mean Square Error, R squared Error, Median error, Median absolute error, Average error etc. were computed.The Quality Metrics for different models are tabulated in table-3. Evaluation of each model is done to estimate the performancefor forecasting.

MAE: Mean Absolute Error is the difference between the original and the forecasted values extracted by averaged the absolute difference over the data.[10][14]

$$MAE = \frac{1}{N}\sum_{k=1}^{N}(|Yi - Y'|)$$

MSE: Mean Square Error is the difference between the original and the forecasted values extracted by square of the difference over the data.[10][14]. MSE is the averaged square per prediction.[15]

$$MSE = \frac{1}{N}\sum_{k=1}^{N}(Yi - Y')^2$$

R-Squared: Coefficient of determination, represents the coefficient of how better the values fit compared to the original values.[10]

$$\boldsymbol{R^2 = 1 - \frac{\sum_{k=1}^{N}(Yi - Y')^2}{\sum_{k=1}^{N}(Yi - Y'')^2}}$$

RMSE: The square root of the difference between the original and forecasted values extracted by the square of the difference over the data.[10]

$$RMSE = \sqrt{MSE} = \sqrt{(\frac{1}{N}\sum_{k=1}^{N}(Yi - Y')^2)}$$

Where Y_i is the current value in Y
Y' is the predicted value of Y
Y'' is the mean value of the Y.

R-Squared value Ranges from 0-1, higher the value of coefficient of determination, the better the model and lower the RMSE is better the performance of the model[12][13].Forecasted results of the test set are compared with the actual results. The results are plotted as in Fig 4.11 using the different regression models.

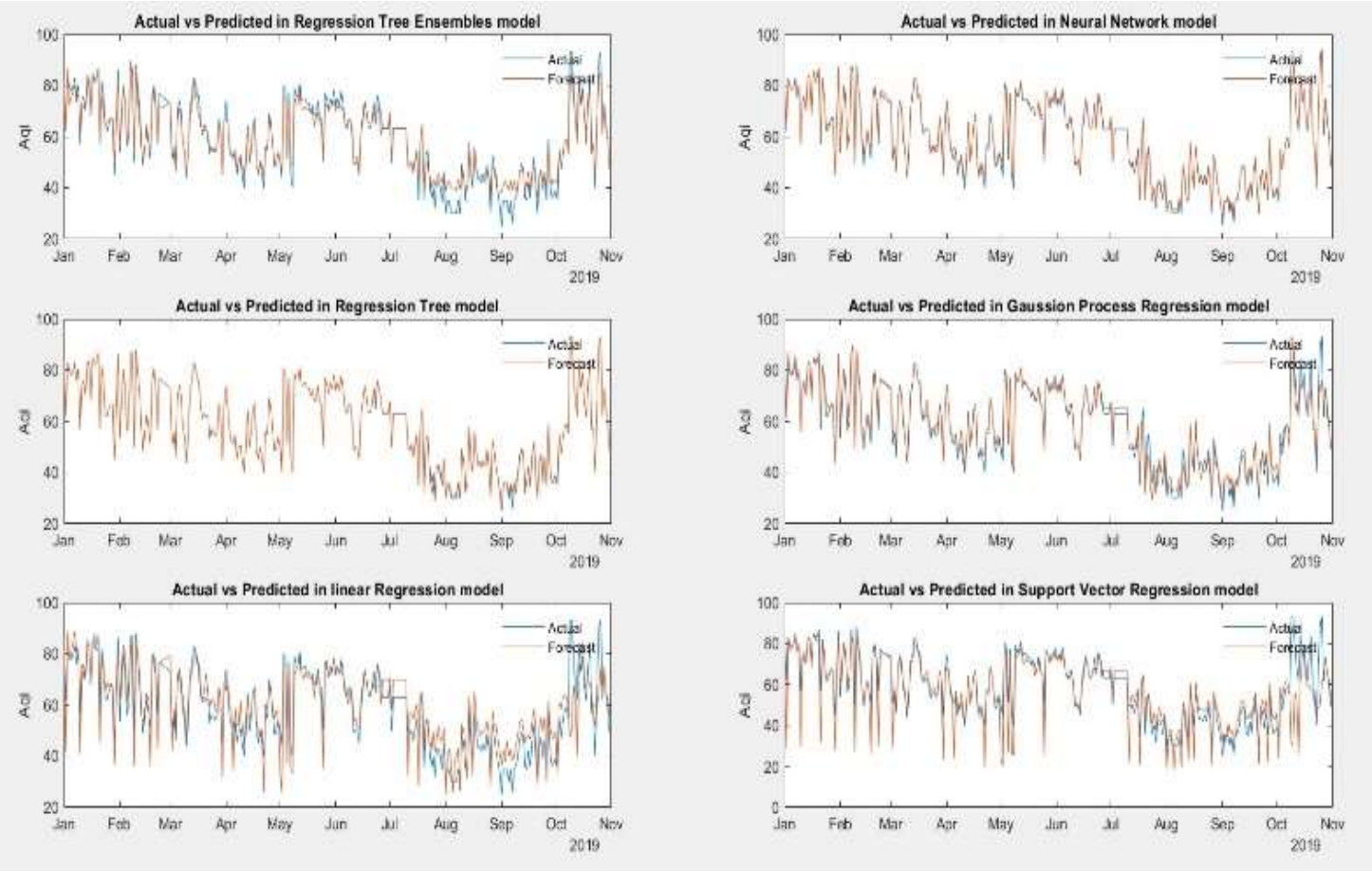

Fig-4.11: *Test Set using different regression models.*

In figure 4.11 represents the final plots of actual versus predicted using different regression models like SVR, GPR LR, etc, and Neural Networks applying the Levenberg- Marquardt training algorithm.

Quality Metrics	Neural Networks	Kriging	Linear	SVR	Tree	Tree Bagger
MSE	0.857	10.355	61.302	98.431	0.744	11.747
MAE	0.657	2.256	5.849	5.542	0.334	2.588
RMSE	0.926	3.218	7.830	9.921	0.863	3.427
R^2 Error	0.997	0.958	0.750	0.599	0.997	0.952
Median Absolute Error	1.000	1.669	4.998	3.159	0.000	2.179
Average Error	-0.490	-0.137	-1.176	2.023	0.037	0.743
Median Error	0.000	0.091	-2.685	-0.345	0.000	0.679

Table-2: *The Quality Metrics for different models*

5. CONCLUSION & FUTURE SCOPE

Different regression modelsand Neural Networksare used for predicting the AQI using the previous data of the Vijayawada City. The AQI value for the test set year 2019 hasbeen forecasted with the different regression models and the Neural Networks. Support vector machine-based regression model has provided MSE of 98.431 and R^2 error of 0.599. Gaussian process regression-based model has provided MSE of 10.355and R^2 error of 0.958. Linear regression model has provided MSE of 61.302and R^2 error of 0.750. Tree regression model has provided MSE of 0.744and R^2 error of 0.997.Tree bagger-based regression model has provided

MSE of 11.747and R^2 error of 0.952. Neural Network has provided the MSE of 0.857 and R^2error of 0.997. Neural network and regression tree have provided same R^2 error. Tree regression model gives lowest MSE. Tree regression model provides better performance when compared to all other models in terms of MSE and R^2 error. Deep learning can be employed to learn features of pollutants and may provide better classification.

ACKNOWLEDGEMENT

The authors acknowledge theauthorities of Andhra Pradesh Pollution Control Board - Vijayawada forproviding with necessary air pollution data.Authors thank their parents, teachers for their constant help and support. Authors extend theirthanks to the director, Andhra Loyola Institute of Engineering and Technology, Vijayawada, Dr. Francis Xavier SJ, Principal of the institute, members of Dr.APJ Abdul kalam research forum, staff of the department of ECE for their constant inspiration and encouragement.

REFERENCES

[1]. Control of urban Pollution series CUPS/ 82/2014-2015 “National Air Quality Index” Central Pollution Control Board, Ministry of Environment Forest and Climate Change.

[2]. Chavi Srivastha, Shyamli Singh, Amit Prakash Singh:’ Estimation of Air Pollution in Delhi using Machine Learning Techniques’,2018 International Conference of Computing, Power and Communication Technologies(GUCON).

[3]. Ka Hu, Ashfaqur Rahman, Vijay Sivaraman: ‘HazeEst: Machine Learning Based Metropolitan Air PollutionEstimation from Fixed and Mobile Sensors’, DOI10.1109/JSEN.2017.2690975 IEEE Sensors journal.

[4] Aditya CR, Chandana R Deshmukh, Nayana D K, PraveenGandhi:’ Detecting and Prediction of Air Pollution UsingMachine Learning Models’, International Journal of Engineering Trends and Technology (IJETT)-volume 59 issue /24-May 2018.

[5]. Sachit Mahajan, Ling-Jyh Chen, Tzu-Chieh Tsai: AnEmpirical Study of PM2.5 Forecasting Using neuralnetwork. IEEE Smart World Congress, At San Francisco,USA 2017.

[6]. Jan Kleine Deters, Rasa Zalakeviciute, Mario Onzalez, Yves Rybarczyk:’Modelling PM2.5 Urban Pollution Using Machine Learning and Selected Meteorological Parameters’ Hindawi, journal of Electrical and Computer Engineering,Volume 2017, Article ID 5106045.

[7].V.Duc Le, Sang Kyun Cha, ‘Real-time Air Pollution prediction model based on Spatiotemporal Big data’.The International Conference on Big data, IoT, and Cloud Computing (BIC 2018)

[8]. Ping Wang a, Yong Liua, Zuodong Qin a, Guisheng Zhang b,’ A novel hybrid forecasting model for PM10 and SO2 daily concentrations’ Science of the Total Environment 505 (2015) 1202–1212.

[9]. Sachin Bhogtie, Sejal Pitale, Pooja Bhalgat’ Air Quality Prediction Using Machine Learning Algorithms’, Internationl Journals of Computer Applications Technology and Research Volume 8-Issue 09,367-370,2019, ISSN: -2319-8656.

[10].Ping Wang a, Yong Liua, Zuodong Qin a, Guisheng Zhang b,’ A novel hybrid forecasting modelforPM10andSO2 daily concentrations’Science of the Total Environment 505 (2015) 1202–1212.

[11]. Z. Qi and et al., “Deep Air Learning: Interpolation, Prediction, and Feature Analysis of Fine-grained Air Quality,” TKDE 2018, IEEE transaction on knowledge anddata engineering vol.30 no.12.

[12].Azman azid, HafizanJuahir, Mohd Khairul Amri Kamaruddin, Ahmad Shakir MohdSoudi,” Prediction of the level of Air pollution using principle component analysis and artificial neural network techniques: a case study in Malaysia”, Water Air Soil pollut(2014) 225:2063, DOI: 10.1007/s 11270-014-2063-1

[13]. Norusis, M.J. (1990). SPSS base system user’s guide. Chicago, IL, USA: SPSS.

[14].Shikha Saxena, Anil K Mathur, ‘Prediction of Respirable Particulate Matter (PM10) Concentration using Artificial Neural Network in Kota city’, Asian Journal of Convergence in Technology Volume III, Issue III ISSN No.:2350-1146, I.F-2.71.

[15].Jan Kleine Deters, Rasa Zalakeviciute, Mario Gonzalez,and Yves Rybarczyk,’ Modeling PM2.5 Urban Pollution Using Machine Learning and Selected Meteorological Parameters’, Journal of Electrical and Computer Engineering,Volume 2017, Article ID 5106045.

IEEE Access
Multidisciplinary | Rapid Review | Open Access Journal

Received March 27, 2019, accepted April 8, 2019, date of publication May 1, 2019, date of current version June 20, 2019.

Digital Object Identifier 10.1109/ACCESS.2019.2914260

Design, Modeling and Analysis of Perforated RF MEMS Capacitive Shunt Switch

K. SRINIVASA RAO[1], (Member, IEEE), CH. GOPI CHAND[1], K. GIRIJA SRAVANI[1,2], D. PRATHYUSHA[1], P. NAVEENA[1], G. SAI LAKSHMI[1], P. ASHOK KUMAR[1], AND T. LAKSHMI NARAYANA[1]

[1]MEMS Research Center, Department of Electronics and Communication Engineering, KL University, Guntur 522502, India
[2]National MEMS Design Center, Department of Electronics and Communication Engineering, National Institute of Technology, Silchar 788010, India

Corresponding author: K. Srinivasa Rao (srinivasakarumuri@gmail.com)

ABSTRACT This paper illustrates the design, modeling, and analysis of bridge type structure based capacitive RF MEMS switch with different beam thickness and materials. We have used Ashby's approach to select the best materials in each and every level which helped to improve the overall performance of the switch in terms of mechanical, electrical, and RF properties. Silicon Nitride thin film ($\varepsilon_r = 7.8$) is used as a dielectric material. The beam structure stiffness is analyzed with different materials, such as gold, titanium, and platinum, within these materials gold with high thermal conductivity and Euler–Young's modulus of 77 GPa is offering the best performance. Incorporation of meanders and perforations to the membrane helped to reduce the pull-in voltage. The proposed switch is offering very low pull-in voltage of 1.9 V. The deflection of beam thickness is tabulated for the three materials among them the 2 ţm thickness is best beam thickness for the switch for X-band applications. The switch offers best return loss (S_{11}) of -21.36 dB, insertion loss (S_{12}) of -0.147 dB, and isolation (S_{21}) of -52.04 dB at 8GHz. The switch presented in this paper is preferable in X-band applications.

INDEX TERMS Fixed-fixed membrane, spring constant, pull-in voltage, switching time, X-band, material science.

I. INTRODUCTION

RF MEMS technology has exhibited great potential in the latest low power and high-frequency communication applications X-band range. Especially X-band radars occupied a major role in military, weather monitoring, air traffic control, vehicle speed detection applications. The performance of the radar depends on the switch present in the radar transceiver module. Design of the switch with low power consumption, high isolation, and low insertion are the potential research problems. RF MEMS switches with high tuning capability proved its ability in low power communication applications. In the last few decades, solid-state technology switches (PIN, FET) fulfill the gap in communication applications, but at high- frequency range their performance is not up to the mark [1]–[5]. In context of high isolation, low insertion and low power consumption RF MEMS switches are dominating the solid state switches in various applications. Design of an RF MEMS switch with low pull-in voltage, high power handling, low spring constant and best RF performance is the major research challenge [6]–[8]. Incorporation of low spring constant (K) micromechanical membrane structure, increasing of actuation area of the electrodes and minimum gap between the actuation electrodes help's to reduce the pull-in voltage. Perforations to the top membrane help to reduce up-state capacitance which majorly influences the switch insertion losses. In an association of high relative permittivity (ε_r) offering dielectric thin film (μm) in RF MEMS switch design helps to increase the switch downstate capacitance which helps to improve the isolation property of the switch [9], [10].

Bridge type capacitive switch having serpentine structure gives high inductance such that high isolation is achieved for X-band applications with the pull-in voltage of the switch is 20.4 V [11]. Asymmetric toggle RF MEMS Switch with a bridge structure is designed based on torsional spring with a movable membrane. The springs are employed to reduce the pull-in voltage is 5 V to 3 V and also to achieve better isolation and low insertion loss, each designed switch is suitable

The associate editor coordinating the review of this manuscript and approving it for publication was Hamid Mohammad-Sedighi.

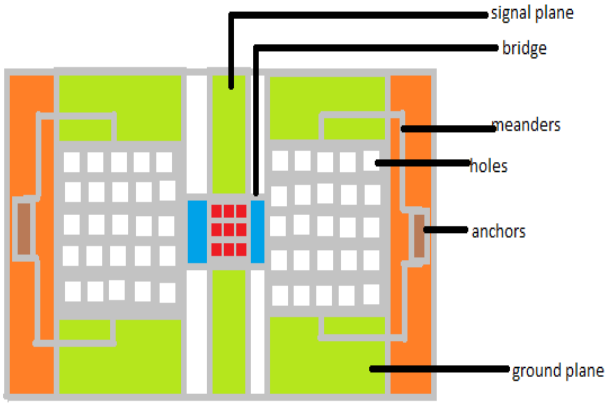

FIGURE 1. The Schematic view of RF MEMS shunt switch.

for low-frequency applications [12]. The switch is designed with GaAs substrate with fixed anchors such that the isolation of −50 dB and low insertion of 0.1dB is achieved at 4GHz which is applicable for X-band applications [13]. RF MEMS switch is designed by holding silicon on a glass substrate. The switch produces high productivity and lower stress and also less fabrication cost. The pull-in voltage achieved is 19 V which operates in low frequency [14].

The structure of the paper is as follows, in section II the structure of the proposed device, working principle, its dimensions, a brief explanation of selecting material for the beam and dielectric layers, and theoretical calculations are discussed. Section III describes the results and discussions of the proposed switch with including different parameters and final section IV is the conclusion of the paper.

II. PROPOSED RF MEMS SWITCH

A. STRUCTURE OF PROPOSED SWITCH

The proposed shunt type switch is designed on a glass substrate with a length of 595 μm and width 600 μm. An insulating material is placed on the top of the substrate to avoid the RF leakage currents through the substrate. A dielectric layer (Si_3N_4) is placed on the top of CPW transmission line middle conductor for capacitive type switching. The figure1 shows that schematic view of the proposed switch.

A fixed-fixed beam structure is used as membrane which helped to improve the electrical properties of the switch. The gap between the signal line and beam is 1.5 μm, the capacitance is developed between the signal line and beam.

B. WORKING PRINCIPLE

The proposed switch is an electrostatically actuated capacitive shunt RF- MEMS switch. The micromechanical structure (beam) is placed on the CPW transmission line. The capacitive shunt type switches are fixed with the two anchors for both sides the actuated beam is separated from the signal line. The CPW is utilized for the RF Signal transmission from the input port to the output port. Initially, the switch is UP state position, when voltage is applied to

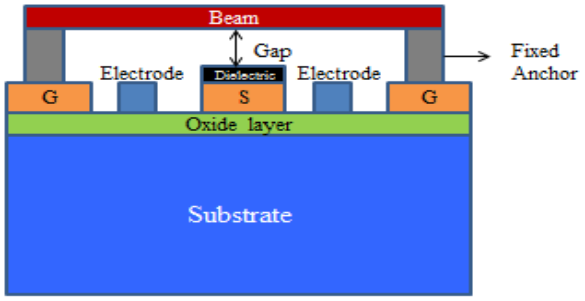

FIGURE 2. ON state condition of RF MEMS switch.

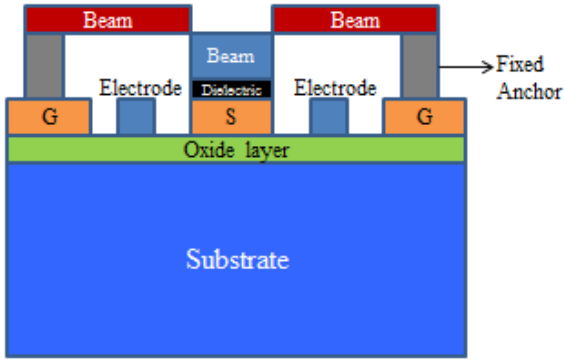

FIGURE 3. Down state condition of RF MEMS switch.

the actuator, the beam moves to the signal dielectric, it will pull down state. The electrostatic force is adding on the beam and load is attached toward the beam, it is distributed one-third of the area it is an impact to the spring constant under the applied some voltage the electrostatic force is generated.

The electro static force is equally distributed over the region of the beam beyond the electrode. The spring constant is generated and it is correlated with the distance travelled below the area of the utilized force. In Upstate capacitance is developed between two electrodes, it is depending on the dielectric. At some particular voltage, the switch is actuated and the beam is displaced by applying electromechanical analysis to simulate the pull-in voltage and spring constant.

The switch consists of a substrate, dielectric substrate, and CPW transmission line which consist of two ground planes and one signal line. The beam is connected between the two fixed anchors. The voltage is applied to the beam is influencing and touches the signal dielectric.

The switch is initially ON state condition when the voltage is applied to the beam it touches the signal line it is in OFF state as shown in figure 2 and figure 3 respectively.

C. DIMENSIONS

The switch associated with membrane with meanders and holes (perforation), a CPW transmission line and a insulated substrate. Materials used and the dimensions of the switch are listed in Table 1.

TABLE 1. Device specifications.

Component	Length (µm)	Width (µm)	Depth (µm)	Material
Substrate	595	600	800	Glass
CPW	200	600	1.5	Gold
Beam	200	300	2	Gold
Signal line	20	600	1.5	Gold
Insulating Layer	595	600	1.2	SiO_2
Meander 1	5	10	1.5	Gold
Meander 2	120	5	1.5	Gold
Middle Beam	60	60	2	Gold
Hole	10	10	2	------

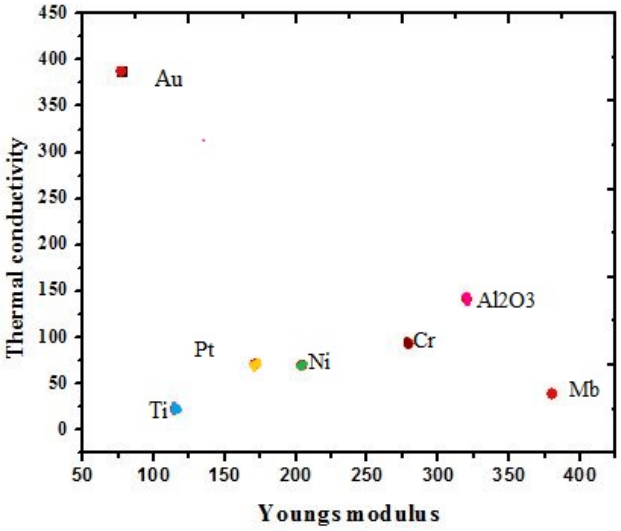

FIGURE 4. Material selections of a beam in a proposed switch.

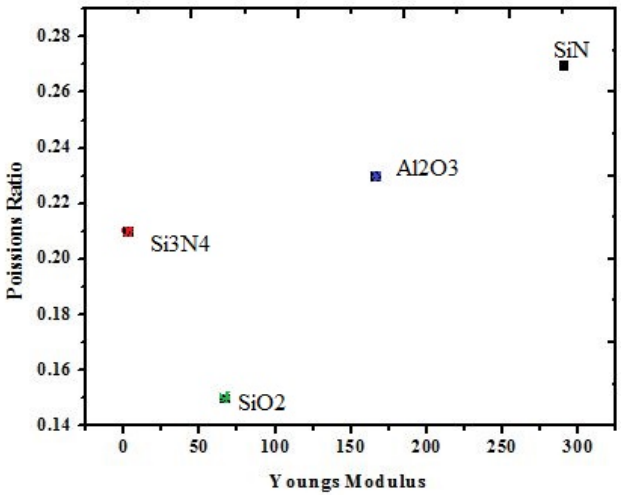

FIGURE 5. Material selections of a dielectric layer in a proposed switch.

TABLE 2. Various materials properties.

Materials	Young's Modulus(E) (GPa)	Poisson's Ratio (v)	Thermal Conductivity (K)
Aluminium	69	0.33	222
Gold	77	0.42	388
Platinum	171	0.39	71
Copper	115	0.33	315
Silicon Nitride	304	0.3	29
Nickel	204	0.31	70
Aluminium Oxide	380	0.22	39
Titanium	110	0.31	68
Chromium	245	0.2	69
Silicon Dioxide	66.3	0.15	1.3

D. MATERIAL SELECTION

Proper material selection is the key performance deciding factor in RF MEMS switches design. Ashby's material selection method is used to select the materials for different thin films in the switch design process. The appearance of the proposed switch is depending on the beam and dielectric materials. In this, we have considered high conductive metals for the beam, and to select some insulators for dielectric [15]. The beam material majority influence the electrical and mechanical parameters of the switch like spring constant, pull-in voltage, switching speed.

Before finalising the material for beam and dielectric thin films, we have done the analysis with different materials by taking their properties in to consideration. In figure 4, we have shown the relation between thermal conductivity of different high conductive materials (Au, Pt, Ti,Ni,Cr,Nb,Al_2O_3) and young's modulus which helps to select appropriate material for beam to achieve low pull-in voltage.

The capacitive RF MEMS switches insertion and isolation properties depend on the properties of dielectric material. So, here we have done an analysis on the properties of different dielectric materials as shown in figure 5. Based on the properties, its Poisson ratio is high, and generating good capacitance between the beam and dielectric. After analysis on material selection, we have noted that gold and Si_3N_4 are appropriate materials for beam and dielectric materials respectively.

Some variable material properties, like Euler-Young's modulus (E), Poisson's Ratio (v), Thermal Conductivity (K) considering beam and dielectric materials taken by Ashby's approach model. Table 2 shows material properties of different conductors and dielectric materials [16].

E. PERFORATIONS AND MEANDERS

The switch beam is associated with perforations and meanders which help to improve the performance of the switch as shown in figure 6. Because of meanders the spring constant of the beam reduces and proportionally the pull-in voltage also reduces. Perforation to the beam helps to reduce the mass of the beam and increase the performance of the switch like switching speed, reducing the pull-in voltage and offer low insertion losses. The beam perforation shows the impact on the upstate capacitance of the switch. The Non-uniform meander technique is used to increase the speed of switch and decrease the spring constant.

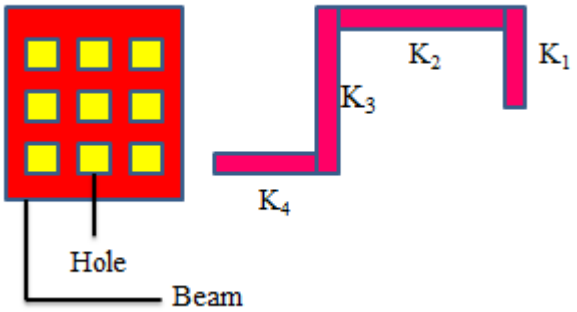

FIGURE 6. Beam with holes and meander of the proposed switch.

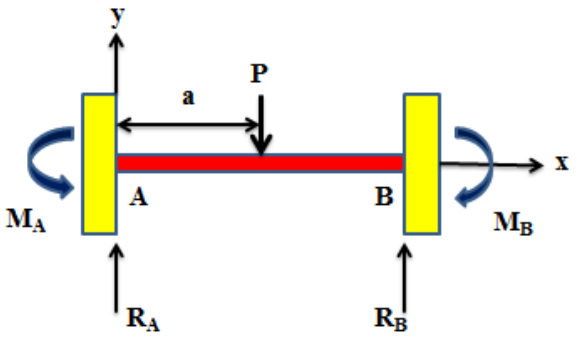

FIGURE 7. Fixed-fixed beam with concentrated vertical load.

The area loss because of the perforation is not more than 60% of the overall area of the membrane. If the holes area is more than the limit it may leads to breaks in the beam. Each hole releases the some resudual stress of the beam and reduces the young's modulus of the structure. The electrostatic force is not influence by the hole density. The capacitance analysis is relaying on the holes. The effect of holes on the upstate is negligible beacause of the fringing field that fills the area of holes. In down state capacitance there is no effect and reduced capacitance ratio.

F. THEORITICAL PARAMETERS

RF MEMS switch performance depends on the mechanical, electrical and Radio Frequency parameters. The one of the mechanical property of the RF MEMS switch is spring constant [17].

The spring constant is the parameter, which indicates the stiffness of the beam. The beam is focused on the load as shown in figure 7. The formula for beam deflection versus position of load is

$$EI\frac{d^2y}{dx^2} = M_A + R_A x \tag{1}$$

By writing 'y' as

$$y = \frac{M_A x^2}{2EI} + \frac{R_A x^3}{6EI} \tag{2}$$

$$M_A = -\frac{Pa}{l^2}(l-a)^2 \tag{3}$$

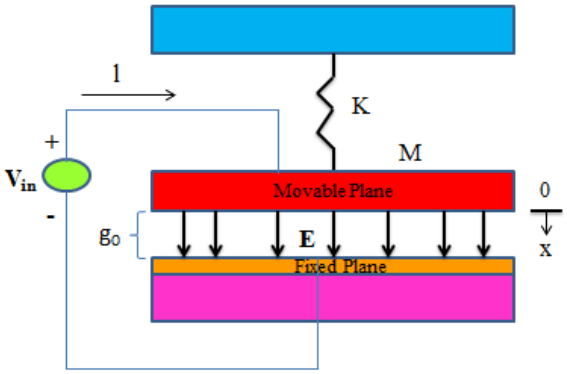

FIGURE 8. Mechanical model of fixed-fixed beam.

$$R_A = \frac{P}{l^3}(l-a)^2(l+2a) \tag{4}$$

where, 'l' is the length of the beam, 'M_A' is the reaction of moment at the left end, 'R_A' is the vertical reaction of the left end, '$I = wt^3/12$' is the moment of inertia, 't' is the thickness and 'w' is width of the beam.

The load is equally distributed to the beam, and also caused some deflections at the middle point, substituting $x = l/2$ in equation 1 and 2.

At some point 'a' the deflection is identified, and the load is equally distributed on the beam. The spring constant with respected to the beam is

$$k'_a = -\frac{p}{y} = -\frac{\varepsilon l}{y} = Ew(\frac{t}{l})^3 \tag{5}$$

where,

$$P = \varepsilon l$$
$$y = \frac{2}{El}\int \frac{\varepsilon}{48}(l^3 - 6l^2a + 9la^2 - 4a^3)da \tag{6}$$

The spring constant for fixed-fixed beam with meanders can be calculate using formula [17]–[19],

$$k_{eq} = k_1 + k_2 + k_3 + k_4 \tag{7}$$

$$K_{(1,2,3,4)} = \frac{Ewt^3}{l^3} \tag{8}$$

where 'E' is Young's modulus, 'w' is the width,' t' is the thickness, 'l' is the length of the beam.

The pull-in voltage is depending on the spring constant, where the DC voltage is applied on the beam through the RF signal line. The electro static force is generated between the movable plates and fixed plane the operation as shown in figure 8. The mechanical force is equal to the potential energy [18]–[20]. The electro static energy is

$$m\frac{d^2x}{dt^2} + Kx = Fe(x) \tag{9}$$

The mechanical elastic force is

$$F_m(x) = Kx$$

The capacitance of movable parallel-plate is

$$C(x) = \frac{\varepsilon_0 A}{g_0 x} \tag{10}$$

Area (A) is impact on the beam, the energy is stored in the capacitor, with respect to the movable plate is

$$F_e(x) = \frac{d}{dx}\left(\frac{1}{2}V^2 C(x)\right) = \frac{\varepsilon_0 A V^2}{2\,(g_0 - x)^2} \tag{11}$$

where,

$$V = (g_0 - x)\sqrt{\frac{2kx}{(\varepsilon_0 A)}} \tag{12}$$

The equation shows that relation between the voltage and displacement. The maximum voltage is utilizing on the beam.

$$\frac{dv}{dx} = -\sqrt{\frac{2kx}{\varepsilon_0 A} + (g_0 - x)\,k\sqrt{\frac{1}{(2Kx\varepsilon_0 A)}}} \tag{13}$$

The pull-in voltage of fixed-fixed beam is

$$V_p = \sqrt{\frac{8kg_0^3}{27\varepsilon_0 A}} \tag{14}$$

where

K – spring constant

A – over lapping area of electrodes

g_o - Air gap between beam and signal line

$\mathcal{E}_o$ - permitivity of in free space

The capacitance study is estimated during UP state and downstate. The upstate capacitance is

$$c_u = \frac{\varepsilon_0 A}{g_0 + \frac{t_d}{\varepsilon_r}} \tag{15}$$

The downstate capacitance is figured by using formula

$$C_d = \frac{\varepsilon_0 \varepsilon_r A}{t_d} \tag{16}$$

where A is the area, 't' is the thickness of the beam. The resonant frequency is calculated by using an equation.

$$F_r = \frac{1}{2\pi}\sqrt{\frac{K}{m}} \tag{17}$$

where, 'k' is the spring constant, 'm' is the mass of the beam.

Damping ratio and quality factors are the important parameter of the RF MEMS switch, It is depending on gap between the beam, dielectric and also overlapping area of the beam. By changing the gap damping ratio will also changes, It is calculated by

$$b = \frac{3}{2\pi}\frac{\mu A^2}{g^3} \tag{18}$$

where, 'μ' is the viscosity of air, 'A' overlapping area, 'g' gap between the electrodes.

TABLE 3. Spring constant and pull-in voltages for gold.

Thickness of beam (µm)	Spring Constant (N/m)	Pull-in voltage (V)
0.5	0.50	0.74
1	4.04	0.67
1.5	13.65	1.22
2	32.35	1.9
2.5	63.2	2.33
3	109.2	3.4

TABLE 4. Spring constant and pull-in voltages for platinum.

Thickness of beam (µm)	Spring Constant (N/m)	Pull-in voltage (V)
0.5	1.08	0.63
1	8.65	1.79
1.5	29.20	3.29
2	69.22	2.76
2.5	135.2	7.09
3	233.62	9.32

TABLE 5. Spring constant and pull-in voltages for titanium.

Thickness of beam (µm)	Spring Constant (N/m)	Pull-in voltage (V)
0.5	0.74	0.52
1	5.92	1.48
1.5	19.9	2.72
2	47.39	2.28
2.5	92.56	5.86
3	159.9	7.71

The quality factor of the switch influences the switching parameters such as spring constant, resonant frequency. The quality factor of the switch is obtaining by using the equation,

$$Q = \frac{K}{2\pi f_0 b} \tag{19}$$

where, 'b' is the damping ratio, 'k' is the spring constant, 'f_o' is resonant frequency.

The switching time is important factor for the speed of the switch. It is calculated by using formula,

$$T_s = \frac{3.67 V_p}{V_s \omega_0} \tag{20}$$

where, 'V_p' is pull in voltage, 'V_s' is actuated voltage.

Table 3, 4, 5 demonstrates the effect of beam thickness and materials on the spring constant and pull-in voltage. In this gold material offering low pull-in voltage than platinum and titanium. From tables we have observed that increasing of beam thickness effecting the spring constant proportionally, and simultaneously the pull-in voltage is also increase.

III. RESULTS AND DISCUSSIONS

A. SPRING CONSTANT

The performance of RF MEMS switch is associated with the spring constant. The effective spring constant of the beam associated with meanders indicates the stiffness and how

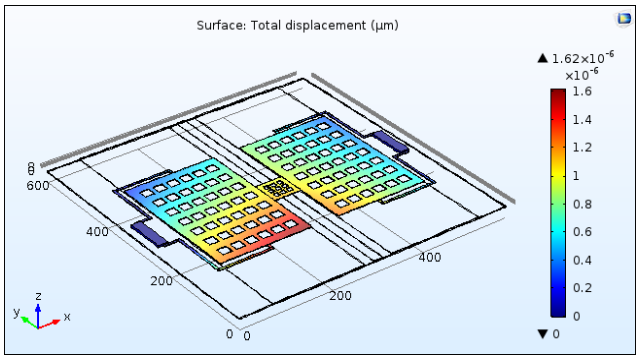

FIGURE 9. Simulation of switch membrane by gold.

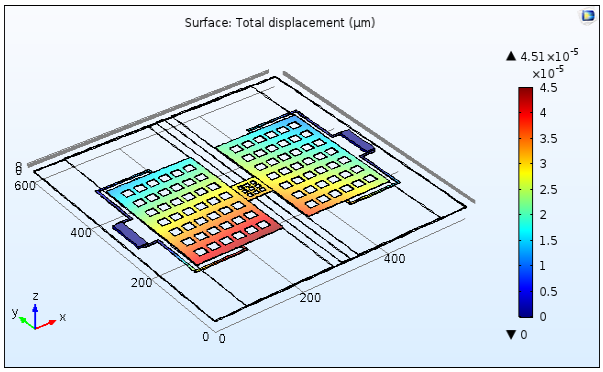

FIGURE 11. Simulation of switch membrane by pull-in voltage.

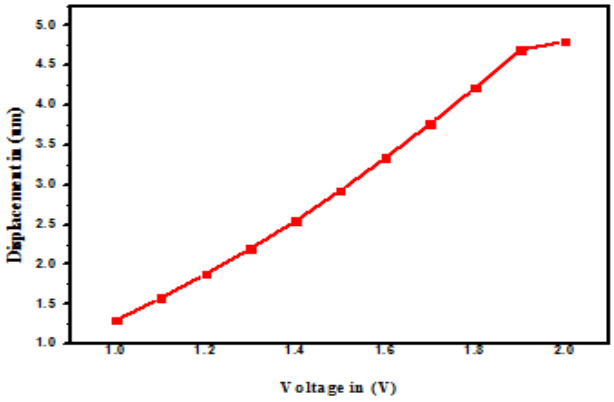

FIGURE 10. Voltage vs displacement for gold.

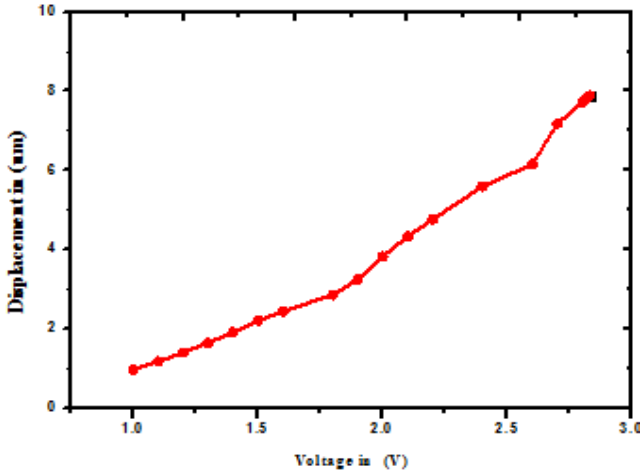

FIGURE 12. Voltage vs displacement for platinum.

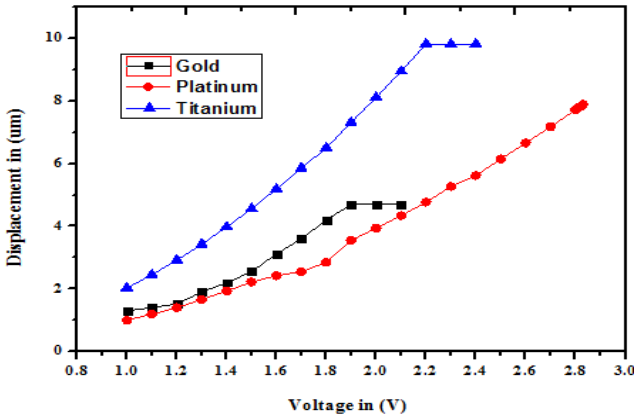

FIGURE 13. Voltage vs displacement for three materials.

much residual stress it can obey. The proposed switch beam is associated with perforations, these are helped to reduce the spring constant. The spring constant of proposed switch beam is 32.35 N/m.

B. PULL-IN VOLTAGE

Pull-in voltage is one of the key electrical parameter of the switch. The switch requires DC voltage to actuate the beam and the voltage required to deform beam 2/3 of its initial position is known as pull-in voltage. The beam spring constant majorly decides the pull-in voltage of the switch, by selecting low spring constant beam structure, we can reduce the required pull-in voltage.

The switch is designed and analyzed the performance with different dimensions and materials using the FEM tool. When the DC voltage is applied between beam and actuation electrodes, the switch beam is actuated [21].

By simulate the proposed switch and to observe the beam is displaced at a particular voltage. At appropriate voltage, beam is actuated and the displacement is constant. The figure 9,10, 11 shows that the beam displacement at different DC voltages.

The role of materials on the pull-in voltage is analyzed by designing beam with high conducting metals like gold, platinum, titanium. In figure12 shows that voltage Vs displacement for platinum. We have noticed that the spring constant of the beam depends on the material, the beam with gold material offering low spring constant. The figure13 show that voltage vs displacement of different materials having various pull-in voltages likes Gold, Platinum, and Titanium [22]–[24]. It is clear that the low spring constant offering gold based beam is requiring the low pull-in voltage. With this we would like to conclude that gold is the best material to get the good pull-in voltage i.e., 1.9 V.

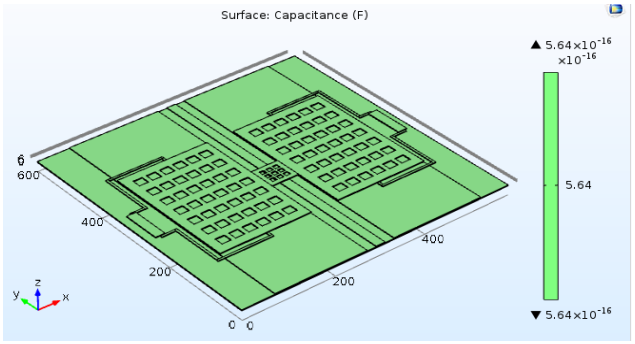

FIGURE 14. Down state capacitance of the proposed switch.

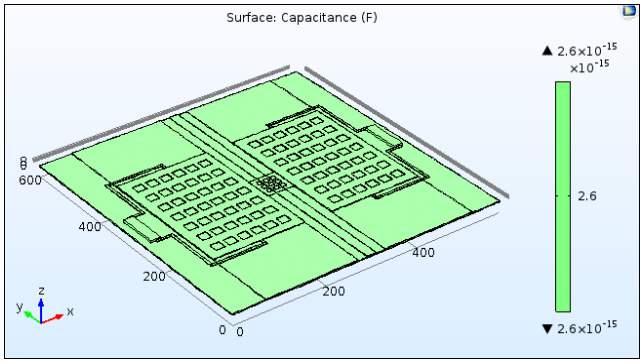

FIGURE 15. UP state capacitance of the proposed switch.

C. CAPACITANCE ANALYSIS

The proposed switch works depends on the upstate and downstate capacitances. The upstate capacitances influence the insertion losses and the downstate capacitances influences the isolation losses of the switch. By reducing the upstate capacitance and improving the downstate capacitance we can active the best radio frequency performance of the switch. The dielectric thin film decides the capacitance of the switch.

The proposed switch is using Si_3N_4 as the dielectric thin film offering a downstate capacitance of 4.47 pF and the upstate capacitance is 2.47 fF as shown in figure 14 and 15.

D. RESONANT FREQUENCY ANALYSIS

The resonant frequency is known as rate of change of displacement with respect to applied DC voltage. It's depending on the gap between the beam and actuation electrodes. The resonant frequency of the proposed switch is obtained from the FEM tool simulation i.e., 5 KHz which is closely matched with the theoretical value.

E. SWITCHING TIME ANALYSIS

The ratio of pull-in voltage to the actuation voltage is known as switching time. It is depending on the speed of beam deformation.

The switching time is depending on the pull-in voltage. If the voltage is increased the switching time is also increasing. At particular voltage the switching time is constant.

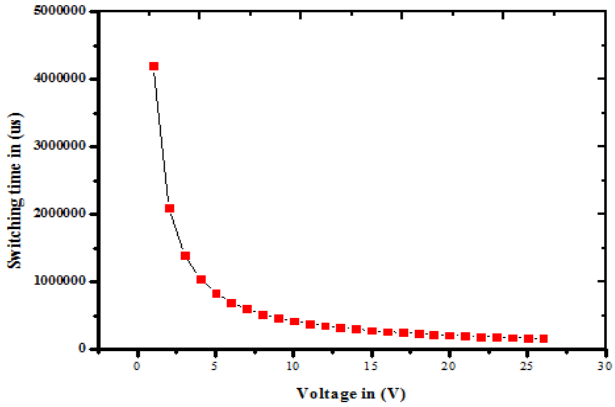

FIGURE 16. Switching time analysis of the switch.

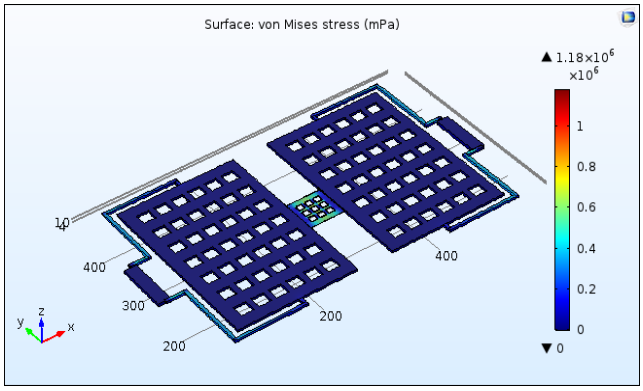

FIGURE 17. Stress analysis of proposed switch.

TABLE 6. Comparing switching parameters of three materials.

Parameters	Gold	Platinum	Titanium
Spring Constant (N/m)	32.35	69.22	47.39
Pull-in Voltage (V)	1.9	2.7	2.2
Switching Time (μs)	9	9.7	9.9
Up state Capacitance (fF)	2.7	1.06	2.88
Down state Capacitance (pF)	4.47	1.75	2.99
Quality Factor	2.3e-3	4.1e-3	3.43e-3
Resonant Frequency (KHz)	2.6	3.8	3.2

The switching time of the proposed switch is 9 μs as shown in figure 16.

F. QUALITY FACTOR

The spring constant, resonant frequency and damping coefficients decides the quality factor of the switch. If the quality factor of the switch is low it indicates the settling time of the beam is low. It is depending on the beam structure and actuation electrodes area of the switch. The quality factor of proposed switch is Q = 2.3e-3. This is good toward the switch settling time is very low.

TABLE 7. S-parameters of proposed switch.

Losses	In dB(Decibel)	Frequency (GHz)
Return loss(S_{11})	-21 dB	8 GHz
Insertion loss(S_{21})	-0.14 dB	10 GHz
Isolation loss(S_{21})	-52.04 dB	12 GHz

G. STRESS ANALYSIS

The stress analysis on the beam helps to analyze the scope of unnecessary deformation which leads to the switch permanent failure. The stress is equally distributed by applying some force on the beam. Here the figure 17 shows that stress analysis for gold beam material. First, we calculate the force by using the formula 21, calculated force is 3.2 micro Newton [25]–[27].

$$\sigma_{cr} = \frac{\pi^2 E t^2}{3l^2(1-v)} \tag{21}$$

where 'E' is the Young's modulus of material, 't' is the thickness of beam and 'l' is the length of the beam. While here we taking gold as beam material, because of it is high conducting material and Young's modulus is 79 Gpa.

The switching parameters of the three materials are given in table 6, we observed that material of gold is shows good results by comparing Platinum and Titanium.

H. RF PERFORMANCE ANALYSIS

The shunt capacitive RF MEMS Radio frequency performance are analyzed using HFSS tool. The scattering parameters like S_{11}, S_{12}, S_{21} are recorded to analyze the insertion isolation behavior of the switch. When the switch is ON State condition will occur S_{11} and S_{12} are return loss and insertion loss generated. The switch is OFF state it exhibits the isolation loss (S_{21}) The RF performance is evaluated at the switch is ON and OFF state conditions [28]–[35].

These S-parameters are analyzed at 8 GHz to 60 GHz. The simulation results shows that the switch offering best return loss and high isolation in x-band range as shown in figure 18, 19, 20. So we are proposing the switch for X-band frequency.

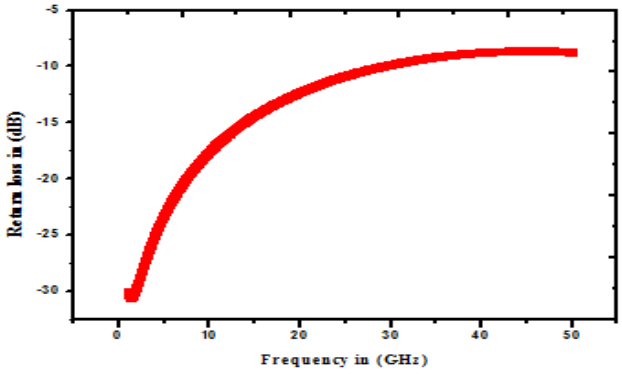

FIGURE 18. Return loss of proposed switch.

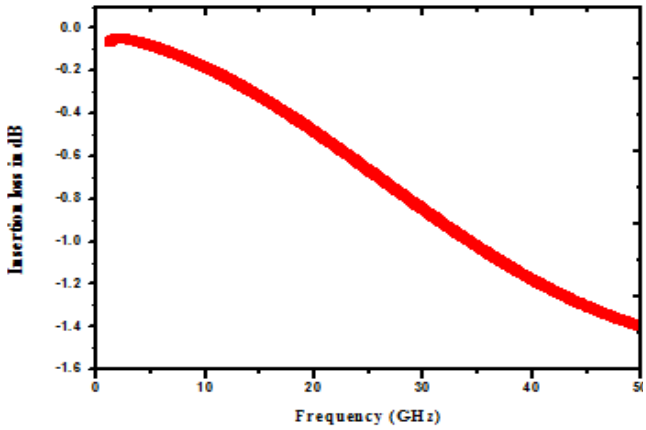

FIGURE 19. Insertion loss of proposed switch.

From Table 7, we have obtained the return loss is less than −21.36 dB at 8 GHz, and the insertion loss is up to −0.14 dB at 10 GHz and the isolation of proposed switch is 52.04 dB at 12 GHz. The switch offering good performance in X-band region, so it is applicable in reconfigurable antennas for satellite communications. Here, Table.8, shows that comparison

TABLE 8. Comparison of proposed switch pameters with previous works.

Switching Parameters	A. Ziaei et.al.[6]	Wei-Bin Zheng.et.al.[5]	Linda.et.al.[8]	Proposed work
Pull-in voltage	60 V	17 V	6 V	1.9V
Capacitance (up)	40 fF	-------	----	2.7 fF
Capacitance (down)	3.1 pF	-------	----	4.47 pF
Switching time	----	-------	----	9μs
Return loss	----	------		-21 dB at 8 GHz
Insertion loss	----	-0.25 dB at 24.5 GHz	-0.2 dB at 40 GHz	-0.147 dB at 8 GHz
Isolation loss	-30 dB at 10 GHz	-42 dB at 24.5 GHz	-30 dB at 40 GHz	-52.04 dB at 8 GHz

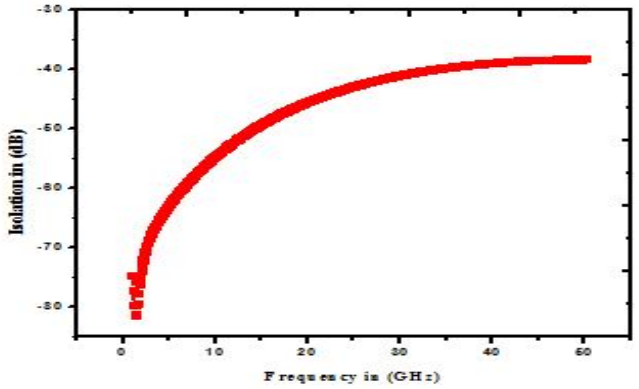

FIGURE 20. Isolation loss of proposed switch.

of all parameters of the proposed RF MEMS Switch with previous work.

IV. CONCLUSIONS

In this paper, we have designed and simulated capacitive shunt type RF MEMS switch for X-band applications. Meanders and perforations play a key role to reduce the spring constant and pull-in voltage. The switch electrical and RF parameters are extracted by using COMSOL FEM & HFSS tools respectively. The switch offering low pull-in voltage of 1.9 V. The materials impact is present on the switch having good performance. The device shows a low switching time of 9 μ s. The result shows that return loss and insertion losses are -21 dB and -0.147 dB and high isolation of -52.04 dB at 8 to 12 GHz. The theoretical and simulation values are very close agreement. The proposed switch offering best performance in X-band range i.e 8-12 GHz. Therefore, the proposed RF MEMS Switch is used in radars occupied a major role in military, weather monitoring, air traffic control, vehicle speed detection applications.

ACKNOWLEDGMENT

The authors would like to thank to NMDC supported by NPMASS, for providing the necessary computational tools.

REFERENCES

[1] E. A. Savin, K. A. Chadin, and R. V. Kirtaev, "Design and manufacturing of X-band RF MEMS switches," *Microsyst. Technol.*, vol. 24, pp. 2783–2788, Jun. 2018.

[2] K. Maninder, K. J. Rangra, D. Kumar, and S. Singh, "Parametric optimization of symmetric toggle RF MEMS switch for X-band applications," *Int. J. Recent Trends Eng.*, vol. 2, p. 95, Nov. 2009.

[3] H. Yan, X. Liao, C. Chen, and C. Li, "High-power handling analysis of a capacitive MEMS power sensor at band," *IEEE Sensors J.*, vol. 18, no. 13, pp. 5272–5277, Jul. 2018.

[4] A. Malczewski, S. Eshelman, B. Pillans, J. Ehmke, and C. L. Goldsmith, "X-band RF MEMS phase shifters for phased array applications," *IEEE Microw. Guided Wave Lett.*, vol. 9, no. 12, pp. 517–519, Dec. 1999.

[5] W.-B. Zheng, Q.-A. Huang, X.-P. Liao, and F.-X. Li, "RF MEMS membrane switches on GaAs substrates for X-band applications," *J. Microelectromech. Syst.*, vol. 14, no. 3, pp. 464–471, Jun. 2005.

[6] A. Ziaei, S. Bansropun, P. Martins, and M. L. Baillif, "Fast high power capacitive RF-MEMS switch for X-Band applications," in *Proc. 45th Eur. Solid State Device Res. Conf.*, Sep. 2015, pp. 153–155.

[7] T. Singh, and K. J. Rangra, "Compact low-loss high-performance single-pole six-throw RF MEMS switch design and modeling for DC to 6 GHz," *Microsyst. Technol.*, vol. 21, pp. 2387–2396, Nov. 2015.

[8] L. P. B. Katehi, J. F. Harvey, and E. Brown, "MEMS and Si micromachined circuits for high-frequency applications," *IEEE Trans. Microw. Theory Techn.*, vol. 50, no. 3, pp. 858–866, Mar. 2002.

[9] J.-H. Park *et al.*, "A fully wafer-level packaged RF MEMS switch with low actuation voltage using a piezoelectric actuator," *J. Micromech. Microeng.*, vol. 16, no. 11, p. 2281, Sep. 2006.

[10] J. B. Muldavin and G. M. Rebeiz, "Novel series and shunt MEMS switch geometries for X-band applications," in *Proc. 30th Eur. Microw. Conf.*, Oct. 2000, pp. 1–4.

[11] M. Tang, A. B. Yu, A. Q. Liu, A. Agarwal, S. Aditya, and Z. S. Liu, "High isolation X-band MEMS capacitive switches," *Sens. Actuators A, Phys.*, vol. 120, pp. 241–248, Apr. 2005.

[12] K. Rangra, M. Kaur, and D. Kumar, "Design optimization of RF MEMS capacitive symmetric toggle switch for X-band wireless applications," in *Proc. ISSS*, Nov. 2016, pp. 16–17.

[13] J. J. Yao and M. F. Chang, "A surface micromachined miniature switch for telecommunications applications with signal frequencies from DC up to 4 GHz," in *Proc. Int. Solid-State Sens. Actuators Conf.*, Jun. 1995, pp. 384–387.

[14] J.-M. Kim, J.-H. Park, C.-W. Baek, and Y.-K. Kim, "The SiOG-based single-crystalline silicon (SCS) RF MEMS switch with uniform characteristics," *J. Microelectromech. Syst.*, vol. 13, no. 6, pp. 1036–1042, Dec. 2004.

[15] A. K. Sharma and N. Gupta, "Material selection of RF-MEMS switch used for reconfigurable antenna using Ashby's methodology," *Prog. Electromagn. Res. Lett.*, vol. 31, pp. 147–157, Apr. 2012.

[16] A. Paldas and N. Gupta, "Material selection and parameter characterization for RF MEMS switches," *Int. J. Mech. Prod. Eng.*, vol. 1, no. 3, pp. 7–12, 2013.

[17] K. G. Sravani and K. S. Rao, "Analysis of RF MEMS shunt capacitive switch with uniform and non-uniform meanders," *Microsyst. Technol.*, vol. 24, pp. 1309–1315, Feb. 2018.

[18] K. S. Rao, L. N. Thalluri, K. Guha, and K. G. Sravani, "Fabrication and characterization of capacitive RF MEMS perforated switch," *IEEE Access*, vol. 6, pp. 77519–77528, 2018.

[19] S. Molaei and B. A. Ganji, "Design and simulation of a novel RF MEMS shunt capacitive switch with low actuation voltage and high isolation," *Microsyst. Technol*, vol. 23, no. 6, pp. 1907–1912, Jun. 2017.

[20] J. Y. Park, G. H. Kim, K. W. Chung, and J. U. Bu, "Monolithically integrated micromachined RF MEMS capacitive switches," *Sens. Actuators A, Phys.*, vol. 89, pp. 88–94, Mar. 2001.

[21] K. Rangra *et al.*, "Symmetric toggle switch—A new type of rf MEMS switch for telecommunication applications: Design and fabrication," *Sens. Actuators A, Phys.*, vol. 123, pp. 505–514, Sep. 2005.

[22] E. M. Miandoab, H. N. Pishkenari, A. Yousefi-Koma, F. Tajaddodianfar, and H. Ouakad, "Size effect impact on the mechanical behavior of an electrically actuated polysilicon nanobeam based NEMS resonator," *J. Appl. Comput. Mech.*, vol. 3, pp. 135–143, Jun. 2017.

[23] R. Barretta, M. Diaco, L. Feo, R. Luciano, F. M. D. Sciarra, and R. Penna, "Stress-driven integral elastic theory for torsion of nano-beams," *Mech. Res. Commun.*, vol. 87, pp. 35–41, Jan. 2018.

[24] D. Salamat and H. M. Sedighi, "The effect of small scale on the vibrational behavior of single-walled carbon nanotubes with a moving nanoparticle," *J. Appl. Comput. Mech.*, vol. 3, pp. 208–217, Aug. 2017.

[25] M. A. Eltaher, M. Agwa, and A. Kabeel, "Vibration analysis of material size-dependent CNTs using energy equivalent model," *J. Appl. Comput. Mech.*, vol. 4, pp. 75–86, Apr. 2018.

[26] H. M. Sedighi and N. Farja, "A modified model for dynamic instability of CNT based actuators by considering rippling deformation, tip-charge concentration and Casimir attraction," *Microsyst. Technol.*, vol. 23, pp. 2175–2191, Jun. 2017.

[27] R. Barretta, S. A. Faghidian, and R. Luciano, "Longitudinal vibrations of nano-rods by stress-driven integral elasticity," *Mech. Adv. Mater. Struct.*, vol. 10, pp. 1–9, Feb. 2018.

[28] D. Peroulis, S. P. Pacheco, K. Sarabandhi, and L. P. B. Katehi, "Electromechanical considerations in developing low-voltage RF MEMS switches," *IEEE Trans. Microw. Theory Techn.*, vol. 51, no. 1, pp. 259–270, Jan. 2003.

[29] C. L. Goldsmith, Z. Yao, S. Eshelman, and D. Denniston, "Performance of low-loss RF MEMS capacitive switches," *IEEE Microw. Guided Wave Lett.*, vol. 8, no. 8, pp. 269–271, Aug. 1998.

[30] C.-H. Chu, W.-P. Shih, S.-Y. Chung, H.-C. Tsai, T.-K. Shing, and P.-Z. Chang, "A low actuation voltage electrostatic actuator for RF MEMS switch applications," *J. Micromech. Microeng.*, vol. 17, p. 1649, Jul. 2007.
[31] H.-C. Lee, J.-Y. Park, and J.-U. Bu, "Piezoelectrically actuated RF MEMS DC contact switches with low voltage operation," *IEEE Microw. Wireless Compon. Lett.*, vol. 15, no. 4, pp. 202–204, Apr. 2005.
[32] J. B. Muldavin and G. M. Rebeiz, "All-metal high-isolation series and series/shunt MEMS switches," *IEEE Microw. Wireless Compon. Lett.*, vol. 11, no. 9, pp. 373–375, Sep. 2001.
[33] J.-M. Huang, K. M. Liew, C. H. Wong, S. Rajendran, M. J. Tan, and A. Q. Liu, "Mechanical design and optimization of capacitive micromachined switch," *Sens. Actuators A, Phys.*, vol. 93, pp. 273–285, Oct. 2001.
[34] M. Angira and K. Rangra, "A novel design for low insertion loss, multi-band RF-MEMS switch with low pull-in voltage," *Eng. Sci. Technol., Int. J.*, vol. 19, pp. 171–177, Mar. 2009.
[35] M. S. Giridhar, A. Jambhalikar, J. John, R. Islam, C. L. Nagendra, and T. K. Alex, "An X band RF MEMS switch based on silicon-on-glass architecture," *Sadhana*, vol. 34, p. 625, Oct. 2009.

K. SRINIVASA RAO (M'17) was born in India. He received the master's and Ph.D. degrees from Central University. He is currently a Professor and the Head of the Microelectronics Research Group, Department of Electronics and Communication Engineering, KL University, Guntur, India. He is working on MEMS Project worth of 40 Lakhs funded by SERB, India. He has published more than 5 papers in the IEEE journals and more than 90 in international research publications (SCI) and presented more than 45 conference technical papers around the world. He has collaborated research work with NIT's, Central Universities, IIT's, and so on. Three Ph.D. Scholars has been Awarded under his guidelines and seven Ph.D. Scholars are currently working with him. His current research interests include MEMS-based reconfigurable antenna's actuators, Bio-MEMS, RF MEMS switches, and RF MEMS filters. He received the Young Scientist Award from the Department of Science & Technology, India, in 2011. He also received UGC Major Research Project, in 2012. He received the Early Career Research Award from SERB, India, in 2016. He is a member of IETE and ISTE.

CH. GOPI CHAND was born in India. He received the bachelor's degree in electronics and communication engineering from JNTUK, in 2016. He is currently pursuing the master's degree in VLSI with the Department of Electronics and Communication Engineering, KL University, Guntur, India. He is currently doing project in MEMS. He published two IEEE and one SCI Journal papers. He has attended two conferences and published a paper, and those papers are under review in Springer.

K. GIRIJA SRAVANI was born in India. She received the bachelor's degree in electronics and communication engineering, and the master's degree in VLSI and embedded systems from JNTUK. She is currently pursuing the Ph.D. degree in MEMS research domain with the National Institute of Technology, Silchar. She is also an Assistant Professor with the Department of Electronics & Communication Engineering, KL University, Guntur, India. She is also working on MEMS project worth of 40 Lakhs funded by SERB, India. She has published more than five IEEE Paper and more than 25 International research publications (SCI) and presented more than five conference technical papers around the world. Her current research interests include MEMS and RF MEMS.

D. PRATHYUSHA was born in India. She received the bachelor's degree in electronics and communication engineering from SCSVMV University, Kanchipuram, in 2016. She is currently pursuing the master's degree in VLSI with the Department of Electronics and Communication Engineering, KL University, Guntur, India. She is currently doing project in area of MEMS. She published two IEEE and one SCI journal papers. She has attended two conference and published a paper, and those papers are under the review in Springer.

P. NAVEENA was born in India. She received the bachelor's degree in electronics and communication engineering from Vignana's University, in 2016. She is currently pursuing the master's degree in VLSI with the Department of Electronics and Communication Engineering, KL University, Guntur, India. She is currently doing project in the area of MEMS. She published one IEEE and one Scopus journal paper. She attended one conference and that paper is accepted in MST journal.

G. SAI LAKSHMI was born in India. She received the bachelor's degree in electronics and instrumentation engineering from JNTUK, in 2016. She is currently pursuing the master's degree in VLSI with the Department of Electronics and Communication Engineering, KL University, Guntur, India. She is currently doing project in the area of MEMS. She published two IEEE and one SCI journal papers. She has attended two conference and published a paper and one paper is under review in Springer.

P. ASHOK KUMAR was born in India. He received the bachelor's degree in electronics and communication engineering from JNTUH, in 2012, and the master's degree in VLSI from KL University, in 2017, where he is currently pursuing the Ph.D. degree in MEMS research domain. He has published 20 International research publications and presented more than five conference technical papers around the world.

T. LAKSHMI NARAYANA was born in India. He received the bachelor's degree in electronics and communication engineering from JNTUK, in 2009, and the master's degree in VLSI from KL University, in 2012. He is currently pursuing the part time Ph.D. degree with KL University, Guntur, India. He is also an Assistant Professor with the Department of Electronics and Communication Engineering, Andhra Loyola Institute of Engineering Technology (ALIET), Vijayawada, India. His current research interests include RF MEMS switches, the Internet of Things (IoT), and digital system design. He is a member of IE and IACSIT.

Secure Boot of Zynq Ultra Scale+ ZCU102 FPGA used in 5G Communications

[1]K. B. S. D. Sai Praneeth, [2]K. Appalaraju, [3]Dr. G. Radha Krishna, [4]Dr. K. B. S. Sastry, [5]CH. Girivardhan, [6]L. Raviteja, [7]N. Avinash,

[1,5,6,7] B.Tech, Final Year, Dept of ECE, ALIET, Vijayawada.
[2]Assistant Professor, Dept of ECE, ALIET, Vijayawada.
[3]Associate Professor, Dept of EE, IITM, Chennai.
[4]Professor, Dept of CSE, ALC, Vijayawada.

Abstract:

The advancements in technology, has paved way towards many milestones in the field of communication. Running on such path the upgraded newly developed 5G: NEWRADIO communication protocol has grabbed all the heads towards it. But, there is always a need to secure the information that is being communicated from one end to another end. Every user likes his/her data to be secured. So this work is an approach to secure the information in various ways. By using bootable files in two ways namely Analog Device Kernel and Petalinux we are securing the hardware components used in 5G communication. Using the files generated with the much utilized processes, secure bootable files will be generated. The Hardware component includes a Zynq ultrascale+ MPSOC and the bootable files are created in such a way that the files will work only on the device because of it being encrypted. As a result only files that are encrypted priorly or secured priorly are only run on the board and the rest will not function.

KEYWORDS: New Radio, MPSOC, Petalinux, Analog Device Kernel.

Introduction:

These days security has become a primary issue because the users always aspire to have their data secured always. Security is basically a complex topic that deals with protection which means to safeguard the information that is being traversed and must be trojan free. So basically the platform level security can be talked under five main aspects such as

1. Trust
2. Information Assurance
3. Cyber Security
4. Anti tamper
5. Protection against all odds.

1. Trust:

Basically Trust focuses on the level and the extent of system solutions, silicon providers, hardware and software. The key area of focus is risk management and trojan free hardware and software. A user basically falls for this aspect and the usual silicon providers must impress in this aspect and must make a trust worthy environment

2. Information Assurance:

Information Assurance is based on basically protecting the information, the data that the device is handling or processing.
This usually is done through cipher and cryptographic techniques such as encryption and authentication.

3. Cyber Security:

Information assurance assures all information in all forms of media whereas cyber security focusses on protecting the information in the cyber domain.

4. Anti tamper:

Anti tamper talks the economic sense which focuses on protecting a customer's intellectual property that is deployed in their product and contained within the device either as hardware and software.

5. Protection against all odds:

As discussed in the above categories protection of data endeavors a scope for the users data to be secured making the information protected and edible for usage.

Literature Survey:

Secure Boot is designed to protect a system against the malicious and trojan code being loaded and executed early in the boot process, before the operating system has been loaded. This is a code that is trojan to our hardware. Usually we secure boot a device by generating a binary file. If an invalid binary is loaded while secure boot is enabled, the user is alerted, and the system will refuse to boot the tampered binary and as a result there will be no damage or trojan based code running in our system. The system here is Zynq UltraScale + MPSoC (ZC102) whose architecture consists of mainly a Programmable logic (PL) and processing system (PS) block.PS is a standalone device which is used for booting. PL is used when there is a continuous

stream of data or when there are tasks that are to be constantly processed in defined time limits. Here the processor is based on Application Processing Unit (APU) which makes use of ARM Cortex- A53 and a Real Time Processing Unit (RPU) which makes use of ARM Cortex- R5. A RAM DDR4 is utilized here. My context talks about APU ARM Cortex-A53 only.

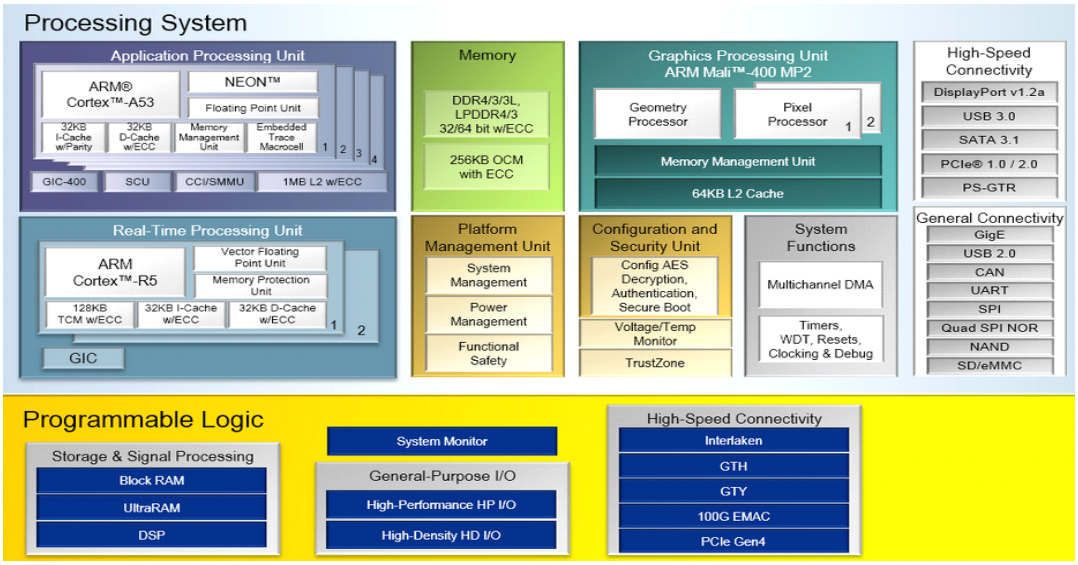

Fig-1: Architecture of Zynq Ultrascale+

Proposed system AND System Architecture:

BASIC BOOT PROCESS:

Depending on the requirements of the system, boot time performance may be critical to the application. So, it's important to know how the system boots, as some operations will only be conducted during the boot process.

The blocks that are involved in the boot process are

- PMU
- CSU
- APU
- PL

The binary components that are used by the blocks are

- Platform Management Unit firmware (PMU)
- Configuration and Security Unit (CSU) boot ROM
- Programming Logic (PL) Bitstream
- First-Stage Boot Loader (FSBL)
- ARM Trusted Firmware (ATF)

There are three main stages in the boot process.

• Pre-configuration stage: The PMU mainly controls the pre-configuration stage which executes the PMU ROM to set up the system. PMU takes care of all of the processes related to wake-up and reset.
• Configuration stage: In this stage, the first-stage boot loader (FSBL) code will be loaded into the on-chip RAM (OCM). It supports both secure and non-secure boot modes. APU will load FSBL.
• Post-configuration stage: Once FSBL execution starts, the Zynq UltraScale+ MPSoC device will enter into the post configuration stage.

We talk about two boot processes
-Non- Secure Boot Process
-Secure Boot Process

Non-Secure Boot Process:

On the initiation of the boot process, the control is basically passed or is released from PMU to the CSU Boot ROM, to determine if authentication is required or not. Then FSBL is loaded into the on-chip memory (OCM) by CSU. If so, the FSBL gets executed on the APU. The FSBL then starts the second stage boot loader called U-Boot. Any process continues with FSBL and SSBL(Secondary Stage Boot loader) which we prefer it to call it as U-Boot. FSBL, PMU firmware and CSU Boot ROM are required to establish hardware root of trust. This is included in just a case to know about the whereabouts of non secure boot process.

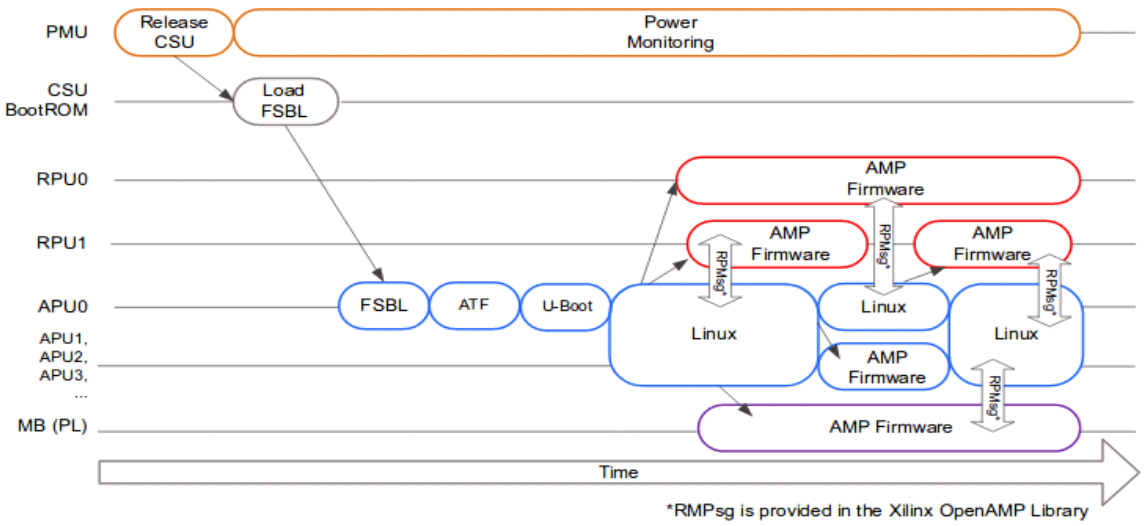

Fig-2: Non-Secure boot process functioning

Secure Boot Process:

As like in the Non-Secure Boot process, here also the control is passed released from PMU to CSU to determine if authentication is required. But here CSU proceeds further only if it passes

the authentication check which is clearly indicated in the secure boot process diagram as tamper monitoring. This is not a part of non-secure boot process as shown above. Basically here the CSU being a security based unit checks for any tampering or trojans and it also checks for any encrypted partitions. If any encrypted partitions are detected by CSU, decryption is performed by CSU and fsbl is loaded into the on-chip memory. The encryption and decryption are such sets we commonly concentrate on.

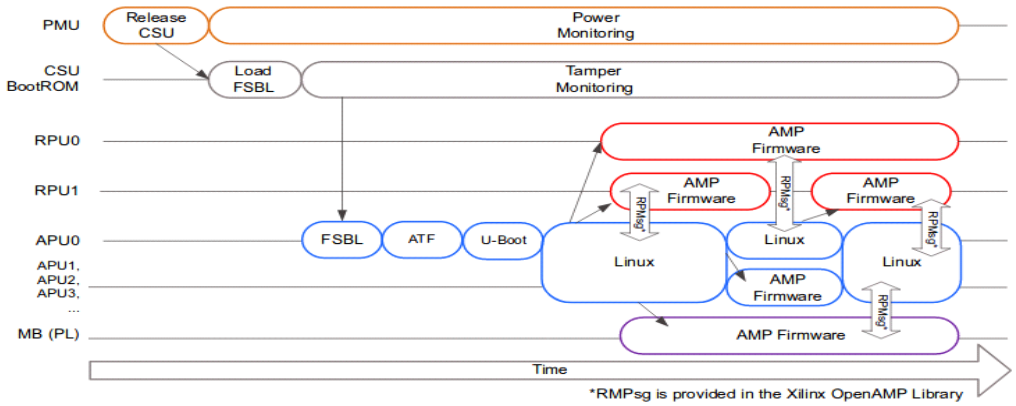

Fig-3: Secure boot process functioning

In case of a Secure Boot process two boot modes are implied:

• Hardware root of trust

• Encrypt only

Both of these are as discussed above.

For secure boot process, if the booting is unsuccessful, only a few commands using JTAG can be used which don't have any connection with the data.

So this is how a secure boot process is initialized and done.

And considering this above mentioned secure boot process we now try to boot sd card and encrypt FPGA (ZCU102) by programming efuses and also how to encrypt a flash programmable drives.

The Primary secure booting consists of the following 6 category of work to be implemented.

• SD card Booting.

• Secure boot on zcu102 board.

Before doing so, lets see what basically secure boot implies and later device encryption as shown below.

Creating Bootable Linux Images:

1) SD card Booting:

There are two different procedures to create a bootable Linux Image.

• Analog Device Kernel

• Petalinux Kernel

Note:
• Petalinux should be installed before the following procedures are followed, since we will be using petalinux toolchain to compile the kernel.
• Along with Petalinux, Vivado should also be installed as we will be generate the bitstream in Vivado.
• Petalinux and Vivado should be sourced before the start of the process.
• All the repositories linux-xlnx, linux-master, u-boot-xlnx, device tree, ARM trusted Firmware and rootfs needs to be downloaded to create a bootable image through both the procedures.

ANALOG DEVICE KERNEL:
Open Vivado and create a project by selecting the required board. The board here is zcu102-evaluation board.
• Create Block design by selecting Zynq UltraScale+ .
• After selecting it, automate the block and make the changes as per the requirements. deselect AXI HPM0FPD and AXI HPM1 FPD in PS-PL Configuration.
• Then check whether the design has any errors by validating the design. If there are no errors, then generate the block design and create a HDL wrapper.
• After creating the wrapper, we need to generate the bitstream.
• But in order to generate a bitstream, we need to synthesis the design and evaluate it.
• Once the bitstream is generated, export the hardware by including the bitstream.
• From the previously downloaded repositories, go to the u-boot-xlnx repository and generate u-boot and u-boot.elf files by opening terminal in that repository and run the following commands.
– export CROSS COMPILE=aarch64-linux-gnu-
– make xilinx zynqmp zcu102 rev1 0 defconfig
– make
• After generating the above mentioned files, go to the linux-master repository and generate the kernel image and required device tree blob by running the following commands.
– export CROSS COMPILE=aarch64-linux-gnu-
– make ARCH=arm64 adi zynqmp defconfig
– make ARCH=arm64

specific device tree blob is required, so run the following commands. For example,
∗ make ARCH=arm64 modules install INSTALL MOD PATH = <path-to-rootfs>
∗ make ARCH=arm64 zynqmp-zcu102-rev10-adrv9371.dtb
– By running these commands, device tree blob of adrv has been generated.
– If any drivers need to be loaded, we will run.,
make ARCH=arm64 menuconfig
to make the additional changes.
• Go to arm trusted firmware repository to generate bl31.elf file, run the following commands.
– export CROSS COMPILE=aarch64-linux-gnu-

– PLAT=zynqmp RESET TO BL31=1
• Using all the above generated files, we will generate a bootable image.
Thus the image formed along with necessary files as discussed above will finalyze our booting of an sd card.

Petalinux Kernel:

• As like in Analog device kernel,we will use Vivado to generate bitstream and export the hardware by including the bitstream and launch SDK.
• Once SDK is launched, We will create an application project for fsbl and pmufw to generate their executable files.
• In order to create a bootable image through petalinux, we need to download board support package(bsp) for the device which we are using.
• As we are using Petalinux 2018.2 version and ZCU102 board, we will download ZCU102-v2018.2.bsp file.
• Using the previously downloaded bsp, we will create a new petalinux project using the command
– petalinux-create -t project -s <path to xilinx-ZCU102-v2018.2 final.bsp>
• A new project will be created named xilinx-ZCU102-v2018.2 and we will go into that directory.
• Using the hdf wrapper generated when hardware is exported, we will configure petalinux according to the requirements using the following command
– petalinux-config –get-hw-description=<path containing wrapper.hdf>/
• As we are using SD Boot mood we will make the following changes in the configuration window.

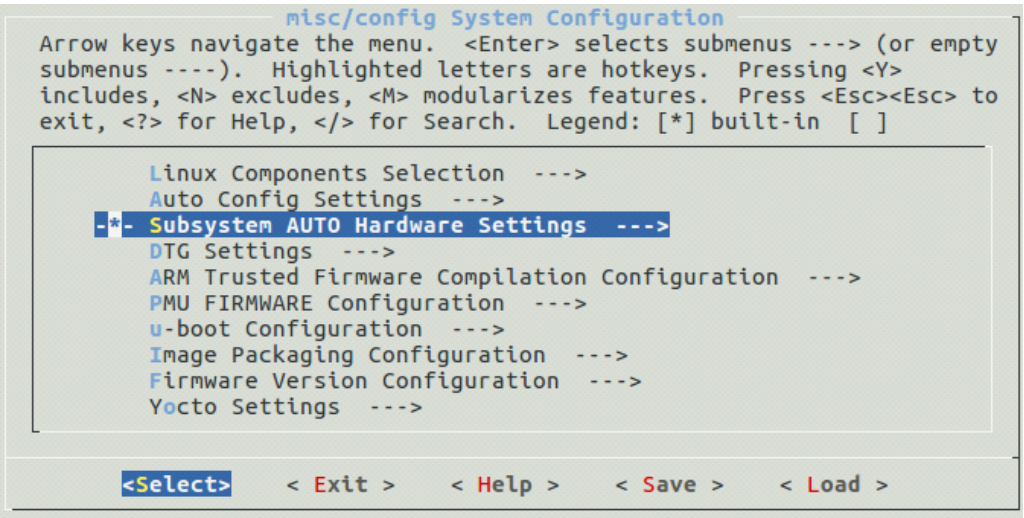

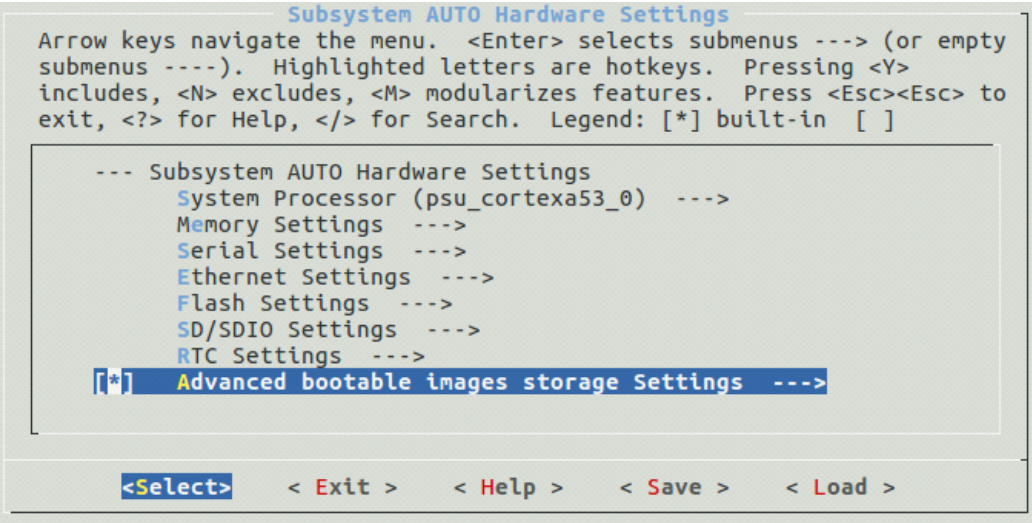

Enter the Advanced bootable image settings where we will have boot image settings and kernel image settings.

• Select primary sd as the storage device in both of these settings as we are using sd card to boot.

• Build the petalinux project to create the kernel image using the following command.

– petalinux-build

• With the above generated files, we can generate a bootable image though petalinux.

Partitioning the SD Card:

• Connect the SD card and find the location using the command 'lsblk'.

• Check for any partitions. If partitions are present delete them.

• Create two new partitions with 90 percent of the memory to one partition and remaining to the other.

• Name the partitions are BOOT and rootfs with the partition with maximum memory named as rootfs.

• Copy the bootable image generated in the both the processes one at a time into the BOOT partition and rootfs from the rootfs downloaded into the other partition.

Thus this is how booting an sd card is done.

Using Device:

• Connect 12V power to the device.

• Set the device to SD Mode and place the SD card containing the files in the SD card slot of the device.

• Check whether the Linux has been loaded on the device.

• If the Linux is loaded, then the device has been booted. Else there might be a problem in the generated files. So try to regenerate them.

2) Secure boot on zcu102 board:

• Using the above discussed procedures and making the required changes, we will generate the Bootable image for secure boot on the board and try to boot it with the corresponding image.

Experimental Results:

• The booting of the device has been done through the SD mode using Analog Device Kernel and Petalinux by creating the bootable images respectively. This way of booting through SD mode is the non-secure boot process which is basic and not recommendable.

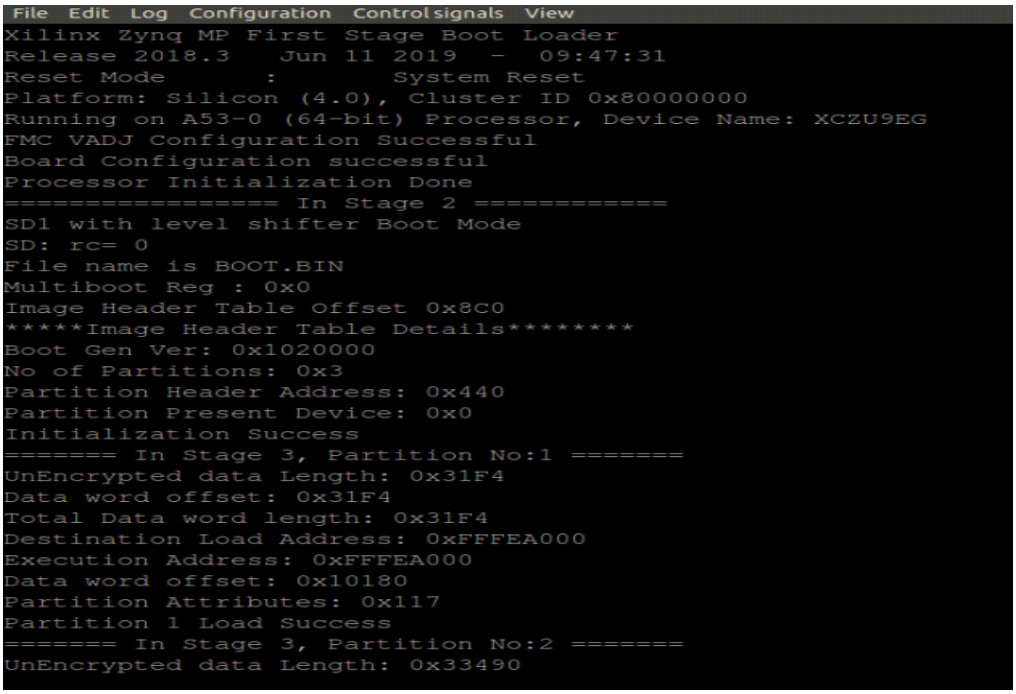

Figure 4: Non-Secure Boot Process

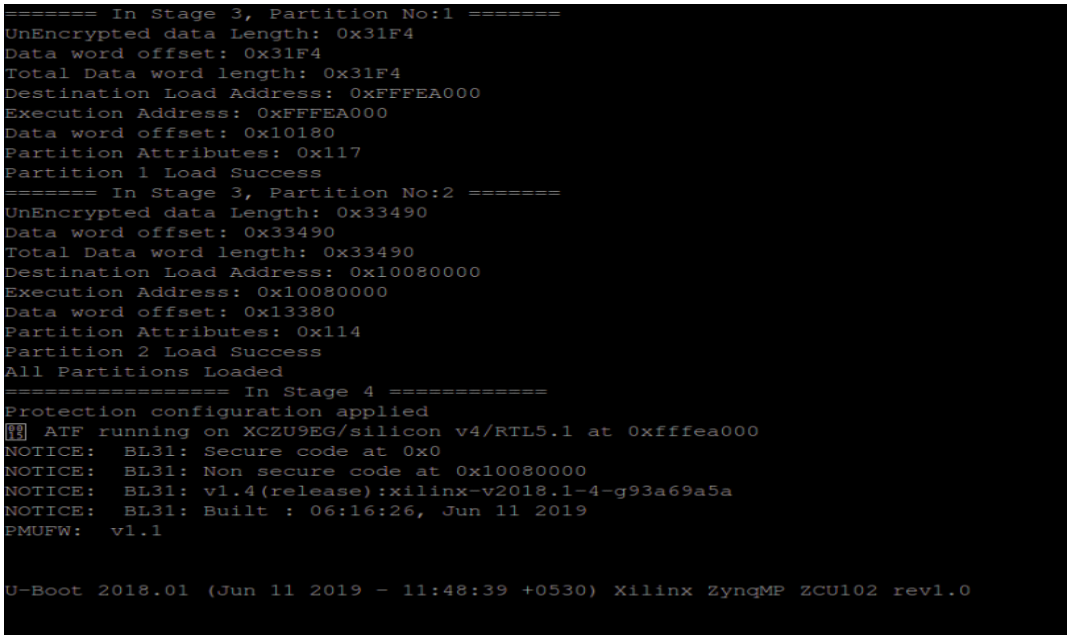

Fig 5: Non-Secure Boot Process

Conclusion:

Secure boot has been initialized by establishing the hardware root of trust according to the requirements and the non secure boot process as shown sbove is not a feasible method to establish security for our device. The files generated during Analog Device Kernel and Petalinux has been secured and the bootable image has been regenerated using both the processes. Using the secure bootable image, the device has been booted and this way of booting through SD mode is the secure boot process. The flash memory on the device has also been programmed through the similar way using both the processes making the necessary changes.

References:

• *Xilinx UG-1228*
• *Xilinx-wiki.atlassian.net-Zynq Ultrascale + MPSOC design Secure Boot*
• *Xilinx.com- Zynq-eg-block (architecture of ZCU102).*

ISSN 2347 - 3983
Volume 8. No. 9, September 2020
International Journal of Emerging Trends in Engineering Research
Available Online at http://www.warse.org/IJETER/static/pdf/file/ijeter39892020.pdf
https://doi.org/10.30534/ijeter/2020/39892020

Performance Analysis and Identification Malicious nodes in the MANET using Trust Based and Auditor Based Methods

Lankapalli V. Ramesh[1*] , Chettiar R. Bharathi[2]
[1]Dept. of Computer Science and Engineering, Vel Tech Rangarajan Dr. Sagunthala R&D Institute of Science and Technology, Chennai, Tamil Nadu. & Dept. of Computer Science and Engineering, ALIET, Vijayawada, A.P, India.
[2]Dept. of Electronics and Communication Engineering, Vel Tech Rangarajan Dr. Sagunthala R&D Institute of Science and Technology, Chennai, Tamil Nadu, India.

ABSTRACT

In this communication, we have analyzed the performance of MANET network by adopting the trust based and the auditor based mechanisms with this we are able to identify the malicious nodes in the network. With the incorporation of performance improved watchdog in the MANET, overall network performance is improved in terms of security and the energy effectiveness. The two mechanisms are involved in the performance improved watchdog to identify the malicious nodes in the network, i.e., in primary level we have combined one-hop with auditor node and in the secondary level we have placed an active watchdog. Because of this to level mechanism all the malicious nodes in the MANET are effectively identified and the security of the system is improved.

Key words: MANET, watchdog, WSN, malicious nodes, auditor node.

1. INTRODUCTION

MANET has emerged into many wireless communication applications because of its great ability and potential. MANET topology is complex in nature since the mobile nod s interconnected across multihop communication paths wher e mobile nodes determine the topology[1-4]. Because of MANET topology dynamic nature the probability of malicious nodes is very high. The primary challenges in the MANET is improving the energy effectiveness and improving the network security.

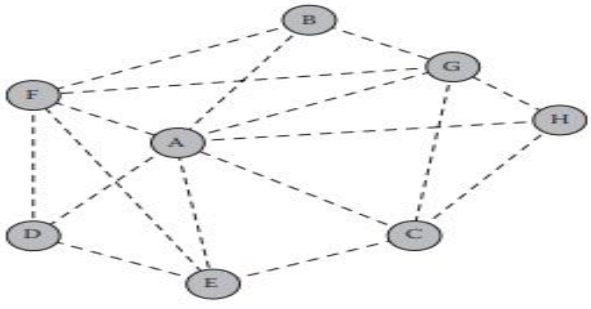

Figure 1: MANET sample model

MANETs are especially susceptible to numerous forms of attacks and threats to security due to maximum sovereignty of the user nodes and absence of any centralized infrastructure. The integration of credibility- and trust-based structures into MANET will help overcome these problems. In a MANET, both nodes may be local, because there is no n etwork connectivity or network back-haul. The network energy effectiveness and security primarily depends on the how effectively we can identify the malicious nodes in the topology. There are so many mechanisms like trust based, audit based and credit based. Active watchdog comes under trust based mechanism to identify the malicious nodes in the network.

In promiscuous mode,watchdog overhears themessage sent b y its neighbors. If it finds any data transmitting anomalies or a malicious data from a neighbor, it may identify the neig hbor as misbehaving.

Condition is generated by taking an extra hop of traversal in which the hostile nodes appear to drop their own packet s while the auditor node attempts to key out nodes that are hostile contributing to their eventual removal. Wireless con nections may be prone to erratic node motions in Mobile A d Hoc Networks (MANET), contributing to regular bond er rors and unexpected topology adjustments. Maintaining the network connection in MANETs can therefore be diffi cult.Mobility control is a significant problem in ad hoc mobi le networks (manets), owing in part to rapidly evolving to pologies of the network[5-8].

A monitor that detects misbehaving nodes and a pathratin g system that allows routinprotocols to stop certain nodes.Th e two methods used to identify and minimize routing misbeh avior are Monitor and Path rate.

The Watchdog identifies nodes that are misbehaving by hold ing a buffer of packets that have just been received. The Deb ugger then tries to check if the next node has already trans mitted a packet by overhearing the adjacent nodes transmiss ions.The Monitor extracts the packet from its buffer as it c oncludes that the next node has forwarded the packet[9-12].

The safeguard system consists of multiple modules, each monitoring module having a different role. The larger t henumber of modules, the greater the amount of resource on

thenode. A likelihood distribution is believed to obey the cr edibi-lity equation.

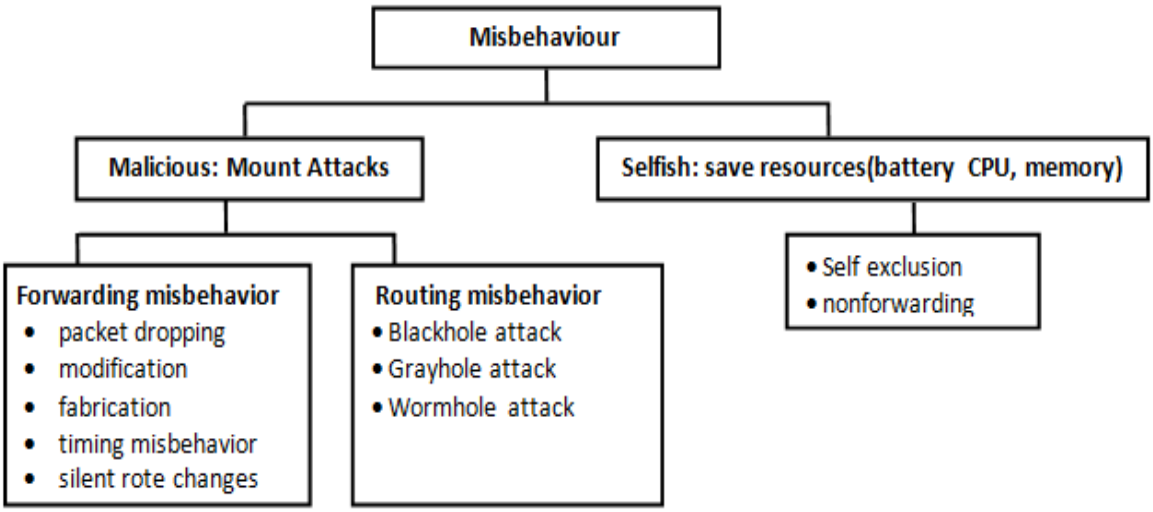

Figure 2: Node's misbehavior in MANET.

2. Related Work

The Watch dog technique is a critical building block for several confidence schemes built to protect wireless sensor networks (WSNs). Unfortunately, this form of procedure requires a great deal of energy and thus effectively reduces WSN's lifetime. The comparison of a transaction is not clear in the case of credibility schemes for MANETs because of the restricted observability and detectability of a mobile node. To track misbehaviour, nodes promiscuously overhear their neighbours conversations.

The part used for this form of monitoring is named Watchdog[9], Monitor [10], or Neighbour Watch[11-12]. Wireless channel instability and energy conservation are the key problems for watchdog systems. Every monitor is located so close to its goal node that communications require minimal resources. In the other hand, mission frequencies are chosen according to the trust worthiness of the goal nodes. the lower frequency of the activities is appropriate when the goal nodes are secure. This saves electricity by cutting back on transmission numbers. The findings also shown effectively that our watchdog optimization strategies will save at least 39.44 percent of energy without losing any reliability (less than 0.06 in terms of confidence precision and robustness), including in certain instances improving safety against some assaults. Several monitoring issues have been found in, such as the challenge of unambiguously detecting that a node is not transmitting packets in the face of collations or in the cases of insufficient transmission capacity.

The watchdog function in CORE is focused on the promiscuous style of wireless node device operations. Moreover, by ranking the end-to-end link the nodes will determine the outcome of a transaction. CONFIDANT utilizes passive acknowledgement not only to check that a node can forward packets, but also as a way of detecting when a packet has been illegitimately changed before forwarding. Marti et al.[13] suggested watchdog and path ratter components for minimizing routing misbehaviour. They found improved performance in MANETs by complementing the DSR protocol with a watchdog for detecting rejected packet forwarding and a path rate for confidence management and routing procedure, ranking any path used.

This makes any node on its routing path to stop malicious nodes. Watchdog measures a node's wrong doing by copying packets to be transmitted to a buffer and tracking the adjacent nodes actions against such packets. Promiscuously the inspector snoops to verify whether the nearby nodes forward the packets without alteration. If the snooped packets fit those in the control node buffer, they will simply be discarded. The packets that persist past a specified among of time in the control node buffer are marked as having been dropped or charged. The node responsible for transmitting the packets would then be identified as a suspect node. If a specified threshold value increases the amount of such failures to forward packets, the guilty node would be marked as a malicious node. Knowledge regarding hazardous nodes is forwarded to the feature pathrater for use in path evaluation [14].

3. Proposed Method

The proposed framework utilizes the Active Watch dog methods for MANET. This procedure is utilized to adjust vitality proficiency and security as far as trust exactness. In this powerful Watch dog enhancement strategy the data sends from source to destination node in the way huge numbers of the nodes are accessible. The neighbour or closest node is considered for data

transmission that is selected Active Watch Dog node with the goal to decrease the consumption of power and increasing security. This Watch dog is called as a Active Watch dog as it continuously monitors all the nodes transactions during data communication.

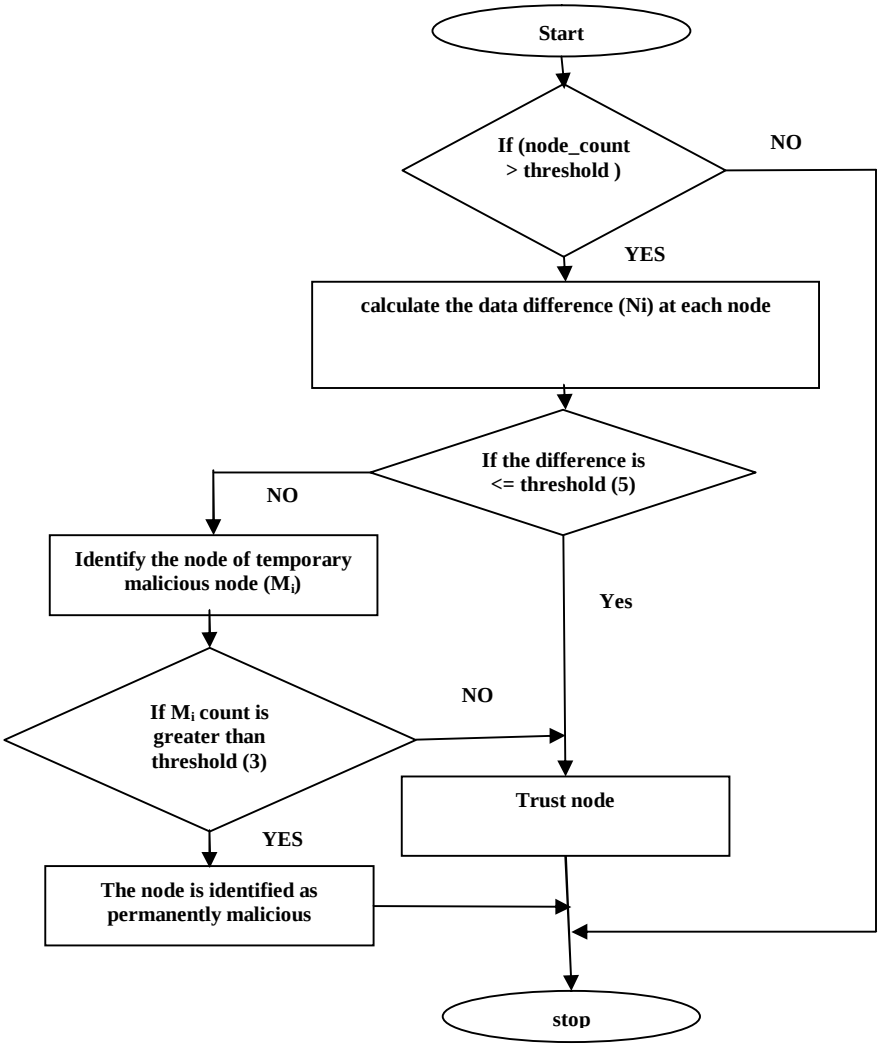

Figure 3: performance improved active watchdog algorithm flowchart.

Initially when a MANET is established, the nodes in the network are dynamic in nature and then the administrator nodes are selected for key generation and maintenance. Among the nodes initially a node having high computational power and energy efficiency is considered as Active Watchdog node and when the communication is initiated, the node will calculate the data packets received by the node and send to neighbor nodes as

Data Transferred (N_i) = Data Received – Data Send to Neighbor node. (1)

Here N_i represents specific node i.
If there is any change in the data transferred level, the node is marked as malicious node and the remaining nodes are certified as trusted nodes. A node whose data transferred rate is less than '5' is certified as trusted nodes. After the communication is completed, the network marks all nodes as trusted or malicious nodes.

The Active watchdog node will be dynamically changed for every transaction and the data maintained by the Active watch dog node should be transferred to the new Active Watchdog node before leaving the MANET. The watch dog node records the malicious activities caused by several nodes and those nodes are not considered from next communications. Extreme objective is to lessen the power consumption by Watch dog.

4. RESULTS AND DISCUSSIONS

4.1. Auditor based

The test was performed in the simulator at NS2. A distincti on was made between the approaches introduced and the pro cedures used during the audit. The findings are illustrated gr aphically below based on the research which focuses on the packet distribution ratio. In the experiment,three approaches were analysed. It includes; Normal Auditor Process process Auditor & One Hop (AOH) system.

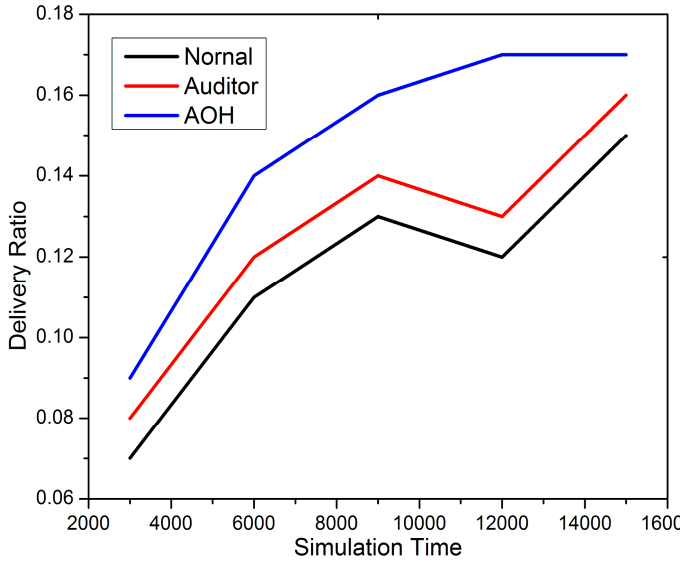

Figure 4: Delivery ratio: 10% malicious nodes.

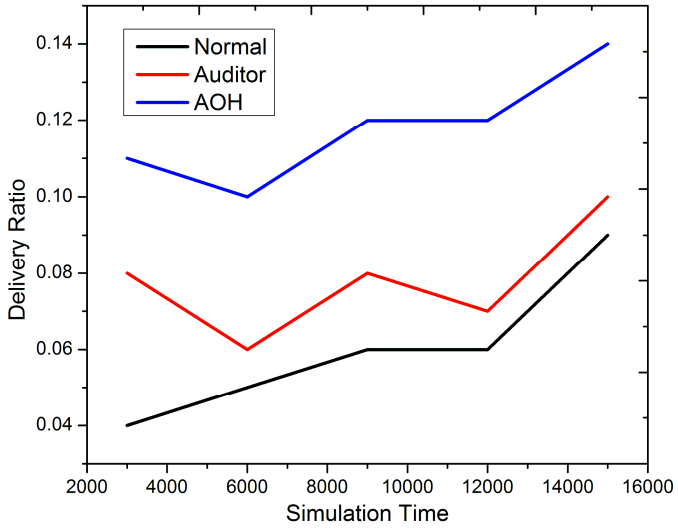

Figure 5: Delivery ratio: 20% malicious nodes.

The distribution ratio is the percentage of the message trans mitted to the message produced.

$$Deliveryratio = \frac{Number\ of\ messages\ delivered}{Number\ of\ messages\ created} \qquad (2)$$

In Figure 3 and Figure 4, the three strategies are compared

and contrasted respectively with 10 percent and 20 percent malicious nodes. With the rising amount of malicious nodes, the amount of packet droppings is growing. The AOH approaches thus demonstrates significantly improved distribution efficiency than other approaches. In the proposed AOH process, the pause in data transmission between the nodes is minimized and is shown in the figure below.

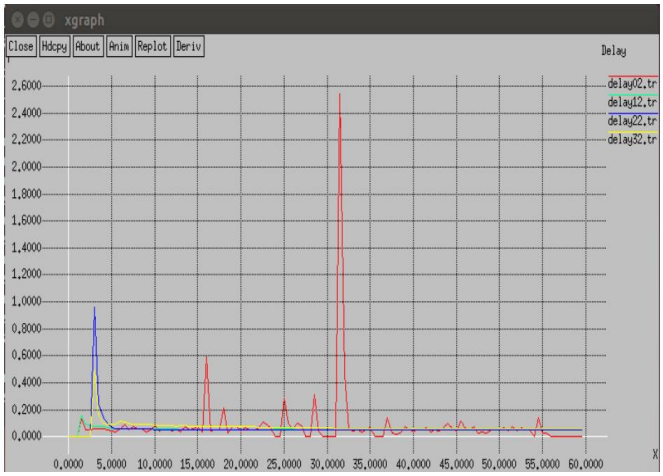

Figure 6: Delay in data transfer.

The two mechanisms are involved in the performance improved watchdog to identify the malicious nodes in the network, i.e., in primary level we have combined one-hop with auditor node and in the secondary level we have placed an active watchdog. The approach suggested eliminates the failure of the packets during contact. Any node essentially has the auditor and on e hop method if it has forwarded the packets to next nodes w ithout any miscellaneous intervention. Reduction of packet l oss rate is seen in the figure below.

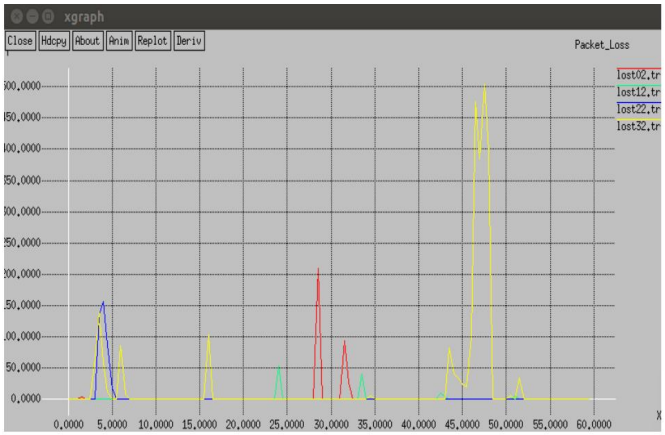

Figure 7: Packet loss reduction.

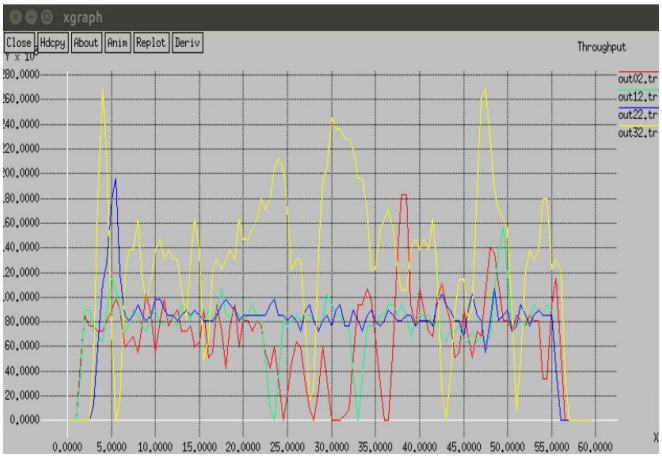

Figure 8: Throughput level.

The suggested system efficiency is higher than the current methods. The findings indicate that the AOH approach suggested demonstrates greater and better efficiency than conventional methodologies.

4.2. Trust based

The proposed method is implemented in NS2 and the proposed watchdog method is implemented which provides security to the data and identifies the malicious nodes in the MANET for secure data transmission. The parameters used for establishing a MANET is depicted in Table 1.

Table 1: Experimental Parameters

PARAMETER	VALUES
Simulation time	5 mins
Topology size	1000 X 1000
No. of nodes	10
No. of clusters	2
Node mobility	0 to 20m/sec
Routing Protocol	DSDV
Frequency	11 MHz
Traffic type	CBR
MAC	IEEE 802.11
Mobility model	Random Waypoint
Max. no. of packets	10000
Pause time	10sec

The overall communication overhead of the proposed active watch dog method is compared with the traditional watch dog method and the results are depicted in figure 9.

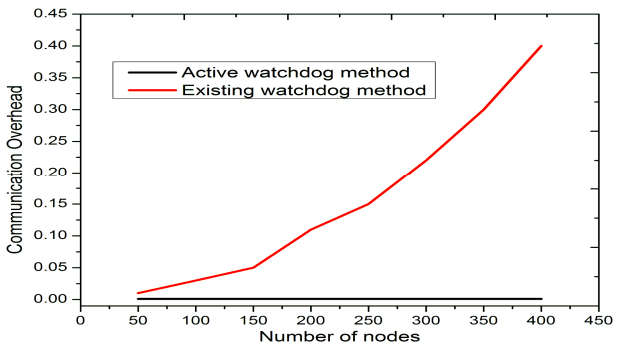

Figure 9: Communication Overhead levels.

After the MANET is established and the watch dog node is selected, the identification rate of the malicious nodes are depicted in Figure 10.

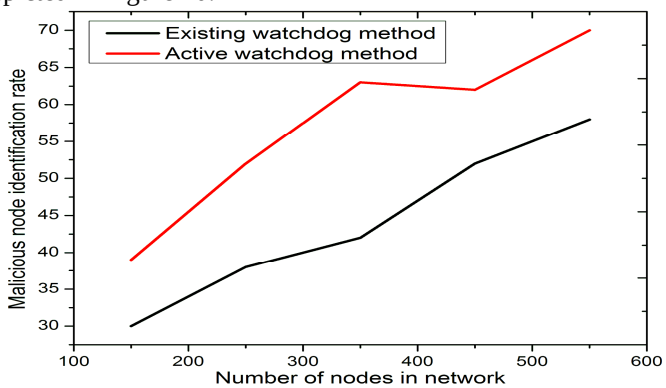

Figure 10: Active Watch dog system identification rate.

The proposed active watch dog method effectively identifies the malicious nodes in the network. As all nodes are trusted nodes, the packet delivery rate in the proposed method is high as shown in Figure 11.

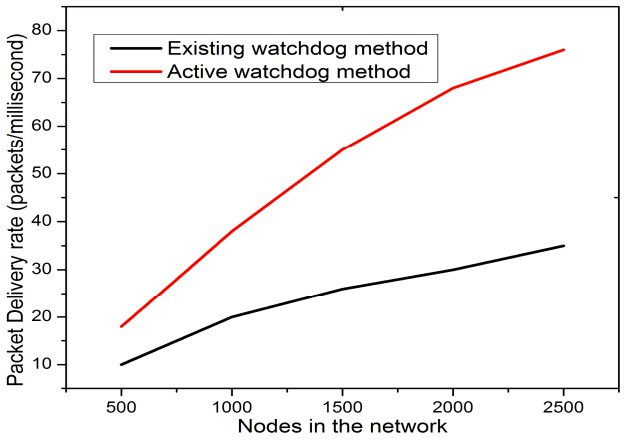

Figure 11. Packet Delivery Ratio.

The energy consumption rate of the proposed method is very less when compared to traditional methods. The energy consumption rate is depicted in Figure 12.

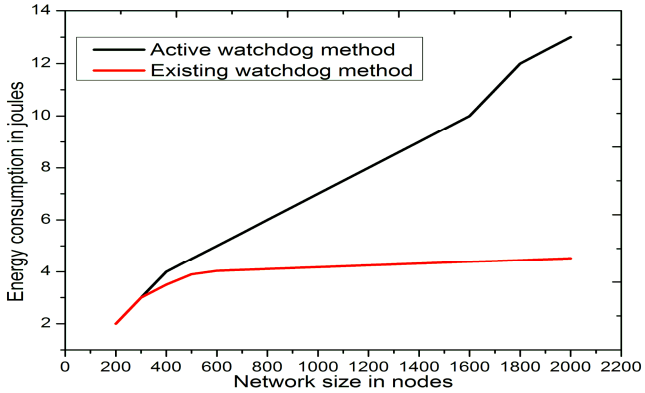

Figure 12: Energy Consumption Ratio.

The data security level of the proposed method is illustrated in Figure 13.

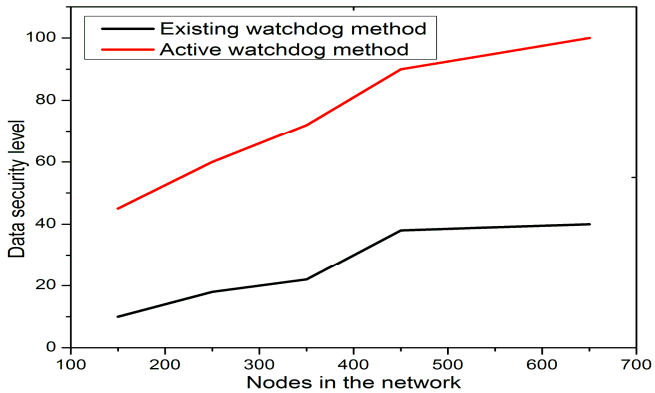

Figure 13: Data Security Level.

5. CONCLUSION

we have improved the watchdog performance in the MANET network which is able to identify the malicious nodes in the network. With the incorporation of performance improved watchdog in the MANET, overall network performance is improved in terms of security and the energy effectiveness. The two mechanisms are involved in the performance improved watchdog to identify the malicious nodes in the network, i.e., in primary level we have combined one-hop with auditor node and in the secondary level we have placed an active watchdog. Because of this to level mechanism all the malicious nodes in the MANET are effectively identified and the security of the system is improved.

REFERENCES

1. Anto Ramya S.I, **Mobile ad-hoc Netwoek Topology and its Algorithms**, *International Journal of Trend in Research and Development*, 2(5), Pp 16-21, 2015.
2. Narendra Reddy .P, Vishnuvardhan C.H, Ramesh.V, **Routing Attacks in Mobile ad-hoc Networks**, 2(5), pp 360-367, 2013.
3. O.Kachirski, R. Guha, **Effective Intrusion Detection Using multiple sensors in Wireless ad-hoc Networks**, *International Conference on System Sciences*, 2003.
4. S. Marti, T.J. Giuli, K. Lai, and M.Baker. **Mitigating routing misbehavior in mobile ad hoc networks,** *6th MobiCom, Boston*, Massachusetts, 2000.
5. Evgeniy Ivanovich Trubilin, Svetlana Ivanovna Borisova, Vladimir Ivanovich Konovalov, Mikhail. **Experimental Studies of Parameters of Pneumatic Slot Sprayer**, *International Journal of Emerging Trends in Engineering Research*, 8(1), 2020.
6. Karti kumar Srivasta, Avinash Tripathi, Anjnesh kumar Tiwari, **Secure Data Transmission in MANET Routing Protocol,** *International Journal of Computer Technology& Applications*, 3(6), pp 1915-1921, 2012.
7. R. Bhuvaneshwari, G. Nalina keerthana, A. Rachel Roselin, **Improving Selfish Node Detection In MANET Using A Collaborative Watchdog**, *International Journal of Advanced Research Trends in Endineering and Technology*, vol 3, No 15, pp 17-21, 2016.
8. Harold Robinson, M. Rajaram, E. Golden Julie, S. Balaji. **Detection of Black Holes in MANET Using Collaborative Watchdog with Fuzzy Logic**, *International Journal of Computer and Information Engineering*, Vol 10, No 3, pp 622-628, 2016.
9. Sun B, Guan Y, Chen J, Pooch U. **Detecting black hole attack in mobile ad hoc networks**, *IEEE Transactions on Vehicular Technology*, 490-495, 2003.
10. Buttyan L, Hubaux JP. **Stimulating cooperation in self organizing mobile ad hoc networks**. *ACM/Kluwer Mobile Netw.* PP-579-592, 2003.
11. Zhong S, Chen J, Yang YR. **Sprite: A simple cheat-proof, creditbased system for mobile ad-hoc networks**. *In Proc. IEEE INFOCOM Conf* , PP-1987- 1997, 2003.
12. Balakrishnan K, Deng J, Varshney P. **TWOACK: Preventing selfishness in mobile ad hoc networks**. *In Proc. IEEE Wireless Commun. Netw. Conf* , pp: 2137-2142, 2005.
13. Hennadii Khudov, Irina Khizhnyak, Fedor Zots, Galina Misiyuk, Oleksii Serdiu. **The Bayes Rule of Decision Making in Joint Optimization of Search and Detection of Objects in Technical Systems**, *International Journal of Emerging Trends in Engineering Research*, 8(1), 2020.
14. JKR Sastry, M Trinath Basu, **Multi-Factor Authentication through Integration with IMS System**, *International Journal of Emerging Trends in Engineering Research*, 8(1), 2020.

Secure Data Communication Using Internet Of Things

C.R.Bharathi, Vejendla. Lakshman Narayana, L.V. Ramesh

Abstract: The rapid growth of the Internet of Things (IoT) has led to a situation where individual manufacturers develop their own communication protocols and frameworks that are often incompatible with other systems. Part of this is due to the use of incompatible communication hardware, and part is due to the entrenched proprietary systems. This has created a heterogeneous communication landscape, where it is difficult for devices to coordinate their efforts. To remedy this, a number of IoT Frameworks have been proposed to provide a common interface between IoT devices. There are many approaches to common frameworks, each with their strengths and weaknesses, but there is no clear winner among them. This proposed work presents a virtual network testbed for implementing smart home IoT Frameworks. The components of various IoT architecture proposals as well as the novel component, the Thing Management System, were combined, consolidated and related to each other to develop the Holistic IoT Architecture Framework. Subsequently, it was shown that the specifications of the architecture framework are suitable to guide the implementation of a prototype.

Index Terms: Secure data Tansfer, Internet of Things, Security, Protocols, IoT Devices..

1 INTRODUCTION

The Internet of Things (IoT) is growing quickly. Some estimates indicate that there will be 13.5 billion consumer IoT devices in use by 2020, and that excludes business and industrial applications [1]. The term “Internet of Things” has become something of a buzzword, but what does it mean? In this case, the name is somewhat apt. IoT devices are “things” that are networked together and connected to the Internet. This can be anything from an array of hundreds of weather sensors to a coffee maker that starts brewing when your alarm clock goes off. Home automation is not a new thing, but until recently it has been done primarily by amateur tinkerers and hobbyists rigging something together to make it work. Now, there are thousands of devices that are sold Internet-ready; they can often be set up in a few minutes by a layperson. Among these devices are things like door locks, lightbulbs, thermostats, security cameras and practically anything else you can imagine. IoT platforms aim to enable secure connectivity between things, be it humans, sensor-devices or services of some sort, and are regarded as an integral part of any IoT architecture. These platforms provide software suites and various cloud based services to facilitate the operation of “IoT endpoints” to enable communication between various, different devices. Currently available IoT platforms provide functions for device and application management (PaaS), data aggregation, transformation, storage and management as well as some means to analyze and visualize data streams [12]. However, if a user wants to use the functionalities of any IoT platform he must adhere to some constraints imposed by IoT platforms.

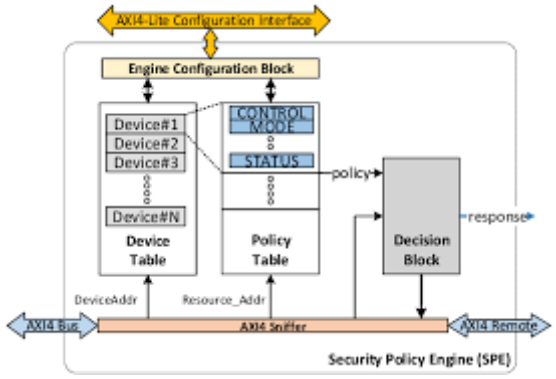

Fig 1. *Block diagram for a typical IoT configuration.*

The reason for this lack of dynamics lies in the low level of abstraction of IoT application development required by current IoT platforms. On the one hand, users have visual tools (e.g. node based and visual development tools) to create an application. On the other hand, users need to directly address devices (e.g. provide a one-to-one mapping of an “IoT endpoint” node to a device talking to that endpoint [13]. Thus, adding a new device requires creation of a new node on the respective application, provision of a device-node mapping, manually normalizing of the retrieved data and redeploying the application on the IoT platform. The goal of this proposed work is to illustrate how IoT devices can be accurately simulated. Specifically, the focus is on communication between devices, so a particular emphasis will be on building simulated devices that can accurately mimic their real-life counterpart to the extent possible. Further, this proposed work will illustrate how these simulated devices can be combined in simulated networks using an IoT Framework. This will provide a base from which new devices can be simulated and different frameworks can be implemented [14]. Ultimately, having simulated smart home devices on a simulated smart home network can serve as a testbed for IoT Frameworks. Different frameworks can be applied to the same devices to see how well they interact, students can study protocols and interact with modeled devices in a virtual setting and developers can test how new devices and applications interact with already-modeled setups. This architecture framework aims to combine the various IoT architecture proposals to a common denominator. Based on this holistic framework literature

- *Associate Professor , Department of ECE, Vel Tech Rangarajan Dr.Sagunthala R&D Institute of Science & Technology, Avadi , Chennai , Tamil Nadu. E-mail: crbharathi@veltechuniv.edu.in*
- *Assoc.Professor, Department of IT, Vignan’s Nirula Institute of Technology and Science for Women, Peda Palakaluru, Guntur-522009,Andhra Pradesh, India.. E-mail: lakshmanv58@gmail.com*
- *Assoc.Professor, CSE Department, Andhra Loyola Institute of Engineering & technology, Vijayawada, Andhra Pradesh, India. E-mail: lvarunramesh@gmail.com*

proposing implementations, technologies or behaviours for each component of the architecture can be examined and the definition of each architectural component can be refined [15]. An increased level of abstraction in the development process addresses both issues of IoT development platforms mentioned previously. The lack of system dynamics (e.g. because a user cannot simply add new IoT endpoints with respective devices on-the-fly) is reduced by introducing and specifying high level architectural elements. These high-level elements, their behavior, interfaces, roles and data structures are to be defined by the holistic architecture framework [16]. These high-level elements could then be used by users in the development process.

2 LITERATURE SURVEY

The Internet of Things is deemed to have a high impact on every aspect of everyday life. It is envisioned to be the integration of the physical world into the digital world or vice versa. Enterprises and countries alike have already assessed the importance of IoT and started to move into strategically advantageous positions to exploit the most value of IoT. For example, the National Intelligence Council (2008) sees IoT as one of the Five Disruptive Civil Technologies, which has a potentially important impact on the country´s interests out to 2025. Ahmad et al [3] also assumes that by 2020 there will be a black market worth of five billion US$ for fake sensor data, which emphasizes the need for information reputation and evaluation techniques in IoT. For IoT to be successful, a trust environment has to be established. As already elaborated on and highlighted again in this chapter, IoT can very well be considered as a hyped technology. With IoT being a relatively new concept and under high coverage of both media, businesses and researchers it is not surprising that the term itself and related research field lack a commonly accepted and established definition. Designed to operate in a noisy environment, the 802.15.4 standard uses Direct-Sequence Spread Spectrum (DSSS), which minimizes the effect of random noise [17]. This makes it ideal for a cluttered environment like one would expect in IoT applications. These underlying features of 802.15.4 as a whole provide a stable foundation, on top of which several different protocols have been built. Many of these protocols are ideally suited to smart home applications because they provide communication within a house-sized area and use very low power [18]. Both ZigBee and 6LoWPAN are built on the same physical and data-link layers, this means they use the same physical hardware. The difference is the implementation of the higher levels. ZigBee has been around longer and is supported by more devices, but 6LoWPAN is easier to use with the Internet [19]. This is because 6LoWPAN is essentially a low power version of IPv6. This mimicking of IP formatting allows it to communicate with things outside the local network using a simple gateway. ZigBee can also do this, but the conversion required at the gateway is more involved and adds overhead [20]. 6LoWPAN has an adaptation layer that is between the link layer and network layer, and it provides a few solutions that allow for IPv6 traffic to translate to 6LoWPAN traffic relatively seamlessly. It fragments and reorders IPv6 packets to account for smaller packet size, compresses the headers as much as possible, allows for stateless addressing, and provides infrastructure for mesh routing [21]. This sounds like a lot, but it's significantly easier than translating from Bluetooth or ZigBee to and from IPv6. Fenn et al. [10] also say that IoT can and will not merely be a global EPC system based on RFID. More different and kinds of things will be added and connected by using different communication technologies. Things will need to be managed and organized into networks (e.g. Wireless Sensing and Actuating Networks (WSAN)). The upcoming heterogeneity was already considered in the formal definition of IoT provided by the International Telecommunications Union (2005). The definition states that the internet cannot only connect anyone at any time and any place but anything at any time and any place. This view focuses more on the networking aspect of IoT and Atzori et al. (Atzori et al. 2010) name it the Internet Oriented Vision of IoT. Having agreed upon these ideas and with IoT gaining significant interest, both research and industry tried to develop relevant use cases for IoT.

3 PROPOSED METHOD

The first step in simulating a smart home network will be to simulate a home network. As prior research shows, there are many ways to do this, and any of them can work. This proposed work proposes to use Virtual Machines running on the same physical host computer to handle the networking. This has a few benefits. First, by running locally, the local network can be simulated while offline, which allows for more flexible development. Also, by using Virtual Machine software like VMware or VirtualBox, the Physical and Data Link layer implementations are handled by the hypervisor. This allows the development process to work at the Network level and up. Lastly, VM environments can be easily translated to cloud services to host the network on the cloud after its development period [22]. The next step will be to simulate individual IoT devices. Simulating IoT Devices is a little open-ended because of the abundance of different IoT devices available. However, as proof of concept, it would be helpful to simulate a couple of very different devices and illustrate how existing simulations can be tied together via a framework. One device will be a LIFX lightbulb, which works in an unencrypted fashion using a published UDP packet format for commands [23]. Because the packet specification is documented, this proposed work will show how documentation like this can be translated to a simple program. Another important concept for simulating a smart home network is to be able to incorporate other simulations [24]. To accomplish this, the Nest Home Simulator will be used and incorporated into the wider simulation. Finally, an IoT framework will be implemented on the simulated network, communicating with the simulated devices. The main point of this research is to show how device simulations can be leveraged to simulate an IoT framework. To this end, another Virtual Machine will be made that will serve as an OpenHAB server to coordinate simulated devices. If the devices are properly simulated, and the OpenHAB bindings are correct, then this part may be very simple. However, if functionality is lacking or partial, extensive configuration editing may be necessary. Since OpenHAB has hundreds of bindings and an active development community, there should be sample resources if problems are encountered.

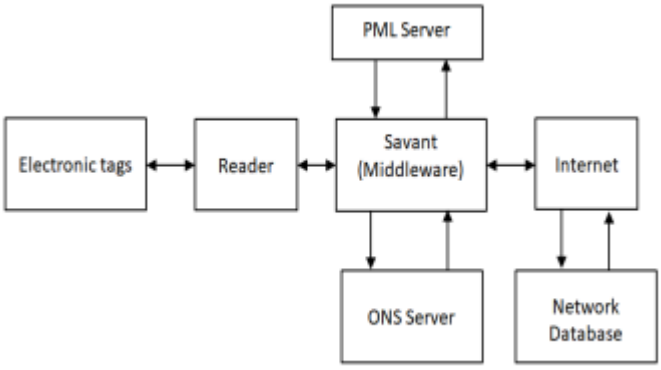

***Fig 2**: RFID Working Principle of Internet of Thing*

In the daily life, things are generating so fast. The RFID technology has already been implemented everywhere. In Figure 3, it shows the size of RFID chip in 2016. It can exist in anything, such like the passport, library cards or even some advanced business application. Moreover, RFID is commonly applied in the asset tracking industry to manage the huge information that is happening around the world. This technology helps user to improve the efficiency and transparency in the supply chain among all the aspects.

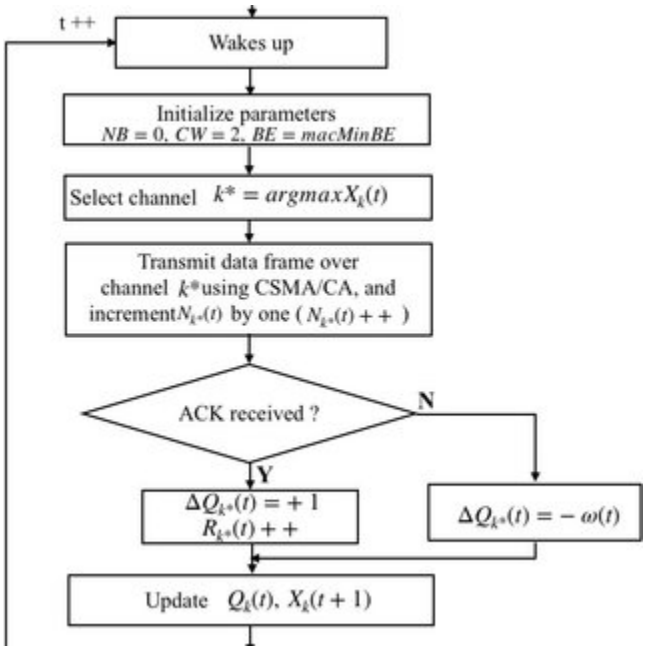

***Fig 3:** Flow Char for Cognitive IoT*

As mentioned before, cognitive IoT is trying to mimic the way the human brain works. It involves self-learning system. The cognitive IoT does not have a certain module, but it should start with certain basic knowledge block. With the IoT application implement, all the data that have been collected to the IoT platform should be stored and personalized in order to fit the different need in real life acquirement.

Extended service providers provide value added services to sensor data consumers, this component of S2aaS as the most “intelligent” one, as it provides a wide variety of different services, where each requires different methods, technologies and approaches to transform the requirements set by sensor data consumers to sensing tasks and analyze as well as present the resulting data. One of the main tasks of an extended service provider is to formalize the informal sensing requests of sensor data consumers into sensing tasks. These tasks must be generic and universal, so that each sensor publisher can understand and handle the task. Additionally, extended service providers need to be able to support different sensing paradigms as well as incentive mechanisms. Based on the Generic IoT Architecture, described and the individual components of IoT architecture proposals are analyzed in order to work out common concepts of each component´s tasks, responsibilities and requirements. Therefore, each IoT architecture proposal is examined and the descriptions, requirements, tasks and intentions of each component are categorized based on the Generic IoT Architecture’s layers. Ideally, each component is described with each layer of the Generic IoT Architecture in mind, which would mean in conclusion that the component is holistically described. A holistic IoT architecture component description will consider the Business-, Application-, Middleware-, Network- and Perception Layer of the Generic IoT Architecture. The previous method suggested the so-called Thing Management System as a tool for Owners to manage their Things and share their Things services with Publishers. By being responsible for these tasks, the Thing Management System is expected to ensure the privacy and anonymity of a Thing´s Owner while simultaneously simplifying the management of these Things. In order to be able to design and develop such a system guiding principles or a domain model need to either be developed or identified and transferred from other research or problem domains

4 RESULTS

The main deliverable was definitely the bulb simulation, but its development also necessitated the creation of a control interface that allowed users to send specific packets and make sure the simulation was behaving correctly. This ended up being a couple of different program. The first program merely sent one packet and printed the replies. This was useful for testing corner cases or probing unexpected behavior.

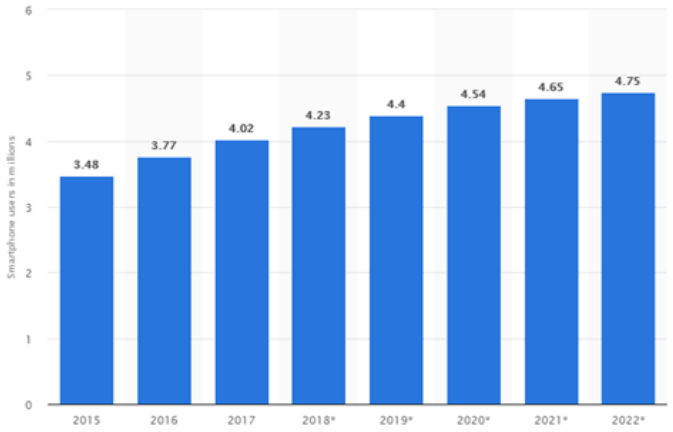

***Fig 4**: IOT users Range*

Figure 5 shows its simple interface.

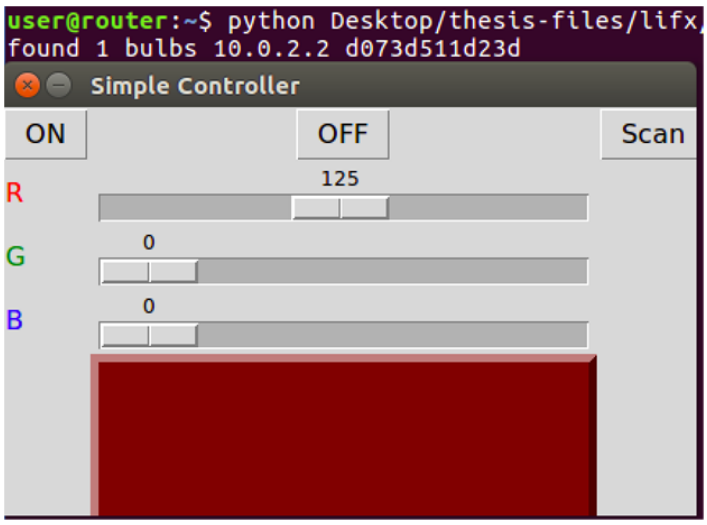

Fig 5: *User interface for control.py.*

A simple GUI controller was also made that performed the base functions of controlling power, color and performing device discovery.

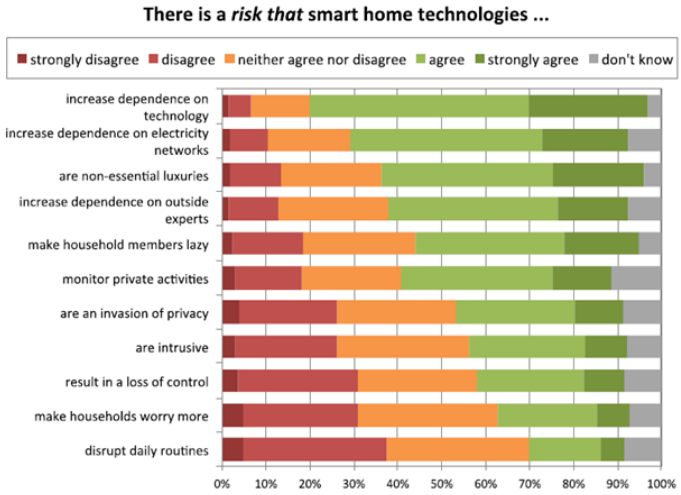

Fig 6: *smart home technologies risks.*

5 CONCLUSION

The primary goal of this proposed work was to illustrate how simulating IoT devices and networks can be used to build a testbed for IoT Frameworks. First, a home network was successfully simulated using separate Virtual Machines for each node on the network, linked together through a VM hypervisor. The network behaved just like a home network, relying on the Router VM for things like DNS lookup and routing outside the network. Next, IoT Device simulations were implemented. A simulation of a LIFX Smart Lightbulb was implemented from scratch based on published specifications and observations from actual hardware. Also, the existing Nest Home Simulator was employed to illustrate that other simulations can be incorporated. Finally, the OpenHAB IoT Framework was implemented in the simulated network on simulated devices, being unable to distinguish the simulations from actual hardware. The successful implementations of the simulations and Framework shows the feasibility of using a simple testbed like this to perform analysis of Frameworks without having to use physical hardware. In its current form, this can be used as a tool for observing an accurate representation of the network traffic generated by the simulated devices. This can be an educational tool to illustrate how IoT devices work under the hood, or it can be used for more practical applications like optimization.

REFERENCES

[1]. Abdelwahab, S. et al., 2015. Cloud of Things for Sensing as a Service: Sensing Resource Discovery and Virtualization. In 2015 IEEE Global Communications Conference (GLOBECOM). IEEE, pp. 1–7. Available at: http://ieeexplore.ieee.org/document/7417252/.

[2]. Abdelwahab, S. et al., 2014. Enabling Smart Cloud Services Through Remote Sensing: An Internet of Everything Enabler. IEEE Internet of Things Journal, 1(3), pp.276–288. Available at: http://ieeexplore.ieee.org/document/6817547/.

[3]. Ahmad, A. et al., 2016. Model-Based Testing as a Service for IoT Platforms. In Leveraging Applications of Formal Methods, Verification and Validation: Discussion, Dissemination, Applications. Cham: Springer International Publishing, pp. 727–742. Available at: http://link.springer.com/10.1007/978-3-540-88479-8.

[4]. ARM Limited, 2017. CoAP. Available at: http://coap.technology/ [Accessed January 28, 2017].

[5]. Ashton, K., 2009. That “Internet of Things” Thing. RFID Journal. Available at: http://www.itrco.jp/libraries/RFIDjournal-That Internet of Things Thing.pdf [Accessed February 15, 2017].

[6]. Atzori, L., Iera, A. & Botterman, M., 2009. Internet of Things: an early reality of the Future Internet, Available at: http://scholar.google.com/scholar?hl=en&btnG=Search&q=intitle:Internet+of+Things+:+an+early+reality+of+the+Future+Internet#0.

[7]. Bradner, S., 1997. Key words for use in RFCs to Indicate Requirement Levels. , pp.1–3. Available at: https://www.ietf.org/rfc/rfc2119.txt.

[8]. Burke, J. et al., 2006. Participatory sensing. In ACM SenSys 2006. Boulder, Colorado, USA. Available at: http://citeseerx.ist.psu.edu/viewdoc/summary?doi=10.1.1.122.3024.

[9]. Emmerich, W., Aoyama, M. & Sventek, J., 2008. The impact of research on the development of middleware technology. ACM Trans Softw Eng Methodol, 17(4), pp.1–48. Available at: http://discovery.ucl.ac.uk/46712/.

[10]. Fenn, J. & LeHong, H., 2011. Hype Cycle for Emerging Technologies, Stamford. Available at: http://www.gartner.com/newsroom/id/2819918%5Cnhttps://www.google.be/url?sa=t&rct=j&q=&esrc=s&source=web&cd=9&cad=rja&uact=8&ved=0ahUKEwjxzq6mnr3JAhUGPQ8KHR-WBGgQFghRMAg&url=http://isites.harvard.edu/fs/docs/icb.topic1360759.files/hype_cycle_for_emerging_t.

[11]. Ferna et al., 2015. Ubiquitous Computing and Ambient Intelligence. Sensing, Processing, and Using Environmental Information J. M. García-Chamizo, G. Fortino, & S. F. Ochoa, eds., Cham: Springer International Publishing. Available at:

http://link.springer.com/10.1007/978-3-642-35377-2.

[12]. Lakshman Narayana Vejendla and Bharathi C R ,(2018),"Multi-mode Routing Algorithm with Cryptographic Techniques and Reduction of Packet Drop using 2ACK scheme in MANETs", Smart Intelligent Computing and Applications, Vo1.1, pp.649-658. DOI: 10.1007/978-981-13-1921-1_63 DOI: 10.1007/978-981-13-1921-1_63

[13]. Lakshman Narayana Vejendla and Bharathi C R, (2018), "Effective multi-mode routing mechanism with master-slave technique and reduction of packet droppings using 2-ACK scheme in MANETS", Modelling, Measurement and Control A, Vol.91, Issue.2, pp.73-76. DOI: 10.18280/mmc_a.910207

[14]. Lakshman Narayana Vejendla , A Peda Gopi and N.Ashok Kumar,(2018)," Different techniques for hiding the text information using text steganography techniques: A survey", Ingénierie des Systèmes d'Information, Vol.23, Issue.6,pp.115-125 DOI: 10.3166/ISI.23.6.115-125

[15]. A Peda Gopi and Lakshman Narayana Vejendla (2018), "Dynamic load balancing for client server assignment in distributed system using genetic algorithm", Ingénierie des Systèmes d'Information, Vol.23, Issue.6, pp. 87-98. DOI: 10.3166/ISI.23.6.87-98

[16]. Lakshman Narayana Vejendla and Bharathi C R,(2017),"Using customized Active Resource Routing and Tenable Association using Licentious Method Algorithm for secured mobile ad hoc network Management", Advances in Modeling and Analysis B, Vol.60, Issue.1, pp.270-282. DOI: 10.18280/ama_b.600117

[17]. Lakshman Narayana Vejendla and Bharathi C R,(2017),"Identity Based Cryptography for Mobile ad hoc Networks", Journal of Theoretical and Applied Information Technology, Vol.95, Issue.5, pp.1173-1181. EID: 2-s2.0-85015373447

[18]. Lakshman Narayana Vejendla and A Peda Gopi, (2017)," Visual cryptography for gray scale images with enhanced security mechanisms", Traitement du Signal,Vol.35, No.3-4,pp.197-208. DOI: 10.3166/ts.34.197-208

[19]. A Peda Gopi and Lakshman Narayana Vejendla, (2017)," Protected strength approach for image steganography", Traitement du Signal, Vol.35, No.3-4,pp.175-181. DOI: 10.3166/TS.34.175-181

[20]. Lakshman Narayana Vejendla and Bharathi C R,(2016),"Secured Key Production and Circulation in Mobile Ad hoc Networks Using Identity Based Cryptography", International conference on Engineering and Technology, Vol.1, pp.202-206.

[21]. A Peda Gopi and Lakshman Narayana Vejendla, (2019)," Certified Node Frequency in Social Network Using Parallel Diffusion Methods", Ingénierie des Systèmes d' Information, Vol. 24, No. 1, 2019,pp.113-117.. DOI: 10.18280/isi.240117

[22]. Lakshman Narayana Vejendla and A Peda Gopi, (2019)," Avoiding Interoperability and Delay in Healthcare Monitoring System Using Block Chain Technology", Revue d'Intelligence Artificielle , Vol. 33, No. 1, 2019,pp.45-48.

[23]. Yang, D. et al., 2012. Crowdsourcing to smartphones. In Proceedings of the 18th annual international conference on Mobile computing and networking - Mobicom '12. New York, New York, USA: ACM Press, p. 173. Available at: http://dl.acm.org/citation.cfm?doid=2348543.2348567.

[24]. Yasrab, R. & Gu, N., 2016. Multi-cloud PaaS Architecture (MCPA): A Solution to Cloud Lock-In. In 2016 3rd International Conference on Information Science and Control Engineering (ICISCE). IEEE, pp. 473–477. Available at: http://ieeexplore.ieee.org/document/7726205/.

[25]. Fleisch, E., 2010. What is the Internet of Things? An Economic Perspective (white paper). In Zurich, Switzerland: Auto-ID Labs, pp. 1–27.

[26]. Fremantle, P. et al., 2014. Federated Identity and Access Management for the Internet of Things. In 2014 International Workshop on Secure Internet of Things. IEEE, pp. 10–17. Available at: http://www.scopus.com/inward/record.url?eid=2-s2.0-84926431695&partnerID=40&md5=2726c8ea5ad90df99e17f7e8099ca815.

[27]. Gamma, E. et al., 1995. Design Patterns Elements of Reusable Object-Oriented Software, Boston, MA, USA: Addison-Wesley Longman Publishing Co., Inc. Available at: http://www.cs.up.ac.za/cs/aboake/sws780/references/patternstoarchitecture/Gamma-DesignPatternsIntro.pdf.

[28]. Vaishnavi, V. & Kuechler, W., 2007. Design Science Research Methods and Patterns, Boca Raton, USA: Auerbach Publications. Available at: http://www.crcnetbase.com/doi/book/10.1201/9781420059335.

[29]. Vazquez, J.I. & Lopez-de-ipina, D., 2008. Social Devices : Autonomous Artifacts That Communicate on the Internet. In pp. 308–324.

[30]. Velosa, A., Schulte, R.W. & Lheureux, B.J., 2015. Hype Cycle for the Internet of Things, 2015. , (July), pp.1–69. Available at: http://www.gartner.com/document/3098434?ref=solrAll&refval=161158590&qid=40f7a175899f78812787998fff35a614.

[31]. Wortmann, F. & Flüchter, K., 2015. Internet of Things. Business & Information Systems Engineering, 57(3), pp.221–224. Available at: http://link.springer.com/10.1007/s12599-015-0383-3.

[32]. Zachariah, T. et al., 2015. The Internet of Things Has a Gateway Problem. In Proceedings of the 16th International Workshop on Mobile Computing Systems and Applications - HotMobile '15. New York, New York, USA: ACM Press, pp. 27–32. Available at: http://web.eecs.umich.edu/~prabal/pubs/papers/zachariah15gateway.pdf.

Disquisition of Sentiment Inquiry with Hashing and Counting Vectorizer using Machine Learning Classification

Kota Venkateswara Rao, M. Shyamala Devi

Abstract*: With the rapid growth in technology, analysis of feedback and reviews by the customers in companies and industries becomes a major challenge. The profit of the company mainly depends on the customer satisfaction. The view of the customer can be analyzed only through feedback. The review analysis can be utilized for the prediction of current sales and future sales of the company. With this overview, the paper aims in performing the sentiment analysis of the movie review. The Type of comment given by the customer is predicted and categorized into classes. The sentiment Analysis on movie Review dataset taken from the KAGGLE leading Dataset repository is used for implementation. The categorization of sentiment classes is achieved in five categories. Firstly, the target count for each sentiment is portrayed. The Resampling is done for equalizing the target sentiment count. Secondly, the extraction of sentiment feature words for each target is displayed and the data cleaning is done with Term Frequency Inverse document Frequency method. Thirdly, the resampled dataset is then fitted with the various classifiers like Multinomial Naives Bayes Classifier, Logistic Regression Classifier, KNearest Neighbors Classifier, Bernoulli Naives Bayes Classifier, Complement Naives Bayes Classifier, Nearest Centroid Classifer, Passive Aggressive Classifier, SGD Classifier, Ridge Classifier, Perceptron Classifier. Fourth, the feature extraction is done with Hashing Vectorizer and Counting Vectorizer. The vocabulary features are also displayed from the dataset. Fifth, the Performance analysis of clasifier is done with metrics like Accuracy, Recall, FScore and Precision. The implementation is carried out using python code in Spyder Anaconda Navigator IP Console. Experimental results shows that the sentiment prediction and classification done by Ridge classifier is found to be effective with Precision of 0.89, Recall of 0.88, FScore of 0.87 and Accuracy of 89%.

***Index Terms*: Accuracy, Recall, FScore, Sentiment and Precision**

I. INTRODUCTION

Sentiment processing and analysis is a major task in the field of Prediction of language processors [1]. Nowadays companies are moving forward to spend for feedback analysis of their customers and employees for forecasting the company revenue and turnover. with the technological growth, the customers are giving their feedback in the social media which is viewed and influenced by the people all over the country. So analyzing the online reviews of their products becomes a challenging issue for the manufacturing companies. The purpose of the sentiment analysis is to analyze and determine the type of sentiment of the text review messages given by the customers. Each text given by the customers are highly sensitive with non standard grammatical text structures and with low or high integrity. So determining the polarity and the sensitiveness of the feedback review is a challenging task. This makes the application of machine learning and natural language processing to come into picture for predicting the sentiment analysis on movie reviews.

The paper is prepared with the Section 2 exploring the literature survey and related works. Section 3 deals with the proposed work continued with execution details and performance comparison in Section 4. Finally the paper is concluded in Section 5.

II. RELATED WORK

A. Literature Review

The sentiment classification method mainly focuses on machine learning methods along with the natural language processing. The large scale sentiment dictionary is designed to enhance the sentiment classification method and performance. The machine learning methods were used based on the parsing and sentiment information to predict the sentiment type [2].

The phrase level emotion detection model is designed to predict the implicit emotion detection and sentiment classification [3]. The Support vector machine is used along with the probability output text weighting in order to enhance the sentiment classification accuracy metric [4].

The LSTM (Long Short-Term Memory) is a kind of neural network which can detain long term text dependencies in a sentence sequence. This is done by designing the block of storage units and it is used to update the block information in the storage and to make the permanent memory thereby enhancing the depth calculation of the sentiment tree analysis [5]. The Long Short-Term Memory combined with the target dependent variable is used to improve the prediction accuracy [6]. The concept of forward tree-structured long short-term memory networks is designed to enhance the sentiment classification [7].

Revised Manuscript Received on November 06, 2019.

Kota Venkateswara Rao, Research Scholar**,** Computer Science and Engineering, Vel Tech Rangarajan Dr. Sagunthala R&D Institute of Science and Technology, Avadi, Chennai, TamilNadu, India.

M. Shyamala Devi, Associate Professor, Computer Science and Engineering, Vel Tech Rangarajan Dr. Sagunthala R&D Institute of Science and Technology, Avadi, Chennai, TamilNadu, India.

With the enormous applications of machine learning techniques, the deep neural network combined with attention model to improvise the sentiment prediction analysis by focusing on classification relationships and text evaluation [8]. A neural architecture is proposed to exploit the instant available sentimental lexicon resources like lexicon-driven contextual attention and contrastive co-attention to improve the sentimental classification accuracy [9]. A capsule network is designed with activity vector denoting the sentiment instantiation parameters. Single lower level capsule tends to send its corresponding output to higher level capsules having a large scalar product and sentiment prediction from the lower level capsule [10]. Three methods were proposed to enhance the dynamic routing process to improve the interruption of some error capsule that may contain redundant information or it would have not been trained properly. This makes the sentiment prediction in capsule network with high precision and accuracy [11]. An effective routing technique that effectively reduces the computational complexity in case of multiple sentiment analysis data sets [12]. The attention mechanism is incorporated with the capsule sentiment network for the extraction of relation in a multi-label learning framework [13]. The Capsule network for sentiment type analysis is done in domain adaptation scenario with adaptation of semantic rules to improve the comprehensive sentence representation learning [14]. The concept of classification and its methodology is learnt [15]-[33].

III. PROPOSED WORK

A. Preliminaries

B. Term Frequency Inverse Document Frequency

There are various methods to find the TFDF and it has two metrics namely Term Frequency and Inverse document frequency. The Term frequency represents the amount of time a particular term appears on a page by dividing it with number word in a text document and it is given below.

$$Term\ Frequency = \frac{1 + \log(Keyword\ Count)}{log(total\ word\ count\ in\ the\ document)}$$

The formula for finding the inverse document frequency is given below.

$$IDF = \log of \frac{1 + \text{Total Documents}}{Documents\ with\ keywords}$$

C. Proposed System Architecture

The overall framework of this paper is shown in Fig. 1

IV. PROPOSED WORK

In this work, the counting vectorizer and hashing vectorizer are used to predict the sentiment type of the people using their movie reviews. Our contribution of this work is pointed out here.

(i) Firstly, the target count for each sentiment is portrayed. The Resampling is done for equalizing the target sentiment count.

(ii) Secondly, the extraction of sentiment feature words for each target is displayed and the data cleaning is done with Term Frequency Inverse document Frequency method.

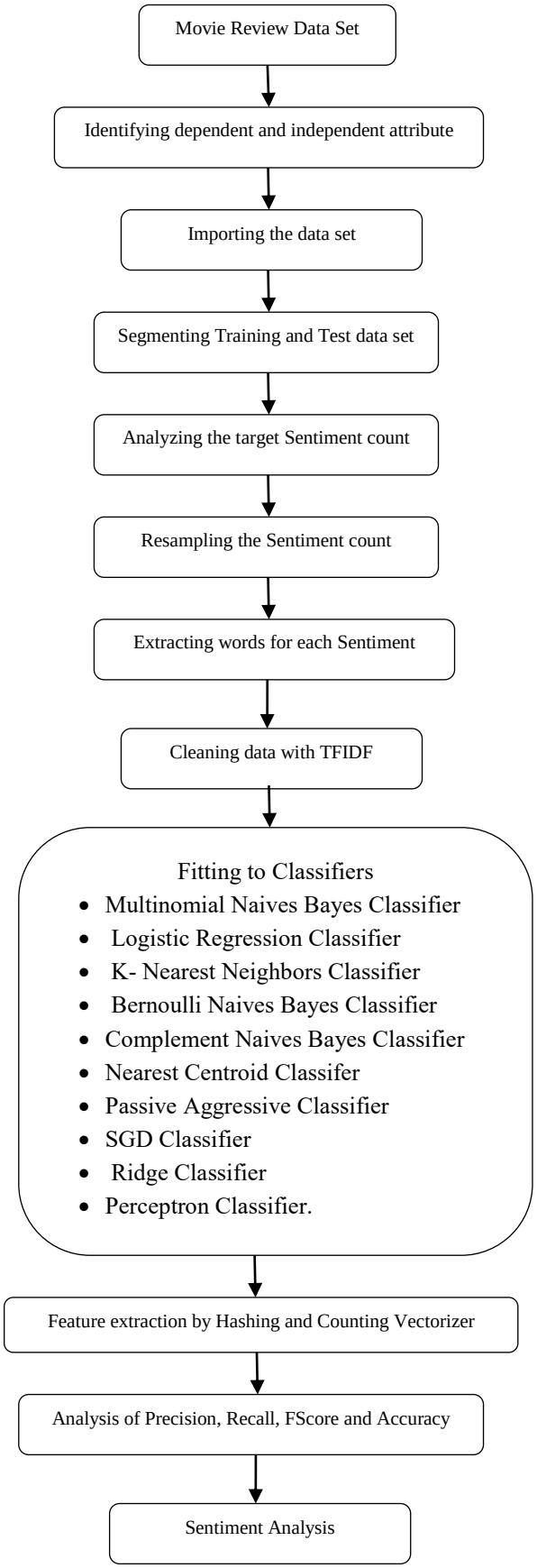

Fig. 1 System Architecture of Sentiment Analysis

(iii) Thirdly, the resampled dataset is then fitted with the various classifiers like Multinomial Naives Bayes Classifier, Logistic Regression Classifier, KNearest Neighbors Classifier, Bernoulli Naives Bayes Classifier, Complement Naives Bayes Classifier, Nearest Centroid Classifer, Passive Aggressive Classifier, SGD Classifier, Ridge Classifier, Perceptron Classifier.

(iv) Fourth, the feature extraction is done with Hashing Vectorizer and Counting Vectorizer. The vocabulary features are also displayed from the dataset.

(v) Fifth, the execution assessment of clasifier is done with metrics like Accuracy, FScore, Recall and Precision

V. IMPLEMENTATION AND PERFORMANCE ANALYSIS

A. Sentiment Analysis and Prediction

The Sentiment Analysis for Movie Reviews Dataset extracted from Kaggle ML dataset warehouse is used for implementation with 2 independent variable and 1 Sentiment dependent variable. The dataset consists of 1,56,060 individual's data. The attribute are shown below.

1. Sentence Id
2. Phrase
3. Sentiment - Dependent Attribute

The type of sentiment of the dependent variable is shown below.

B. Performance Analysis

The target count for each sentiment dependent variable of the Sentiment Analysis of the Movie Review dataset is shown in the fig 2.

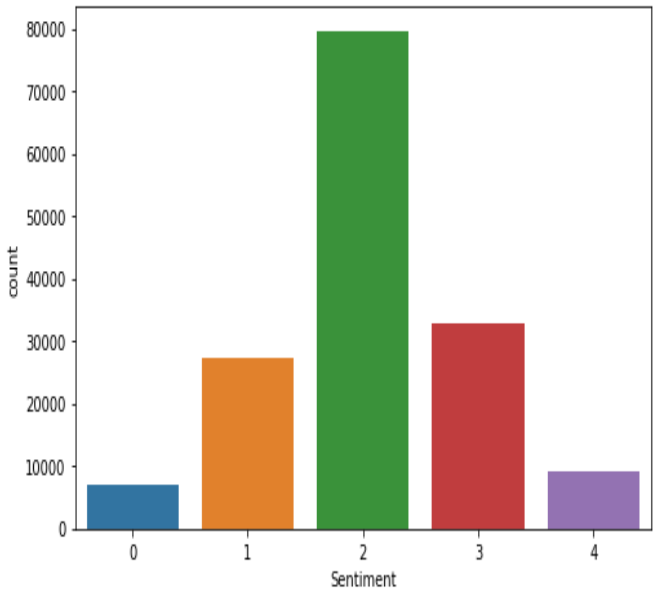

Fig. 2. Target count of sentiment dependent variable

The resampling of the target count for each sentiment dependent variable of the Sentiment Analysis of the Movie Review dataset is done and is shown in fig 3.

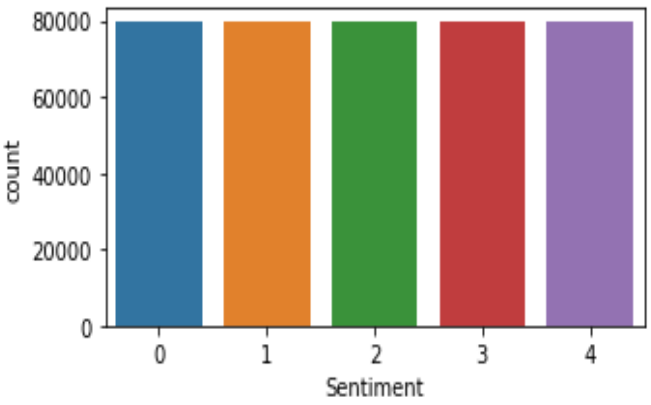

Fig. 3. Resampling of Target count of sentiment dependent variable

The extraction of sentiment feature words for negative target is displayed and is shown in fig 4.

Fig. 4. Sentiment feature words for negative target

The extraction of sentiment feature words for somewhat negative target is displayed and is shown in fig 5.

Fig. 5. Sentiment feature words for somewhat negative target

The extraction of sentiment feature words for neutral target is displayed and is shown in fig 6.

Fig. 6. Sentiment feature words for neutral target

The extraction of sentiment feature words for somewhat positive target is displayed and is shown in fig 7.

Fig. 7. Sentiment feature words for somewhat positive target

The extraction of sentiment feature words for positive target is displayed and is shown in fig 8.

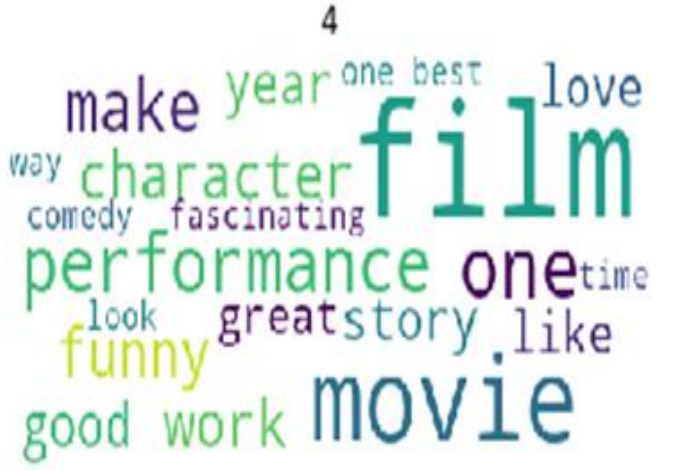

Fig. 8. Sentiment feature words for positive target

The starting and ending time of Term Frequency and inverse document frequency is shown in Fig. 9.

end	float	1	1563088823.119122
expected	Series	(39015,)	Series object of pandas.core.series module
predicted	int64	(39015,)	[1 3 2 ... 3 3 2]
start	float	1	1563088812.6347218

Fig. 9. Starting and ending time of TFIDF

The resampled dataset is then fitted with the various classifiers like Multinomial Naives Bayes Classifier, Logistic Regression Classifier, KNearest Neighbors Classifier, Bernoulli Naives Bayes Classifier, Complement Naives Bayes Classifier, Nearest Centroid Classifer, Passive Aggressive Classifier, SGD Classifier, Ridge Classifier, Perceptron Classifier. The obtained confusion matrix for each of the classifiers is shown from Fig. 10 – Fig. 19.

cm_MultinomialNB_Feature - NumPy array

	0	1	2	3	4
0	99	865	810	19	1
1	37	2152	4560	171	0
2	5	821	17858	1072	5
3	0	73	4450	3615	85
4	0	6	662	1434	215

Fig. 10. Confusion Matrix of Multinomial NBayes Classifier

cm_logreg_Feature - NumPy array

	0	1	2	3	4
0	293	815	656	29	1
1	125	2128	4460	198	9
2	22	851	17850	1003	35
3	3	103	4339	3525	253
4	0	12	520	1274	511

Fig. 11. Logistic Regression Confusion Matrix

cm_KNN_Feature - NumPy array

	0	1	2	3	4
0	403	500	877	14	0
1	273	1712	4821	106	8
2	75	914	18028	706	38
3	14	149	5931	1851	278
4	1	19	1278	643	376

Fig. 12. KNN Confusion Matrix

cm_BernoulliNB_Feature - NumPy array

	0	1	2	3	4
0	416	743	610	24	1
1	348	2437	3879	235	21
2	118	1239	16929	1353	122
3	15	227	4301	3163	517
4	3	14	735	1038	527

Fig. 13. Bernoulli N Bayes Classifier Confusion Matrix

cm_ComplementNB_Feature - NumPy array

	0	1	2	3	4
0	745	817	195	28	9
1	821	3797	1867	374	61
2	1161	3282	11240	3462	616
3	132	435	1977	4645	1034
4	12	29	168	1117	991

Fig. 14. Confusion Matrix of Complement NBayes Classifier

cm_NearestCentroid_Feature - NumPy array

	0	1	2	3	4
0	803	585	273	89	44
1	844	2871	2482	476	247
2	712	2779	13551	1979	740
3	120	618	3103	3010	1372
4	13	94	350	694	1166

Fig. 15. Confusion Matrix of Nearest Centroid Classifier

cm_PassiveAggressiveClassifier_Feature - NumPy array

	0	1	2	3	4
0	726	821	232	13	2
1	630	3270	2762	222	36
2	226	1860	15627	1876	172
3	40	256	3001	3880	1046
4	5	22	220	1006	1064

Fig. 16. Passive Aggressive Confusion Matrix

cm_SGDClassifier_Feature - NumPy array

	0	1	2	3	4
0	125	156	1495	18	0
1	62	367	6359	123	9
2	19	178	19213	315	36
3	3	32	6908	1154	126
4	0	6	1502	523	286

Fig. 17. SGD Confusion Matrix

cm_RidgeClassifier_Feature - NumPy array

	0	1	2	3	4
0	595	902	272	24	1
1	404	3139	3139	222	16
2	113	1478	16553	1554	63
3	10	195	3276	4152	590
4	3	14	259	1231	810

Fig. 18. Ridge Confusion Matrix

cm_PerceptronClassifier_Feature - NumPy array

	0	1	2	3	4
0	716	791	237	49	1
1	735	3153	2570	438	24
2	308	2160	14131	3010	152
3	34	295	2724	4338	832
4	7	42	225	1198	845

Fig. 19. Perceptron Confusion Matrix

The performance metrics and its prediction analysis is shown in the Table 1 - Table. 2. The parameters that are used to measure the performance of the sentiment type prediction is shown in Fig. 22 – Fig. 25.

Table. 1 Analysis of Precision and Recall Score parameters

Classifier	Precision	Recall
Multinomial NBayes Classifier	0.74	0.73
Logistic Regression Classifier	0.81	0.80
K Nearest Neighbors Classifier	0.84	0.82
Bernoulli Naives Bayes Classifier	0.79	0.78
Complement N Bayes Classifier	0.76	0.75
Nearest Centroid Classifer	0.77	0.76
Passive Aggressive Classifier	0.87	0.86
SGD Classifier	0.86	0.84
Ridge Classifier	0.89	0.88
Perceptron Classifier	0.79	0.77

The Starting and ending time for the hashing vectorizer is shown in Fig. 20.

```
In [22]: print("Starting Processing time = ",start)
    ...: print("End Processing time = ",end)
Starting Processing time =  1563124772.7563655
End Processing time =  1563124783.7343657

In [23]: print("HashingVectorizer finished in: ", end - start)
HashingVectorizer finished in:  10.978000164031982
```

Fig. 20. Processing time of hashing vectorizer

The Starting and ending time for the Counting vectorizer is shown in Fig. 21.

```
In [88]: end = time.time()
    ...: print("Starting Processing time = ",start)
    ...: print("End Processing time = ",end)
    ...: print("CountVectorizer finished in: ", end - start)
Starting Processing time =  1563126651.1747735
End Processing time =  1563126655.4137735
CountVectorizer finished in:  4.239000082015991
```

Fig. 21. Processing time of Counting vectorizer

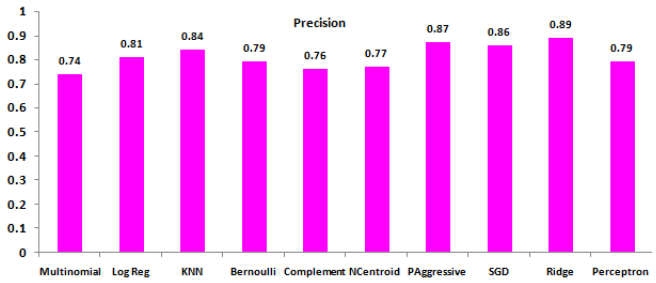

Fig. 22. Precision of Classifiers

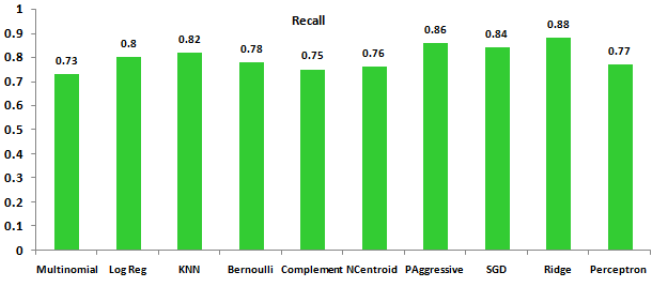

Fig. 23. Recall of Classifiers

Table. 1 Analysis of FScore parameters

Classifier	FScore	Accuracy (%)
Multinomial Naives Bayes Classifier	0.72	74
Logistic Regression Classifier	0.80	80
K Nearest Neighbors Classifier	0.83	84
Bernoulli Naives Bayes Classifier	0.77	78
Complement Naives Bayes Classifier	0.76	77
Nearest Centroid Classifer	0.75	76
Passive Aggressive Classifier	0.84	83
SGD Classifier	0.85	84
Ridge Classifier	0.87	89
Perceptron Classifier	0.76	73

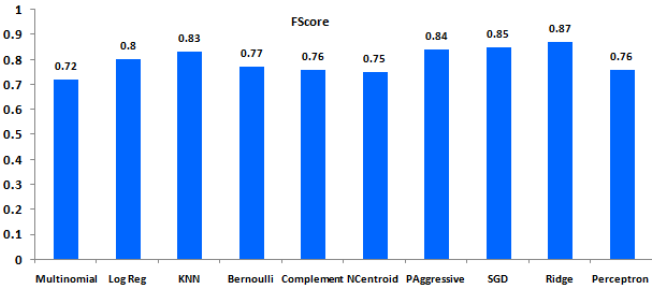

Fig. 24. FScore of Classifiers

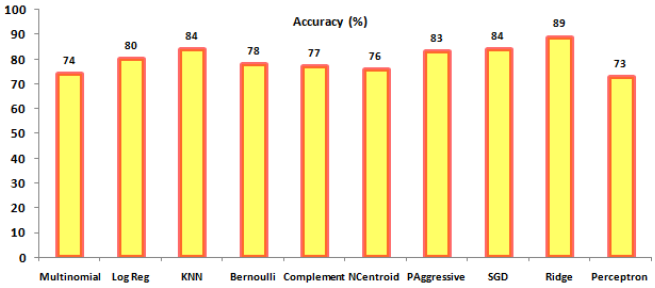

Fig. 25. Accuracy of Classifiers

VI. CONCLUSION

This paper analyzes the sentiment type prediction by using various classification algorithms. The extraction of feature words for each of the sentiment target variable is found and is displayed. The Resampling of the dataset is also done based on the target variable. Experimental results shows that the sentiment prediction and classification done by Ridge classifier is found to be effective with Precision of 0.89, Recall of 0.88, FScore of 0.87 and Accuracy of 89%.

REFERENCES

1. B. Liu, ``Sentiment analysis and opinion mining," Synth. Lectures Hum.Lang. Technol., vol. 5, no. 1, pp. 1_167, May 2012.
2. Z. Y. Yan, Q. Bin, S. Q. Hui, and L. Ting, ``Large-scale sentiment lexicon collection and its application in sentiment classification," J. Chin. Inf. Process., vol. 31, no. 2, pp. 187-193, 2017.
3. Odbal and Z. F. Wang, ``Emotion analysis model using Compositional
4. Semantics," Acta Automatica Sinica, vol. 41, no. 12, pp. 2125_2137, 2015.
5. P. Li,W. Xu, C. Ma, J. Sun, and Y. Yan, ``IOA: Improving SVM based sentiment classification through post processing," in Proc. 9th Int. Workshop Semantic Eval., Jun. 2015, pp. 545_550.
6. J. Xu, D. Chen, X. Qiu, and X. Huang, ``Cached long short-term memory neural networks for document-level sentiment classification," in Proc. Conf. Empirical Methods Natural Lang. Process., Nov. 2016, pp. 1660_1669.
7. D. Tang, B. Qin, X. Feng, and T. Liu, ``Effective LSTMs for target dependent sentiment classification," in Proc. COLING 26th Int.l Conf.
8. Comput. Linguistics, Tech. Papers, Dec. 2015, pp. 3298_3307.
9. K. S. Tai, R. Socher, and C. D. Manning, ``Improved semantic representations from tree-structured long short-term memory networks," in Proc. 53rd Annu. Meeting Assoc. Comput. Linguistics, 7th Int. Joint Conf. Nat-ural Lang. Process., Jul. 2015, pp. 1556_1566.
10. P. Zhou et al., ``Attention-based bidirectional long short-term memory
11. networks for relation classification," in Proc. 54th Annu. Meeting Assoc.
12. Comput. Linguistics, Aug. 2016, pp. 207_212.
13. A. Galassi, M. Lippi, and P. Torroni. (Feb. 2019). ``Attention, please!Acritical review of neural attention models in natural language processing." [Online]. Available: https://arxiv.org/abs/1902.02181
14. S. Sabour, N. Frosst, and G. E. Hinton. (2017).``Dynamic routing between capsules." [Online]. Available: https://arxiv.org/abs/1710.09829
15. W. Zhao, J. Ye, M. Yang, Z. Lei, S. Zhang, and Z. Zhao. (2018). ``Investigating capsule networks with dynamic routing for text classification." [Online]. Available: https://arxiv.org/abs/1804.00538
16. J. Kim, S. Jang, S. Choi, and E. Park. (2018). ``Text classification using
17. capsules." [Online]. Available: https://arxiv.org/abs/1808.03976
18. N. Zhang, S. Deng, Z. Sun, X. Chen, W. Zhang, and H. Chen, ``Attention based capsule networks with dynamic routing for relation extraction," in Proc. Conf. Empirical Methods Natural Lang. Process. (EMNLP), Nov. 2018, pp. 986_992.
19. B. Zhang, X. Xu, M. Yang, X. Chen, and Y. Ye, ``Cross-domain sentiment classification by capsule network with semantic rules," IEEE Access, vol. 6, pp. 58284_58294, Oct. 2018
20. M. Shyamala Devi, Shakila Basheer, Rincy Merlin Mathew, "Exploration of Multiple Linear Regression with Ensembling Schemes for Roof Fall Assessment using Machine Learning", International Journal of Innovative Technology and Exploring Engineering, vol. 8, no.12, October 2019.
21. Shakila Basheer, Rincy Merlin Mathew, M. Shyamala Devi, "Ensembling Coalesce of Logistic Regression Classifier for Heart Disease Prediction using Machine Learning", International Journal of Innovative Technology and Exploring Engineering, vol. 8, no.12, October 2019, pp. 127-133.
22. Rincy Merlin Mathew, M. Shyamala Devi, Shakila Basheer," Exploration of Neighbor Kernels and Feature Estimators for Heart Disease Prediction using Machine Learning", International Journal of Innovative Technology and Exploring Engineering, vol. 8, no.12, October 2019, pp. 597-605.

23. M. Shyamala Devi, Shefali Dewangan, Satwat Kumar Ambashta, Anjali Jaiswal, Nariboyena Vijaya Sai Ram, "Backward Eliminated Formulation of Fire Area Coverage using Machine Learning Regression", International Journal of Innovative Technology and Exploring Engineering, vol. 8, no.12, October 2019, pp.1565-1569
24. M. Shyamala Devi, Ankita Shil, Prakhar Katyayan, Tanmay Surana, "Constituent Depletion and Divination of Hypothyroid Prevalance using Machine Learning Classification", International Journal of Innovative Technology and Exploring Engineering, vol. 8, no.12, October 2019, pp. 1607-1612
25. M. Shyamala Devi, Shefali Dewangan, Satwat Kumar Ambashta, Anjali Jaiswal, Sairam Kondapalli, "Recognition of Forest Fire Spruce Type Tagging using Machine Learning Classification", International Journal of Recent Technology and Engineering, Volume-8 Issue-3, pp. 4309 – 4313, 16 September 2019.
26. M. Shyamala Devi, Usha Vudatha, Sukriti Mukherjee, Bhavya Reddy Donthiri, S B Adhiyan, Nallareddy Jishnu, " Linear Attribute Projection and Performance Assessment for Signifying the Absenteeism at Work using Machine Learning", International Journal of Recent Technology and Engineering, Volume-8 Issue-3, pp. 1262 – 1267, 16 September 2019.
27. M. Shyamala Devi, Mothe Sunil Goud, G. Sai Teja, MallyPally Sai Bharath, "Heart Disease Prediction and Performance Assessment through Attribute Element Diminution using Machine Learning", International Journal of Innovative Technology and Exploring Engineering, vol. 8, no.11, pp. 604 – 609, 30 September 2019.
28. M. Shyamala Devi, Rincy Merlin Mathew, R. Suguna, " Regressor Fitting of Feature Importance for Customer Segment Prediction with Ensembling Schemes using Machine Learning", International Journal of Engineering and Advanced Technology, Volume-8 Issue-6, pp. 952 – 956, 30 August 2019.
29. R. Suguna, M. Shyamala Devi, Rincy Merlin Mathew, "Integrating Ensembling Schemes with Classification for Customer Group Prediction using Machine Learning", International Journal of Engineering and Advanced Technology, Volume-8 Issue-6, pp. 957 – 961, 30 August 2019.
30. Rincy Merlin Mathew, R. Suguna, M. Shyamala Devi, "Composite Model Fabrication of Classification with Transformed Target Regressor for Customer Segmentation using Machine Learning", International Journal of Engineering and Advanced Technology, Volume-8 Issue-6, pp. 962 – 966, 30 August 2019.
31. M. Shyamala Devi, Rincy Merlin Mathew, R. Suguna, "Feature Snatching and Performance Analysis for Connoting the Admittance Likelihood of student using Principal Component Analysis", International Journal of Recent Technology and Engineering, Volume-8 Issue-2, 30 July 2019. pp. 4800-4807.
32. R. Suguna, M. Shyamala Devi, Rincy Merlin Mathew, "Customer Segment Prognostic System by Machine Learning using Principal Component and Linear Discriminant Analysis", International Journal of Recent Technology and Engineering, Volume-8 Issue-2, 30 July 2019. pp. 6198-6203.
33. R.Suguna, M. Shyamala Devi, Rupali Amit Bagate, Aparna Shashikant Joshi, "Assessment of Feature Selection for Student Academic Performance through Machine Learning Classification", Journal of Statistics and Management Systems, Taylor Francis, , vol. 22, no. 4, 25 June 2019, pp. 729-739. DOI: 10.1080/09720510.2019.1609729ISSN: 0972-0510 (Print), 2169-0014 (Online).
34. R.Suguna, M. Shyamala Devi, Rupali Amit Bagate, Aparna Shashikant Joshi, "Assessment of Feature Selection for Student Academic Performance through Machine Learning Classification", Journal of Statistics and Management Systems, Taylor Francis, vol. 22, no. 4, 25 June 2019, pp. 729-739. DOI: 10.1080/09720510.2019.1609729ISSN: 0972-0510 (Print), 2169-0014 (Online).
35. Shyamala Devi Munisamy, Suguna Ramadass Aparna Joshi, "Cultivar Prediction of Target Consumer Class using Feature Selection with Machine Learning Classification", Learning and Analytics in Intelligent Systems, LAIS, Springer, vol. 3, pp. 604-612, June 2019.
36. Suguna Ramadass, Shyamala Devi Munisamy, Praveen Kumar P, Naresh P, "Prediction of Customer Attrition using Feature Extraction Techniques and its Performance Assessment through dissimilar Classifiers", Springer's book series entitled "Learning and Analytics in Intelligent Systems, Springer, LAIS vol. 3, pp. 613-620, June 2019.
37. M. Shyamala Devi, Rincy Merlin Mathew, R. Suguna, "Attribute Heaving Extraction and Performance Analysis for the Prophesy of Roof Fall Rate using Principal Component Analysis", International Journal of Innovative Technology and Exploring Engineering, vol. 8, no.8, June 2019, pp. 2319-2323.
38. R. Suguna, M. Shyamala Devi, Rincy Merlin Mathew, "Customer Churn Predictive Analysis by Component Minimization using Machine Learning", International Journal of Innovative Technology and Exploring Engineering, vol. 8, no.8, June 2019, pp. 2329-2333.

Modified Dynamic Hash Table with Threshold RSA for Dynamic and Public Auditing on Cloud Data

T. Kishore Babu,.Guruprakash C D

Abstract: ***Cloud storage is one of the major application in the cloud, which can provide the on-demand outsourcing data service for both organizations as well as individuals. The Data Integrity (DI) check in the cloud is applied by the user to ensure the integrity of data. The Third Party Auditing (TPA) technique is later introduced to check the cloud DI. Many research has been carried out in the public auditing to minimize the computation cost of the integrity check. The most existing method involves in lack of security and low computation overhead. In this research, the Modified Dynamic Hash Table with threshold Rivest, Shamir, and Adelman Algorithm (RSA) algorithm (MDHT-RSA) is proposed to improve the security and reduce the computation cost. The threshold RSA cryptography system increase the security by generating the secret key to the user and reduce the computation cost. The Modified Dynamic Hash Table (MDHT) is used to record the data information for dynamic auditing, which is located in the TPA. The MDHT is differed from the Dynamic hash table, that the MDHT doesn't contain the tag block whereas the dynamic hash table has the tag block. The MDHT-RSA is analyzed with the computation cost and compared with existing method. The experimental result proved that the MDHT-RSA method has low computation cost than state-of-art method in public auditing. The verification cost of the MDHT-RSA is 1.3 s while a state-of-art method DHT-PA has the 1.35 s for the 200 blocks of data.***

Index Terms**: *Cloud storage, Modified Dynamic Hash Table algorithm, Public Auditing, Tag Block and Third Party Auditing.***

I. INTRODUCTION

Many people can work on the same resource and easily share their data with each other in a cloud by using sharing and data storage services such as Google Drive. After storing the shared data in the cloud by user, the other people in a group can able to modify, access and share the latest version of data to another group of people [1]. In order to avoid the profit losses or to maintain the reputation among user, cloud owner may do the data error accidents in the worst case [2]. There is still a hesitation and discussion on the usage of cloud, even though proliferation and development of cloud computing are rapid, because data security is the major concern of user in cloud environment [3]. The users are unable to move their valuable data from the cloud, once the user loses their direct control on data, Specially in public cloud with multi-tendency and high consolidation [4]. The ordinary user's rarely accessed data may be neglect to keep or delete by Cloud Service Providers (CSPs) for saving more storage space, which is considered as most severe case [5].

With the concern on DI of cloud storage services, users wish to have a way of auditing the cloud server to ensure that the server stores all their latest data without any corruption [6]. The integrity of their data should be guaranteed by clients in the cloud storage system, but user cannot eliminate the weak cloud servers, which are vulnerable to security threats [7]. The three main objectives of security are integrity, availability and confidentiality, where integrity can be assured by auditing the cloud data i.e., verification of DI from an external party, has been an extensively investigated research problem in recent years [8]. In cloud, the DI is periodically check by introducing the TPA to help the end users for reducing the computational burden [9]. But, most of existing methods face challenges like high computation cost of TPA and still there is a need for improving the security of TPA [10]. To overcome the issues of security and computation cost, this research works designed an MDHT-RSA. The proposed method is analyzed and compared with the existing dynamic hash table method. The threshold RSA is designed because the algorithm is easy to implement, secure and also ensured the fast computation of MDHT with threshold RSA signature. There are no strict pre-conditions in RSA and also applied to almost all circumstances where secret sharing signature is required.

The organization of the paper is in the form of Related Works on recent techniques used to secure the data in section II, the proposed method is explained in section III, Experimental result illustrated in section IV. The conclusion of this research work is made in section V.

II. RELATED WORKS

The process of verifying the DI in the cloud is very difficult due to the increasing number of data in the cloud. The TPA auditing technique is used effectively to guarantee the DI and data encryption system is used in the TPA to secure the data. Recent method involves in the TPA aried [11-15] in this section to analyze its performance.

Anbuchelian, et al. [11] established secure cryptography hashing algorithm in the TPA to improve the security.

Revised Manuscript Received on September 2, 2019.

T. Kishore Babu, Department of CSE, Visvesvaraya Technological University, Gulbarga, India.

Dr. Guruprakash C D, Department of CSE, Sri Siddharatha Institute of Engineering & Technology, Maraluru, Tumakuru, India

After uploading the data, the user was provided with a private and public key for trustworthy retrieval of the data file, where modified RSA algorithm was used to generate these keys. The data files were effectively audit by using a multilevel hash tree algorithm occasionally. This method was tested with attacks and this provided the privacy against the attacks. The complexity is high for developed hash tree function, which needs more time for the auditing process.

Cheng Guo, et al. [12] generated a constant-size key to support the flexible delegation of decryption for cipher texts by key-aggregate authentication cryptosystem. The expense of this scheme was stable and solved the problem of key-leakage to share the data. The message in authentication key was denied to access and unable to copy the data, which was proven by this method. This showed that the method achieved secure data sharing and leakage-resilient in dynamic cloud storage. The developed methodology provides insecure data sharing in the condition of one to one solution.

Yue Zhang, et al. [13] developed a storage auditing scheme for key generation and method for updating the private key to achieve highly-efficient user revocation method. The total number of file blocks were totally independent of this revocation method which was possessed by revoked user in cloud. The private keys of non-revoked user group were just updated by user revocation method than authenticators of revoked user, which was observed by this technique. The security and computation cost of the method are needed to be optimized.

Daeyeong Kim, et al. [14] developed a public auditing scheme to provide the data privacy and integrity for the educational multimedia data. This auditing method supported fully dynamic data as well as protect the data against both the untrusted cloud server and the TPA under the loss and tamper attacks by using the random values and homomorphic hash function. The data security was preserved against TPA and cloud by combining the data block of homomorphic authenticator and data owner with random values. The computation cost between the user and the TPA is high because the protocol is needed to ensure security.

Hui Tian, et al. [15] designed a Dynamic Hash Table (DHT) which was located at TPA for recording the data property information for dynamic public auditing. DHT method reduced the communication overhead and computation cost by migrating the information to TPA from CSP. According to public key, the homomorphic authenticator was combined with random masking which was generated by TPA to support the privacy preservation. The batch auditing was achieved by employing the bilinear maps and Boneh-Lynn-Shacham (BLS) signature. When compared with previous scheme, the DHT method reduces the storage costs, communication and computation cost by achieving secured auditing in clouds. The table size can be reduced to improve the effectiveness and decreasing the computation cost.

A. Problem Statement

The traditional cloud data storage service includes numerous challenging design issues, which have a profound influence on the security and performance of the overall system. The significant issues of cloud auditing process is addressed in the following sections.

- The privacy preserving of cloud user's data is a significant task during the whole auditing process. But, the cloud server is not a fully trusted entity and outsourced data in cloud may revealed and significant information may have leaked.
- In complex methods, the computation overheads of TPA increases, which will automatically increase the computation time of encryption systems.
- Multi-tenancy implies the sharing of the application resources by more than one user. Hence, lack of confidentiality occurs due to multi-tenancy.
- In data auditing process, the traditional methods used the number of Meta data, which is stored in a huge dataset, and consumed more storage space.

III. PROPOSED METHOD

In the cloud, the DI is checked by auditing process, which will reduce the user's computation load. The security of cloud data is improved by verifying the DI in cloud using various existing methods. In this research work, MDHT-RSA algorithm is developed to reduce the computation cost and also to increase the security of outsourced data. The RSA cryptographic system is used to secure the data and MDHT to store the records of the dynamic changes in the cloud.

A. System Model

Figure 1 shows the auditing system used in this research work for cloud storage, which consists of TPA, cloud users and Cloud Storage Service (CSS). The cloud users are the data owners, who have a bulk of data to be stored in CSS. A massive amount of computational resources and storage space are effectively handled by CSP, which is used to manage the CSS. The CSP managed and maintained the user's data which is stored in CSS, where the user can dynamically update or access their remote data whenever they need. Most of user are lacked in auditing the outsourced data due to less expert and capabilities in this process, which are effectively handled by TPA.

Fig. 1. The system architecture of TPA

1) Data Owner:

The data are stored in the cloud by the data owner, which can interact with CSP for managing their stored data on cloud.

Without having the local copy of data, the security of data should be periodically verified by the owner. If they don't have time or resource to verify the security, these jobs can be assigned to trusted TPA by the data owner.

2) Cloud Service Provider:

The distributed cloud storage servers are built with major resources and managed by CSP, which is also offered software or storage services to the end user over the Internet. The major role of the CSP is to response the verifier queries and maintain the data properly.

3) Third Party Auditor:

The vulnerability of user's privacy data is improved by the auditing process and the DI which is stored in the cloud is checked by TPA. The outsourced data can be managed or monitored under the delegation of data owner which is considered as a major responsibility of TPA. Whenever TPA receives the DI verification request from the data owner, immediately TPA send the challenge request to the cloud server. The TPA receives the proper response from cloud auditing task and sends the result back to the user. In proposed MDHT, these three entities performed the following activities such as:

1. The pre-processed files are sent to CSP by the data owner and also sends the metadata to TPA or user can keep locally for verifying the integrity later.
2. Then, files are stored by CSP, where metadata is stored by TPA.
3. The validity of response is checked and generated a challenge by verifier (either TPA or user), then send it to CSP. If the response is valid, it will return 1, otherwise return 0.
4. The response is generated by CSP, then sends to verifier.
5. An update request is generated by data owner and send to CSP for verification.
6. The CSP updates data and generates an update response based on data owner's requests.
7. When the insertion or modification process occurred, the updated metadata should be stored by TPA.

Even though TPA is secure, there are also some challenges faced by these models because of CSP. These threat model are described as below.

B. Threat Model

In this work, consider the CSP as semi-honest, but it is a curious server for securing the end user's data. A passive attacker is a probabilistic polynomial time adversary, which is a traditional honest-but-curious model and follows the designed specification correctly. An ability-limited active attacker adversary is considered as semi-honest-but-curious model, which can able to modify the designed specifications such as insert, update, delete and return only a small portion of search results, instead of retrieving all the query results.

C. Bilinear Mapping

Let $G1, G2, G_T$ be three cyclic multiplicative groups with the prime order q . Let g_1, g_2 be the generators of groups An admissible pairing $e: G1 \times G2 \to GT$, which satisfies the following three properties:

– Bilinear: If $u \in G_1, v \in G_2$ and $a, b \in Z_q^*$, then $e(ua, vb) = e(u, v)ab$;

– Non-degenerate: There exists a $g_1 \in G_1, g_2 \in G_2$ such that $e(g_1, g_2) \neq 1$;

– Computable: If $u \in G_1, v \in G_2$ one can compute $e(u, v) \in G_T$ in polynomial time.

D. Modified Dynamic Hash Table

This is popular to introduce an authenticated data structure to achieve dynamic auditing and this DHT from the research [15] is used in this experiment. During the verification and updation process, the MHT-based auditing scheme and PDP based skip list face some challenges like large communication overhead and heavy computational costs of TPA [16,17]. Thus, the changes in data blocks are recorded and the hash values of every block are generated by using Index Hash Table (IHT), which is proposed by Zhu et al. [18] in verification process. The IHT are inefficient for updation process like insertion and deletion because of sequence structure, this leads to the adjustments in average elements i.e. $N/2$, where N is a total number of blocks.

In addition, the regeneration of block tags is occurred by the modification of block numbers (Bi) of that corresponding blocks during insertion or deletion process. This process will eventually cause high computation costs of user and communication overhead, which leads to inefficient of IHT. Therefore, a new data structure called DHT is developed to overcome the issues of IHT and provides better auditing efficiency. Like IHT, the latest Version of Information (VI) user's data is tracked by employing the TPA in DHT for auditing process. There are two basic elements in DHT such as file and block elements. Each file element consists of the File identifier (ID_i) and the index number (NO_i) of the given file (e.g. F_i). The files are stored in array-like structure by using pointer that indicates the first block element, and every file is arranged by a linked list with the corresponding file element as the header node.

The DHT operations are classified into two types such as file operations and block operations, where search, insert, modify and delete mechanisms are carried out on both the file operations. According to index, the files can be searched for finding the location of elements, and manipulations on both elements for file and blocks are done by other operations. The file elements are inserted into arrays by using insertion and the linked list are constructed that contains corresponding block elements. The files and its elements can be deleted from the linked list using delete operation and modification can be carried on both the elements of files and blocks.

The insertion and deletion of blocks in IHT is significantly improved by using the linked lists and DHT. Further, the hash values of VI records in DHT will not be influenced by blocks of insertion and deletion in IHT. The communication overhead and computational costs of CSP are significantly reduced by MDHT-RSA in the updation process, when compared with IHT scheme. During the verification, the

search operation cost of DHT is more than IHT, because the material impact on whole verification time cannot be able to neglect by DHT. The verification time of MDHT scheme is validated and showed that it is substantially smaller than the IHT.

E. Threshold-Rivest, Shamir, and Adelman Algorithm (Threshold-RSA)

The detailed descriptions of these algorithm (RSA) of three phases are described in the following sections.

1) Setup Phase

Before storing the file in cloud, it should be pre-processed by user for ensuring the availability, DI and confidentiality of file.

- **Encoding:** The file is encoded by user to check the availability of data in cloud.
- **KeyGeneration:** In this algorithm, the user generates private and public key pair for the later processing the file in the propose system.
- **Encryption:** In case, the data owner wants to ensure the data Confidentiality, the users encrypts the data using public key cryptography.
- **MetadataGeneration:** The metadata for each block of file is computed by user for verifying the DI stored in cloud storage system.

2) Verification Phase:

Whenever the user wants to verify the data that is stored in the cloud servers, the verifier (either user himself or his arranged agent TPA) checks the DI without having the local copy of data through Challenge-Response Protocol. The verification phase consists of three methods described below.

- **Challenge:** A random challenge is created and send it to CSP by verifier to check the DI.
- **Response:** Once a challenge request received from the verifier, the integrity proof as response is generated by CSP based on the challenge and forward back to verifier.
- **Check Integrity:** The response received from CSP is compared with previously computed metadata and identified whether the updated proof is valid or not by verifier. To hold the Integrity, the response must be equal with the metadata otherwise it indicates data have corrupted.

3) Secret sharing RSA Threshold Algorithm

A new threshold RSA algorithm is developed by applying the digital signature to secret sharing scheme, that are as follows:

Digital signature scheme is a triple (KeyGen, Sign, Ver) of efficient algorithms.

- KeyGen is the key generation algorithm. This outputs a key pair (P,S). P is the public key and S is the secret or private key.
- Sign is the signing algorithm. Given a message μ and the secret key S, it outputs a digital signature σ.
- Ver is the verification algorithm. Given a message μ, the corresponding signature and the public key P, it succeeds if σ is a valid signature of the message μ.

There are four major components presents in a RSA threshold signature scheme, that are described as below:

- Consider n as security parameters, generation of Q_N using k number of elements, singing servers as l,t as threshold parameters and ω is a random string, which are all taken as input for key generation algorithm and produce the outputs as (N,e) is a public key, where n is the size in bits of N, the private keys $d_1,...d_l$ only known by the correct server and for each $u \in [1,k]$ a list $v_u, v_{u,1} = v_u^{d_1}, ..., v_{u,l} = v_u^{dl} \bmod N$ of verification keys.
- The input of a share signature algorithm is (N,e), an index $1 \le i \le l$, the private key d_i and a message m; this outputs a signature share $s_i = x^{d_i} \bmod N, where\, x = H(m)$ and $H(.)$ is a hash-and-pad function, and a proof of its validity
- $proof_i \left(for\ all\ u \in [1,k], \log_{vu} v_{u,i} = \log_x s_i \right)$
- The public key (N,e), a message m, a list $s_1,...,s_l$ of signature shares, for each $u \in [1,k]$ the list $v_u, v_{u,1}, ...v_{u,l}$ of verification keys and a list $proof_1,...proof_l$ of validity proofs are considered as input and a signature s may be an output of combining algorithm.
- Consider, (N,e) as a input public key, m as message and s as signature for verification algorithm and it outputs a bit b indicating whether the signature is correct or not.

In this research work, verification process of the proposed dynamic auditing protocol is presented and also design consideration for efficiency and security are introduced which are explained in the following section.

F. Blockless verification

Without retrieving the original data, the public auditing is achieved and the block tags are generated for data blocks. In verification process, block tags are authenticated instead of original data blocks. In this research work, RSA and BLS are employed, but BLS preferred more for shorter length of each block tag.

G. Sampling verification:

Given the huge amount of data outsourced in the cloud, it is inadvisable to challenge all data blocks for checking the integrity. Instead of checking the whole data files, checking a small portion of data files is more suitable for CSP and TPA to achieve the high verification accuracy, is known as sampling verification. The previous studies have demonstrated the rationality and feasibility of this strategy. Consider t is a fraction of given data, which is corrupted, the detection probability of the verification by checking randomly sampled c blocks is $P = 1-(1-t)c$.

H. Privacy preservation:

The data proof A is generated for preventing the privacy leakage, the M sampled blocks with R random masking is provided by TPA and u is considered as a public key. Under DL assumption, the process of obtaining the user′s privacy data is computationally infeasible for TPA, even though it knows the $A, R,$ and u .

I. Data Freshness:

In existing works like DAP [19], data proof is computed by CSP, but the linear combination of sampled blocks is not computed, which is a major issue of CSP. Due to the continuous updation of dynamic data, dishonest behavior is easily identified in dynamic data auditing [20]. i.e. the CSP could not pass the verification without actually storing the latest version of the data in the dynamic audit. However, the archived data is not updated frequently, the CSP may indeed to have the chance to pass the verification. Therefore, in future, different and more proper auditing methods are developed for diverse data.

IV. Results and Discussion

The computation load of user is decreased by checking the DI in the cloud, and this process are carried out by TPA. Many research has been conducted to improve the effectiveness of the integrity check and reduce the computation cost. In this research, RSA encryption system is proposed for key generation and computation cost is reduced by MDHT. The experiments are implemented using JAVA 1.8 Netbeans 8.2 MySQL 8 on a computer with Intel Core i5 CPU 2.2 GHz with 8.00 GB RAM. In this section, the proposed MDHT-RSA method is analyzed with the different computation cost and compared with the existing method. To validate the efficiency of proposed MDHT-RSA method, the experiments are conducted on verification time, processing time, computation cost and searching time when compared with existing methods such as DHT-PA [15], IHT-PA [18] and DAP [19].

A. Computation cost in the setup phase

The computation cost of the setup phase is calculated for the existing and proposed method for the different block number. The values are shown in Table 1. The computation time of existing and proposed method is shown in Fig. (2).

Table I. Setup phase computation cost

Block Number	IHT-PA	DAP	DHT-PA	MDHT-RSA
10	0.33	0.2	0.18	0.16
15	0.46	0.25	0.23	0.21
40	1.02	0.97	0.92	0.87
60	1.54	1.24	1.2	1.07
80	2.14	1.82	1.73	1.63
100	2.46	2.18	2.12	2.11
120	2.62	2.72	2.57	2.49
140	2.82	3.17	3.02	3
160	4.24	3.72	3.51	3.45
180	4.98	4.12	3.74	3.72
200	5.31	4.78	3.67	3.49

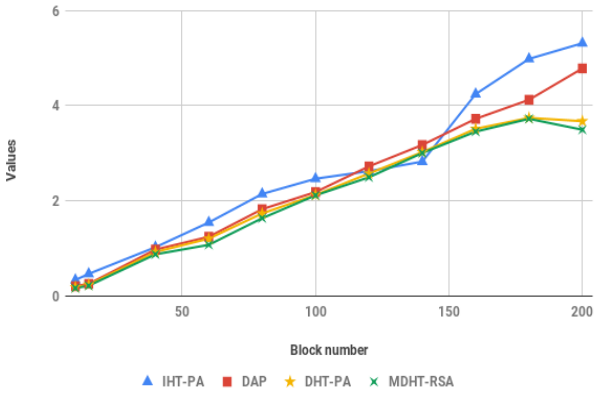

Fig. 2. Setup processing time for different blocks

This shows the computation cost is propositional to the block size. The proposed method has less computation time compared to that other existing method. The proposed MDHT-RSA has the computation time of 3.49 second for the 200 block size, while state-of-art method DHT-PA has the computation time of 3.67 seconds for same block size. When the block size is 10, the proposed MDHT-RSA achieved 0.16 seconds whereas the existing method IHT-PA achieved 0.33 seconds for same block size.

B. Searching Time

The verification of searching time of the existing and proposed method is measured in the different block size which are given in Table 2. Figure. (3) shows that the searching time of the public auditing methods in the different block size.

Table II. Search time for proposed MDHT-RSA

Block Number	IHT - PA	DAP	DHT- PA	MDHT-RSA
10	262	34	32	30
25	187	34	32	30
30	124	34	32	30
50	98	34	32	30
100	81	34	32	30
200	76	34	32	30
300	65	34	32	30
400	60	34	32	30
500	52	34	32	30

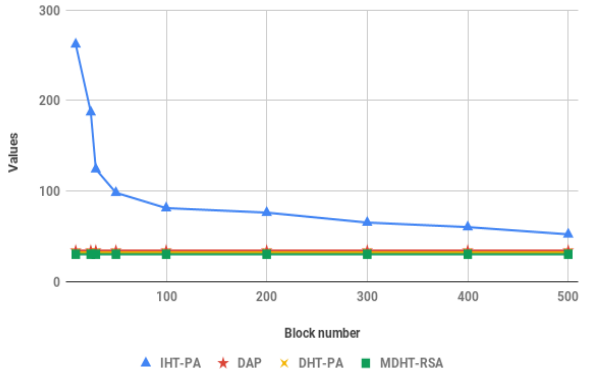

Fig. 3. Searching time of MDHT – RSA

The proposed MDHT-RSA method has a lower computation time compared to the other existing method. The searching time is low for the various block size and block size are increased, which decreases the searching time of the MDHT. The searching time during verification of the proposed MDHT-RSA is 30 ms for the 500 block size in KB, while the existing method has 32 ms for the same block size. In this searching time, all other methods are constant at certain point in block size, but IHT-PA alone varies the searching time depends on block size. For instance, IHT-PA achieved 26 ms for 10 block size, 76 ms for 100 block size and 52 ms for 500 block size.

C. Computation in Verification time

The verification time of the different block size is measured for the existing and proposed method, as shown in the Table 3 and Fig. (4).

Table III. Verification Time of MDHT – RSA

Block Number	IHT - PA	DAP	DHT-PA	MDHT-RSA
10	2.24	1.68	1.5	1.42
20	2.25	1.69	1.47	1.52
30	2.27	1.71	1.46	1.41
50	2.28	1.71	1.45	1.39
70	2.28	1.71	1.38	1.41
100	2.32	1.71	1.36	1.34
150	2.34	1.72	1.35	1.2
200	2.37	1.73	1.35	1.2

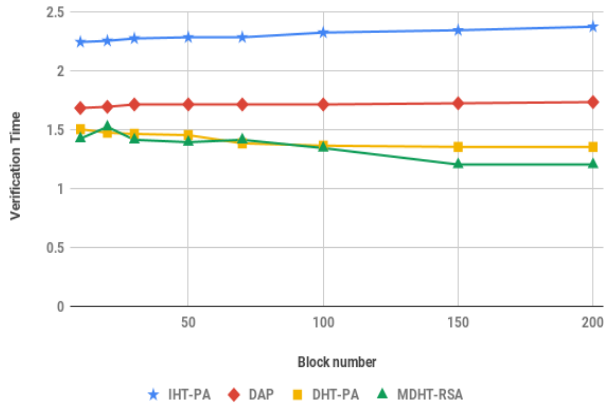

Fig. 4. Verification of MDHT-RSA for different block size

The proposed MDHT-RSA has the lower verification time compared to the other existing method. The verification time of the DHT-PA and MDHT-RSA methods has the much lower computational time than IHT-PA due to the significantly outweigh the disadvantage include by searching operation. When compared with other existing techniques, the proposed method achieved 1.2 sec for block number 200.

D. Operation time for Block Insertion

The computation cost of the block insertion for the existing and proposed method is calculated in this experimental setup. The computation cost for the different file size is measured varying 1 to 10 GB of data is measured and shown in Table 4 and Fig. (5).

Table IV. Block Insertion of MDHT-RSA

Block Number	IHT - PA	DAP	DHT-PA	MDHT-RSA
1	0.02	0.02	0.02	0.02
2	0.1	0.1	0.05	0.05
3	0.18	0.17	0.06	0.05
4	0.21	0.21	0.09	0.08
5	0.28	0.26	0.1	0.1
6	0.32	0.31	0.12	0.12
7	0.41	0.41	0.15	0.147
8	0.46	0.45	0.18	0.173
9	0.52	0.51	0.19	0.182
10	0.57	0.55	0.21	0.205

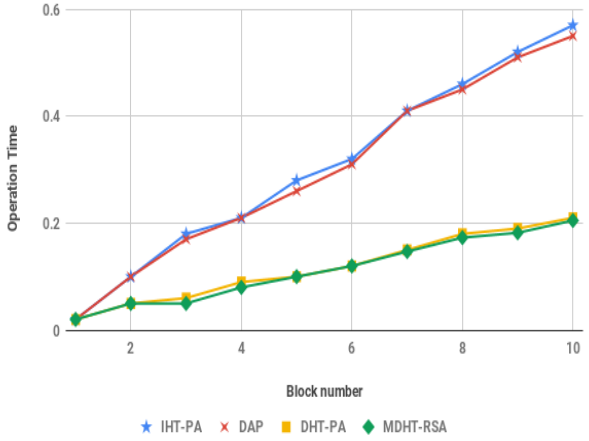

Fig. 5. Operation time for Block Insertion

The proposed MDHT-RSA has lower computation time compared to the other existing method. The MDHT-RSA has the computation time of 0.20 s compared to the state-of-art method which has 0.21 s for the file size 10 GB. When the size of the file is low, all the methods have the same computation time of 0.02 second. But, as the size of file increases, the computation time of existing methods are also increased.

E. Operation time for Block Updation

The computation time for the updating operation is measured for the existing and proposed method. The computation time of updating process for the different file size is measured and shown in Table 5 and Fig. (6).

Table V. Computation time for Block Updation

Block Number	IHT - PA	DAP	DHT- PA	MDHT-RSA
1	1.58	1.58	1.08	1.04
2	1.59	1.59	1.1	0.9
3	1.6	1.6	1.12	1.11
4	1.62	1.62	1.21	1.18
5	1.64	1.64	1.24	1.22
6	1.66	1.66	1.26	1.22
7	1.72	1.72	1.27	1.25
8	1.73	1.73	1.28	1.24
9	1.75	1.75	1.32	1.3
10	1.76	1.76	1.41	1.38

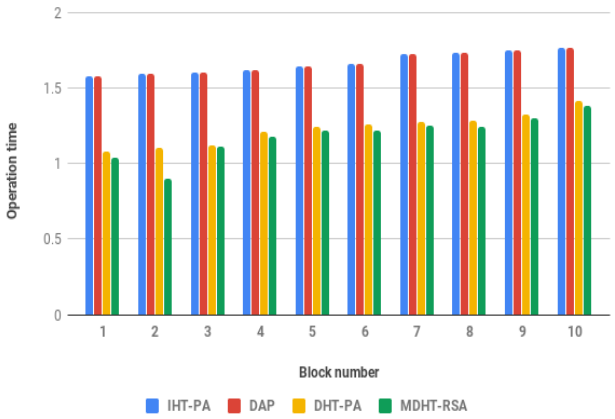

Fig. 6. Operation Time for Block Updation

This shows that the proposed MDHT-RSA has the lower computation time compared to the other existing method. The MDHT-RSA has the computation time of updating process is 1.38 s while existing method has computation time of 1.41 s for 10 GB file. The computation time for block updation are constant for both existing methods such as IHT-PA and DAP in all block size. But, the existing technique DHT-PA slightly varies from MDHT-RSA computation time for block updation.

F. Operation time for Block Deletion

The computation time of the block deletion is calculated for the different file size, which are analyzed for the existing and proposed method. The computation time is compared for the different methods in public auditing and shown in Table 6 and Fig. (7).

Table VI. Computation time for Block Deletion

Block Number	IHT - PA	DAP	DHT-PA	MDHT-RSA
1	0.02	0.02	0.02	0.02
2	0.1	0.1	0.05	0.05
3	0.18	0.17	0.06	0.05
4	0.21	0.21	0.09	0.07
5	0.28	0.26	0.1	0.1
6	0.32	0.31	0.12	0.115
7	0.41	0.41	0.15	0.142
8	0.46	0.45	0.18	0.171
9	0.52	0.51	0.19	0.196
10	0.57	0.55	0.21	0.208

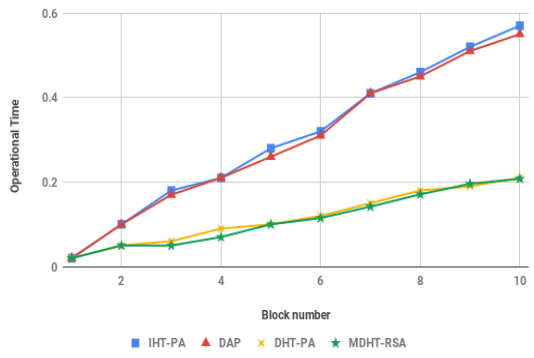

Fig. 7. Operational Time for Block Deletion of MDHT-RSA

The MDHT-RSA has the lower computation time compared to the other existing methods. The MDHT-RSA method has the computation time of 0.2 sec compared to the state-of-art method 0.21 sec. The deletion time of MDHT-RSA achieved 0.115 sec for block size 6, whereas the existing method IHT-PA achieved 0.32 sec for same block size. The MDHT-RSA didn't attain great performance in block deletion time for different block size. The method needs further improvements for achieving better performance in computation time for different block sizes.

G. Auditing Time for MDHT-RSA

The experiments also evaluate the performance of MDHT-RSA in the batch auditing scenario and compare it with IHT-PA and DAP. The experimental results are as shown in Table 7 and Fig. 8.

Table VII. Auditing Time of MDHT-RSA

Block Number	IHT - PA	DAP	DHT-PA	MDHT-RSA
1	1.95	1.81	1.58	1.04
2	1.92	1.79	1.59	0.98
3	1.86	1.76	1.6	1.09
4	1.83	1.75	1.62	1.15
5	1.79	1.7	1.67	1.21
6	1.76	1.69	1.65	1.23
7	1.72	1.66	1.75	1.22
8	1.73	1.64	1.74	1.26
9	1.75	1.67	1.79	1.31
10	1.76	1.69	1.76	1.39

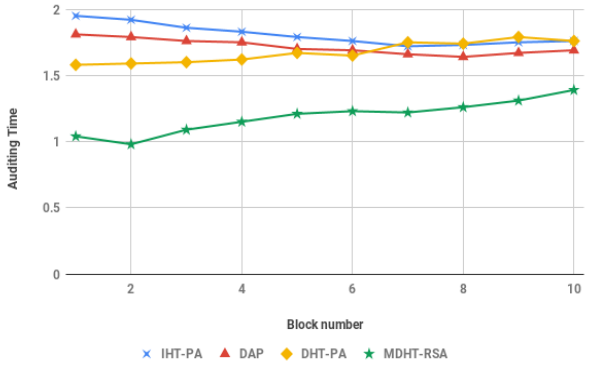

Fig. 8. Auditing Time for Proposed MDHT-RSA

The experimental results suggested that the batch auditing can't handle only verifications from multiple-users simultaneously, and while performing the individual auditing for multiple times, this MDHT-RSA reduces the computational costs of TPA. Also, the results proved that the batch auditing protocol in MDHT-RSA is more efficient than that in DAP, DHT-PA and IHT-PA. The MDHT-RSA has lower computation time compared to the other existing method. The security of the method is increased by using the secure key generation method. Hence, the proposed method can be applicable to practical use in the cloud auditing system.

V. Conclusion

Nowadays, the cloud storage system becomes popular for the different kinds of services storing, managing and processing the large amount of data. The data security is an important to concern in the cloud storage due to the development of different attacks on the cloud. The computation load of user is minimized by checking the DI of data using TPA in the cloud.

The various methods are developed for the TPA to check the DI without increasing the computation cost of the system. In this research work, the security is increased by RSA encryption algorithm and dynamic changes are recorded by MDHT which is used to reduce the computation cost of TPA in cloud system. MDHT is two-dimensional data structure is used instead of the DHT. The tag block is removed in the MDHT and this increase the computation cost of the system. The insertion and deletion are carried out by the identification block instead of tag block that helps to increase the efficiency. The cost of the MDHT is measured for the different file block and compared with existing method. The result shows that MDHT has lower computation cost compared to the other existing method in cloud auditing. The verification time of the MDHT-RSA is 1.2 sec while other existing methods such as DHT-PA and IHT-PA has the verification time of 1.35 sec and 2.37 sec. The results of MDHT-RSA for data insertion, updation, deletion and auditing process achieved 0.205 sec, 1.35 sec, 0.208 sec and 1.39 sec for block size 10. In future work, the proposed MDHT-RSA algorithm will be improved to audit for all types of cloud data by implementing different audit strategies.

REFERENCES

1. B. Wang, B. Li, and H. Li. (2015). Panda: Public auditing for shared data with efficient user revocation in the cloud. *IEEE Transactions on services computing*, *8(1)*, pp.92-106.
2. A. Fu, S. Yu, Y. Zhang, H. Wang, and C. Huang. (2017). NPP: a new privacy-aware public auditing scheme for cloud data sharing with group users. *IEEE Transactions on Big Data*.
3. C. Liu, J. Chen, L. T. Yang, X. Zhang, C. Yang, R. Ranjan, and R. Kotagiri. (2014). Authorized public auditing of dynamic big data storage on cloud with efficient verifiable fine-grained updates. *IEEE Transactions on Parallel and Distributed Systems*, *25(9)*, pp. 2234-2244.
4. C. Liu, R. Ranjan, C. Yang, X. Zhang, L. Wang, and J. Chen. (2015). MuR-DPA: Top-down levelled multi-replica merkle hash tree based secure public auditing for dynamic big data storage on cloud. *IEEE Transactions on Computers*, *64(9)*, pp. 2609-2622.
5. M. Thangavel and P. Varalakshmi. (2018). Enhanced DNA and ElGamal cryptosystem for secure data storage and retrieval in cloud. *Cluster Computing*, *21(2)*, pp. 1411-1437.
6. J. Yuan, and S. Yu. (2015). Public integrity auditing for dynamic data sharing with multiuser modification. *IEEE Transactions on Information Forensics and Security*, *10(8)*, pp. 1717-1726.
7. T. Y. Youn, K. Y. Chang, K. H. Rhee, and S. U. Shin. (2018). Efficient client-side deduplication of encrypted data with public auditing in cloud storage. *IEEE Access*, *6*, pp. 26578-26587.
8. H. Tian, F. Nan, H. Jiang, C. C. Chang, J. Ning, and Y. Huang. (2019). Public auditing for shared cloud data with efficient and secure group management. *Information Sciences*, *472*, pp. 107-125.
9. J. Yu, K. Ren, C. Wang, and V. Varadharajan. (2015). Enabling cloud storage auditing with key-exposure resistance. *IEEE Transactions on Information forensics and security*, *10(6)*, pp. 1167-1179.
10. J. Shen, J. Shen, X. Chen, X. Huang, and W. Susilo. (2017). An efficient public auditing protocol with novel dynamic structure for cloud data. *IEEE Transactions on Information Forensics and Security*, *12(10)*, pp. 2402-2415.
11. S. Anbuchelian, C. M. Sowmya, and C. Ramesh. (2017). Efficient and secure auditing scheme for privacy preserving data storage in cloud. *Cluster Computing*, pp. 1-9.
12. C. Guo, N. Luo, M. Z. A. Bhuiyan, Y. Jie, Y. Chen, B. Feng, and M. Alam. (2018). Key-aggregate authentication cryptosystem for data sharing in dynamic cloud storage. *Future Generation Computer Systems*, *84*, pp.190-199.
13. Y. Zhang, J. Yu, R. Hao, C. Wang, and K. Ren. (2018). Enabling efficient user revocation in identity-based cloud storage auditing for shared big data. *IEEE Transactions on Dependable and Secure Computing.*
14. D. Kim, H. Kwon, C. Hahn, and J. Hur. (2016). Privacy-preserving public auditing for educational multimedia data in cloud computing. *Multimedia Tools and Applications*, *75(21)*, pp.13077-13091.
15. H. Tian, Y. Chen, C. C. Chang, H. Jiang, Y. Huang, Y. Chen, and J. Liu. (2017). Dynamic-hash-table based public auditing for secure cloud storage. *IEEE Transactions on Services Computing*, *10(5)*, pp.701-714.
16. C. C. Erway, A. Küpçü, C. Papamanthou, and R. Tamassia, (2015). Dynamic provable data possession. *ACM Transactions on Information and System Security (TISSEC)*, *17(4)*, pp. 15.
17. Q. Wang, C. Wang, K. Ren, W. Lou, and J. Li. (2011). Enabling public auditability and data dynamics for storage security in cloud computing. *IEEE transactions on parallel and distributed systems*, *22(5)*, pp. 847-859.
18. Y. Zhu, G. J. Ahn, H. Hu, S. S. Yau, H. G. An, and C. J. Hu. (2013). Dynamic audit services for outsourced storages in clouds. *IEEE Transactions on Services Computing*, *6(2)*, pp.227-238.
19. K. Yang, and X. Jia. (2013). An efficient and secure dynamic auditing protocol for data storage in cloud computing. *IEEE transactions on parallel and distributed systems*, *24(9)*, pp. 1717-1726.
20. H. Jin, H. Jiang, and K. Zhou. (2016). Dynamic and public auditing with fair arbitration for cloud data. *IEEE transactions on cloud computing*, *6(3)*, pp. 680-693.

AUTHORS PROFILE

Mr. Tunuguntla Kishore Babu is a research scholar from Visvesvaraya Technological University (VTU), Belagavi, karnataka in computer science and engineering and currently working as Assistant professor in Dept. of CSE in Andhra Loyola institute of engineering and technology, Vijayawada and has experience of 7 years in teaching and 3 years in research published various papers in international conferences/ journals. Area of interest Cloud Computing, Data mining and information security.

Dr. Guruprakash C D is currently working as professor in department of computer science and engineering SSIT, Tumkur Karnataka and has experience of 17 years in teaching, published various papers in international conferences/ journals. Area of interest Networking.